Instituto de Ciencia de Materiales de Madrid

CSIC

Universidad de Oviedo

Universidad de Oviedo

Física de la Materia Condensada y Nanotecnología

∞∞∞

Doctoral Thesis

Simulation of vibrational properties of nanostructures

Author:
Diego
Martínez Gutiérrez

Supervisor:
Dr. Víctor Ramón
Velasco Rodriguez

March 13, 2014

Dedicado a
mi familia

Agradecimientos

Quisiera expresar la más profunda gratitud a todas las personas sin las cuales esta tesis no habría sido posible. En primer lugar quiero agradecer la guía y apoyo ofrecido por Victor R. Velasco, mi director de tesis, a la Profesora María del Carmen Muñoz de Pablo y la Dra. Silvia Gallego.

Gracias a los compañeros de despacho Lucía y Carlos durante los primeros años en el I.C.M.M. y Aurora, Beatriz, Ji Chao y Bruno en los últimos. Recuerdo las discusiones,comentarios y bromas con Lucía y Carlos (Carlos y Lucía) consultando cada dos por tres las definiciones de palabras en el diccionario de la lengua española "buscón" de la RAE).

También quiero dar las gracias a los compañeros con los que he compartido las comidas y otros "eventos sociales", Fernando, Míriam, Ricardo, Samuel, Álvaro, Jángel, María, Covadonga, Sigmund, Mathias y Robert entre otros.

Quiero dar las gracias a los profesores de la Universidad de Oviedo que de alguna forma lograron meter algo con sentido en mi cabezota, María Vélez Fraga, Luis Manuel Álvarez Prado, Javier Ignacio Díaz, José Ignacio Martín Carbajo, Carlos Quirós, Jaime Ferrer Rodríguez, Jose María Alameda Maestro, y amigos como Víctor Manuel García Suarez (alias VIMAGASU), Lucas Fernández Seivane y otros muchos compañeros cuyos nombres no logro recordar. Asimismo a los profesores de la Universidad Autónoma de Madrid como al Profesor Fernando Flores Sintas por lo aprendido durante los cursos de Doctorado.

He de agradecer asimismo a los investigadores y estudiantes de la Universidad *degli Studi-Bicocca* de Milán y más especialmente al Profesor Leo Miglio por los seis meses que pasé con ellos aprendiendo y disfrutando.

En terreno personal, quiero agradecer a mi familia por soportarme tanto cuando estaba con ellos como cuando estaba alejado de ellos. Sin su apoyo nunca hubiera sido posible acabar ...

¡Muchas gracias a todos!

iv

Abstract

In this thesis we study the vibrational properties of different nanostructures by using the continuum and the discrete models.

The continuum method is based on the elasticity theory while the discrete method employs the molecular dynamics.

With the continuum method we obtain the dispersion curves and the displacement patterns of the vibrational modes. We also calculate the radial acoustic modes of cylinders, cylindrical shells, "core-shell" and composite cylinders of general anisotropy.

We finally use the Surface Green Function Matching method to obtain the acoustic waves dispersion curves in superlattices formed by anisotropic hexagonal crystallographic materials.

With the discrete method, we develop a technique for the calculation of the density of states and the Raman spectra from the data obtained by the molecular dynamics approach.

Contents

List of Figures

List of Tables

xvii

Chapter 1

Introduction

This thesis describes the work I have done during my PhD, under the supervision of Prof. Victor R. Velasco, on the study of phonons in nanometric structures.

The famous Richard Feynman's talk (1959) to the American Physical Society, entitled "There's Plenty of Room at the Bottom" [1] discussed microtechnology as a frontier to overcome. Feynman suggested the possibility to manipulate matter at atomic levels in order to achieve electronic or mechanical systems with molecular size levels. At his speech conclusion, Feynman told the audience that a new world of possibilities would arise that could radically change our technology.

Also, as shown by K. Eric Drexler [2] , Nature already exhibits that kind of systems inside all biological life forms. Nevertheless, artificial systems can go far beyond those biological models. Today, the subject generally known as nanotechnology is an interdisciplinary science aiming to the understanding, fabrication and control of such atomic scale systems.

Computer simulations are a useful instrument to provide insights and answers on the behaviour of complex systems, which otherwise could only be treated as rough approximations. Basically, a computer simulation is a test on the theoretical model, and as such it had been used to discriminate between well-founded approximations and ideas that were plausible but wrong. If the model is accurate, it may even be possible to assist in novel interpretations of experimental data and contribute to the discovery of new results. As illustrated in figure 1.1 computer simulations work as a bridge between theoretical models and experimental results.

This connecting role between theoretical predictions and experimental results, and the way the simulations are tested and analysed are the basis for the term "computer experiments" [4].

While it may be almost impossible to perform experiments under certain
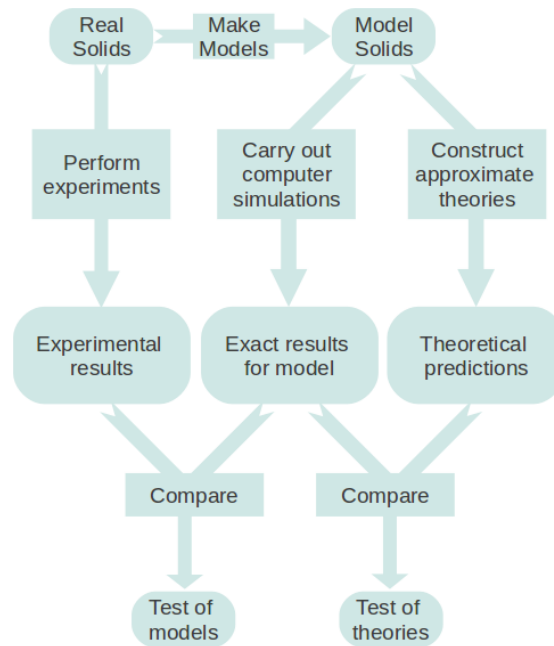
Figure 1.1: Connection between experiments, theory and computer simulation.(Source: Samuel Peláez Machado [3] with thanks)

extreme values of temperature, pressure, radiation, etc., a computer simulation of a material in, for example, a shock wave or a planetary core, would be perfectly feasible. Also, subtle details of molecular motion and structure playing an important part in phenomena such as, for example the heterogeneous catalysis, or thermal phonon percolation by defects scattering, that are difficult to probe experimentally can be extracted readily from a computer simulation. Finally, while the speed of some physical events constitutes an experimental difficulty, it is not a hindrance to computer simulations. Therefore a wide range of physical phenomena, from the atomic or even nuclear scale to the galactic one, may be studied using some form of computer simulation.

In the area of nanotechnology the usage of continuum models, if employed with care, is of substantial value in the design and analysis of nanoscale systems. Continuum models also represent the first step into a hierarchy of approximations of increasing accuracy and complexity. On the other hand, the use of computer molecular dynamics simulation gives us the ability to make "experiments" providing the knowledge of the exact positions and velocities of each particle as they evolve in time. Of course, the model used in such "experiments" determines the accuracy, and the available computa-

tional resources determine the possible models.

In most instances the use of approximations is unavoidable. While real nano-systems are governed by the laws of quantum mechanics, these systems typically contain many electrons and nuclei. This usually means that the calculation of exact solutions with full quantum theories is not possible. Nowadays the most fundamental technique, the so called *ab-initio*, is the density functional theory which is a stationary electronic state approximation on the Schrödinger equation, which approximates the Dirac equation, which approximates the quantum electrodynamics, etc.

We must balance the models between accuracy, system size, and the simulation time frame in order to make a reliable (and accurate enough) calculation with the available computers in a reasonable time.

1.1   Scientific context of the thesis

There is a great interest in the physics of the nanoscale because the behaviour of nano systems is different from that of the known macroscopic systems. Usually the origin of those differences comes from two sources: the surface effects and the quantum confinement effects.

Surface effects come from the surface atoms of the system. Those atoms experience a different environment due to the neighbourhood atoms and usually this difference consist in the lack of first or second neighbours in a direction. Therefore in nanoscale systems the surface vs. bulk ratio is greater and those effects increase.

The quantum effects arise when the wavelenght of an electron or phonon in the material has the same order of magnitude than a geometrical dimension of the material, which makes the electron or phonon state quantized in the confined dimension. Therefore the density of states changes depending on the dimensions of the system.

The usual nanoscale systems on study are the dots and the wires. The dots are clusters, islands and other quasi-1D systems like quantum dots. The wires are nanotubes, nanowires (hollow or not) and nanoribbons.

The study of vibrations in nanostructures is of great interest for different reasons. In the first place, the possible thermoelectric applications [5] and on the other hand for the thermal dissipation problem that modern microchips have as they reduce their dimensions while increasing the number of transistors. As modern technology tends to reduce the scale of the electronic components to their limits, the understanding of the effects of the nanoscale becomes very important as they usually differ from the macroscale behaviour. Finally nowadays is possible to make phonon engineering and manipulate the

phonon behaviour at the nanoscale (phonon filters [6])

Also, in some situations [7] , only a detailed knowledge of the phonon spectrum allows to understand a great variety of phenomena such as charge and heat transport, infrared, Raman and electron-phonon scattering and give a view on related effects like superconductivity and resistivity.

The concept of phonon was introduced by Debye in 1912 [8]. The phonon is defined as a quantum of vibration energy in the crystal structure and is a quasi-particle with angular frequency ω and wave-vector q. The energy of a phonon mode is $\hbar\omega$ and the momentum is $\hbar q$.

From a theoretical point of view, discrete and continuum models have been employed for the study of vibrational modes in nanostructures.

Discrete methods employ phenomenological (usually by means of force constants) models or *ab initio* approaches and provide reliable results for acoustic and optical modes. Continuum approaches rely on elasticity theory.

Continuum approaches based on the elasticity theory [9] allow for a first step in the study of the vibrational properties of nanosystems.

Discrete approaches based on phenomenological models allow for more accurate study of the dynamics of the nanostructures while still being fast enough to deal with a great number of particles.

Discrete approaches based on *ab-initio* methods are the most slow techniques but do not need any parameter in order to solve the calculations. This is perfect in order to study unknown systems but not always gives new knowledge on the physics or ideas for modelization.

1.1.1   Properties of Nanostructures

Due to their size, the nanostructures show unusual properties. Many of these features such as quantisation and integer current flow cannot be observed in their "bulk" counterparts. Some of these characteristic properties are described in the following sections.

1.1.1.1   Electronic and optical properties

Nanostructures exhibit different electronic properties than their "bulk" equivalents due to their small size. In particular, silicon and carbon nanotubes show several changes from their respective "bulk" structures.

The electronic properties of a nanotube are determined by its structure, therefore these properties are dependent on the tube's chiral number[1] (n_1, n_2). For carbon nanotubes, the chiral number determines if the

---

[1]For information about CNT's chirality see Apendix in page 192

nanotube is metallic or semiconductor and for nitride nanotubes, the chiral number determines the size of the electronic band gap. For example, for a carbon nanotube, if the chiral number obey the formula $(n_2 + 2n_1) = 3i$ for i an integer, then the nanotube is metallic. However, if the carbon nanotube does not obey the previous formula, then the nanotube is a semiconductor with a band gap between 0.0 eV and 3.0 eV. For single walled carbon nanotubes, this bandgap is inversely proportional to the radius of the nanotube. This is already explained using the electron dispersion curves of graphene, which can be simply calculated from a tight-binding method [10, 11]. By applying a technique known as zone-folding, the electron bands of a carbon nanotube can be approximately obtained from the graphene ones. This results in the one-dimensional energy bands of a carbon nanotube being cross sections of those for a two-dimensional graphene-type structure [10]. *Ab initio* calculations of the electronic structure of carbon nanotubes have shown this relatively simple model to be reasonably accurate [12, 13, 14]. One of the results of this behaviour in carbon nanotubes is the appearance of a plasmon mode which has an energy between 5 eV and 7 eV independent of the chiral number [15]. This mode is a result of the π-bonds on nanotube's surface and a divergence in the electronic density of states near the band edge. This plasmon shows strong optical properties under electron emission loss spectroscopy and shows the graphene sheet as the common heritage of all carbon nanotubes. Calculations have also revealed higher energy plasmons, but these have weaker optical properties.

Nanotubes, due to their unique structure, are expected to act as quantum wires. Multi-wall nanotubes have been shown to have two-dimensional behaviour, but single wall carbon nanotubes show quantised step like flow. This is characteristic of a one-dimensional system. However, due to the contacts resistance, which is greater than the quantum resistance within the nanotube, Coulomb charging occurs as the capacitance of the nanotube/nanowire is very small. This leads to the Coulomb blockade effect and the electron pump. This shows that quantised conductance can be expected in most one-dimensional conducting materials, even if they have a very different basic structure. In fact, quantised characteristics are a key feature in such systems [16].

Electronic properties of silicon nanowires also change substantially in character from their corresponding "bulk" counterpart and some have been shown to have direct bandgaps. These structures may also be metallic or semi-metallic if the surface is clean and allowed to relax [17, 18] and have also been joined with carbon nanotubes to form heterojunctions [19].

Also of interest in nanostructures is the highest optical active vibrational mode, which can be detected via Raman scattering [20, 21]. This mode is highly affected by the confining dimension(s) of the nanostructure and thus,

Raman scattering measurements can be a fundamental technique for the characterisation of the size of the nanostructures.

1.1.1.2 Magnetic properties

Nanostructures show interesting magnetic properties. A thin sheet of material grown between two larger materials can be used to form a tunnel junction. A current flow across a tunnel junction is dependent on the spin of the charge carriers and the thickness of the barrier. As the barrier is, in-effect, a two-dimensional nanoslab joining two separate systems, the reduced size enables electrons to tunnel through the material from one side to the other.

Carbon nanotubes have also been shown to perform electron spin transport. As long as the two contacts are comparatively close ($< 100 \ nm$), nanotubes show clear hysteretic switching in the magnetoresistace, providing the basis for a single-wall nanotube spin transistor.

Graphene also shows magnetic properties. Whereas bulk graphene is a diamagnetic semimetal, simple tight-binding models predict that one-dimensional ribbons with zigzag edges are paramagnetic metals [22].

1.1.1.3 Thermal properties

Promising and attractive thermal properties are shown in nanostructures which are dramatically different from their "bulk" counterparts. Some nanostructures (like carbon nanotubes) have shown much greater thermal conductivity than that found in their "bulk", while others (like silicon nanowires) display a much lower thermal conductivity than in the "bulk". Due to the increased density of components on processor chips, these factors are becoming increasingly important in the field of heat management. Without effective methods for reducing the heat built in such components, electronics error due to electron-phonon interaction and lattice distortion increases and makes these components useless. On the other hand, for thermoelectric systems (thermoelectric refrigeration/electric generator) the thermoelectric performance depends on the relation between the heat flux and the electric conductivity.

The electronic applications also emphasise a second feature which changes in nanostructures, the specific heat capacity. It was predicted early that the temperature dependence for structures of reduced dimension would be different from that of "bulk" materials. In particular, the change in specific heat capacity in nanotubes and nanowires, with temperature, is expected to show a change from one-dimensional behaviour to two- (three-)dimensional, in the case of nanotubes (nanowires).

1.1.1.4 Vibrational properties

Understanding the vibrational features of a material is the first step in order to understand the thermal properties. Theoretical calculations of the vibrational characteristics of a structure are usually carried out by two methods: discrete atomistic dynamical calculations and continuum medium calculations. While continuum techniques are generally only applicable to the low energy ranges (the acoustic branches) and long wave-length regions of the Brillouin zone(the zone centre), these techniques are often more able to yield useful analytic expressions. Also, the dominant contributors to the thermal properties of a material are usually the acoustic phonon branches.

Now, for nanostructures, all these methods have been used with varying degrees of success for different materials and most techniques produce qualitatively similar results. There are several vibrational features existing on nanostructures. The most common to all nanostructures are:

- The appearance of new low-lying vibrational modes near the zone centre which have energies comparable to the zone edge frequency of the acoustic modes. Those new phonon branches with zone centre frequency ω, have a large non-zero group velocity (unlike optical modes in the "bulk") and are a direct result of quantisation within these structures.

- The appearance of a fourth acoustic mode. Normally, for "bulk" materials, there are three acoustic modes, one longitudinal and two transverse. In nanotubes these three modes exist and a new fourth mode known as the *twist* mode is added. This mode is a result of the "twisting" degree of freedom available to the nanotube (and nanowire) which is not normally available to "bulk" objects. In nanowires, the four acoustic branches are the dilatational, the doubly degenerated flexural, and the torsional mode [23]. These four branches in nanotubes and nanowires are expected to have a major effect on the thermal properties of these structures.

1.2 Objectives

Vibrational properties play an important role on different areas. Phonons influence the thermal properties and electron-phonon interaction is the key feature in conventional superconductivity.

The physical properties of nanostructures are different from those of the bulk materials. The vibrational properties of these systems exhibit different

characteristics from those of their bulk constituent materials. In spite of their interest, vibrational properties in nanostructures have received less attention than the electronic ones.

Different approaches can be considered for their study. The continuum approach based on the elasticity theory and the discrete approach based on molecular dynamics are used in this work.

In this thesis we work with semiconductor nanowires and nanodots but not in exclusive, as the methods used are able to work with a great variety of materials. The analysis has been presented for nanowires of various sizes in order to obtain the dimensionality behaviour of these effects.

In the case of nanodots the presence of structural defects has been studied in order to quantify the influence of the defects on the properties of interest.

We will also obtain the vibrational density of states which is related to the dispersion curves and the Raman spectra.

Therefore, the objectives are:

- To analyse the strengths and weaknesses of the main numerical methods based on continuum and discrete models.

- To understand the basic technique needed to obtain the spectra (VDOS and Raman), first from a theoretical point of view and then in practice by creating and testing an algorithm that will work on the data extracted from the numerical methods.

- To analyse the spectra of different nanosystems: Nanowires, nanodots to compare with bulk and surface systems.

1.3   Document organisation
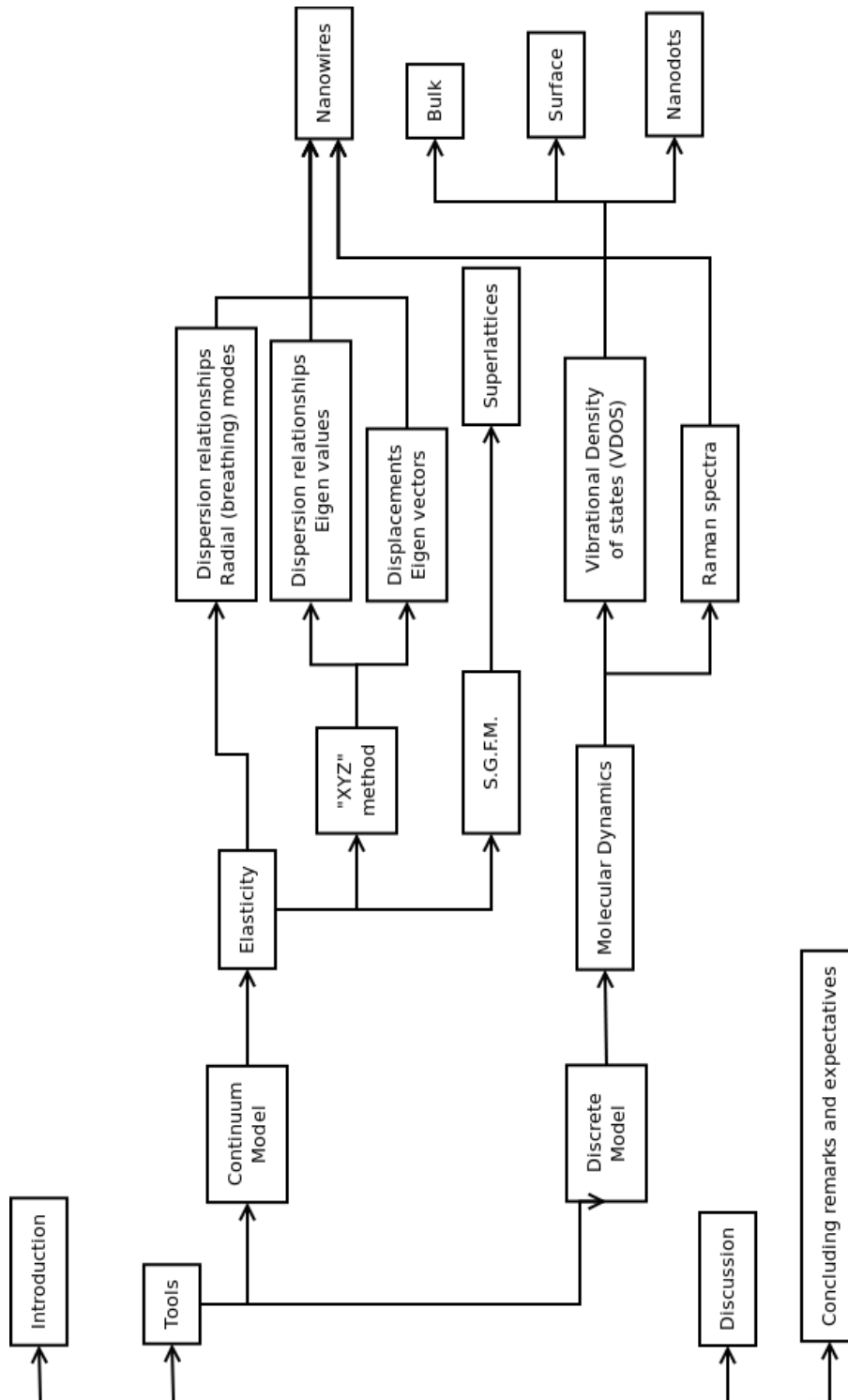
Figure 1.2: Organisation diagram

Chapter 2

Methodology: Tools, techniques and models

In this chapter we will discus the different tools and the methodology used in order to get information on the vibrational characteristics of the nanostructures.

The main ingredient of any computer simulation is to define the models for the physical system. In this thesis we will use two models, the continuum media and the discrete media models.

We will divide the techniques between the continuum approach and the discrete one.

In the continuum approach we will use the elasticity theory in order to obtain the dispersion relations, and the amplitude and directionality of the displacements (displacement pattern).

In the discrete approach we will use the molecular dynamics technique to obtain the vibrational density of states (VDOS) and the Raman spectra.

2.1 Dispersion curves

The representation of the phonon frequencies ω against the wave number q is called the dispersion relation or the dispersion curves.

For a crystal that has at least two atoms in its primitive cell we have in the bulk that the dispersion relations show two kinds of phonons:

Acoustic phonons: The acoustic modes corresponds to the lower sets of curves in the dispersion curves. Acoustic phonons are coherent movements of atoms of the lattice out of their equilibrium positions. Acoustic phonons exhibit a linear relationship between frequency and phonon wavevector for long wavelengths Also if the wavelength of acoustic

phonons goes to infinity, this corresponds to a simple displacement of the whole crystal, and this costs zero energy[1]. If the phonon displacement is along the propagation direction , then in some areas the atoms will be closer, in others further apart, as in a sound wave in air (hence the name acoustic). These phonons are called *Longitudinal Acoustic* modes. If the displacement is perpendicular to the propagation direction then the phonon is called *Transverse Acoustic* mode and it is similar to waves in water. Longitudinal and transverse acoustic phonons are often abbreviated as LA and TA phonons, respectively. The speed of propagation of an acoustic phonon, which is also the speed of sound in the material, is obtained by the slope of the acoustic dispersion curve $\frac{\partial \omega_q}{\partial q}$.

Optical phonons: The optical modes corresponds to the upper sets of curves in the dispersion curves. The optical phonons are an out of phase movement of the atoms in the lattice, one atom moving to the left, and its neighbour to the right. They are called optical because in ionic crystals, such as sodium chloride, they are excited by infra-red radiation. The electric field of the light will move every positive sodium ion in the direction of the field, and every negative chloride ion in the other direction, starting the crystal vibration. Optical phonons have a non-zero frequency at the Brillouin zone centre and show no dispersion near that long wavelength limit. Optical phonons that are Raman active can interact indirectly with light, through Raman scattering. Optical phonons are often abbreviated as LO and TO phonons, for the longitudinal and transverse modes respectively.

In confined systems like nanowires, we still have the acoustic modes with the characteristic null frequency at zero wave number and the optical modes, but there are also some modes whose slope is not that of the typical optical phonon and their frequencies are not zero at $q = 0$. These are a kind of "mixed" modes whose origin comes from the reduced dimensions and the free surfaces.

The thermodynamic properties of a solid are directly related to its phonon structure[2]. The entire set of all possible phonons that are described by the above phonon dispersion relations combine in what is known as the phonon density of states which determines the heat capacity of a crystal.

---

[1]This means that the dispersion curves of the acoustic phonons have zero frequency at the Brillouin zone center $q = 0$

[2]Shiomi and Maruyama [24] used the dispersion curve in their analysis of thermal conduction in carbon nanowires.
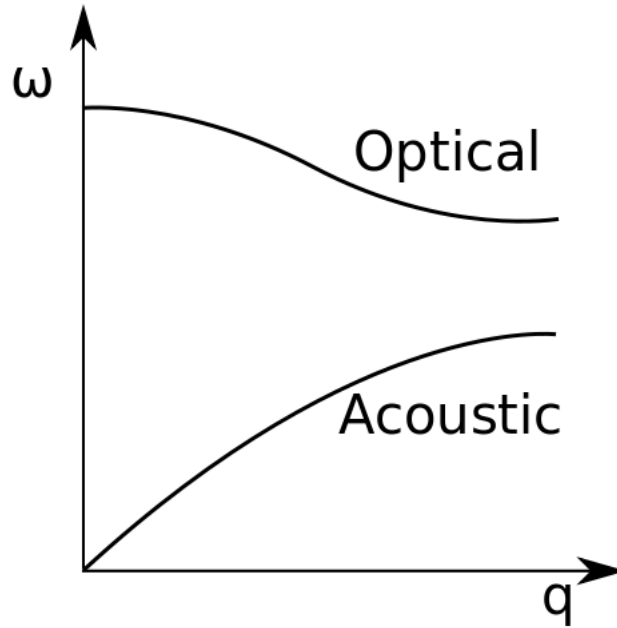
Figure 2.1: Dispersion curves in a linear diatomic chain

2.2 Continuum approach

Continuum mechanics is a branch of mechanics that deals with the analysis of the kinematics and the mechanical behaviour of materials modelled as a continuum medium rather than as discrete particles. The French mathematician Augustin Louis Cauchy was the first to formulate such models in the 19th century, but research in the area continues today, in different areas, ranging from engineering to nanostructures.

Mathematically speaking, a continuum is a body that can be continually sub-divided into infinitesimal elements with the properties being those of the bulk material.

The assumption of the continuum approach is that the substance of the material fills completely the space it occupies, thus ignoring the atomistic nature of matter. Also in this approximation, every portion of the continuum exhibit the macroscopic physical properties of the bulk, no matter how small the portion is. The field variables such as mass density, displacement and velocity, are conceptual constructs. They are defined at all points of the continuum and their values are calculated via axiomatic rules of procedure.

This approach is highly accurate for length scales being orders of magnitude bigger than the interatomic distances. But used with caution may be employed to approximate some mechanical and dynamical properties of

smaller structures.

Continuum mechanics deals with physical properties of solids and fluids which are independent of any particular coordinate system in which they are observed. These physical properties are then represented by tensors, which are mathematical objects having the required property of being independent of coordinate systems. These tensors can be expressed in coordinate systems for computational convenience.

$$\text{Continuum mechanics} \begin{cases} \text{Solid mechanics} \begin{cases} \text{Elasticity} \\ \text{Plasticity} \end{cases} \\ \text{Fluid mechanics} \begin{cases} \text{Newtonian fluids} \\ \text{Non-Newtonian fluids} \end{cases} \end{cases}$$

$$\boxed{\text{Plasticity} + \text{Non-Newtonian fluids} \rightarrow \text{Rheology}}$$
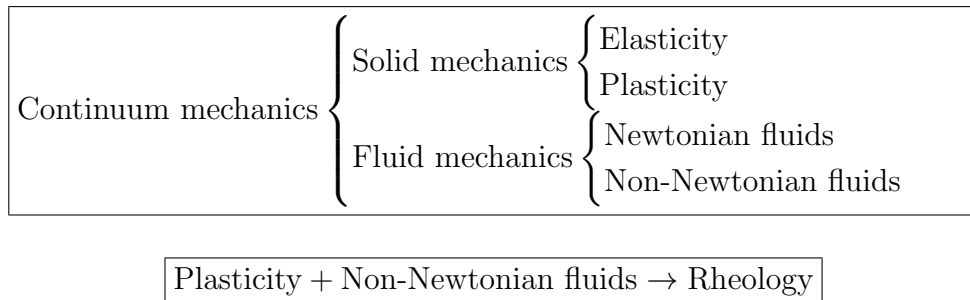
Table 2.1: Major areas of continuum mechanics

Within the continuum model the behaviour is determined by:

1. Conservation of mass.

2. Linear momentum balance. The rate of change of the total linear momentum is equal to the sum of the external forces.

3. Angular momentum balance.

The continuum hypothesis enables the use of these laws on the local scale as well as on the global scale.

Deformation of matter is a geometrical problem that may be treated out from two different points of view:

Lagrangian: With respect to the undeformed state.

Eulerian: With respect to the deformed state.

Locally, the mapping of the deformed to the undeformed state can be assumed to be linear and described by a differential relationship, which is a combination of a pure stretch and a pure rotation. The mechanical effects of the deformation are confined to the stretch and are characterised by a *strain* measure. For example, in a wire under load in the direction of its main axis,

the strain ε will be $\varepsilon = \frac{\text{change in length}}{\text{initial length}}$. The generalisation of this requires to introduce a strain *tensor* at each point of the continuum.

Let us consider a string with one end fixed and under the action of a force on the other end. As it is not necessary that all parts of the string are stretched in the same way, it must be defined the deformation of a small element. Lets suppose a section between x and $x + \Delta x$. When the force is applied, these points come to $x + u(x)$ and $x + u(x + \Delta x) + \Delta x$ and the relative deformation is $\frac{u(x+\Delta x)-u(x)}{\Delta x}$. By definition, in the continuum model, the strain is the limit when Δx goes to 0, i.e. $\varepsilon = \lim_{\Delta x \to 0} \frac{u(x+\Delta x)-u(x)}{\Delta x} = \frac{du}{dx}$

For a solid of general shape all points of the solid under deformation are determined by the vector $\vec{x'} = \vec{x} + \vec{u}$. The square of the distance between two points separated by the vector $\vec{dx'} = d\vec{x} + d\vec{u}$ is:

$$(\vec{dx'})^2 = (d\vec{x})^2 + 2(d\vec{x})(d\vec{u}) + (d\vec{u})^2 \tag{2.1}$$

Expanding the scalar products:

$$(\vec{dx'})^2 - (d\vec{x})^2 = 2dx_i du_i + du_k du_k \tag{2.2}$$

where $d\vec{u} = \sum_i \frac{\partial \vec{u}}{\partial x_i} dx_i$, so in Einstein notation we obtain:

$$(\vec{dx'})^2 - (d\vec{x})^2 = 2\frac{\partial u_i}{\partial x_j}dx_i dx_j + \frac{\partial u_k}{\partial x_i}\frac{\partial u_k}{\partial x_j}dx_i dx_j \tag{2.3}$$

The sum is not changed by permuting the indices i and j so eq.(2.3) can be written as:

$$(\vec{dx'})^2 - (d\vec{x})^2 = \left(\frac{\partial u_i}{\partial x_j} + \frac{\partial u_j}{\partial x_i} + \frac{\partial u_k}{\partial x_i}\frac{\partial u_k}{\partial x_j}\right) dx_i dx_j \tag{2.4}$$

or

$$(\vec{dx'})^2 - (d\vec{x})^2 = 2\varepsilon_{ij} dx_i dx_j \tag{2.5}$$

being

$$\varepsilon_{ij} = \frac{1}{2}\left(\frac{\partial u_i}{\partial x_j} + \frac{\partial u_j}{\partial x_i} + \frac{\partial u_k}{\partial x_i}\frac{\partial u_k}{\partial x_j}\right) \tag{2.6}$$

the strain tensor.

If the deformations are small, as in most of the situations in solids, the relative variations of distances inside the solid are small $\frac{\partial u_i}{\partial x_j} << 1$ so the strain tensor can be reduced to:

$$\varepsilon_{ij} = \frac{1}{2}\left(\frac{\partial u_i}{\partial x_j} + \frac{\partial u_j}{\partial x_i}\right) \tag{2.7}$$

The value of the strain depends on the point where the deformation is observed. Thus the strain in a generic medium is a tensor field consisting of symmetric second rank tensors.

Following classical Newtonian and Eulerian dynamics, the motion of a material body is produced by the action of externally applied forces which are assumed to be of two kinds: surface forces and body forces. When external contact forces act on a body, internal contact forces pass from point to point inside the body to balance their action, according to Newton's second law of motion of conservation of linear momentum and angular momentum.

Stress can be thought as a measure of the internal contact forces' intensity acting between particles of the body across imaginary internal surfaces. In other words, stress is a measure of the average amount of force exerted per unit area of the surface on which these internal forces act.

In an orthonormal reference frame, ΔF_i is the i-th component of the force $\Delta \vec{F}$ exerted on the surface element perpendicular to the k-axis ΔS_k by the medium in the positive direction. The stress T_{ik} is defined as the limit, of the ratio $\frac{\Delta F_i}{\Delta S_k}$ when ΔS_k tends to zero, :

$$T_{ik} = \lim_{\Delta S_k \to 0} \frac{\Delta F_i}{\Delta S_k} \tag{2.8}$$

The mechanical stress vector $\vec{T}(\vec{n})$ at any point P in a continuum associated to a plane with normal unit vector $\vec{n}$ can be expressed as a function of the stress vectors on the planes perpendicular to the coordinate axes, i.e. in terms of the components T_{ik} of the stress tensor.

$$T_i(\vec{n}) = T_{ik} \cdot n_k \tag{2.9}$$

For a material in static equilibrium, the net force and torque on any given volume must be zero. Let us assume that the stress comes from forces applied to the surface. Then from the principle of action and reaction, the net force arising from the interactions between different parts of a volume inside the solid must be zero. Since the forces are applied on the boundary surface S, the force $\vec{F}$ is the integral over S of the mechanical stress:

$$\vec{F} = \int_S \vec{T}(\vec{n}) dS \tag{2.10}$$

and after substituting with eq.(2.9):

$$F_i = \int_S T_{ik} n_k dS \tag{2.11}$$

with can be converted into a volume integral due to the Green's theorem:

$$F_i = \int_V \frac{\partial T_{ik}}{\partial x_k} dV \tag{2.12}$$

The integrand can be regarded as the density of force per unit volume:

$$f_i = \frac{\partial T_{ik}}{\partial x_k} \tag{2.13}$$

So the static equilibrium condition $F_i = 0$ implies $f_i = 0$ or:

$$\frac{\partial T_{ik}}{\partial x_k} = 0 \tag{2.14}$$

If the solid is elastic, then by definition it will return to its initial state after the external forces are removed. This return to the initial state is due to the internal stress, therefore there is a correspondence between stress and strain.

For small deformations the elastic behaviour can be described by the first order term in the Taylor expansion, so:

$$T_{ij}(\varepsilon_{kl}) = T_{ij}(0) + \left(\frac{\partial T_{ij}}{\partial \varepsilon_{kl}}\right)_{\varepsilon_{kl}=0} \varepsilon_{kl} + \frac{1}{2}\left(\frac{\partial^2 T_{ij}}{\partial \varepsilon_{kl}\partial \varepsilon_{mn}}\right)_{\varepsilon_{kl}=0;\varepsilon_{mn}=0} \varepsilon_{kl}\varepsilon_{mn} + \ldots \tag{2.15}$$

or, since $T_{ij}(0) = 0$

$$T_{ij} = C_{ijkl}\varepsilon_{kl} \tag{2.16}$$

where C_{ijkl} is the *stiffness tensor*:

$$C_{ijkl} = \left(\frac{\partial T_{ij}}{\partial \varepsilon_{kl}}\right)_{\varepsilon_{kl}=0}. \tag{2.17}$$

Thus substituting from eq.(2.7) in eq.(2.16):

$$T_{ij} = \frac{1}{2}C_{ijkl}\frac{\partial u_k}{\partial x_l} + \frac{1}{2}C_{ijkl}\frac{\partial u_l}{\partial x_k} \tag{2.18}$$

and since $C_{ijkl} = C_{ijlk}$ due to the fact that T_{ij} and ε_{kl} are symmetric tensors:

$$T_{ij} = C_{ijkl}\frac{\partial u_l}{\partial x_k} \tag{2.19}$$

With this it is possible to calculate the equation of motion from the fundamental law of classical dynamics $\vec{F} = M\vec{a}$ which can be rewritten for the

continuum calculus into $f_i = \rho \dfrac{\partial^2 u_i}{\partial t^2}$. As it was shown, the force density per unit volume of stressed material is given by:

$$f_i = \frac{\partial T_{ij}}{\partial x_j} \tag{2.20}$$

So if the effect of gravity is neglected, the fundamental law is:

$$\rho \frac{\partial^2 u_i}{\partial t^2} = \frac{\partial T_{ij}}{\partial x_j} \tag{2.21}$$

and using eq.(2.19) the equation of motion becomes:

$$\rho \frac{\partial^2 u_i}{\partial t^2} = C_{ijkl} \frac{\partial^2 u_l}{\partial x_j \partial x_k} \tag{2.22}$$

Continuum approaches based on the elasticity theory allow for a first step in the study of the vibrational properties of nanostructures. This has been done for superlattices [26, 27], including the elastic anisotropy of the constituent materials. Also in the case of CNT, where the elastic isotropy in the graphene plane and the cylindrical shape allow for a solution in closed form [28]. In the case of wires (treated in this work) they are thick thus making necessary the inclusion of the elastic anisotropy of the materials considered. In the case of general anisotropy it is not possible to obtain a solution in closed form even for nanotubes [29].

The use of elasticity theory for the calculation of the phonons in nanostructures is, in principle, only applicable in the vicinity of the centre of the Brillouin zone, but it has been found that in fact the elasticity theory gives a good qualitative approximation for bigger ranges.

Elasticity has been employed to study the elastic waves of carbon nanotubes. A solution for infinitely long cylindrical shells of isotropic materials was obtained [28]. The limit of very thin shells allows for an analytical expression that can be used for carbon nanotubes, assuming carbon as an isotropic material. As shown in Velasco and Muñoz [30] it is possible to obtain a solution in closed form for nanotubes of materials having hexagonal symmetry. It was shown there that the former approaches considering carbon as an isotropic elastic material remained valid for the carbon nanotubes due to the transverse elastic isotropy of the hexagonal systems in the basal plane. This was not valid for wires.

In order to deal with nanowires of elastically anisotropic crystals and different cross sections, as those obtained experimentally, a theoretical method originally developed in resonant ultrasound spectroscopy to obtain the free

vibrational modes of inhomogeneous objects [31, 32, 33, 34] can be used. The method studies the free vibrations of elastic anisotropic systems having arbitrary shape and mass density variation, thus being quite adequate for the present case. This is performed by expanding the elastic displacements in terms of a set of basis functions. The method has been applied to macroscopic samples, having varied cross sections, to obtain the vibrational frequencies (direct problem) and in other cases for the calculation of the elastic constants of the sample (inverse problem) [31, 32, 33, 34] . Recently this method has also been applied to the study of acoustic modes in a wide variety of nanotubes and nanowires having different cross-sections [23, 35, 36, 37, 38].

The Surface Green Function Matching (SGFM) method provides a very efficient way to study the vibrational modes of superlattices [39, 40, 41, 42, 43, 44, 45, 46]. With this method, it is possible to consider two or more materials in the superlattices, and also to account for the effect of the elastic anisotropy of the constituent materials. Thus this method also allows the study of periodic, quasiregular and hybrid superlattices [27, 47, 48, 49, 50, 51]. It provides not only the dispersion relations but also the local density of states (LDOS) in such a way that it is possible to obtain the spatial distribution of the different modes in the structure.

2.2.1 Nanowires: Elasticity theory

The elasticity theory constitutes a first step, in the theoretical toolkit, to study the dynamical properties of nanowires.

Isotropic continuum models have been widely used to study the vibrational properties of nanowires and nanotubes [53, 54, 55, 56, 57, 58] considered as cylindrical shells thick or thin, respectively. In the case of carbon nanotubes, the elastic studies assumed that graphene was isotropic and good agreement with first principles calculations has been found, provided the NT wall thickness is an adjustable parameter [57]. However III-V nitride NT's and other hexagonal materials NT with several nanometer thick walls have been synthesised in the last years [59, 60]. The analysis of their vibrational spectra needs the introduction of the full bulk hexagonal symmetry and therefore to go beyond the isotropic model.

The three-dimensional equations of motion (eq.(2.22)) in cylindrical coordinates (r, θ, z) of an elastic medium having transverse isotropy are given by

$$\left[C_{11} \left(\frac{\partial^2}{\partial r^2} + \frac{1}{r}\frac{\partial}{\partial r} - \frac{1}{r^2} \right) + C_{66}\frac{1}{r^2}\frac{\partial^2}{\partial \theta^2} + C_{44}\frac{\partial^2}{\partial z^2} \right] u_r \quad +$$

$$\left[(C_{12} + C_{66})\frac{1}{r}\frac{\partial^2}{\partial \theta \partial r} - (C_{11} + C_{66})\frac{1}{r^2}\frac{\partial}{\partial \theta} \right] u_\theta \qquad +$$

$$(C_{13} + C_{44})\frac{\partial^2 u_z}{\partial r \partial z} \qquad\qquad\qquad = \quad \rho\frac{\partial^2 u_r}{\partial t^2} \quad ,$$

$$\left[(C_{12} + C_{66})\frac{1}{r}\frac{\partial^2}{\partial \theta \partial r} + (C_{11} + C_{66})\frac{1}{r^2}\frac{\partial}{\partial \theta} \right] u_r \qquad +$$

$$\left[C_{66} \left(\frac{\partial^2}{\partial r^2} + \frac{1}{r}\frac{\partial}{\partial r} - \frac{1}{r^2} \right) + C_{11}\frac{1}{r^2}\frac{\partial^2}{\partial \theta^2} + C_{44}\frac{\partial^2}{\partial z^2} \right] u_\theta \quad +$$

$$(C_{13} + C_{44})\frac{1}{r}\frac{\partial^2 u_z}{\partial \theta \partial z} \qquad\qquad\qquad = \quad \rho\frac{\partial^2 u_\theta}{\partial t^2} \quad ,$$

$$(C_{13} + C_{44})\left(\frac{\partial^2}{\partial r \partial z} + \frac{1}{r}\frac{\partial}{\partial z} \right) u_r + (C_{13} + C_{44})\frac{1}{r}\frac{\partial^2 u_\theta}{\partial \theta \partial z} \quad +$$

$$\left[C_{44} \left(\frac{\partial^2}{\partial r^2} + \frac{1}{r}\frac{\partial}{\partial r} + \frac{1}{r^2}\frac{\partial^2}{\partial \theta^2} \right) + C_{33}\frac{\partial^2}{\partial z^2} \right] u_z \qquad = \quad \rho\frac{\partial^2 u_z}{\partial t^2} \quad ,$$

$$(2.23)$$

where C_{ij} are the elastic coefficients of the material and ρ the mass density. Then solutions of these equations are looked for in the form

$$\mathbf{u} = \nabla\varphi + \mathbf{rot}(\psi\hat{\mathbf{e}}_z) \qquad\qquad (2.24)$$

and then the $\mathbf{u}$ components are

$$u_r = \left[\frac{\partial\varphi}{\partial r} + \frac{1}{r}\frac{\partial\psi}{\partial \theta} \right] \cos(\omega t + kz) \quad ,$$

$$u_\theta = \left[\frac{1}{r}\frac{\partial\varphi}{\partial \theta} - \frac{\partial\psi}{\partial r} \right] \cos(\omega t + kz) \quad , \qquad (2.25)$$

$$u_z = \beta\varphi\sin(\omega t + kz) \quad ,$$

being ω the frequency, k the wavenumber and β an arbitrary constant to be determined. By substituting eq.(2.25) in eq.(2.23) we obtain the following expressions

$$\frac{\partial}{\partial r}\left[C_{11}\vec{\nabla}^2\varphi + (\rho\omega^2 - C_{44}k^2 + (C_{13}+C_{44})k\beta)\varphi\right] \quad +$$

$$\frac{1}{r}\frac{\partial}{\partial\theta}\left[C_{66}\vec{\nabla}^2\psi + (\rho\omega^2 - C_{44}k^2)\psi\right] \qquad = \quad 0 \quad ,$$

$$\frac{1}{r}\frac{\partial}{\partial\theta}\left[C_{11}\vec{\nabla}^2\varphi + (\rho\omega^2 - C_{44}k^2 + (C_{13}+C_{44})k\beta)\varphi\right] \quad - \qquad (2.26)$$

$$\frac{\partial}{\partial r}\left[C_{66}\vec{\nabla}^2\psi + (\rho\omega^2 - C_{44}k^2)\psi\right] \qquad = \quad 0 \quad ,$$

$$[C_{44}\beta - (C_{13}+C_{44})k]\vec{\nabla}^2\varphi + (\rho\omega^2 - C_{33}k^2)\beta\varphi \qquad = \quad 0 \quad ,$$

being

$$\vec{\nabla}^2 = \frac{\partial^2}{\partial r^2} + \frac{1}{r}\frac{\partial}{\partial r} + \frac{1}{r^2}\frac{\partial^2}{\partial\theta^2} \tag{2.27}$$

instead of the complete ∇^2 operator including $\dfrac{\partial^2}{\partial z^2}$.

The two first equations are verified if

$$C_{11}\vec{\nabla}^2\varphi + [\rho\omega^2 - C_{44}k^2 + (C_{13}+C_{44})k\beta]\varphi = 0 \quad ,$$

$$C_{66}\vec{\nabla}^2\psi + (\rho\omega^2 - C_{44}k^2)\psi \qquad\qquad = 0 \quad , \tag{2.28}$$

are satisfied.

In addition, all equations (2.26) are consistent if β satisfies

$$\frac{\beta(\rho\omega^2 - C_{33}k^2)}{C_{44}\beta - (C_{13}+C_{44})k} = \frac{\rho\omega^2 - C_{44}k^2 + (C_{13}+C_{44})k\beta}{C_{11}} \equiv -\Upsilon^2 \quad . \tag{2.29}$$

This leads to the following equation

$$C_{11}C_{44}(\Upsilon^2)^2 + \Upsilon^2[(C_{11}+C_{44})\rho\omega^2 \quad +$$

$$(C_{13}^2 + 2C_{13}C_{44} - C_{11}C_{33})k^2] \qquad + \qquad (2.30)$$

$$(\rho\omega^2 - C_{44}k^2)(\rho\omega^2 - C_{33}k^2) \qquad = \quad 0 \; .$$

Being Υ_1^2 and Υ_2^2 the solutions of eq.(2.30) the potential functions will be given by

$$\vec{\nabla}^2\varphi_1 - \Upsilon_1^2\varphi_1 \qquad\qquad = \quad 0 \quad,$$

$$\vec{\nabla}^2\varphi_2 - \Upsilon_2^2\varphi_2 \qquad\qquad = \quad 0 \quad, \qquad\qquad (2.31)$$

$$\vec{\nabla}^2\psi + (\rho\omega^2 - C_{44}k^2)\frac{\psi}{C_{66}} \quad = \quad 0 \quad.$$

If we choose $\psi(r,\theta)$ in the form

$$\psi(r,\theta) = f(r)\sin(n\theta) \quad (n = 0, 1, 2, \ldots) \qquad\qquad (2.32)$$

when substituting in eq.(2.31) we obtain:

$$r^2\frac{d^2f}{dr^2} + r\frac{df}{dr} + [(\rho\omega^2 - C_{44}k^2)\frac{r^2}{C_{66}} - n^2]f = 0 \quad, \qquad\qquad (2.33)$$

which is the Bessel equation for $f(r)$ [61]. The solution will be then

$$f(r) = A_t J_n(\beta_t r) + B_t Y_n(\beta_t r) \quad, \quad \rho\omega^2 > C_{44}k^2 \quad,$$

$$f(r) = A_t I_n(\beta_t r) + B_t K_n(\beta_t r) \quad, \quad \rho\omega^2 < C_{44}k^2 \quad, \qquad\qquad (2.34)$$

with

$$\beta_t = |(\rho\omega^2 - C_{44}k^2)/C_{66}|^{1/2} \quad. \qquad\qquad (2.35)$$

On the other hand the solutions of eq.(2.30) are

$$\Upsilon_1^2 = \frac{-B+D}{2A} \quad, \quad \Upsilon_2^2 = -\frac{B+D}{2A} \quad, \qquad\qquad (2.36)$$

with

$$A \quad = \quad C_{11}C_{44} \quad,$$

$$B \quad = \quad (C_{11} + C_{44})\rho\omega^2 + (C_{13}^2 + 2C_{13}C_{44} - C_{11}C_{33})k^2 \quad,$$

$$C \quad = \quad (\rho\omega^2 - C_{44}k^2)(\rho\omega^2 - C_{33}k^2) \quad, \qquad\qquad (2.37)$$

$$D \quad = \quad \sqrt{B^2 - 4AC} \quad.$$

The main difference with the isotropic case, besides the appearance of all the elastic constants, is that Υ_1^2 and Υ_2^2 can be real or complex conjugates,

instead of real or pure imaginary. The nature, real or complex, of these solutions depends on the frequency range and the material considered.

By assuming

$$
\begin{aligned}
\varphi_1(r,\theta) &= g_1(r)\cos(n\theta) \quad, \\
\varphi_2(r,\theta) &= g_2(r)\cos(n\theta) \quad,
\end{aligned}
\tag{2.38}
$$

we obtain the following equation

$$
r^2\frac{d^2 g_i}{dr^2} + r\frac{dg_i}{dr} - (\Upsilon_i^2 r^2 + n^2)g_i = 0 \quad, \quad (i = 1,2) \quad,
\tag{2.39}
$$

and we obtain the Bessel equation anew.

For the solutions we must distinguish the two cases, $\Upsilon_i^2 > 0$ and $\Upsilon_i^2 < 0$, respectively.

When $\Upsilon_i^2 > 0$ we have

$$
g_i(r) = A_i I_n(\gamma_i r) + B_i K_n(\gamma_i r) \quad, \quad (i = 1,2)
\tag{2.40}
$$

being $\gamma_i = |\Upsilon_i^2|^{1/2}$.

When $\Upsilon_i^2 < 0$ we have

$$
g_i(r) = A_i J_n(\gamma_i r) + B_i Y_n(\gamma_i r) \quad, \quad (i = 1,2) .
\tag{2.41}
$$

The displacement components are then given by

$$
\begin{aligned}
u_r &= \left[\frac{dg_1}{dr} + \frac{dg_2}{dr} + \frac{1}{r}nf\right]\cos(n\theta)\cos(kz + \omega t) \quad, \\
u_\theta &= -\left[\frac{n}{r}(g_1 + g_2) + \frac{df}{dr}\right]\sin(n\theta)\cos(kz + \omega t) \quad, \\
u_z &= [\Upsilon_1 g_1 + \Upsilon_2 g_2]\cos(n\theta)\sin(kz + \omega t) \quad.
\end{aligned}
\tag{2.42}
$$

In the case of wave propagation with stress-free boundary conditions the stress must vanish on the cylindrical shell boundaries, $r = a, b$, thus the boundary conditions at $r = a$ and $r = b$ are

$$C_{11}\frac{\partial u_r}{\partial r} + C_{12}\left(\frac{u_r}{r} + \frac{1}{r}\frac{\partial u_\theta}{\partial \theta}\right) + C_{13}\frac{\partial u_z}{\partial z} \quad = \quad 0 \quad,$$

$$C_{66}\left(\frac{\partial u_\theta}{\partial r} - \frac{u_\theta}{r} + \frac{1}{r}\frac{\partial u_r}{\partial \theta}\right) \qquad\qquad = \quad 0 \quad, \qquad\qquad (2.43)$$

$$C_{44}\left(\frac{\partial u_r}{\partial z} + \frac{\partial u_z}{\partial r}\right) \qquad\qquad = \quad 0 \quad,$$

that can be written as

$$[(C_{11}\Upsilon_1^2 + C_{13}k\beta_1)g_1 + (C_{11}\Upsilon_2^2 \qquad\qquad\qquad +$$

$$C_{13}k\beta_2)g_2 + 2nC_{66}\left(\frac{1}{r}\frac{df}{dr} - \frac{f}{r^2}\right) \qquad\qquad -$$

$$\frac{2C_{66}}{r}\left(\frac{dg_1}{dr} + \frac{dg_2}{dr}\right) \qquad\qquad\qquad +$$

$$\frac{2n^2}{r^2}C_{66}(g_1 + g_2)]\cos(n\theta)\cos(kz + \omega t) \qquad = \quad 0 \quad,$$

$$\qquad\qquad\qquad\qquad\qquad\qquad\qquad\qquad\qquad\qquad (2.44)$$

$$C_{66}[\frac{2n}{r^2}(g_1 + g_2) - \frac{2n}{r}\left(\frac{dg_1}{dr} + \frac{dg_2}{dr}\right) + \frac{2}{r}\frac{df}{dr} - \frac{2n^2}{r^2}f \quad +$$

$$\frac{(\rho\omega^2 - C_{44}k^2)}{C_{66}}f]\sin(n\theta)\cos(kz + \omega t) \qquad = \quad 0 \quad,$$

$$C_{44}\left[(\beta_1 - k)\frac{dg_1}{dr} + (\beta_2 - k)\frac{dg_2}{dr} - \frac{nk}{r}f\right] \qquad\qquad \times$$

$$\cos(n\theta)\sin(kz + \omega t) \qquad\qquad\qquad = \quad 0 \quad.$$

The dispersion relations are obtained by forming the determinant of the coefficients A_t, B_t, A_1, B_1, A_2 and B_2. In this way we obtain

$$|d_{ij}| = 0 \quad, \quad (i,j = 1,\dots,6) \qquad\qquad (2.45)$$

where

$$
\begin{aligned}
d_{11} &= C_{66}[2n(n-1)F_n(\beta_t a) - 2n\beta_t a\sigma_2 F_{n+1}(\beta_t a)] \quad, \\
d_{12} &= C_{66}[2n(n-1)S_n(\beta_t a) - 2n\beta_t aS_{n+1}(\beta_t a)] \quad, \\
d_{13} &= [2n(n-1)C_{66} + a^2(C_{44}k^2 - \rho\omega^2 - C_{44}k\beta_1)]F_n(\gamma_1 a) + 2C_{66}\gamma_1 a\sigma_1 F_{n+1}(\gamma_1 a) \quad, \\
d_{14} &= [2n(n-1)C_{66} + a^2(C_{44}k^2 - \rho\omega^2 - C_{44}k\beta_1)]S_n(\gamma_1 a) + 2C_{66}\gamma_1 aS_{n+1}(\gamma_1 a) \quad, \\
d_{15} &= [2n(n-1)C_{66} + a^2(C_{44}k^2 - \rho\omega^2 - C_{44}k\beta_2)]F_n(\gamma_2 a) + 2C_{66}\gamma_2 a\sigma_2 F_{n+1}(\gamma_2 a) \quad, \\
d_{16} &= [2n(n-1)C_{66} + a^2(C_{44}k^2 - \rho\omega^2 - C_{44}k\beta_2)]S_n(\gamma_2 a) + 2C_{66}\gamma_2 aS_{n+1}(\gamma_2 a) \quad, \\
d_{21} &= C_{66}\left[\left(\frac{\rho\omega^2 - C_{44}k^2}{C_{66}} - 2n(n-1)\right)F_n(\beta_t a) - 2n\beta_t a\sigma_2 F_{n+1}(\beta_t a)\right] \quad, \\
d_{22} &= C_{66}\left[\left(\frac{\rho\omega^2 - C_{44}k^2}{C_{66}} - 2n(n-1)\right)S_n(\beta_t a) - 2n\beta_t aS_{n+1}(\beta_t a)\right] \quad, \\
d_{23} &= C_{66}[-2n(n-1)F_n(\gamma_1 a) + 2n\gamma_1 a\sigma_1 F_{n+1}(\gamma_1 a)] \quad, \\
d_{24} &= C_{66}[-2n(n-1)S_n(\gamma_1 a) + 2n\gamma_1 aS_{n+1}(\gamma_1 a)] \quad, \\
d_{25} &= C_{66}[-2n(n-1)F_n(\gamma_2 a) + 2n\gamma_2 a\sigma_2 F_{n+1}(\gamma_2 a)] \quad, \\
d_{26} &= C_{66}[-2n(n-1)S_n(\gamma_2 a) + 2n\gamma_2 aS_{n+1}(\gamma_2 a)] \quad, \\
d_{31} &= C_{44}[-nkF_n(\beta_t a)] \quad, \\
d_{32} &= C_{44}[-nkS_n(\beta_t a)] \quad, \\
d_{33} &= C_{44}[(\beta_1 - k)nF_n(\gamma_1 a) - (\beta_1 - k)\gamma_1 a\sigma_1 F_{n+1}(\gamma_1 a)] \quad, \\
d_{34} &= C_{44}[(\beta_1 - k)nS_n(\gamma_1 a) - (\beta_1 - k)\gamma_1 aS_{n+1}(\gamma_1 a)] \quad, \\
d_{35} &= C_{44}[(\beta_2 - k)nF_n(\gamma_2 a) - (\beta_2 - k)\gamma_2 a\sigma_2 F_{n+1}(\gamma_2 a)] \quad, \\
d_{36} &= C_{44}[(\beta_2 - k)nS_n(\gamma_2 a) - (\beta_2 - k)\gamma_2 aS_{n+1}(\gamma_2 a)] \quad,
\end{aligned}
$$

and the remaining three rows are obtained from these given above by substituting b for a. F denotes either a J or I Bessel function, whereas S denotes either a Y or K Bessel function, the proper choice being given by

$$
(0 < \rho\omega^2 < C_{44}k^2)\begin{cases} f &\longrightarrow I_n(\beta_t r) , K_n(\beta_t r) \quad, \\ g_1 &\longrightarrow I_n(\gamma_1 r) , K_n(\gamma_1 r) \quad, \\ g_2 &\longrightarrow I_n(\gamma_2 r) , K_n(\gamma_2 r) \quad, \end{cases}
$$

$$
(C_{44}k^2 < \rho\omega^2 < C_{33}k^2)\begin{cases} f &\longrightarrow J_n(\beta_t r) , Y_n(\beta_t r) \quad, \\ g_1 &\longrightarrow I_n(\gamma_1 r) , K_n(\gamma_1 r) \quad, \\ g_2 &\longrightarrow J_n(\gamma_2 r) , Y_n(\gamma_2 r) \quad, \end{cases}
$$

$$
(\rho\omega^2 > C_{33}k^2)\begin{cases} f &\longrightarrow J_n(\beta_t r) , Y_n(\beta_t r) \quad, \\ g_1 &\longrightarrow J_n(\gamma_1 r) , Y_n(\gamma_1 r) \quad, \\ g_2 &\longrightarrow J_n(\gamma_2 r) , Y_n(\gamma_2 r) \quad, \end{cases}
$$

The parameters σ_1 and σ_2 are associated to the differences in the recursion and differentiation relations between the different kinds of Bessel functions. They take the value 1 when J and Y functions are used and the value -1 when I and K functions are used. For the different frequency ranges they have the following values

$$
\begin{aligned}
0 < \rho\omega^2 < C_{44}k^2 \, , & \quad \sigma_1 = -1 \, , \quad \sigma_2 = -1 \quad , \\
C_{44}k^2 < \rho\omega^2 < C_{33}k^2 \, , & \quad \sigma_1 = -1 \, , \quad \sigma_2 = 1 \quad , \\
\rho\omega^2 > C_{33}k^2 \, , & \quad \sigma_1 = 1 \, , \quad \sigma_2 = 1 \quad .
\end{aligned}
$$

For motion independent of θ and z, corresponding to $n=0$ and $k=0$, we would have only the radial component of the displacement. It is easy to see that in that case

$$
\Upsilon_1^2 = -\frac{\rho\omega^2}{C_{11}} \quad , \qquad\qquad \Upsilon_2^2 = -\frac{\rho\omega^2}{C_{44}} \quad ,
$$

$$
\beta_1 \simeq -\frac{(C_{13}+C_{44})k}{(C_{11}-C_{44})} \quad , \qquad \beta_2 k \simeq \frac{(C_{11}-C_{44})\rho\omega^2}{C_{44}(C_{13}+C_{44})} \quad .
$$

Then the secular determinant can be factored as

$$
\begin{vmatrix} d_{21} & d_{22} \\ d_{51} & d_{52} \end{vmatrix} = 0 \quad , \qquad
\begin{vmatrix} d_{13} & d_{14} & d_{15} & d_{16} \\ d_{43} & d_{44} & d_{45} & d_{46} \\ 0 & 0 & d_{35} & d_{36} \\ 0 & 0 & d_{65} & d_{66} \end{vmatrix} = 0 \quad .
$$

The second determinant is also factored as

$$
\begin{vmatrix} d_{13} & d_{14} \\ d_{43} & d_{44} \end{vmatrix} \times \begin{vmatrix} d_{35} & d_{36} \\ d_{65} & d_{66} \end{vmatrix} = 0 \, ,
$$

and when

$$
\begin{vmatrix} d_{13} & d_{14} \\ d_{43} & d_{44} \end{vmatrix} = 0 \quad ,
$$

we obtain

$$
\begin{vmatrix} A_1 a^2 J_0(A_2 a) - 2C_{66}A_2 a J_1(A_2 a) & A_1 a^2 Y_0(A_2 a) - 2C_{66}A_2 a Y_1(A_2 a) \\ A_1 b^2 J_0(A_2 b) - 2C_{66}A_2 b J_1(A_2 b) & A_1 b^2 Y_0(A_2 b) - 2C_{66}A_2 b Y_1(A_2 b) \end{vmatrix} = 0 \quad .
$$

$$\tag{2.46}$$

where

$$A_1 = \rho\omega^2$$
$$A_2 = \sqrt{\frac{\rho\omega^2}{C_{11}}} \qquad . \tag{2.47}$$

By considering $b = a + h$, h being the thickness of the cylindrical shell, and expanding (2.46) to first order in h/a we arrive to

$$[J_1(\sqrt{\tfrac{\rho\omega^2}{C_{11}}}a)Y_0(\sqrt{\tfrac{\rho\omega^2}{C_{11}}}a) - J_0(\sqrt{\tfrac{\rho\omega^2}{C_{11}}}a)Y_1(\sqrt{\tfrac{\rho\omega^2}{C_{11}}}a)] \quad \times$$

$$[-2C_{12}C_{66}\gamma_1 a + C_{11}\gamma_1 a[C_{11}\gamma_1^2 a^2 - 2C_{66}]] \qquad = \quad 0 \ .$$

The dispersion relation is then given by

$$C_{11}^2 \gamma_1^2 a^2 = 2C_{66}(C_{11} + C_{12}) \tag{2.48}$$

and from here we arrive to the following expression for the radial breathing mode

$$\omega = \frac{1}{a}\sqrt{\frac{2C_{66}(C_{11} + C_{12})}{\rho C_{11}}} \tag{2.49}$$

equivalent to

$$\omega = \frac{2}{a}\sqrt{\frac{C_{66}(C_{12} + C_{66})}{\rho(C_{12} + 2C_{66})}} \ . \tag{2.50}$$

This expression is the same used in the isotropic case. In hexagonal crystals the in-plane transverse waves are associated to C_{66}, whereas the out-plane transverse waves are associated to the C_{44} coefficient. Therefore the isotropic approximation would be reasonable for NT of hexagonal crystals having almost negligible thickness where the influence of the C_{44} coefficient could be neglected. This could be the case of single wall (SW) CNT and BN NT formed by rolling up a monolayer of the corresponding material. Clearly this would not be suitable for other hexagonal materials nanotubes having non-negligible thickness and thus inclusion of the full anisotropy of the constituent material is necessary.

It has been possible to solve the equations of motion of nanowires and nanotubes with circular cross-sections, for isotropic and hexagonal materials. On the other hand , it was impossible to extend this approach to the cylyndrical structures of other anisotropic crystal systems [29, 62, 63]. To our knowledge, this continues to be the situation. Although a general solution has not been found, solutions for some types of vibrational modes of general anisotropic crystals can be found.

2.2.2   Acoustic radial (breathing) frequency modes in cylinders, cylindrical shells and composite cylinders of general anisotropic crystals

The radial (breathing) modes are a characteristic signature in the nanotubes and nanowires spectra. They are also of interest in the design of resonators and to generate sound radiation [64].

Besides this, the vibrational radial (breathing) modes of cylinders have a much simpler form than a general vibrational mode, thus making easier the obtention of its dispersion relation for general anisotropic crystals.

We shall consider here an infinitely long cylinder, a cylindrical shell, a core-shell cylinder and a composite cylinder of general anisotropic materials and we shall obtain the frequency values of the acoustic breathing modes of these systems.

In subsection 2.2.2.1 we present the formal equations for the thick cylinders and cylindrical shells. Subsection 2.2.2.2 deals with the core-shell and composite cylinders formed by several materials. Subsection 3.4.2.1 deals with the results for nanowires of different materials, belonging to different crystals systems, grown in the last years. In subsection 3.4.2.2 an application to recently grown core-shell Au/Ag and ZnS/SiO$_2$ nanowires is done.

2.2.2.1   Radial acoustic breathing modes in cylinders and cylindrical shells of general anisotropic crystals

We shall consider a general anisotropic crystal. We shall assume that the systems possess cylindrical anisotropy. In this case two of the material axes coincide with the tangent and the normal to concentric circles in a given plane, while the third one coincides with the normal to that plane.

The matrix transforming both coordinate systems is given by

$$M \;\; = \;\; \begin{bmatrix} \cos\theta & \sin\theta & 0 \\ -\sin\theta & \cos\theta & 0 \\ 0 & 0 & 1 \end{bmatrix} .$$

The cylindrical anisotropy can be defined as the case where at each point, the material has the properties of a material of Cartesian anisotropy with its coordinate directions x, y and z coinciding with the local r, θ and z directions, respectively [65]. In this way the material properties become independent of θ, and the material stiffness and compliance matrices are constants. If we choose $\theta = 0$, the matrix M becomes the unit matrix and those matrices become identical to those of the Cartesian anisotropy. We present in Fig.2.2
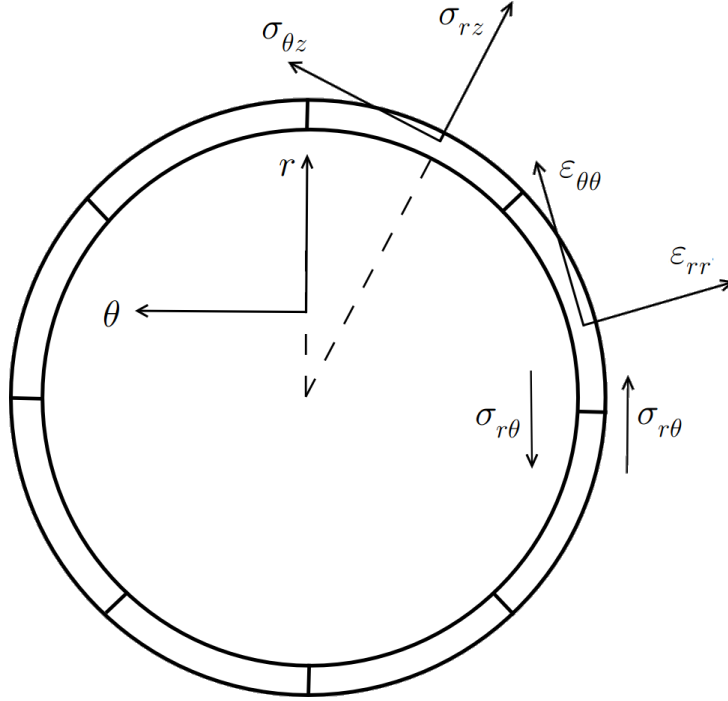
Figure 2.2: Sketch of the top view of a thin material shell of cylindrical anisotropy with the strains and stresses.

a sketch of the top view of a thin material shell of cylindrical anisotropy with the strains and stresses. This could be interpreted as a thin layer of a Cartesian anisotropic material folded over the surface of a circular tube. Many of the nanowires have a structure of "concentrical" atom layers and the cylindrical anisotropy can be considered as a reasonable starting point for these systems.

The matrix of elastic coefficients will be given in this case by

$$
C_{\alpha\beta} \;=\; \begin{bmatrix}
C_{11} & C_{12} & C_{13} & C_{14} & C_{15} & C_{16} \\
C_{12} & C_{22} & C_{23} & C_{24} & C_{25} & C_{26} \\
C_{13} & C_{23} & C_{33} & C_{34} & C_{35} & C_{36} \\
C_{14} & C_{24} & C_{34} & C_{44} & C_{45} & C_{46} \\
C_{15} & C_{25} & C_{35} & C_{45} & C_{55} & C_{56} \\
C_{16} & C_{26} & C_{36} & C_{46} & C_{56} & C_{66}
\end{bmatrix}, \tag{2.51}
$$

including up to twenty-one independent elastic constants.

We shall consider a homogeneous thick cylinder of infinite length and radius R, or a homogeneous cylindrical shell of infinite length, inner radius

a, outer radius b and thickness h ($b = a + h$). We shall use the cylindrical coordinate system (r,θ,z).

We assume that the mass density ρ is constant in the cylinder (cylindrical shell). The cylinder axis coincides with the crystalline axis z and the surfaces are stress free.

The strain-displacement relations are

$$\epsilon_{rr} = \frac{\partial u_r}{\partial r} \; ; \quad \epsilon_{r\theta} = \frac{1}{2} \left(\frac{1}{r} \frac{\partial u_r}{\partial \theta} + \frac{\partial u_\theta}{\partial r} - \frac{u_\theta}{r} \right)$$

$$\epsilon_{\theta\theta} = \frac{1}{r} \left(\frac{\partial u_\theta}{\partial \theta} + u_r \right) \; ; \qquad \epsilon_{\theta z} = \frac{1}{2} \left(\frac{\partial u_\theta}{\partial z} + \frac{\partial u_z}{\partial \theta} \right) \qquad (2.52)$$

$$\epsilon_{zz} = \frac{\partial u_z}{\partial z} \; ; \qquad \epsilon_{rz} = \frac{1}{2} \left(\frac{\partial u_r}{\partial z} + \frac{\partial u_z}{\partial r} \right) \; .$$

The equations of motion are given now by

$$\frac{\partial \sigma_{rr}}{\partial r} + \frac{1}{r} \frac{\partial \sigma_{r\theta}}{\partial \theta} + \frac{\partial \sigma_{rz}}{\partial z} + \frac{1}{r}(\sigma_{rr} - \sigma_{\theta\theta}) = \rho \frac{\partial^2 u_r}{\partial t^2}$$

$$\frac{\partial \sigma_{r\theta}}{\partial r} + \frac{1}{r} \frac{\partial \sigma_{\theta\theta}}{\partial \theta} + \frac{\partial \sigma_{\theta z}}{\partial z} + \frac{2}{r}\sigma_{r\theta} = \rho \frac{\partial^2 u_\theta}{\partial t^2} \qquad (2.53)$$

$$\frac{\partial \sigma_{rz}}{\partial r} + \frac{1}{r} \frac{\partial \sigma_{\theta z}}{\partial \theta} + \frac{\partial \sigma_{zz}}{\partial z} + \frac{1}{r}\sigma_{rz} = \rho \frac{\partial^2 u_z}{\partial t^2} \; ,$$

where

$$\begin{bmatrix} \sigma_{rr} \\ \sigma_{\theta\theta} \\ \sigma_{zz} \\ \sigma_{\theta z} \\ \sigma_{rz} \\ \sigma_{r\theta} \end{bmatrix} = \begin{bmatrix} C_{11} & C_{12} & C_{13} & C_{14} & C_{15} & C_{16} \\ C_{12} & C_{22} & C_{23} & C_{24} & C_{25} & C_{26} \\ C_{13} & C_{23} & C_{33} & C_{34} & C_{35} & C_{36} \\ C_{14} & C_{24} & C_{34} & C_{44} & C_{45} & C_{46} \\ C_{15} & C_{25} & C_{35} & C_{45} & C_{55} & C_{56} \\ C_{16} & C_{26} & C_{36} & C_{46} & C_{56} & C_{66} \end{bmatrix} \begin{bmatrix} \epsilon_{rr} \\ \epsilon_{\theta\theta} \\ \epsilon_{zz} \\ 2\,\epsilon_{\theta z} \\ 2\,\epsilon_{rz} \\ 2\,\epsilon_{r\theta} \end{bmatrix} \; . \qquad (2.54)$$

The general solution of this problem, as we told before, must be obtained numerically, but we shall consider now the particular case of the radial breathing modes.

The radial breathing modes are purely radial vibrations, so that $u_r \neq 0$ and $u_\theta = u_z = 0$. In the same way

$$\frac{\partial u_r}{\partial \theta} = \frac{\partial u_r}{\partial z} = 0 \; . \qquad (2.55)$$

It can be shown that the second and third equations in (2.53) are satisfied automatically and we are left with

$$\frac{d^2 u_r}{dr^2} + \frac{1}{r}\frac{du_r}{dr} + (\beta_l^2 - \frac{\mu^2}{r^2})u_r = 0 \ , \tag{2.56}$$

with $\beta_l^2 = \dfrac{\rho\omega^2}{C_{11}}$ and $\mu^2 = \dfrac{C_{22}}{C_{11}}$.

Eq.(2.56) is a Bessel equation of non-integer order. Thus we have the solution

$$u_r(r) \quad = \quad \begin{cases} AJ_\mu(\beta_l r) + BJ_{-\mu}(\beta_l r) & , \quad \beta_l > 0 \\ Ar + \dfrac{B}{r} & , \quad \beta_l = 0 \ . \end{cases} \tag{2.57}$$

It is easy to see that if $C_{22} = C_{11}$ we have $\mu=1$ and we recover the Bessel equation of integer order. In that case the solution is given by

$$u_r(r) \quad = \quad \begin{cases} AJ_1(\beta_l r) + BY_1(\beta_l r) & , \quad \beta_l > 0 \\ Ar + \dfrac{B}{r} & , \quad \beta_l = 0 \ , \end{cases} \tag{2.58}$$

Y_1 being the second-kind Bessel function of order 1.

The boundary conditions at the surfaces are now

$$C_{11}\frac{du_r}{dr} + C_{12}\frac{u_r}{r} = 0 \ . \tag{2.59}$$

In the case of a thick cylinder, in order that u_r be finite at $r=0$, we must have $B=0$. Thus we shall have:

$$u_r(r) \quad = \quad \begin{cases} AJ_\mu(\beta_l r) & , \quad \beta_l > 0 \\ Ar & , \quad \beta_l = 0 \ . \end{cases} \tag{2.60}$$

If $\sigma_{rr}(R)=0$, $A=0$ when $\beta_l=0$, and for $\beta_l > 0$ we have

$$C_{11}J_\mu'(\beta_l R) + C_{12}\frac{1}{R}J_\mu(\beta_l R) = 0 \ . \tag{2.61}$$

As

$$J_\mu'(\beta_l r) = \beta_l J_{\mu-1}(\beta_l r) - \frac{\mu}{r}J_\mu(\beta_l r) \tag{2.62}$$

eq.(2.61) becomes

$$C_{11}\beta_l J_{\mu-1}(\beta_l R) + (C_{12} - C_{11}\mu)\frac{1}{R}J_\mu(\beta_l R) = 0 \ , \tag{2.63}$$

thus giving

$$\beta_l R J_{\mu-1}(\beta_l R) = (\mu - \frac{C_{12}}{C_{11}})J_\mu(\beta_l R) \ . \tag{2.64}$$

This equation is a generalization of the expression obtained by Hu et al. [66] for an infinitely long isotropic cylinder

$$\beta_l J_0(\beta_l R) = \frac{1}{R}\frac{(1-2\nu)}{1-\nu}J_1(\beta_l R) \tag{2.65}$$

with the Poisson's factor $\nu = \dfrac{C_{12}}{2(C_{12} + C_{44})}$.

In the isotropic case $C_{11} = C_{22}$ and $C_{11} = C_{12} + 2C_{44}$. Thus it is easy to see that eq.(2.64) becomes eq.(2.65).

In the case of the cylindrical shell, using the boundary conditions given in eq.(2.59) we would have:

$$A(C_{11}J'_\mu(\beta_l r) + C_{12}\frac{1}{r}J_\mu(\beta_l r)) + B(C_{11}J'_{-\mu}(\beta_l r) + C_{12}\frac{1}{r}J_{-\mu}(\beta_l r)) \quad , \quad \beta_l > 0$$

$$\tag{2.66}$$

$$A(C_{11} - C_{12}) - B(C_{11} - C_{12})\frac{1}{r^2} \quad , \quad \beta_l = 0 \ .$$

As $\sigma_{rr}(a) = \sigma_{rr}(b)=0$, we must have $A = B = 0$, for $\beta_l=0$, whereas for $\beta_l >0$ we have

$$\begin{vmatrix} C_{11}\beta_l J'_\mu(\beta_l a) + C_{12}\frac{1}{a}J_\mu(\beta_l a) & C_{11}\beta_l J'_{-\mu}(\beta_l a) + C_{12}\frac{1}{a}J_{-\mu}(\beta_l a) \\ \\ C_{11}\beta_l J'_\mu(\beta_l b) + C_{12}\frac{1}{b}J_\mu(\beta_l b) & C_{11}\beta_l J'_{-\mu}(\beta_l b) + C_{12}\frac{1}{b}J_{-\mu}(\beta_l b) \end{vmatrix} = 0 \tag{2.67}$$

This is the secular determinant giving the elastic radial breathing mode frequencies of an infinitely long cylindrical shell in the case of general anisotropy. In hexagonal crystals $C_{22} = C_{11}$ and $C_{12} = C_{11}-2C_{66}$. Then the last equation reduces to eq.(2.46) , for the hexagonal crystals.

In the case of a thin shell it is possible to expand eq.(2.67) to first order in $\dfrac{h}{a}$. Then we arrive to

$$[(C_{12}^2 - C_{11}C_{22}) + C_{11}^2\beta_l^2 a^2]\beta_l a[2\mu J_\mu(\beta_l a)J_{-\mu}(\beta_l a) \quad +$$
$$\beta_l a J_\mu(\beta_l a)J_{-\mu-1}(\beta_l a) - \beta_l a J_{\mu-1}(\beta_l a)J_{-\mu}(\beta_l a)] \quad = \quad 0 . \qquad (2.68)$$

Taking into account that

$$J_\mu'(\beta_l a) = \beta_l J_{\mu-1}(\beta_l a) - \frac{\mu}{a}J_\mu(\beta_l a)$$
$$J_{-\mu}'(\beta_l a) = \beta_l J_{-\mu-1}(\beta_l a) + \frac{\mu}{a}J_{-\mu}(\beta_l a) \qquad (2.69)$$

it can be seen that the factor involving the Bessel functions in eq.(2.68) is the Wronskian, having the value

$$J_\mu(\beta_l a)J_{-\mu}'(\beta_l a) - J_\mu'(\beta_l a)J_{-\mu}(\beta_l a) = -\frac{2\sin(\mu\pi)}{\pi\beta_l a} \neq 0 . \qquad (2.70)$$

Thus the expression for the lowest breathing mode frequency of a thin cylindrical shell of a general anisotropic crystal is given by

$$(C_{12}^2 - C_{11}C_{22}) + C_{11}^2\beta_l^2 a^2 = 0 , \qquad (2.71)$$

which can be put in the form

$$\omega = \frac{1}{a}\sqrt{\frac{C_{11}C_{22} - C_{12}^2}{\rho C_{11}}} = \frac{2}{d}\sqrt{\frac{C_{11}C_{22} - C_{12}^2}{\rho C_{11}}} , \qquad (2.72)$$

$d = 2a$ being the diameter.

In the case of hexagonal crystals $C_{22} = C_{11}$, $C_{12} = C_{11} - 2C_{66}$ and eq.(2.72) reduces to

$$\omega = \frac{2}{a}\sqrt{\frac{C_{66}(C_{12} + C_{66})}{\rho(C_{12} + 2C_{66})}} \qquad (2.73)$$

given in eq.(2.50).

For an isotropic crystal $C_{22} = C_{11}$ and $C_{12} = C_{11} - 2C_{44}$. Then eq.(2.72) reduces to

$$\omega = \frac{2}{a}\sqrt{\frac{C_{44}(C_{12} + C_{44})}{\rho(C_{12} + 2C_{44})}} \qquad (2.74)$$

which coincides with the expressions given in Refs. [30, 55].

On the other hand, for the cubic and other crystal systems $C_{22} = C_{11}$, but $C_{12} \neq C_{11} - 2C_{44}$, and then eq.(22) reads

$$\omega = \frac{1}{a}\sqrt{\frac{C_{11}^2 - C_{12}^2}{\rho C_{11}}} \ . \tag{2.75}$$

Eq.(2.72) is a simple analytic expression valid for all crystal systems. It provides in a quick way a first estimate of the lowest breathing mode frequency for nanotubes. It was seen [30] that eq.(2.73) and eq.(2.74) gave extremely good agreement with experimental and first principles theoretical values of the lowest breathing mode frequency of different carbon and other materials nanotubes.

Eq.(2.67) gives the frequencies of higher order breathing modes.

2.2.2.2 Core-shell and composite cylinders

We shall consider in the first place a core-shell cylinder formed by two different materials denoted by 1 and 2. The core will be of material 1 in a region $0 \leq r \leq R_1$. The shell will be formed by material 2 in a region $R_1 \leq r \leq R_2$.

The displacement would be now

$$u_r(r) \ = \ \begin{cases} A^{(1)} J_{\mu^{(1)}}(\beta_1 r) + B^{(1)} J_{-\mu^{(1)}}(\beta_1 r) \ , & 0 \leq r \leq R_1 \\ A^{(2)} J_{\mu^{(2)}}(\beta_2 r) + B^{(2)} J_{-\mu^{(2)}}(\beta_2 r) \ , & R_1 \leq r \leq R_2 \ . \end{cases} \tag{2.76}$$

As the displacement must be finite at $r = 0$ this implies that $B^{(1)} = 0$.
We must apply now the boundary conditions to this system.
At $r = R_1$ the displacement must be continuous, thus giving

$$A^{(1)} J_{\mu^{(1)}}(\beta_1 R_1) - A^{(2)} J_{\mu^{(2)}}(\beta_2 R_1) - B^{(2)} J_{-\mu^{(2)}}(\beta_2 R_1) = 0 \ . \tag{2.77}$$

As the normal stress must also be continuous we must have $\sigma_{rr}^{(1)}(R_1) = \sigma_{rr}^{(2)}(R_1)$, and

$$A^{(1)}(C_{11}^{(1)} J'_{\mu^{(1)}}(\beta_1 R_1) + C_{12}^{(1)} \frac{1}{R_1} J_{\mu^{(1)}}(\beta_1 R_1)) \ -$$

$$A^{(2)}(C_{11}^{(2)} J'_{\mu^{(2)}}(\beta_2 R_1) + C_{12}^{(2)} \frac{1}{R_1} J_{\mu^{(2)}}(\beta_2 R_1)) \ - \tag{2.78}$$

$$B^{(2)}(C_{11}^{(2)} J'_{-\mu^{(2)}}(\beta_2 R_1) + C_{12}^{(2)} \frac{1}{R_1} J_{-\mu^{(2)}}(\beta_2 R_1)) \ = \ 0 \ .$$

The outer surface at $r = R_2$ is stress free, $\sigma_{rr}^{(2)}(R_2) = 0$, thus

$$A^{(2)}(C_{11}^{(2)} J'_{\mu^{(2)}}(\beta_2 R_2) + C_{12}^{(2)} \frac{1}{R_2} J_{\mu^{(2)}}(\beta_2 R_2)) \quad +$$

$$B^{(2)}(C_{11}^{(2)} J'_{-\mu^{(2)}}(\beta_2 R_2) + C_{12}^{(2)} \frac{1}{R_2} J_{-\mu^{(2)}}(\beta_2 R_2)) \quad = \quad 0 \; . \qquad (2.79)$$

As a consequence, the frequencies of the acoustic radial breathing modes of the cylindrical core shell system are obtained from the secular determinant

$$\begin{vmatrix} d_{11} & d_{12} & d_{13} \\ d_{21} & d_{22} & d_{23} \\ 0 & d_{32} & d_{33} \end{vmatrix} = 0 \; , \qquad (2.80)$$

being

$$
\begin{aligned}
d_{11} &= J_{\mu^{(1)}}(\beta_1 R_1) \\
d_{12} &= -J_{\mu^{(2)}}(\beta_2 R_1) \\
d_{13} &= -J_{-\mu^{(2)}}(\beta_2 R_1) \\
d_{21} &= (C_{11}^{(1)} J'_{\mu^{(1)}}(\beta_1 R_1) + C_{12}^{(1)} \frac{1}{R_1} J_{\mu^{(1)}}(\beta_1 R_1)) \\
d_{22} &= -(C_{11}^{(2)} J'_{\mu^{(2)}}(\beta_2 R_1) + C_{12}^{(2)} \frac{1}{R_1} J_{\mu^{(2)}}(\beta_2 R_1)) \\
d_{23} &= -(C_{11}^{(2)} J'_{-\mu^{(2)}}(\beta_2 R_1) + C_{12}^{(2)} \frac{1}{R_1} J_{-\mu^{(2)}}(\beta_2 R_1)) \\
d_{32} &= -(C_{11}^{(2)} J'_{\mu^{(2)}}(\beta_2 R_2) + C_{12}^{(2)} \frac{1}{R_2} J_{\mu^{(2)}}(\beta_2 R_2)) \\
d_{33} &= -(C_{11}^{(2)} J'_{-\mu^{(2)}}(\beta_2 R_2) + C_{12}^{(2)} \frac{1}{R_2} J_{-\mu^{(2)}}(\beta_2 R_2)) \; . \qquad (2.81)
\end{aligned}
$$

The most general composite cylinder is formed by N different materials covering the range $0 \le R_1 \le R_2 \le R_3 \le \cdots \le R_N$. This problem is a generalization of the core-shell one. It is easy to see that the secular determinant is of dimension $(2N - 1) \times (2N - 1)$, having the structure

$$
\begin{vmatrix}
d_{11} & d_{12} & d_{13} & 0 & 0 & 0 & 0 & \cdots & 0 & 0 \\
d_{21} & d_{22} & d_{23} & 0 & 0 & 0 & 0 & \cdots & 0 & 0 \\
0 & d_{32} & d_{33} & d_{34} & d_{35} & 0 & 0 & \cdots & 0 & 0 \\
0 & d_{42} & d_{43} & d_{44} & d_{45} & 0 & 0 & \cdots & 0 & 0 \\
0 & 0 & 0 & d_{54} & d_{55} & d_{56} & d_{57} & \cdots & 0 & 0 \\
0 & 0 & 0 & d_{64} & d_{65} & d_{66} & d_{67} & \cdots & 0 & 0 \\
\vdots & \vdots & \vdots & \vdots & \vdots & \vdots & \vdots & \ddots & \vdots & \vdots \\
0 & 0 & 0 & 0 & 0 & 0 & 0 & \cdots & d_{2N-2,2N-2} & d_{2N-2,2N-1} \\
0 & 0 & 0 & 0 & 0 & 0 & 0 & \cdots & d_{2N-1,2N-2} & d_{2N-1,2N-1}
\end{vmatrix} = 0 \, ,
$$

$$(2.82)$$

where $d_{11}, d_{12}, d_{13}, d_{21}, d_{22}, d_{23}$ are given in eq.(2.81). For $2 < n \leq N - 1$ the non-zero elements in the secular determinant have the form

$$
\begin{aligned}
d_{2n-1,2n-2} &= J_{\mu^{(n)}}(\beta_n R_n) \\
d_{2n-1,2n-1} &= J_{-\mu^{(n)}}(\beta_n R_n) \\
d_{2n-1,2n} &= -J_{\mu^{(n+1)}}(\beta_{n+1} R_n) \\
d_{2n-1,2n} &= -J_{-\mu^{(n+1)}}(\beta_{n+1} R_n) \\
d_{2n,2n-2} &= C_{11}^{(n)} J'_{\mu^{(n)}}(\beta_n R_n) + C_{12}^{(n)} \frac{1}{R_n} J_{\mu^{(n)}}(\beta_n R_n) \\
\\
d_{2n,2n-1} &= C_{11}^{(n)} J'_{-\mu^{(n)}}(\beta_n R_n) + C_{12}^{(n)} \frac{1}{R_n} J_{-\mu^{(n)}}(\beta_n R_n) \\
\\
d_{2n,2n} &= -C_{11}^{(n+1)} J'_{\mu^{(n+1)}}(\beta_{n+1} R_n) - C_{12}^{(n+1)} \frac{1}{R_n} J_{\mu^{(n+1)}}(\beta_{n+1} R_n) \\
\\
d_{2n,2n+1} &= -C_{11}^{(n+1)} J'_{-\mu^{(n+1)}}(\beta_{n+1} R_n) - C_{12}^{(n+1)} \frac{1}{R_n} J_{-\mu^{(n+1)}}(\beta_{n+1} R_n) \, .
\end{aligned}
$$

$$(2.83)$$

The last row, corresponding to $n = N$, has only two non-zero terms given by

$$
\begin{aligned}
d_{2N-1,2N-2} &= -C_{11}^{(N)} J'_{\mu^{(N)}}(\beta_N R_N) - C_{12}^{(N)} \frac{1}{R_N} J_{\mu^{(N)}}(\beta_N R_N) \\
\\
d_{2N-1,2N-1} &= -C_{11}^{(N)} J'_{-\mu^{(N)}}(\beta_N R_N) - C_{12}^{(N)} \frac{1}{R_N} J_{-\mu^{(N)}}(\beta_N R_N)
\end{aligned}
$$

$$(2.84)$$

When $C_{22} = C_{11}$ we must substitute $J_\mu, J'_\mu, J_{-\mu}, J'_{-\mu}$ by J_1, J'_1, Y_1, Y'_1 in eqs.(2.81, 2.83, 2.84).

In this way we have obtained in eq.(2.80) and eq.(2.82) the secular determinant of acoustic radial (breathing) modes in closed form for core-shell and composite cylinders of anisotropic crystals.

2.2.3 XYZ method

In recent years, different experimental groups have grown nanowires having circular, square or hexagonal cross-sections [67, 68, 60, 69, 70, 71, 72, 73, 74, 75, 19, 76]. As we have seen in the previous section, there is no way to solve, in a general form, the equations of motion for cylindrical wires of anisotropic crystals. The same is true for wires with different cross-sections. In order to deal with this kind of nanowires, a theoretical method originally developed in resonant ultrasound spectroscopy to obtain the free vibrational modes of inhomogeneous objects [31, 32, 33, 34] can be used. The method studies the free vibrations of elastic anisotropic systems having arbitrary shape and mass density variation, thus being quite adequate for the present case. This is performed by expanding the elastic displacements in terms of a set of basis functions that are products of powers of the Cartesian coordinates, being then called the xyz-algorithm.

In order to obtain the acoustic modes of the anisotropic nanowires we shall use the theory of linear elasticity. In this way the Lagrangian of the system comes in terms of the elastic displacement components u_i, elastic stiffness tensor C_{ijkl}, mass density ρ and frequency ω in the form

$$L = \frac{1}{2} \int_V (\rho \omega^2 u_i u_i - C_{ijkl} \frac{\partial u_j}{\partial x_i} \frac{\partial u_l}{\partial x_k}) dV \quad , \tag{2.85}$$

V being the volume of the nanowire.

The change in the elastic displacement components $u_i' = u_i + \delta_i$ induces the variation δL of the Lagrangian given by

$$\delta L = \int_V [\rho \omega^2 u_i + \frac{\partial}{\partial x_j} C_{ijkl} \frac{\partial u_l}{\partial x_k}] \delta u_i dV - \int_s n_j C_{jikl} \frac{\partial u_l}{\partial x_k} \delta u_i dS \quad , \tag{2.86}$$

where n_j is the j-th component of the unit vector normal to the surface S of the nanowire, while

$$\sigma_{ij} = C_{ijkl} \frac{\partial u_l}{\partial x_k} \quad , \tag{2.87}$$

is the stress tensor.

For a stress-free nanowire the stress field must vanish at the nanowire surface, then:

$$[\sigma_{ij} n_j]_S = 0 \; . \tag{2.88}$$

If we postulate now that the Lagrangian has a minimum with respect to u_i, we arrive to the elastic wave equation:

$$\rho \omega^2 u_i + \frac{\partial}{\partial x_j} C_{ijkl} \frac{\partial u_l}{\partial x_k} = 0 \; . \tag{2.89}$$

Now we can expand the displacement components u_i in terms of a complete set of functions Ψ_λ

$$u_i = \sum_\lambda a_{i\lambda} \Psi_\lambda \; . \tag{2.90}$$

Substitution of this expansion in the wave equation gives

$$a_{i\lambda} \rho \omega^2 \Psi_\lambda + a_{j\lambda} C_{ijkl} \frac{\partial^2 \Psi_\lambda}{\partial x_j \partial x_k} = 0 \; . \tag{2.91}$$

Multiplying by $\Psi_{\lambda'}^*$ and integrating over the volume of the nanowire, V, we get the following eigenvalue equation

$$a_{i\lambda} \rho \omega^2 \int_V \Psi_{\lambda'}^* \Psi_\lambda dV - a_{j\lambda} C_{ijkl} \int_V \frac{\partial \Psi_{\lambda'}^*}{\partial x_j} \frac{\partial \Psi_\lambda}{\partial x_k} dV = 0 \; . \tag{2.92}$$

Now it is possible to define the following matrix elements [32]

$$
\begin{aligned}
E_{i\lambda',j\lambda} &= \delta_{ij} \frac{\rho}{V} \int_V \Psi_{\lambda'}^* \Psi_\lambda dV \; , \\[2mm]
\Phi_{i\lambda',j\lambda} &= \frac{C_{ijkl}}{V} \int_V \frac{\partial \Psi_{\lambda'}^*}{\partial x_j} \frac{\partial \Psi_\lambda}{\partial x_k} dV \; ,
\end{aligned}
\tag{2.93}
$$

and to express the eigenvalue equation in the following form

$$[\omega^2 \mathbf{E} - \mathbf{\Phi}] \mathbf{a} = 0 \; . \tag{2.94}$$

Obviously different choices for the basis functions are possible. In order to perform numerical calculations for a variety of nanowire shapes the most practical choice is the simplest possible complete set of functions [32]. This choice is provided by the powers of the Cartesian coordinates, and then we get the following set of basis functions

$$\Psi_\lambda(x,y,z) = \left(\frac{x}{A}\right)^l \left(\frac{y}{B}\right)^m \left(\frac{z}{L}\right)^n \;, \tag{2.95}$$

for a finite nanowire of dimensions (A, B, L), where $\lambda = (l, m, n)$ the function label is a set of three non-negative integers, or

$$\Psi_\lambda(x,y,z) = \left(\frac{x}{A}\right)^l \left(\frac{y}{B}\right)^m \exp(iQz) \;, \tag{2.96}$$

for an infinite nanowire, Q being the longitudinal wavevector of the elastic modes along the wire axis. $\lambda = (l, m)$ the function label is a set of two non-negative integers.

In terms of the basis the displacements are expanded in a truncated basis until a maximum number N to obtain convergence. In the case of the finite nanowire $l + m + n \leq N$, whereas for the infinite nanowire $l + m \leq N$.

The price paid for not using an orthonormal basis set is that $\mathbf{E}$ is not the identity matrix. On the other hand the use of an orthonormal set would entail the need to choose a different $\{\Psi_\lambda\}$ set for each different shape and for each different mass density ρ, which can be a function with arbitrary position dependence. As a consequence the required matrix elements could not be expressed in closed form.

Applications to wires with square, rectangular and circular cross-sections have been presented in Visscher[32], Nishiguchi et al.[23] and Li et al.[37], but no application to hexagonal cross-section has been done until now.

We shall consider now in some detail the hexagonal cross-section case.

We shall choose in this case the following basis functions

$$\Psi_\lambda(x,y,z) = \left(\frac{x}{A}\right)^l \left(\frac{2y}{\sqrt{3}A}\right)^m \exp(iQz) \;, \tag{2.97}$$

for an infinite wire, A being the hexagon side.

In this case the integrals entering the $\mathbf{E}$ and $\mathbf{\Phi}$ matrices are of the form

$$\int_V \left(\frac{x}{A}\right)^l \left(\frac{2y}{\sqrt{3}A}\right)^m dV = \frac{2^m}{(\sqrt{3})^m A^{l+m}} \int_V x^l y^m dV \;. \tag{2.98}$$

The volume integral can be divided in three parts

$$\int_V x^l y^m dV = \int_{-A}^{-\frac{A}{2}} \int_{-\sqrt{3}(A+x)}^{\sqrt{3}(A+x)} x^l y^m dy dx + \int_{-\frac{A}{2}}^{\frac{A}{2}} x^l dx \int_{-\frac{\sqrt{3}A}{2}}^{\frac{\sqrt{3}A}{2}} y^m dy +$$

$$(2.99)$$

$$\int_{\frac{A}{2}}^{A} \int_{-\sqrt{3}(A-x)}^{\sqrt{3}(A-x)} x^l y^m dy dx \ .$$

After some manipulation it can be written as

$$\int_V \left(\frac{x}{A}\right)^l \left(\frac{2y}{\sqrt{3}A}\right)^m dV = \frac{2^m \sqrt{3}^{m+1}}{\sqrt{3}^m A^{l+m}} \left(\frac{1-(-1)^{m+1}}{m+1}\right) \left(\frac{1-(-1)^{l+1}}{l+1}\right) \times$$

$$(2.100)$$

$$\left[\frac{A^{l+m+2}}{2^{l+m+2}} + (m+1) \int_{\frac{A}{2}}^{A} x^l (A-x)^{m+1} dx\right] \ .$$

The last integral can be expressed in the form

$$\int_{\frac{A}{2}}^{A} x^l (A-x)^{m+1} dx = \frac{A^{l+m+2}}{l+2} \left(\frac{\Gamma(l+2)\Gamma(m+2)}{\Gamma(l+m+3)} - \right.$$

$$(2.101)$$

$$\left. \frac{_2F_1(l+1;-m-1;l+2;\frac{1}{2})}{2^{l+1}}\right) \ .$$

Thus we have finally

$$\int_V \left(\frac{x}{A}\right)^l \left(\frac{2y}{\sqrt{3}A}\right)^m dV = \frac{A^2\sqrt{3}}{2^{l+2}} \left(\frac{1-(-1)^{m+1}}{m+1}\right) \left(\frac{1-(-1)^{l+1}}{l+1}\right) \times$$

$$\left(1 + 2^{l+m+2}\frac{\Gamma(l+2)\Gamma(m+2)}{\Gamma(l+m+3)}\right. \qquad (2.102)$$

$$\left. -2_2^{m+1}F_1\left(l+1;-m-1;l+2;\frac{1}{2}\right)\right) \ .$$

where $_2F_1(l+1;-m-1;l+2;\frac{1}{2})$ is the Gauss hypergeometric function [61]. We have then all the possible integrals entering the matrices $\mathbf{E}$ and $\mathbf{\Phi}$.

In the case of a hollow nanowire we must take into account that all the integrals can be obtained by integrating over a full prism and then substracting the empty core [37]. In this case no new boundary conditions are needed.

Also in the case of nanowires grown along a direction not coinciding with one of the crystal axes, the elastic stiffness tensor must be transformed to the new reference system.

2.2.4 Multilayer structures: Surface Green Function Matching method (SGFM)

To obtain the dispersion curves of the acoustic waves in the superlattices we employ the Surface Green Function Matching (SGFM) method [40] which is very adequate to study the properties of multi-layer systems formed by anisotropic materials [39].

Figure 2.3: Scheme of the formal framework of the superlattice.

2.2.4.1 SGFM for the superlattice. Continuous media.

The simplest superlattice is formed by the infinite repetition of two materials, labelled 1 and 2, having thicknesses d_1 and d_2 respectively, the superlattice period being $d = d_1 + d_2$. Polytype superlattices are formed by more material layers in the period, but they can be considered as a generalisation of the simplest ones.

The formal framework to describe the superlattice is represented in a schematic way in Figure 2.3. We see a two-interface domain formed by the interfaces l(left) and r(right), with medium 2, contained between l and r, defined as the *internal* one. We see also two external layers designed by 1 and 3. We shall use the symbol P_μ to denote either the projector of domain $\mu = 1, 2, 3$, or a point of this domain. The external and internal domains are

defined as:

$$P_e = P_1 + P_3 \; ; \; P_i = P_2 \tag{2.103}$$

G_μ is the Green function of the bulk medium μ. The Green functions 1 and 3 are equal, because media 1 and 3 are physically equal. We keep the labels 1 and 3 to denote that they are in different domains.

We shall obtain G_S, the Green function of the composite matched system, in terms of the corresponding projections defined by:

$$G_i = P_i G_i P_i' = P_2 G_2 P_2' \; ; \; G_e = P_e G_e P_e' = P_1 G_1 P_1' + P_3 G_3 P_3' \tag{2.104}$$

If t is a translation through a distance d, equal to the superlattice period, then every time we consider a point P_1 we shall consider also its translated point P_3, denoted tP_1 and viceversa, P_1 will be $t^{-1}P_3$. This is convenient because the superlattice states can be labelled by a quantum number q which is the (super)wavevector associated to the (super)periodicity so that the amplitudes at z and $z+d$ are related by the Bloch phase factor:

$$f = e^{i\varphi} = e^{iqd} \; . \tag{2.105}$$

We must note that G_i and G_e *are not* Green functions. They are simply objects defined by the projections specified above.

Our aim is to obtain the system Green function $G_S(\Omega, \kappa, q, z, z')$ from $G_1(\Omega, \kappa, z, z')$ and $G_2(\Omega, \kappa, z, z')$, Ω being the eigenvalue (energy, frequency) of the problem considered.

We *define* the matching surface to consist of both l and r. Now we must specify on which part, left or right, of the matching surface are the variables z and z'. Consequently we define the two-surface or *full interface* projections

$$\hat{\mathbf{G}}_i = \hat{\mathbf{G}}_2 = \left\| \begin{array}{cc} \mathcal{G}_{2l} & \mathbf{G}_2(l,r) \\ \mathbf{G}_2(r,l) & \mathcal{G}_{2r} \end{array} \right\| \; ; \; \hat{\mathbf{G}}_e = \left\| \begin{array}{cc} \mathcal{G}_{1l} & \mathbf{G}_1(l,r) \\ \mathbf{G}_3(r,l) & \mathcal{G}_{3r} \end{array} \right\| . \tag{2.106}$$

where $\mathcal{G}_{\mu l}/\mathcal{G}_{\mu r}$ is the one surface projection at l/r. In general, for a differential system with N coupled differential equations each one of the elements appearing in $\tilde{\mathbf{G}}_i$ and $\tilde{\mathbf{G}}_e$ is an NxN matrix and then $\tilde{\mathbf{G}}_i$ and $\tilde{\mathbf{G}}_e$ are $2N$x$2N$ matrices. We shall refer to any $\mathbf{G}(z, z')$, like $\mathcal{G}_l$ or $\mathbf{G}(l, r)$, as matrix elements - on the understanding that they may not be scalar quantities - and to the objects like $\tilde{\mathbf{G}}_i$ and $\tilde{\mathbf{G}}_e$ as 2×2 supermatrices. The 2×2 supermatrix format is very suitable for the study of the two-surface problem, as will be seen. The purpose of the analysis is to obtain the full $\mathbf{G}_s(z, z')$, which of

course has nonvanishing elements between any (z, z') and, in particular, its full interface projection

$$\tilde{\mathbf{G}}_s = \left\| \begin{array}{cc} \mathcal{G}_{s\ l} & \mathbf{G}_s(l, r) \\ \\ \mathbf{G}_s(r, l) & \mathcal{G}_{s\ r} \end{array} \right\| . \tag{2.107}$$

We can use the symbols l and r according to convenience either as labels or to denote the numerical values of z or z'. We can also use them to denote the corresponding one-surface projectors, in which case the unit $\mathcal{I}$ of the full matching surface is the two-surface projector

$$\mathcal{I} = l + r . \tag{2.108}$$

By definition the new *two-surface objects* carry the projector $\mathcal{I}$ on both sides. For instance $\tilde{\mathbf{G}}_2$ is identically $\mathcal{I}\tilde{\mathbf{G}}_2\mathcal{I}$, but this will only be explicitly shown when it is necessary.

The purpose of this compact notation is to provide a concise way to carry out the $SGFM$ analysis of the two-surface problem so a lengthy explicit algebra is avoided.

Let us now look at the physical picture. Suppose, for instance, a standard unit input starts at some point of the internal domain. It can then propagate to another point inside either directly or after reflection at the two interfaces, and to a point outside only through transmission. We now combine this physical argument with the compact algebraic notation for the two-surface problem and write for the form of $\mathbf{G}_s(z, z')$, when $z, z' \in P_i$,

$$P_i\mathbf{G}_s P_i' = P_2\mathbf{G}_2 P_2' + P_2\mathbf{G}_2 \cdot \tilde{\mathcal{R}} \cdot \mathbf{G}_2 P_2' . \tag{2.109}$$

We have introduced the two-surface object $\tilde{\mathcal{R}}$, a $2{\times}2$ supermatrix related to reflection at the full interface domain. Note the physical picture embodied in the reflection term. Since we use the bulk propagator $\mathbf{G}_2$, before and after $\tilde{\mathcal{R}}$, this is *defined* to be a (reflection) T-matrix in the sense of scattering theory. The fact that it gives by definition the *total* reflection scattering at the full interface has an important practical consequence as it avoids the need to sum the infinite series which would otherwise have to account for the multiple reflections at the two interfaces. By definition these are all included in the last term of (2.109). Now take the full interface projection:

$$\tilde{\mathbf{G}}_s = \tilde{\mathbf{G}}_2 + \tilde{\mathbf{G}}_2 \cdot \tilde{\mathcal{R}} \cdot \tilde{\mathbf{G}}_2 . \tag{2.110}$$

This is an equality among 2×2 supermatrices, whereby by ordinary matrix algebra

$$\tilde{\mathcal{R}} = \tilde{\mathbf{G}}_2^{-1} \cdot (\tilde{\mathbf{G}}_s - \tilde{\mathbf{G}}_2) \cdot \tilde{\mathbf{G}}_2^{-1} \ , \tag{2.111}$$

which substituted in (2.109) yields

$$P_i \mathbf{G}_s P_i' = P_2 \mathbf{G}_2 P_2' + P_2 \mathbf{G}_2 \cdot \tilde{\mathbf{G}}_2^{-1}(\tilde{\mathbf{G}}_s - \tilde{\mathbf{G}}_2) \cdot \tilde{\mathbf{G}}_2^{-1} \cdot \mathbf{G}_2 P_2' \ . \tag{2.112}$$

In the same way, with the unit input at some point inside, the form of the amplitude at a final point outside is

$$P_e \tilde{\mathbf{G}}_s P_i' = P_e \tilde{\mathbf{G}}_e \cdot \tilde{\mathcal{T}} \cdot \tilde{\mathbf{G}}_i P_i' \ , \tag{2.113}$$

whence by projecting

$$\tilde{\mathcal{T}} = \tilde{\mathbf{G}}_e^{-1} \cdot \tilde{\mathbf{G}}_s \cdot \tilde{\mathbf{G}}_i^{-1} \ , \tag{2.114}$$

which substituted in (2.113) yields

$$P_e \mathbf{G}_s P_i' = P_e \mathbf{G}_e \cdot \tilde{\mathbf{G}}_e^{-1} \cdot \tilde{\mathbf{G}}_s \cdot \tilde{\mathbf{G}}_i^{-1} \cdot \mathbf{G}_i P_i' \ . \tag{2.115}$$

The argument can be repeated with the initial point outside and the formulae are of course isomorphic with (2.112), that is,

$$P_e \mathbf{G}_s P_e' = P_e \mathbf{G}_e P_e' + P_e \mathbf{G}_e \cdot \tilde{\mathbf{G}}_e^{-1} \cdot (\tilde{\mathbf{G}}_s - \tilde{\mathbf{G}}_e) \cdot \tilde{\mathbf{G}}_e^{-1} \cdot \mathbf{G}_e P_e' \tag{2.116}$$

and with (2.115), that is

$$P_i \mathbf{G}_s P_e' = P_2 \mathbf{G}_2 \cdot \tilde{\mathbf{G}}_2^{-1} \cdot \tilde{\mathbf{G}}_s \cdot \tilde{\mathbf{G}}_e^{-1} \cdot \mathbf{G}_e P_e' \ , \tag{2.117}$$

but the four formulae lead to different explicit expressions, on account of the different connectivities of P_e and P_i. Let us see how these formulae must be read. We indicate by z_μ the fact that z is in domain μ and likewise for z_μ'. Then the l.h.s. of (2.112), for instance, is $\mathbf{G}_s(z_2, z_2')$. The first term on the r.h.s. is $\mathbf{G}_2(z_2, z_2')$ but the second term requires more detailed scrutiny. The factor $P_2 \mathbf{G}_2$ is actually $P_2 \mathbf{G}_2 \mathcal{I}$, as it is multiplied on the right by a

two-surface object. But $\mathcal{I}$ consists of l and r, so z_2' can be at l or at r and $P_2 \mathbf{G}_2 \mathcal{I}$ is the 2-component row supervector

$$P_2 \mathbf{G}_2 \mathcal{I} = [\mathbf{G}_2(z_2, l), \mathbf{G}_2(z_2, r)] , \tag{2.118}$$

where we recall that each component is in general an NxN matrix. Likewise

$$\mathcal{I} \mathbf{G}_2 P_2' = \begin{bmatrix} \mathbf{G}_2(l, z_2') \\[2mm] \mathbf{G}_2(r, z_2') \end{bmatrix} \tag{2.119}$$

is a 2-component column supervector. Finally

$$\begin{aligned} \mathbf{G}_s(z_2, z_2') &= \mathbf{G}_2(z_2, z_2') + [\mathbf{G}_2(z_2, l), \mathbf{G}_2(z_2, r)] \cdot \tilde{\mathbf{G}}_2^{-1} \cdot (\tilde{\mathbf{G}}_s - \tilde{\mathbf{G}}_2) \cdot \\[4mm] & \quad \tilde{\mathbf{G}}_2^{-1} \cdot \begin{bmatrix} \mathbf{G}_2(l, z_2') \\[2mm] \mathbf{G}_2(r, z_2') \end{bmatrix} . \end{aligned} \tag{2.120}$$

The last term is formally a contracted product of a matrix with a row vector on its left and a column vector on its right, of the form

$$[a_l , a_r] \cdot \left\| \begin{array}{cc} \mathcal{M}_{ll} & \mathcal{M}_{lr} \\[2mm] \mathcal{M}_{rl} & \mathcal{M}_{rr} \end{array} \right\| \cdot \begin{bmatrix} b_l \\[2mm] b_r \end{bmatrix} . \tag{2.121}$$

We recall that we take the pair of surfaces (l, r) as the projection - eventually matching - domain. The form of $P_i \mathbf{G}_s P_i'$ is obviously (2.112) or (2.120). Consider the two cases of $P_e \mathbf{G}_s P_i'$. These will involve $m\mathbf{F}_1$ or $n\mathbf{F}_3$, which we can eliminate from the analysis by using the phase relationships

$$m\mathbf{F}_1 = f^{-1} \times r\mathbf{F}_3 ; \ n\mathbf{F}_3 = f \times l\mathbf{F}_1 . \tag{2.122}$$

Then, for instance

$$\begin{aligned} P_1 \mathbf{G}_s P_i' &= P_1 \mathbf{G}_1 l \cdot l\mathbf{F}_1 + P_1 \mathbf{G}_1 m \cdot m\mathbf{F}_1 \\[3mm] &= P_1 \mathbf{G}_1 l \cdot l\mathbf{F}_1 + f^{-1} \times P_1 \mathbf{G}_1 m \cdot r\mathbf{F}_3 . \end{aligned} \tag{2.123}$$

The meaning of the first line is obvious by inspection of Figure 2.3 and the advantage of the second line is that the form of the two unknown amplitudes can be obtained from the physical picture: A standard unit input at P_2' propagates with propagator $\mathbf{G}_2$ to l and to r and there the amplitudes emitted into domains 1 and 2 are, respectively,

$$l\mathbf{F}_1 = l\tilde{\mathcal{T}}\mathcal{I}\cdot\mathcal{I}\mathbf{G}_2 P_2' \; ; \; r\mathbf{F}_3 = r\tilde{\mathcal{T}}\mathcal{I}\cdot\mathcal{I}\mathbf{G}_2 P_2' \; , \qquad (2.124)$$

where $\tilde{\mathcal{T}}$ is a two-surface transmission T-matrix. Thus

$$P_1\mathbf{G}_s P_i' = P_1\mathbf{G}_1 l\cdot l\tilde{\mathcal{T}}\mathcal{I}\cdot\mathcal{I}\mathbf{G}_2 P_2' + f^{-1}\times P_1\mathbf{G}_1 m\cdot r\tilde{\mathcal{T}}\mathcal{I}\cdot\mathcal{I}\mathbf{G}_2 P_2' \quad (2.125)$$

and, by the same sort of argument

$$P_3\mathbf{G}_s P_i' = f\times P_3\mathbf{G}_3 n\cdot l\tilde{\mathcal{T}}\mathcal{I}\cdot\mathcal{I}\mathbf{G}_2 P_2' + P_3\mathbf{G}_3 r\cdot r\tilde{\mathcal{T}}\mathcal{I}\cdot\mathcal{I}\mathbf{G}_2 P_2' \; . \quad (2.126)$$

Now define an 'external Green function' $\mathbf{G}_e^f$ in the following way

$$
\begin{aligned}
P_1\mathbf{G}_e^f\mathcal{I} &= [P_1\mathbf{G}_1 l, f^{-1}\times P_1\mathbf{G}_1 m] = \\[4pt]
&\big[\mathbf{G}_1(z_1,l), f^{-1}\times\mathbf{G}_1(z_1,m)\big] = [P_1\mathbf{G}_e^f l, P_1\mathbf{G}_e^f r] \; ; \\[4pt]
P_3\mathbf{G}_e^f\mathcal{I} &= [f\times P_3\mathbf{G}_3 n, P_3\mathbf{G}_3 r] = \\[4pt]
&\big[f\times\mathbf{G}_3(z_3,r), \mathbf{G}_3(z_3,r)\big] = [P_3\mathbf{G}_e^f l, P_3\mathbf{G}_e^f r] \; .
\end{aligned}
\qquad (2.127)
$$

Then (2.125) and (2.126) can be condensed into

$$P_e\mathbf{G}_s P_i' = P_e\mathbf{G}_e^f\cdot\tilde{\mathcal{T}}\cdot\mathbf{G}_2 P_2' \; . \qquad (2.128)$$

Now, define the 2×2 supermatrix

$$\hat{\mathbf{G}}_e = \mathcal{I}\mathbf{G}_e^f\mathcal{I} \;\; = \;\; \left\| \begin{array}{cc} \hat{\mathbf{G}}_e(l,l) & \hat{\mathbf{G}}_e(l,r) \\[2mm] \hat{\mathbf{G}}_e(r,l) & \hat{\mathbf{G}}_e(r,r) \end{array} \right\| =$$

$$\left\| \begin{array}{cc} \mathcal{G}_{1l} & f^{-1} \times \mathbf{G}_1(l,m) \\[3mm] f \times \mathbf{G}_3(r,n) & \mathcal{G}_{3r} \end{array} \right\| , \quad (2.129)$$

take the full $\mathcal{I}$ projection of (2.128) and solve for $\tilde{\mathcal{T}}$. Then

$$P_e\mathbf{G}_sP_i' = P_e\mathbf{G}_e^f \cdot \hat{\mathbf{G}}_e^{-1} \cdot \tilde{\mathbf{G}}_s \cdot \tilde{\mathbf{G}}_2^{-1} \cdot \mathbf{G}_2 P_2' . \quad (2.130)$$

Suppose the input is outside. We note that with just a standard unit input at, say, P_1' we cannot generate a superlattice eigenstate satisfying Bloch's theorem. We must put simultaneously δ at P_1' and $f \times \delta$ at $P_3' = tP_1'$. Then the amplitudes of Figure 2.3 have different forms, namely:

$$l\mathbf{F}_1 = \hat{\mathcal{R}}_{ll} \cdot l\mathbf{G}_1 P_1' + f \times \hat{\mathcal{R}}_{lr} \cdot r\mathbf{G}_3 P_3' \;;$$

$$l\mathbf{F}_2 = \hat{\mathcal{T}}_{ll} \cdot l\mathbf{G}_1 P_1' + f \times \hat{\mathcal{T}}_{lr} \cdot r\mathbf{G}_3 P_3' \;;$$

$$\qquad\qquad\qquad\qquad\qquad\qquad\qquad\qquad\qquad (2.131)$$

$$r\mathbf{F}_2 = \hat{\mathcal{T}}_{rl} \cdot l\mathbf{G}_1 P_1' + f \times \hat{\mathcal{T}}_{rr} \cdot r\mathbf{G}_3 P_3' \;;$$

$$r\mathbf{F}_3 = \hat{\mathcal{R}}_{rl} \cdot l\mathbf{G}_1 P_1' + f \times \hat{\mathcal{R}}_{rr} \cdot r\mathbf{G}_3 P_3' .$$

We have introduced appropriate reflection and transmission objects to describe the reemission of amplitudes into the external or internal domains, respectively. We then have

$$\begin{aligned} P_1\mathbf{G}_sP_1' \;\; = \;\; & P_1\mathbf{G}_1 P_1' + P_1\mathbf{G}_1 l \cdot [\hat{\mathcal{R}}_{ll} \cdot l\mathbf{G}_1 P_1' + f \times \hat{\mathcal{R}}_{lr} \cdot r\mathbf{G}_3 P_3'] \\[3mm] & + \;\; f^{-1} \times P_1\mathbf{G}_1 m \cdot [\hat{\mathcal{R}}_{rl} \cdot l\mathbf{G}_1 P_1' + f \times \hat{\mathcal{R}}_{rr} \cdot r\mathbf{G}_3 P_3'] , \end{aligned}$$
$$\qquad\qquad\qquad\qquad\qquad\qquad\qquad\qquad\qquad (2.132)$$

which has an obvious physical interpretation by using the same kind of argument we have repeatedly invoked. Likewise

$$
\begin{aligned}
P_2\mathbf{G}_sP_1' \;\; = \;\; & P_2\mathbf{G}_2l \cdot [\hat{\mathcal{T}}_{ll} \cdot l\mathbf{G}_1P_1' + f \times \hat{\mathcal{T}}_{lr} \cdot r\mathbf{G}_3P_3'] \\[2mm]
& + \;\; P_2\mathbf{G}_2r \cdot [\hat{\mathcal{T}}_{rl} \cdot l\mathbf{G}_1P_1' + f \times \hat{\mathcal{T}}_{rr} \cdot r\mathbf{G}_3P_3'] \qquad (2.133)
\end{aligned}
$$

and

$$
\begin{aligned}
P_3\mathbf{G}_sP_1' \;\; = \;\; & f \times P_3\mathbf{G}_3P_3' + f \times P_3\mathbf{G}_3n \cdot [\hat{\mathcal{R}}_{ll} \cdot l\mathbf{G}_1P_1' + f \times \hat{\mathcal{R}}_{lr} \cdot r\mathbf{G}_3P_3'] \\[2mm]
& + \;\; P_3\mathbf{G}_3r \cdot [\hat{\mathcal{R}}_{rl} \cdot l\mathbf{G}_1P_1' + f \times \hat{\mathcal{R}}_{rr} \cdot r\mathbf{G}_3P_3'] \qquad (2.134)
\end{aligned}
$$

Due to the periodicity we can put

$$
r\mathbf{G}_3P_3' = m\mathbf{G}_1P_1' \qquad\qquad (2.135)
$$

in the above three formulae. The first term on the r.h.s. of (2.134) is also of the right form again because P_3' is tP_1'. This will be sorted out later. The terms $P_\mu\mathbf{G}_sP_3'$ are written in much the same way with the only difference that for these we put a standard unit input δ at P_3' and an input $f^{-1} \times \delta$ at $P_1' = t^{-1}P_3'$. By using systematically the fact that $\mathbf{G}_3$ and $\mathbf{G}_1$ are equal, and the periodicity property

$$
P_3\mathbf{G}_3P_3' = P_1\mathbf{G}_1P_1' \;, \qquad\qquad (2.136)
$$

of which (2.135) is a particular case, the above results and those for $P_\mu\mathbf{G}_sP_3'$ can be finally condensed in the following compact forms:

$$
P_e\mathbf{G}_sP_e' = P_e\mathbf{G}_e^fP_e' + P_e\mathbf{G}_e^f \cdot \hat{\mathcal{R}} \cdot \mathbf{G}_e^fP_e' \qquad\qquad (2.137)
$$

and

$$
P_i\mathbf{G}_sP_e' = \qquad\quad P_2\mathbf{G}_2 \cdot \hat{\mathcal{T}} \cdot \mathbf{G}_e^fP_e' \;, \qquad\qquad (2.138)
$$

where we have defined the 2-component (super)column vectors

$$
\mathcal{I}\mathbf{G}_e^f P_1' \;=\; \begin{bmatrix} l\mathbf{G}_e^f P_1' \\[4pt] r\mathbf{G}_e^f P_1' \end{bmatrix} = \begin{bmatrix} l\mathbf{G}_1 P_1' \\[4pt] f \times m\mathbf{G}_1 P_1' \end{bmatrix} = \begin{bmatrix} \mathbf{G}_1(l, z_1') \\[4pt] f \times \mathbf{G}_1(m, z_1') \end{bmatrix} ;
$$

$$
\mathcal{I}\mathbf{G}_e^f P_3' \;=\; \begin{bmatrix} l\mathbf{G}_e^f P_3' \\[4pt] r\mathbf{G}_e^f P_3' \end{bmatrix} = \begin{bmatrix} f^{-1} \times n\mathbf{G}_1 P_3' \\[4pt] r\mathbf{G}_1 P_3' \end{bmatrix} = \begin{bmatrix} f^{-1} \times \mathbf{G}_1(n, z_3') \\[4pt] \mathbf{G}_1(r, z_3') \end{bmatrix} ,
$$

$$
(2.139)
$$

which are complementary to (2.127). It is now obvious that by projecting (2.137) and (2.138), solving for $\hat{\mathcal{R}}$ and $\hat{\mathcal{T}}$ and substituting back in these formulae we obtain

$$
P_e \mathbf{G}_s P_e' = P_e \mathbf{G}_e^f P_e' + P_e \mathbf{G}_e^f \cdot \hat{\mathbf{G}}_e^{-1} \cdot (\tilde{\mathbf{G}}_s - \hat{\mathbf{G}}_e) \cdot \hat{\mathbf{G}}_e^{-1} \cdot \mathbf{G}_e^f P_e' \qquad (2.140)
$$

and

$$
P_i \mathbf{G}_s P_e' = \qquad\qquad P_2 \mathbf{G}_2 \cdot \tilde{\mathbf{G}}_2^{-1} \cdot \tilde{\mathbf{G}}_s \cdot \hat{\mathbf{G}}_e^{-1} \cdot \mathbf{G}_e^f \cdot P_e' . \qquad (2.141)
$$

Together with (2.130) and (2.112) we have the formulae for all possible elements of $\mathbf{G}_s$ in the superlattice case.

In order to discuss the matching analysis, we must consider the continuity conditions in terms of Green functions. In general the Green function is continuous, but the normal derivative with respect to the interface has a discontinuous jump which depends only on the form of the differential system irrespective of the boundary conditions away from the planes chosen as interfaces.

In a general case, the Green function will be a matrix and the linear differential system can be represented in the form:

$$
\left[\frac{d}{dz} \left[\mathbf{S} \cdot \frac{d}{dz} + \mathbf{P} \right] + \left(\mathbf{Y} \frac{d}{dz} + \mathbf{W} \right) \right] \cdot \mathbf{G}(z, z') = \mathbf{I}\delta(z - z'). \qquad (2.142)
$$

We define also the following linear differential form:

$$
\mathbf{A}(z, z') = \left[\mathbf{S} \cdot \frac{d}{dz} + \mathbf{P} \right] \cdot \mathbf{G}(z, z') \qquad (2.143)
$$

Taking an arbitrary point $z' = 0$, integrating from $-\mu$ to $+\mu$ and letting $\mu \to 0$ we obtain

$$\mathcal{A}(+0) - \mathcal{A}(-0) = -\mathbf{I}. \tag{2.144}$$

Since $\mathbf{A}(z, z')$ contains the first order derivative of $\mathbf{G}(z, z')$, the side where the surface projection $\mathcal{A}$ is evaluated must be specified. Note that

$$\mathcal{A}(\pm 0) = \lim_{z \to \pm 0} \mathbf{A}(z, 0) \equiv \mathcal{A}^{(\mp)} \equiv \mathcal{M}(\pm 0) \cdot {}'\mathcal{G}^{(\mp)} + \mathcal{P}(\pm 0) \cdot \mathcal{G}, \tag{2.145}$$

whence

$$\mathcal{A}^{(+)} - \mathcal{A}^{(-)} = -\mathbf{I} \tag{2.146}$$

and we obtain the general discontinuity condition

$$\left[\mathcal{M}(-0) \cdot {}'\mathcal{G}^{(+)} + \mathcal{P}(-0) \cdot \mathcal{G} \right] - \left[\mathcal{M}(+0) \cdot {}'\mathcal{G}^{(-)} + \mathcal{P}(+0) \cdot \mathcal{G} \right] = -\mathbf{I} \tag{2.147}$$

We are now ready to carry out the matching analysis for the two-surface problem. The idea is to study the configurations (z_1, z_2'), (z_2, z_2') with $z_2 < z_2'$ and (z_2, z_2'), (z_3, z_2') with $z_2 > z_2'$. In the first case we impose the matching conditions at l and *then* let $z_2' \to l + 0$ and $z_2' \to r - 0$ while in the second case we impose the matching conditions at r and then do the same again with z_2'. The four equalities, condensed in the compact 2×2 supermatrix notation yield the matching formula for $\tilde{\mathbf{G}}_s^{-1}$. Then we have

$$\left\{ -\mathbf{s}_1^{-1} \cdot [{}'\mathcal{G}_{1l}^{(+)}, 0] + \mathcal{P}_1 \cdot [\mathcal{G}_{1l}, 0] \right\} \cdot \tilde{\mathbf{G}}_e^{-1} \cdot \tilde{\mathbf{G}}_s \cdot \tilde{\mathbf{G}}_2^{-1} \cdot \begin{bmatrix} \mathbf{G}_2(l, z_2') \\ \\ \mathbf{G}_2(r, z_2') \end{bmatrix} =$$

$$\left\{ -\mathbf{s}_2^{-1} \cdot [{}'\mathcal{G}_{2l}^{(-)}, {}'\mathbf{G}_2(l, r)] \right.$$

$$\left. + \mathcal{P}_2 \cdot [\mathcal{G}_{2l}, \mathbf{G}_2(l, r)] \right\} \cdot \tilde{\mathbf{G}}_2^{-1} \cdot \tilde{\mathbf{G}}_s \cdot \tilde{\mathbf{G}}_2^{-1} \cdot \begin{bmatrix} \mathbf{G}_2(l, z_2') \\ \\ \mathbf{G}_2(r, z_2') \end{bmatrix}$$

$$+ \mathbf{s}_2^{-1} \cdot \left\{ -{}'\mathbf{G}_2(l, z_2') + [{}'\mathcal{G}_{2l}^{(-)}, {}'\mathbf{G}_2(l, r)] \cdot \tilde{\mathbf{G}}_2^{-1} \cdot \begin{bmatrix} \mathbf{G}_2(l, z_2') \\ \\ \mathbf{G}_2(r, z_2') \end{bmatrix} \right\}$$

$$+ \mathcal{P}_2 \cdot \left\{ \mathbf{G}_2(l, z_2') - [\mathcal{G}_{2l}, \mathbf{G}_2(l, r)] \cdot \tilde{\mathbf{G}}_2^{-1} \cdot \begin{bmatrix} \mathbf{G}_2(l, z_2') \\ \\ \mathbf{G}_2(r, z_2') \end{bmatrix} \right\} .$$

$$\tag{2.148}$$

The factor multiplying $\mathcal{P}_2$ is

$$\mathbf{G}_2(l, z_2') - [l, 0] \cdot \begin{bmatrix} \mathbf{G}_2(l, z_2') \\ \mathbf{G}_2(r, z_2') \end{bmatrix} = 0 \; . \tag{2.149}$$

Now take $z_2' \to l + 0$. The second term on the r.h.s. of (2.148) is then

$$\mathbf{s}_2^{-1} \cdot \{ -'\mathcal{G}_{2l}^{(+)} + ['\mathcal{G}_{2l}^{(-)}, '\mathbf{G}_2(l, r)] \cdot \begin{bmatrix} l \\ 0 \end{bmatrix} \} = \\ \mathbf{s}_2^{-1} \cdot \{ '\mathcal{G}_{2l}^{(-)} -' \mathcal{G}_{2l}^{(+)} \} = -l \tag{2.150}$$

and the matching condition (2.148) reads

$$\{ -\mathbf{s}_1^{-1} \cdot ['\mathcal{G}_{1l}^{(+)}, 0] + \mathcal{P}_1 \cdot [\mathcal{G}_{1l}, 0] \} \cdot \tilde{\mathbf{G}}_e^{-1} \cdot \tilde{\mathbf{G}}_s \cdot \begin{bmatrix} l \\ 0 \end{bmatrix} = \\ \{ -\mathbf{s}_2^{-1}['\mathcal{G}_{2l}^{(-)}, '\mathbf{G}_2(l, r)] + \mathcal{P}_2 \cdot [\mathcal{G}_{2l}, \mathbf{G}_2(l, r)] \} \cdot \tilde{\mathbf{G}}_2^{-1} \cdot \tilde{\mathbf{G}}_s \cdot \begin{bmatrix} l \\ 0 \end{bmatrix} - l \; , \tag{2.151}$$

while on taking $z_2' \to r - 0$ the second term on the r.h.s. of (2.148) becomes

$$\mathbf{s}_2^{-1} \cdot \{ -'\mathbf{G}_2(l, r) + ['\mathcal{G}_{2l}^{(-)}, '\mathbf{G}_2(l, r)] \cdot \begin{bmatrix} 0 \\ r \end{bmatrix} \} = \\ \mathbf{s}_2^{-1} \cdot \{ -'\mathbf{G}_2(l, r) +' \mathbf{G}_2(l, r) \} = 0 \tag{2.152}$$

and we obtain

$$\{ -\mathbf{s}_1^{-1} \cdot ['\mathcal{G}_{1l}^{(+)}, 0] + \mathcal{P}_1 \cdot [\mathcal{G}_{1l}, 0] \} \cdot \tilde{\mathbf{G}}_e^{-1} \cdot \tilde{\mathbf{G}}_s \cdot \begin{bmatrix} 0 \\ r \end{bmatrix} = \\ \{ -\mathbf{s}_2^{-1} \cdot ['\mathcal{G}_{2l}^{(-)}, '\mathbf{G}_2(l, r)] + \mathcal{P}_2 \cdot [\mathcal{G}_{2l}, \mathbf{G}_2(l, r)] \} \cdot \tilde{\mathbf{G}}_2^{-1} \cdot \tilde{\mathbf{G}}_s \cdot \begin{bmatrix} 0 \\ r \end{bmatrix} \; . \tag{2.153}$$

For the second configuration we obtain

$$\{-\mathbf{s}_3^{-1} \cdot [0,{}'\mathcal{G}_{3r}^{(-)}] + \mathcal{P}_3 \cdot [0, \mathcal{G}_{3r}]\} \cdot \tilde{\mathbf{G}}_e^{-1} \cdot \tilde{\mathbf{G}}_s \cdot \tilde{\mathbf{G}}_2^{-1} \cdot \begin{bmatrix} \mathbf{G}_2(l, z_2') \\ \\ \mathbf{G}_2(r, z_2') \end{bmatrix} =$$

$$\{-\mathbf{s}_2^{-1} \cdot [{}'\mathbf{G}_2(r, l),{}'\mathcal{G}_{2r}^{(+)}] + \mathcal{P}_2 \cdot [\mathbf{G}_2(r, l), \mathcal{G}_{2r}]\} \cdot \tilde{\mathbf{G}}_2^{-1} \cdot$$

$$\tilde{\mathbf{G}}_s \cdot \begin{bmatrix} \mathbf{G}_2(l, z_2') \\ \\ \mathbf{G}_2(r, z_2') \end{bmatrix} + \mathbf{s}_2^{-1} \cdot \{-{}'\mathbf{G}_2(r, z_2') +$$

$$[{}'\mathbf{G}_2(r, l),{}'\mathcal{G}_{2r}^{(+)}]\} \cdot \tilde{\mathbf{G}}_2^{-1} \cdot \begin{bmatrix} \mathbf{G}_2(l, z_2') \\ \\ \mathbf{G}_2(r, z_2') \end{bmatrix} . \qquad (2.154)$$

By means of a similar algebra we find on taking $z_2' \rightarrow l + 0$:

$$\{-\mathbf{s}_3^{-1} \cdot [0,{}'\mathcal{G}_{3r}^{(-)}] + \mathcal{P}_3 \cdot [0, \mathcal{G}_{3r}]\} \cdot \tilde{\mathbf{G}}_e^{-1} \cdot \tilde{\mathbf{G}}_s \cdot \begin{bmatrix} l \\ 0 \end{bmatrix} =$$

$$\{-\mathbf{s}_2^{-1} \cdot [{}'\mathbf{G}_2(r, l),{}'\mathcal{G}_{2r}^{(+)}] + \mathcal{P}_2 \cdot [\mathbf{G}_2(r, l), \mathcal{G}_{2r}]\} \cdot \tilde{\mathbf{G}}_2^{-1} \cdot \tilde{\mathbf{G}}_s \cdot \begin{bmatrix} l \\ 0 \end{bmatrix}$$

$$(2.155)$$

and on taking $z' \rightarrow r - 0$:

$$\{-\mathbf{s}_3^{-1} \cdot [0,{}'\mathcal{G}_{3r}^{(-)}] + \mathcal{P}_3 \cdot [0, \mathcal{G}_{3r}]\} \cdot \tilde{\mathbf{G}}_e^{-1} \cdot \tilde{\mathbf{G}}_s \cdot \begin{bmatrix} 0 \\ r \end{bmatrix} =$$

$$\{-\mathbf{s}_2^{-1} \cdot [{}'\mathbf{G}_2(r, l),{}'\mathcal{G}_{2r}^{(+)}] + \mathcal{P}_2 \cdot [\mathbf{G}_2(r, l), \mathcal{G}_{2r}]\} \cdot \tilde{\mathbf{G}}_2^{-1} \cdot \tilde{\mathbf{G}}_s \cdot \begin{bmatrix} 0 \\ r \end{bmatrix} + r .$$

$$(2.156)$$

The four equations of interest are (2.151), (2.153), (2.155) and (2.156). In order to condense these in supermatrix format we define

$$'\tilde{\mathbf{G}}_e = \left\| \begin{array}{cc} '\mathcal{G}_{1l}^{(+)} & f^{-1} \times \mathbf{G}_1(l,m) \\ -f \times \mathbf{G}_1(r,n) & -'\mathcal{G}_{1r}^{(-)} \end{array} \right\| \; ; \quad '\tilde{\mathbf{G}}_i = \left\| \begin{array}{cc} '\mathcal{G}_{2l}^{(-)} & '\mathbf{G}_2(l,r) \\ -'\mathbf{G}_2(r,l) & -'\mathcal{G}_{2r}^{(+)} \end{array} \right\| \; ;$$

$$\tilde{\mathcal{S}}_e = \left\| \begin{array}{cc} \mathbf{s}_1 & 0 \\ 0 & \mathbf{s}_3 \end{array} \right\| \; ; \qquad\qquad\qquad \tilde{\mathcal{S}}_i = \left\| \begin{array}{cc} \mathbf{s}_2 & 0 \\ 0 & \mathbf{s}_2 \end{array} \right\| \; ;$$

$$\tilde{\mathcal{P}}_e = \left\| \begin{array}{cc} \mathcal{P}_1 & 0 \\ 0 & \mathcal{P}_3 \end{array} \right\| \; ; \qquad\qquad\qquad \tilde{\mathcal{P}}_i = \left\| \begin{array}{cc} \mathcal{P}_2 & 0 \\ 0 & \mathcal{P}_2 \end{array} \right\| \; .$$

$$(2.157)$$

Then the above four equations are, respectively, the (l,l), (l,r), (r,l) and (r,r) supermatrix elements of the compact equation

$$\{[-\tilde{\mathcal{S}}_e^{-1} \cdot ' \tilde{\mathbf{G}}_e + \tilde{\mathcal{P}}_e \cdot \tilde{\mathbf{G}}_e] \cdot \tilde{\mathbf{G}}_e^{-1} - [-\tilde{\mathcal{S}}_i^{-1} \cdot ' \tilde{\mathbf{G}}_i + \tilde{\mathcal{P}}_i \cdot \tilde{\mathbf{G}}_i] \cdot \tilde{\mathbf{G}}_i^{-1}\} \cdot \mathbf{G}_s = \mathcal{I} \; , \quad (2.158)$$

whence the matching formula

$$\tilde{\mathbf{G}}_s^{-1} = \{\tilde{\mathcal{S}}_e^{-1} \cdot ' \tilde{\mathbf{G}}_e \cdot \tilde{\mathbf{G}}_e^{-1} - \tilde{\mathcal{S}}_i^{-1} \cdot ' \tilde{\mathbf{G}}_i \cdot \tilde{\mathbf{G}}_i^{-1}\} - \{\tilde{\mathcal{P}}_e - \tilde{\mathcal{P}}_i\} \; . \qquad (2.159)$$

Alternatively, we can define

$$\tilde{\mathcal{A}}_e = -\tilde{\mathcal{S}}_e^{-1} \cdot ' \tilde{\mathbf{G}}_e + \tilde{\mathcal{P}}_e \cdot \tilde{\mathbf{G}}_e \; ; \; \tilde{\mathcal{A}}_i = -\tilde{\mathcal{S}}_i^{-1} \cdot ' \tilde{\mathbf{G}}_i + \tilde{\mathcal{P}}_i \cdot \tilde{\mathbf{G}}_i \; . \qquad (2.160)$$

Then (2.159) takes the general form

$$-\tilde{\mathbf{G}}_s^{-1} = \tilde{\mathcal{A}}_e \cdot \tilde{\mathbf{G}}_e^{-1} - \tilde{\mathcal{A}}_i \cdot \tilde{\mathbf{G}}_i^{-1} \; . \qquad (2.161)$$

In the case of a sandwich structure of the type 1–2–3 it is clear that there is no periodicity present and both interfaces, l and r are not coupled. The off-diagonal blocks of the external domain $\left(\tilde{\mathbf{G}}_e, \; '\tilde{\mathbf{G}}_e, \; '\tilde{\mathcal{A}}_e \right)$ vanish and these supermatrices are block-diagonal. This is the modification to be introduced in the formulation described above.

In the case of a polytype layer structure, including N layers, the analysis can be repeated and the general matching formula in that case is given by:

$$-\tilde{\mathbf{G}}_s^{-1} = \mathcal{I} \left(\tilde{\mathcal{A}}_1 \cdot \tilde{\mathbf{G}}_1^{-1} - \sum_{i=2}^{N} \tilde{\mathcal{A}}_i \cdot \tilde{\mathbf{G}}_i^{-1} \right) \mathcal{I} \; . \qquad (2.162)$$

2.2.4.2 SGFM for the superlattice. Hexagonal systems.

We shall give here the detailed expression for the Green's function and normal derivatives particular to the hexagonal system together with the essential formal expressions for the study of the superlattices.

The bulk material Green's function $\mathbf{G}$ for hexagonal crystals is given by

$$
\mathbf{G} \;=\; \begin{bmatrix}
\frac{C_{33}k_z^2+(C_{44}\kappa^2-\rho\omega^2)}{C_{33}C_{44}(\beta_1^2+k_z^2)(\beta_2^2+k_z^2)} & 0 & -\frac{(C_{44}+C_{13})\kappa k_z}{C_{33}C_{44}(\beta_1^2+k_z^2)(\beta_2^2+k_z^2)} \\[2mm]
0 & \frac{1}{C_{44}(\beta_t^2+k_z^2)} & 0 \\[2mm]
-\frac{(C_{44}+C_{13})\kappa k_z}{C_{33}C_{44}(\beta_1^2+k_z^2)(\beta_2^2+k_z^2)} & 0 & \frac{C_{44}k_z^2+(C_{11}\kappa^2-\rho\omega^2)}{C_{33}C_{44}(\beta_1^2+k_z^2)(\beta_2^2+k_z^2)}
\end{bmatrix},
$$
$$(2.163)$$

where

$$
\beta_1^2 \;=\; \frac{1}{2}[B + (B^2 - 4C^2)^{\frac{1}{2}}] \;, \tag{2.164}
$$

$$
\beta_2^2 \;=\; \frac{1}{2}[B - (B^2 - 4C^2)^{\frac{1}{2}}] \;, \tag{2.165}
$$

$$
B \;=\; \frac{1}{C_{33}C_{44}}[(C_{44}^2 + C_{11}C_{33})\kappa^2 -
$$
$$
(C_{13} + C_{44})^2\kappa^2 - (C_{33} + C_{44})\rho\omega^2] \;, \tag{2.166}
$$

$$
C^2 \;=\; \frac{1}{C_{33}C_{44}}(C_{44}\kappa^2 - \rho\omega^2)(C_{11}\kappa^2 - \rho\omega^2) \;, \tag{2.167}
$$

$$
\beta_t \;=\; \left(\frac{C_{11} - C_{12}}{2C_{44}}\kappa^2 - \frac{\rho\omega^2}{C_{44}}\right)^{\frac{1}{2}} = \left(\frac{C_{66}}{C_{44}}\kappa^2 - \frac{\rho\omega^2}{C_{44}}\right)^{\frac{1}{2}} \;, \tag{2.168}
$$

(In all cases $\mathrm{Re}(\beta_i)>0$, $\mathrm{Im}(\beta_i)>0$, $i=1,2,t$.)
The surface projected elements of the Green function are obtained from

$$
\mathcal{G}_{ij}(\kappa, \omega^2) = \lim_{\epsilon \to 0} \frac{1}{2\pi} \int_{-\infty}^{\infty} \exp[i\epsilon k_z] G_{ij}(\kappa, k_z; \omega^2) dk_z \;, \tag{2.169}
$$

whereas the normal derivatives are obtained from

$$
{}'\mathcal{G}_{ij}^{(\pm)}(\kappa, \omega^2) = \lim_{\epsilon \to 0} \frac{1}{2\pi} \int_{-\infty}^{\infty} \exp[\mp i\epsilon k_z] i k_z G_{ij}(\kappa, k_z; \omega^2) dk_z \;, \tag{2.170}
$$

thus giving

$$
\mathcal{G} \;=\; \begin{bmatrix} \dfrac{C_{33}\beta_1\beta_2 + C_{44}\kappa^2 - \rho\omega^2}{2C_{33}C_{44}\beta_1\beta_2(\beta_1+\beta_2)} & 0 & 0 \\[4mm] 0 & \dfrac{1}{2C_{44}\beta_t} & 0 \\[4mm] 0 & 0 & \dfrac{C_{44}\beta_1\beta_2 + C_{11}\kappa^2 - \rho\omega^2}{2C_{33}C_{44}\beta_1\beta_2(\beta_1+\beta_2)} \end{bmatrix},
$$

$$(2.171)$$

and

$$
'\mathcal{G}^{\pm} \;=\; \begin{bmatrix} \pm\dfrac{1}{2C_{44}} & 0 & -\dfrac{i(C_{13}+C_{44})\kappa}{2C_{33}C_{44}(\beta_1+\beta_2)} \\[4mm] 0 & \pm\dfrac{1}{2C_{44}} & 0 \\[4mm] -\dfrac{i(C_{13}+C_{44})\kappa}{2C_{33}C_{44}(\beta_1+\beta_2)} & 0 & \pm\dfrac{1}{2C_{33}} \end{bmatrix} \quad (2.172)
$$

We obtain also

$$
G_{ij}(\kappa,z,z';\omega^2) = \frac{1}{2\pi}\int_{-\infty}^{\infty} \exp[ik_z(z-z')]G_{ij}(\kappa,k_z;\omega^2)dk_z \;, \qquad (2.173)
$$

and

$$
'G_{ij}(\kappa,z,z';\omega^2) = \frac{\partial}{\partial z}\,G_{ij}(\kappa,z,z';\omega^2)\,. \qquad (2.174)
$$

From here we obtain in our case

$$
\begin{aligned}
G_{11}(\kappa, z, z'; \omega^2) &= \frac{1}{2C_{33}C_{44}\beta_1(\beta_1^2 - \beta_2^2)}(C_{33}\beta_1^2 - C_{44}\kappa^2 + \rho\omega^2)exp(-\beta_1|z - z'|) \\
&\quad - \frac{1}{2C_{33}C_{44}\beta_2(\beta_1^2 - \beta_2^2)}(C_{33}\beta_2^2 - C_{44}\kappa^2 + \rho\omega^2)exp(-\beta_2|z - z'|) , \\
G_{13}(\kappa, z, z'; \omega^2) &= sgn(z - z')\frac{i\kappa(C_{13} + C_{44})}{2C_{33}C_{44}(\beta_1^2 - \beta_2^2)}(exp(-\beta_1|z - z'|) - exp(-\beta_2|z - z'|)) , \\
G_{22}(\kappa, z, z'; \omega^2) &= \frac{1}{2C_{44}\beta_t}exp(-\beta_t|z - z'|) , \\
G_{31}(\kappa, z, z'; \omega^2) &= G_{13}(\kappa, z, z'; \omega^2) , \\
G_{33}(\kappa, z, z'; \omega^2) &= \frac{1}{2C_{33}C_{44}\beta_1(\beta_1^2 - \beta_2^2)}(C_{44}\beta_1^2 - C_{11}\kappa^2 + \rho\omega^2)exp(-\beta_1|z - z'|) \\
&\quad - \frac{1}{2C_{33}C_{44}\beta_2(\beta_1^2 - \beta_2^2)}(C_{44}\beta_2^2 - C_{11}\kappa^2 + \rho\omega^2)exp(-\beta_2|z - z'|) ,
\end{aligned}
\tag{2.175}
$$

with $G_{12} = G_{21} = G_{23} = G_{32} = 0$, and

$$
\begin{aligned}
'G_{11}(\kappa, z, z'; \omega^2) &= -\frac{sgn(z - z')}{2C_{33}C_{44}(\beta_1^2 - \beta_2^2)}[(C_{33}\beta_1^2 - C_{44}\kappa^2 + \rho\omega^2)exp(-\beta_1|z - z'|) \\
&\quad - (C_{33}\beta_2^2 - C_{44}\kappa^2 + \rho\omega^2)exp(-\beta_2|z - z'|)] , \\
'G_{13}(\kappa, z, z'; \omega^2) &= -\frac{i\kappa(C_{13} + C_{44})}{2C_{33}C_{44}(\beta_1^2 - \beta_2^2)}[(\beta_1 exp(-\beta_1|z - z'|) - \beta_2 exp(-\beta_2|z - z'|))] , \\
'G_{22}(\kappa, z, z'; \omega^2) &= -\frac{sgn(z - z')}{2C_{44}}exp(-\beta_t|z - z'|) , \\
'G_{31}(\kappa, z, z'; \omega^2) &= 'G_{13}(\kappa, z, z'; \omega^2) , \\
'G_{33}(\kappa, z, z'; \omega^2) &= -\frac{sgn(z - z')}{2C_{33}C_{44}(\beta_1^2 - \beta_2^2)}[(C_{44}\beta_1^2 - C_{11}\kappa^2 + \rho\omega^2)exp(-\beta_1|z - z'|) \\
&\quad - (C_{44}\beta_2^2 - C_{11}\kappa^2 + \rho\omega^2)exp(-\beta_2|z - z'|)] ,
\end{aligned}
\tag{2.176}
$$

with $'G_{12} = {}'G_{21} = {}'G_{23} = {}'G_{32} = 0$.

These projections and the boundary conditions at the different interfaces (continuity of the displacements and normal stress) give the interface projection of the Green function of the system $\tilde{\mathbf{G}}_S$, whose formal representation is given by

$$
\tilde{\mathbf{G}}_s^{-1} = \left(\tilde{\mathcal{A}}_1^{-1} \cdot \tilde{\mathbf{G}}_1^{-1} - \tilde{\mathcal{A}}_2^{-1} \cdot \tilde{\mathbf{G}}_2^{-1} \right) .
\tag{2.177}
$$

The elements entering in the former expression are defined in the following way:

$$
\tilde{\mathbf{G}}_1 \;=\; \begin{bmatrix} \mathcal{G}_1 & e^{-iqd}\,\mathbf{G}_1(l,m) \\[2ex] e^{iqd}\,\mathbf{G}_1(r,p) & \mathcal{G}_1 \end{bmatrix} ;
$$

$$
\tilde{\mathcal{A}}_1 \;=\; \begin{bmatrix} \mathcal{A}_1^{(+)} & e^{-iqd}\,\mathbf{A}_1(l,m) \\[2ex] -e^{iqd}\,\mathbf{A}_1(r,p) & -\mathcal{A}_1^{(-)} \end{bmatrix} ; \tag{2.178}
$$

$$
\tilde{\mathbf{G}}_2 \;=\; \begin{bmatrix} \mathcal{G}_2 & \mathbf{G}_2(l,r) \\[2ex] \mathbf{G}_2(r,l) & \mathcal{G}_2 \end{bmatrix} ;
$$

$$
\tilde{\mathcal{A}}_2 \;=\; \begin{bmatrix} \mathcal{A}_2^{(-)} & \mathbf{A}_2(l,r) \\[2ex] -\mathbf{A}_2(r,l) & -\mathcal{A}_2^{(+)} \end{bmatrix} , \tag{2.179}
$$

where l, m, p and r denote the z coordinates from the interfaces shown in Fig.2.4, q is the normal wavevector associated to the superlattice periodicity and the dependencies on κ and ω^2 must be understood.

The normal components of the stress are represented by the $\tilde{\mathcal{A}}$ through the $\mathbf{A}$ and $\mathcal{A}^{\pm}$ operators. In the present case they are given by

$$
\mathbf{A} \;=\; \begin{bmatrix} C_{44}\left(\dfrac{\partial G_{11}}{\partial z}+i\kappa G_{31}\right) & 0 & C_{44}\left(i\kappa G_{33}+\dfrac{\partial G_{13}}{\partial z}\right) \\[3ex] 0 & C_{44}\dfrac{\partial G_{22}}{\partial z} & 0 \\[3ex] iC_{13}\kappa G_{11}+C_{33}\dfrac{\partial G_{31}}{\partial z} & 0 & iC_{13}\kappa G_{13}+C_{33}\dfrac{\partial G_{33}}{\partial z} \end{bmatrix} , \tag{2.180}
$$

and
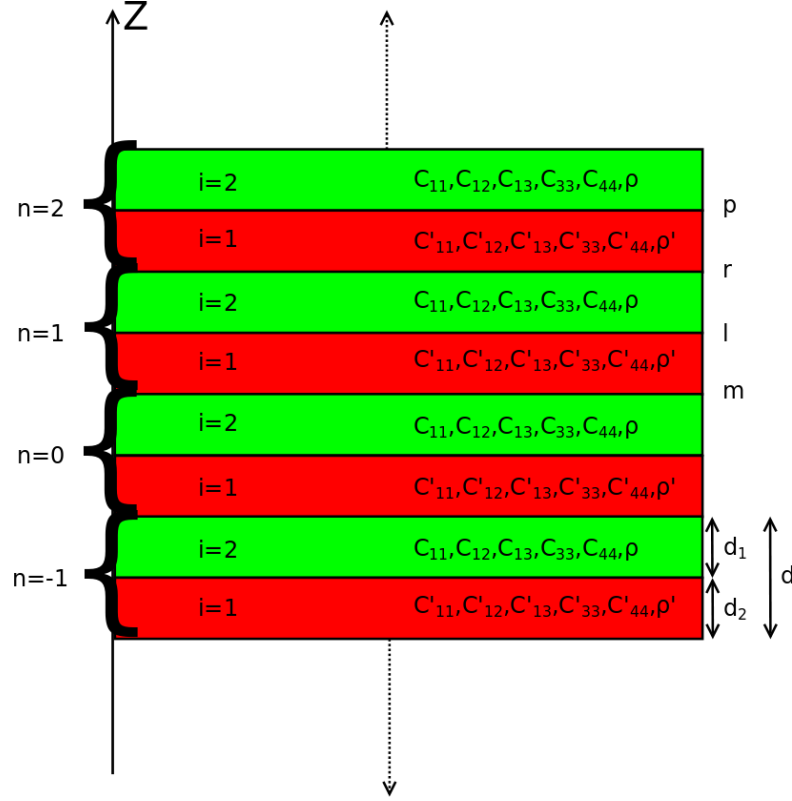
Figure 2.4:   Sketch of the superlattices considered in this work showing the different layers with the corresponding thicknesses, elastic constants and mass densities of the constituent materials.

$$\mathcal{A}^{\pm} \;=\; \begin{bmatrix} C_{44}('\mathcal{G}_{11}^{\pm} + i\kappa\mathcal{G}_{31}) & 0 & C_{44}(i\kappa\mathcal{G}_{33} +' \mathcal{G}_{13}^{\pm}) \\[2ex] 0 & C_{44}\, '\mathcal{G}_{22}^{\pm} & 0 \\[2ex] iC_{13}\kappa\mathcal{G}_{11} + C_{33}\, '\mathcal{G}_{31}^{\pm} & 0 & iC_{13}\kappa\mathcal{G}_{13} + C_{33}\, '\mathcal{G}_{33}^{\pm} \end{bmatrix} \text{(2.181)}$$

It is clear from these expressions that there is a decoupling from the terms corresponding to the x and z axes, the sagittal plane, from those corresponding to the y axis, the transverse motion contained in the basal plane with velocity[3] v_{T2}. This is due to the elastic isotropy of the basal plane in hexagonal systems. It is interesting to note that in this case we have two different transverse waves possessing different propagation velocities. This

---

[3]$v_{T1}^2 = \frac{C_{44}}{\rho}$; $v_{T2}^2 = \frac{C_{66}}{\rho}$; $v_L^2 = \frac{C_{11}}{\rho}$

is a different situation from that found in isotropic crystals where the two transverse waves have the same propagation velocity. This allows the possibility of having more ($v_{T1} > v_{T2}$) or less ($v_{T1} < v_{T2}$) frequency ranges allowed to propagation of transverse waves and forbidden to sagittal waves than in purely isotropic materials.

The dispersion curves are obtained by means of the peaks of the local density of states (LDOS), which is obtained from the trace of the interface projection of the system Green function $\tilde{\mathbf{G}}_S$.

To obtain the dispersion curves we study the LDOS as a function of κd. For each κd value we analyze the LDOS for 100 qd values ranging from zero to π. The allowed acoustic branches exhibit non-zero LDOS values. On the other hand the forbidden gaps have LDOS zero values. A small imaginary part (0.001) is added to the frequency to perform the numerical calculations.

2.2.4.3 SGFM for the superlattice. Piezoelectric hexagonal systems.

In the case of piezoelectric materials belonging to the $6mm$ class with the C-axis parallel to the x_3 direction and the direction x_2 normal to the interface there is a decoupling between motion along the x_1 and x_2 directions and the motion along the x_3 direction, due to the symmetry [77]. We shall consider here only the transverse acoustic wave having the electric potential coupled to the elastic displacement u_3.

We shall give here only the detailed expressions for the Green's functions and normal derivatives particular to the case of the transverse acoustic waves, including the piezoelectric coupling, in hexagonal crystals. The essential formal expressions for the study of the superlattices will be also given.

The bulk material Green's function is given in this case by [78]

$$\mathbf{G} \;=\; \begin{bmatrix} \dfrac{\epsilon_{11}}{N} & -\dfrac{e_{15}}{N} \\[2mm] \dfrac{e_{15}}{N} & \dfrac{C_{44}k^2 - \rho\omega^2}{Nk^2} \end{bmatrix}, \tag{2.182}$$

where

$$N = Ck^2 - \epsilon_{11}\rho\omega^2 \;\;,\;\; C = C_{44}\epsilon_{11} + e_{15}^2 \;. \tag{2.183}$$

$N=0$ gives the dispersion relation of the bulk piezoelectric transverse acoustic wave

$$\omega^2 = v_t^2 k^2 \quad , \quad v_t^2 = \frac{C}{\rho \epsilon_{11}} \; . \tag{2.184}$$

The surface projected elements of the bulk Green function are obtained from equation (2.169), in this case

$$\mathcal{G}_{ij}(\kappa, \omega^2) = \lim_{\epsilon \to 0} \frac{1}{2\pi} \int_{-\infty}^{\infty} \exp[i\epsilon k_{x_2}] G_{ij}(\kappa, k_{x_2}; \omega^2) dk_{x_2} \quad , \tag{2.185}$$

κ being the parallel wavevector, k_{x_2} being the perpendicular wavevector in the bulk and i being the imaginary unit, whereas the normal derivatives are obtained from equation (2.170)

$$'\mathcal{G}_{ij}^{(\pm)}(\kappa, \omega^2) = \lim_{\epsilon \to 0} \frac{1}{2\pi} \int_{-\infty}^{\infty} \exp[\mp i\epsilon k_{x_2}] i k_{x_2} G_{ij}(\kappa, k_{x_2}; \omega^2) dk_{x_2} \quad , \tag{2.186}$$

thus giving [78]

$$\mathcal{G} \; = \; \begin{bmatrix} \dfrac{\epsilon_{11}}{2C\beta} & -\dfrac{e_{15}}{2C\beta} \\[3mm] \dfrac{e_{15}}{2C\beta} & \dfrac{C\beta - e_{15}^2 \kappa}{2\epsilon_{11} C \kappa \beta} \end{bmatrix} , \tag{2.187}$$

and

$$'\mathcal{G}^{\pm} \; = \; \begin{bmatrix} \pm\dfrac{\epsilon_{11}}{2C} & \mp\dfrac{e_{15}}{2C} \\[3mm] \pm\dfrac{e_{15}}{2C} & \pm\dfrac{C - e_{15}^2}{2C\epsilon_{11}} \end{bmatrix} , \tag{2.188}$$

where

$$\beta = (\kappa^2 - \frac{\epsilon_{11} \rho \omega^2}{C})^{\frac{1}{2}} \; . \tag{2.189}$$

We need also equations (2.173)

$$G_{ij}(\kappa, x_2, x_2'; \omega^2) = \frac{1}{2\pi} \int_{-\infty}^{\infty} \exp[i k_{x_2}(x_2 - x_2')] G_{ij}(\kappa, k_{x_2}; \omega^2) dk_{x_2} \quad , \tag{2.190}$$

and equation (2.174)

$$'G_{ij}(\kappa, x_2, x_2'; \omega^2) = \frac{\partial}{\partial x_2} G_{ij}(\kappa, x_2, x_2'; \omega^2) \ . \tag{2.191}$$

They are given by

$$
\begin{aligned}
G_{11}(\kappa, x_2, x_2'; \omega^2) &= \frac{\epsilon_{11}}{2C\beta} exp(-\beta|x_2 - x_2'|) \ , \\
G_{12}(\kappa, x_2, x_2'; \omega^2) &= -\frac{e_{15}}{2C\beta} exp(-\beta|x_2 - x_2'|) \ , \\
G_{21}(\kappa, x_2, x_2'; \omega^2) &= \frac{e_{15}}{2C\beta} exp(-\beta|x_2 - x_2'|) \ , \\
G_{22}(\kappa, x_2, x_2'; \omega^2) &= \frac{1}{2\epsilon_{11}}(\frac{1}{\kappa} exp(-\kappa|x_2 - x_2'|) - \frac{e_{15}^2}{C\beta} exp(-\beta|x_2 - x_2'|)) \ ,
\end{aligned}
\tag{2.192}
$$

and

$$
\begin{aligned}
'G_{11}(\kappa, x_2, x_2'; \omega^2) &= -sgn(x_2 - x_2')\frac{\epsilon_{11}}{2C} exp(-\beta|x_2 - x_2'|) \ , \\
'G_{12}(\kappa, x_2, x_2'; \omega^2) &= sgn(x_2 - x_2')\frac{e_{15}}{2C} exp(-\beta|x_2 - x_2'|) \ , \\
'G_{21}(\kappa, x_2, x_2'; \omega^2) &= -sgn(x_2 - x_2')\frac{e_{15}}{2C} exp(-\beta|x_2 - x_2'|) \ , \\
'G_{22}(\kappa, x_2, x_2'; \omega^2) &= -sgn(x_2 - x_2')\frac{1}{2\epsilon_{11}}(exp(-\kappa|x_2 - x_2'|) - \frac{e_{15}^2}{C} exp(-\beta|x_2 - x_2'|)) \ .
\end{aligned}
\tag{2.193}
$$

The boundary conditions at the different interfaces (continuity of the u_3 displacement, the electric potential, the normal stress and the electric displacement) expressed in terms of these projections give the interface projection of the Green function of the superlattice system [43], whose formal representation is

$$\tilde{\mathbf{G}}_s^{-1} = -\left(\tilde{\mathcal{A}}_1^{-1} \cdot \tilde{\mathbf{G}}_1^{-1} - \tilde{\mathcal{A}}_2^{-1} \cdot \tilde{\mathbf{G}}_2^{-1}\right) \ . \tag{2.194}$$

The generalization for N different interfaces is presented in [39] and shall not be discussed here.

The elements entering in the former expression are defined in the following way:

$$\tilde{\mathbf{G}}_1 \;=\; \begin{bmatrix} \mathcal{G}_1 & e^{-iqd}\,\mathbf{G}_1(l,m) \\[2mm] e^{iqd}\,\mathbf{G}_1(r,p) & \mathcal{G}_1 \end{bmatrix};$$

$$\tilde{\mathcal{A}}_1 \;=\; \begin{bmatrix} \mathcal{A}_1^- & e^{-iqd}\,\mathbf{A}_1(l,m) \\[2mm] -e^{iqd}\,\mathbf{A}_1(r,p) & -\mathcal{A}_1^+ \end{bmatrix}; \qquad (2.195)$$

$$\tilde{\mathbf{G}}_2 \;=\; \begin{bmatrix} \mathcal{G}_2 & \mathbf{G}_2(l,r) \\[2mm] \mathbf{G}_2(r,l) & \mathcal{G}_2 \end{bmatrix};$$

$$\tilde{\mathcal{A}}_2 \;=\; \begin{bmatrix} \mathcal{A}_2^+ & \mathbf{A}_2(l,r) \\[2mm] -\mathbf{A}_2(r,l) & -\mathcal{A}_2^- \end{bmatrix}, \qquad (2.196)$$

where l, m, p and r denote the x_2 coordinates from the interfaces shown in Fig.2.5, d is the superlattice period, q is the normal wavevector associated to the superlattice periodicity and the dependencies on κ and ω^2 must be understood.

The normal components of the stress and the electric displacement are represented by the $\tilde{\mathcal{A}}$ through the $\mathbf{A}$ and $\mathcal{A}^\pm$ operators. In the present case they are given by

$$\mathbf{A} \;=\; \begin{bmatrix} C_{44}\dfrac{\partial G_{11}}{\partial x_2} + e_{15}\dfrac{\partial G_{21}}{\partial x_2} & C_{44}\dfrac{\partial G_{12}}{\partial x_2} + e_{15}\dfrac{\partial G_{22}}{\partial x_2} \\[4mm] -e_{15}\dfrac{\partial G_{11}}{\partial x_2} + \epsilon_{11}\dfrac{\partial G_{21}}{\partial x_2} & -e_{15}\dfrac{\partial G_{12}}{\partial x_2} + \epsilon_{11}\dfrac{\partial G_{22}}{\partial x_2} \end{bmatrix}, \qquad (2.197)$$

and

$$\mathcal{A}^\pm \;=\; \begin{bmatrix} C_{44}\,'\mathcal{G}_{11}^\pm + e_{15}\,'\mathcal{G}_{21}^\pm & C_{44}\,'\mathcal{G}_{12}^\pm + e_{15}\,'\mathcal{G}_{22}^\pm \\[2mm] -e_{15}\,'\mathcal{G}_{11}^\pm + \epsilon_{11}\,'\mathcal{G}_{21}^\pm & -e_{15}\,'\mathcal{G}_{12}^\pm + \epsilon_{11}\,'\mathcal{G}_{22}^\pm \end{bmatrix}. \qquad (2.198)$$
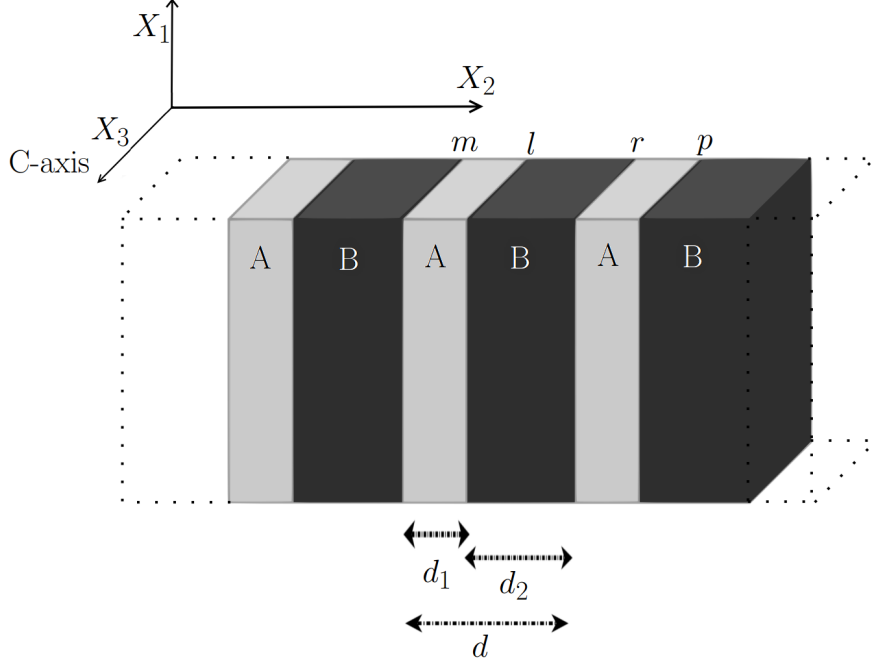
Figure 2.5: Sketch of the superlattice having as period a second Fibonacci generation (it coincides with the usual binary superlattice). The materials belong to the $6mm$ class with the C-axis parallel to the x_3 direction and we choose the normal to the interfaces as the x_2 direction. The different layers with the corresponding thicknesses and the nomenclature for the different interfaces are also shown. The case of more complex superlattice periods, including more interfaces, is a generalization of this picture [39].

The dispersion curves are obtained from the peaks of the local density of states (LDOS), which is obtained from the trace of the interface projection of the system Green function $\tilde{\mathbf{G}}_S$ [43, 39].

To obtain the dispersion curves we study the LDOS as a function of κd. For each κd value we sample the LDOS for 100 qd values ranging from zero to π, "d" being the period of the structure being considered. The allowed transverse acoustic branches have non-zero LDOS values. The forbidden gaps have LDOS zero values. A small imaginary part (0.001) is added to the frequency to perform the numerical calculations.

2.3   Discrete approach

The discrete approach usually gives more accurate results in exchange for a bigger need of computational resources. The most used discrete methods are Monte Carlo (MC) and Molecular Dynamics (MD).

In Molecular Dynamics and Monte Carlo methods, forces are derived from a potential energy function that depends on the particles coordinates $\vec{r_i}$:

$$\vec{F_i} = -\nabla V(\vec{r_1}, \ldots, \vec{r_N}) \tag{2.199}$$

So the capability to generate an accurate potential function $V(\vec{r_1}, \ldots, \vec{r_N})$ for that material is the core of the reliability of the calculations. The material atoms are controlled by the quantum mechanics laws. Besides this, the electrons play a major role in the bond properties. This fact makes the calculation of the potential energy functions a complicated key issue in this kind of computer simulations.

In fact the atoms are composed of nuclei and electrons, therefore, the interactions between atoms are derived from those occurring between these components.

The non-relativistic hamiltonian of imteracting atoms may be written as:

$$H = \sum_i \frac{P_i^2}{2M_i} + \sum_n \frac{p_n^2}{2m}$$
$$+ \frac{1}{2} \sum_{i,j} \frac{Z_i Z_j e^2}{|\vec{R_i} - \vec{R_j}|} + \frac{1}{2} \sum_{n,m} \frac{e^2}{|\vec{r_n} - \vec{r_m}|} - \sum_{i,n} \frac{Z_i e^2}{|\vec{R_i} - \vec{r_n}|} \tag{2.200}$$

where the i, j indices run on the nuclei and n, m on the electrons. $\vec{R_i}$ are the positions and $\vec{P_i}$ the momenta of the nuclei, $\vec{r_n}$ and $\vec{p_n}$ are, respectively, the positions and momenta of the electrons, Z_i and M_i are the atomic number and the mass of the nucleus i, and m and e are the electron mass and charge.

The first two summands/terms of eq.(2.200) are the kinetic energies of nuclei and electrons and the remaining three terms correspond to the Coulomb interaction between pairs of nuclei, pairs of electrons and nucleus-electron pairs respectively. In principle, solving the Schrödinger equation for the total wave function $\Psi(\vec{R_i}, \vec{r_n})$ will give all the information of the system since all the electronic and mechanical properties depend on the electronic structure of the system. However, in practice, this is impossible. Thus the use of approximation schemes is necessary. In 1927 Born and Oppenheimer [79] noticed that the masses of the nuclei are always much bigger than the electron mass, an electron having a mass being approximately $\frac{1}{1836}$ that of the proton. Therefore the electrons move on a frequency scale which is about

two orders of magnitude larger than that of the nuclei:

$$\frac{\omega_{electron}}{\omega_{nucleus}} \sim \sqrt{\frac{M}{m}} > \sqrt{1836} \qquad (2.201)$$

So from the point of view of the electrons, the nuclei are approximately static. Therefore it is possible to decouple the nuclear motion from the electronic one, and factorise the total wavefunction as:

$$\Psi(\vec{R}_i, \vec{r_n}) \simeq \chi(\vec{R}_i)\phi(\vec{r_n}; \vec{R}_i) \qquad (2.202)$$

where $\chi(\vec{R}_i)$ is the wavefunction that describes the nuclei and $\phi(\vec{r_n}; \vec{R}_i)$ is the wavefunction that describes the electrons, which parametrically depends on the positions of the nuclei.

These assumptions of the Born-Oppenheimer approximation make possible to reformulate the problem in two steps. In the first step the nuclear kinetic energy is neglected and the nuclear positions enter as parameters so the Hamiltonian of the system (2.200) gives the "electronic" Hamiltonian:

$$H_{el} = \sum_n \frac{p_n^2}{2m} + \frac{1}{2}\sum_{i,j} \frac{Z_i Z_j e^2}{|\vec{R}_i - \vec{R}_j|} + \frac{1}{2}\sum_{n,m} \frac{e^2}{|\vec{r_n} - \vec{r_m}|} - \sum_{i,n} \frac{Z_i e^2}{|\vec{R}_i - \vec{r_n}|} \qquad (2.203)$$

where in the nuclei Coulomb interaction the nuclei are assumed to be static, and the electron-nucleus interaction is not removed as the electrons still feel the Coulomb potential of the nuclei "clamped" at certain positions in space.

The Schrödinger electronic equation is therefore:

$$H_{el}(\vec{r_n}; \vec{R}_i)\phi(\vec{r_n}; \vec{R}_i) = E_{el}\phi(\vec{r_n}; \vec{R}_i) \qquad (2.204)$$

where the electronic energy eigenvalues E_{el} depend on the "static" positions of the nuclei $\vec{R}_i$.

In the second step of the Born-Oppenheimer approximation the nuclear kinetic energy $T_n(\vec{R}_i) = \sum_i \frac{P_i^2}{2M_i}$ is reintroduced and the Schrödinger equation of the nuclear motion

$$\left[\sum_i \frac{P_i^2}{2M_i} + E_{el}(\vec{R}_i)\right]\chi(\vec{R}_i) = E\chi(\vec{R}_i) \qquad (2.205)$$

is solved. The energy eigenvalues E that include the electrons contributions and the nuclear motion are the total energy of the system.

Notice that the term E_{el}, the eigenvalue of the equation (2.204), can be viewed as an "interatomic potential" of the equation (2.205). This "interatomic potential" $V(\vec{R}_i)$ will give the forces felt by the nuclei. Also note that

in the equation (2.205) no electronic degrees of freedom are present as all the electronic effects are incorporated into $V(\vec{R}_i)$, thus allowing to substitute the electronic equation (2.200) with an approximation.

Finally this separation in electronic and nuclear contributions allows an additional approximation which assumes as adequate the classical description of the nuclear dynamics.

The Born-Oppenheimer approximation is used in both methods (MC and MD) so the nuclear motion is segregated from the electronic motion in the Hamiltonian of the system.

Monte Carlo simulations aim to explore the conformation space of a system in order to determine the equilibrium average of some property [80]. This could be achieved, in principle, by evaluating the integral:

$$< A >= \int A(\vec{r})P(\vec{r})d\vec{r}, \qquad (2.206)$$

where the probability function $P(\vec{r})$ is given by:

$$P(\vec{r}) = \frac{e^{-\frac{E(\vec{r})}{\kappa_B T}}}{\int e^{-\frac{E(\vec{r})}{\kappa_B T}}d\vec{r}}, \qquad (2.207)$$

where $E(\vec{r})$ is the energy of the system characterised by the particle's coordinates $\vec{r}$ and $\int e^{-\frac{E(\vec{r})}{\kappa_B T}}d\vec{r}$ is the partition function of the system. The above equations cannot be evaluated analytically but they could, in principle, be calculated using a numerical integration procedure. However, for all but the very smallest systems this would involve an unfeasible number of calculations. Fortunately there is a numerical method for obtaining numerical solutions to problems which are too complicated to solve analytically based on random sampling. The method was named by S. Ulam, who in 1946 became the first mathematician to dignify this approach with a name, in honour of a relative having a propensity to gamble. In the Monte Carlo integration method, in order to integrate a function over a complicated domain D, Monte Carlo integration picks random points over some simple domain D' which is a superset of D, checks whether each point is within D, and estimates the area of D (volume, n-dimensional content, etc.) as the area of D' multiplied by the fraction of points falling within D. Monte Carlo method is a sampling experiment model based on the generation of random numbers in order to create sample states from a statistical ensemble and then accept or reject the sample according to some rules (usually trying to minimise the energy). The crudest form of MC would consist of making random changes to the coordinates of the system. From the energies calculated at each step, $A(\vec{r})P(\vec{r})$

can be estimated and $< A >$ can be found. This approach is flawed as each different configuration would contribute equally to the integral. Since $P(\vec{r})$ is proportional to the Boltzmann factor $e^{-\frac{E(\vec{r})}{\kappa_B T}}$, only low energy configurations make significant contributions to the integrals. However, a large number of configurations have a small Boltzmann factor due to high energy overlaps between particles. Thus only a small proportion of configuration space corresponds to physically observed states. Therefore many of the generated configurations would have little or no influence and so proper sampling would not have been achieved. The sampling problem above can be solved by employing importance sampling, which is the essence of the *Metropolis Monte Carlo* method [80]. The crucial feature is that it biases the generation of configurations to those that make a significant contribution to the equation (2.207). Specifically it generates a series of states with a Boltzmann distribution and counts them equally. This differs from the crude method outlined above which generates states with equal probability and then assigns them a Boltzmann weight. The simulation must have a procedure for generating new configurations so that at the end of the simulation the appropriate probability distribution has occurred. This is achieved by setting up what is known as a Markov chain [4], which satisfies the following conditions:

- The outcome of each trial belongs to a finite set of possible outcomes.

- Each trial depends only on the outcome of the trial that precedes it.

These conditions are required to produce the correct limiting distribution, i.e. to produce the correct ensemble averages. The advantage of the MC method is that it can be easily adapted to different ensembles (canonical, grand canonical, etc.). Also the MC method is often used in the optimisation of solid state systems. We include its description here only for completeness because we need to know the velocity of the particles in order to obtain the VDOS and Raman spectra, which can not be obtained from MC simulations.

On the other hand Molecular Dynamics studies the dynamical evolution in time of the model. In MD the dynamics of the system is studied by means of a finite difference method. Given the particles positions, velocities, and other dynamical information at a time t, the idea is to calculate the positions, velocities, etc. at a time $t + \delta t$. With the sufficient degree of accuracy and if the finite difference method is stable (it depends on the procedure used to calculate the next state and the time interval δt) then the evolution in time of the system is obtained step by step.

2.3.1   Classical regime in discrete approximations

The adequacy of using the classical approximation for the motion of the nuclei in the discrete approach is related to the de Broglie thermal wavelength of the system:

$$\Lambda = \sqrt{\frac{2\pi\hbar^2}{M\kappa_B T}} \qquad (2.208)$$

where M is the mass of the nuclei (which may be approximated by the atomic mass), T is the temperature, $\hbar$ is the reduced Plank constant ($\hbar = 1.054571726(47) \times 10^{-34} \ \frac{kg \ m^2}{s}$) and κ_B is the Boltzmann constant ($\kappa_B = 1.3806503 \times 10^{-23} \ \frac{m^2 kg}{s^2 K}$).

If the de Broglie wavelength is smaller than the mean nearest neighbour distance of the nuclei ($\Lambda << d_{nn}$) then the classical approximation is justified [81]. For example, in a simulation of an Al crystal at $100 \ K$ the de Broglie length is $\Lambda = 0.336$ Å and the nearest neighbour is at $d_{nn} \simeq 2.86$ Å which is an order of magnitude bigger. Therefore only when lighter elements are considered (Li or Ar) or if the temperature is very low, the classical approximation of the nuclei motion should be interpreted with caution[4].

On the other hand, solving the electronic Schrödinger equation (2.203) directly is technically unfeasible without some approximations, like those used by the *ab initio* methods (which we shall explain later). Even with the usual approximations solving the equation (2.203) requires massive computer resources.

The *classical* approach to the equation (2.203) aims to substitute it and describe the nuclei motion through some potential function $V(\vec{R}_i)$ which depends on the kind of atoms, the structure we want to simulate and the data we want to extract, whose analytical form is specified in advance.

This potential function is selected from some functional forms that mimic the behaviour of the "true" potential under specific conditions. The process of selecting the potential involves two steps: selecting the analytical form that behaves like the "true potential" and finding the appropriate parameters for this function that fit the experimental data available.

A variety of *classical* potentials have been used over the years to this end. And in any case, those potentials are designed with a "range of applicability" in mind. Simulation results should be critically interpreted when obtained in unusual conditions. However, it may be possible to model a bulk and a surface environment with the same potential if the environment does not

---

[4]Also quantum effects begin to rise for light elements below the Debye temperature.

differ dramatically. This ability of a potential to work properly in different enviroments is called *transferability*.

2.3.2 Classical Potentials

Assuming a system of N atoms, the potential energy may be divided into terms depending on the coordinates of individual atoms, pairs of atoms, triplets, etc.

$$V = \sum_i v_1(\vec{r_i}) + \sum_{i,j>i} v_2(\vec{r_i}, \vec{r_j}) + \sum_{i,j>i.k>j>i} v_3(\vec{r_i}, \vec{r_j}, \vec{r_k}) + \dots \qquad (2.209)$$

the first term represents the effect of an external field on the system, the second term is the pair potential, the third term is the tree body potential, etc.

The two body potentials $V = \sum_{i,j>i} v_2(\vec{r_i}, \vec{r_j})$ are the most commonly used, being the Lennard-Jones potential [82] the classical example of two body potential.

$$\phi_{L-J}(r) = 4\epsilon \left[\left(\frac{\sigma}{r} \right)^{12} - \left(\frac{\sigma}{r} \right)^6 \right] \qquad (2.210)$$

where $r = |\vec{r_j} - \vec{r_i}|$ and the parameters ϵ and σ are chosen to fit some of the physical properties of the material.
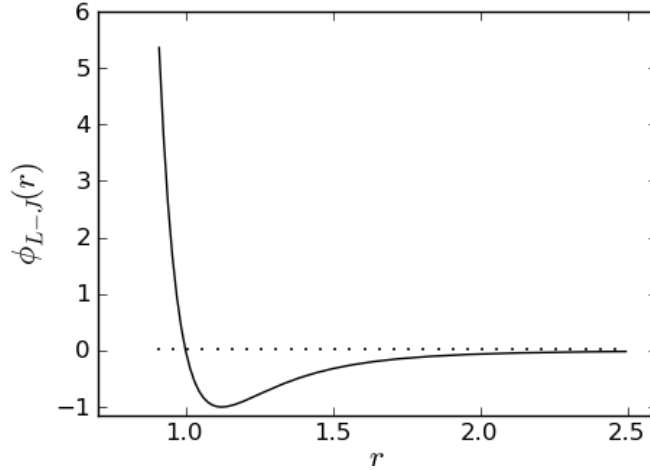
Figure 2.6: Functional form of the Lennard-Jones energy potential with $\epsilon = \sigma = 1$.

Two body potentials are not adequate at all to model systems with strong localised bonds, as covalent systems or where there is a delocalised "electron

sea" as in metals. In these systems the two body interactions fail dramati-
cally. In noble metals there are several experimental data indicators of many
body effects. The ratio between the cohesive energy and the melting tem-
perature indicates that metals show extra cohesion with respect to pairwise
systems. This shows that is less effective than two-body forces in keeping the
system in the crystalline state[83]. The ratio between two elastic constants
of a cubic crystal $\frac{C_{12}}{C_{44}}$, which due to the *Cauchy relation* in two body systems,
is exactly 1, while in real cubic metals deviations of this value are the rule.
In fact the high value in the $\frac{C_{12}}{C_{44}}$ ratio in Au is related to its well known high
ductility and malleability.

In semiconductors the deviations from a two-body behaviour are even
bigger.

Consider for instance silicon. Its most stable phase is the diamond struc-
ture, which is very open and has a coordination number $N_c = 4$. However it
changes rapidly to other structures from tetrahedral to β-tin to simple cubic
to FCC when pressure is applied, which means that these other structures
are not too far away in energy. Besides, its liquid structure is a metal, and
it is more dense than the solid.

In other words, the cohesive energy is nearly independent of the coordi-
nation, while a two-body model should favour the more packed structures,
which have more bonds.

The properties of the semiconductors make the finding of suitable poten-
tial functions describing their properties a specially complex task.

Some approaches to the semiconductor potential function are the Stillinger-
Weber [84] (in which the potential functions have angular terms that favour
some preferred angles) and the Tersoff potential [85] (based on the concept
of bond order).

2.3.3 Periodic boundary conditions

Usually, computer simulations of discrete systems are performed on a rela-
tively small number of particles $10 \leq N \leq 10000$ as the size of a system is
limited by the available data storage and, more crucially, by the calculation
time defined by the processors performance and the design of the computa-
tional code. The time taken for a double logical loop used by the algorithm
to evaluate the forces or the potential energy is proportional to N^2. It may
be possible to reduce this dependence to $\mathcal{O}(N)$ with special techniques for
very large systems, but the force/energy loop dictates inevitably the overall
calculation speed. Smaller systems will always be less time consuming. If
the interest is in the properties of a very small cluster, then the simulation
will be straightforward and the virtual space used in the calculations could

be limitless. However if the interest is in the analysis of a bulk system, it is not possible to simulate with a relatively small number of atoms due to the fact that a representative fraction of particles will lie on the surface of any small sample. Those atoms on the surface will experience quite different forces than those atoms in the bulk. Therefore it is necessary to overcome the finite size effects when using cells for the representation of infinite systems [4].

The problem of surface effects can be overcome by implementing *periodic boundary conditions* [86]. In the periodic boundary conditions the particles are fitted inside a virtual box. This cubic box is replicated indefinitely in order to tessellate the space to form an infinite lattice. During the course of the simulation, as the particles move in the original box, all their image particles in each of the copied boxed move in exactly the same way. Thus, as an atom leaves the "real" box through a given face, one of its images will enter through the opposite face. Therefore there is no surface atoms as there are no walls at the boundary of the "real" box. Figure 2.7 shows a simplified two dimensional version of such periodic system. The image boxes are labelled as Im1, Im2, etc. and the particles A, B, C and D have their respective images A1, B1, C1 and D1 in Im1, and so on. With this scheme, the number of particles in each box is conserved as if a particle exits the box, a neighbour box's image enters. It is not necessary to store the coordinates of all the images in a simulation. When an atom leaves the box by crossing a boundary, the attention then shifts to the atom image just entering into the simulation box through the opposite boundary. Therefore only the atoms in the "real" box count for the simulation.

It is important to consider if the properties of a small, infinitely periodic, system and the macroscopic system which represents are the same. This will depend both on the range of the inter-atomic potential and the phenomenon under investigation. If the potential is long ranged (i.e. $V(r) \sim r^{-\nu}$ where ν is less than the dimensionality of the system) then, for typical size boxes, there will be a substantial interaction between a particle and its own images in neighbouring boxes, and consequently the symmetry of the cell structure is imposed on a system which is actually isotropic.

Also, the use of periodic boundary conditions inhibits the occurence of long-wavelength fluctuations. For a cube of side L, the periodicity will suppress any density waves with a wavelength greater than L. Thus, it would not be possible to simulate a liquid close to the gas-liquid critical point, where the range of critical fluctuations is macroscopic. Furthermore, transitions which are known to be first order often exhibit the characteristics of higher order transitions when modelled in a small box, because of the suppression of fluctuations. The same limitations apply to the simulation of long-wavelength
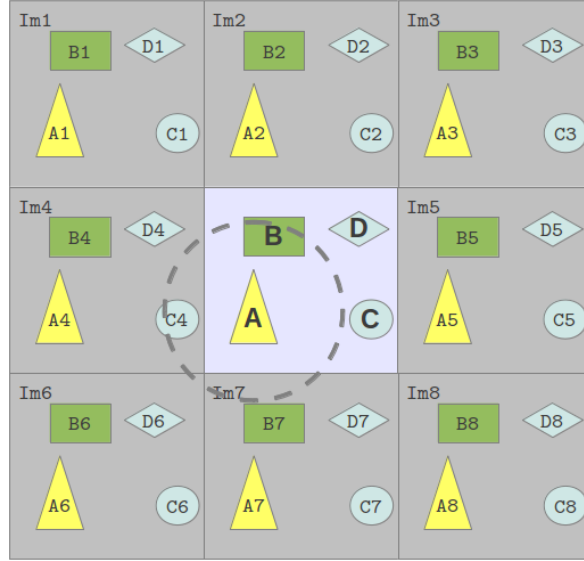
Figure 2.7: Two-dimensional representation of a simulation box with its 8 surrounding image boxes.(Source:Samuel Peláez Machado, with thanks.)

phonons in model solids, where, in addition, the cell periodicity picks out a discrete set of available wave-vectors (i.e. $\vec{k} = (k_x, k_y, k_z)2\pi/L$, where k_x, k_y, k_z are integers) in the first Brillouin zone [87].

Despite the above remarks, the common experience in simulation work is that PBC have little effect on the equilibrium thermodynamic properties and structures of fluids away from phase transitions and where interactions are short-ranged. However, it is always important to check that this holds for each model studied. It should be checked that increasing the number of particles (and box size, so as to maintain constant density) does not influence the results.

2.3.3.1 Potential truncation

Now let us consider the question of how to calculate the properties of systems subject to periodic boundary conditions. The core of any Monte Carlo or Molecular Dynamic simulation program is the calculation of the potential energy (and/or force in the case of MD) of a particular configuration. To this end, we must include interactions between particle i and every other particle j in the simulation box. There are $N - 1$ terms in this sum. However, we must also include all interactions between particle i and image particles lying in the surrounding boxes. This is an infinite number of terms, and of course impossible to calculate in practice. For a short-ranged potential en-

(a) Full potential

(b) Cut potential: Discontinuous

(c) Displaced potential:
Shifted to $V(r_c) = 0$

(d) Adjusted potential:
Set to 0 for $r > r_c$
interpolate for $r' < r < r_c$
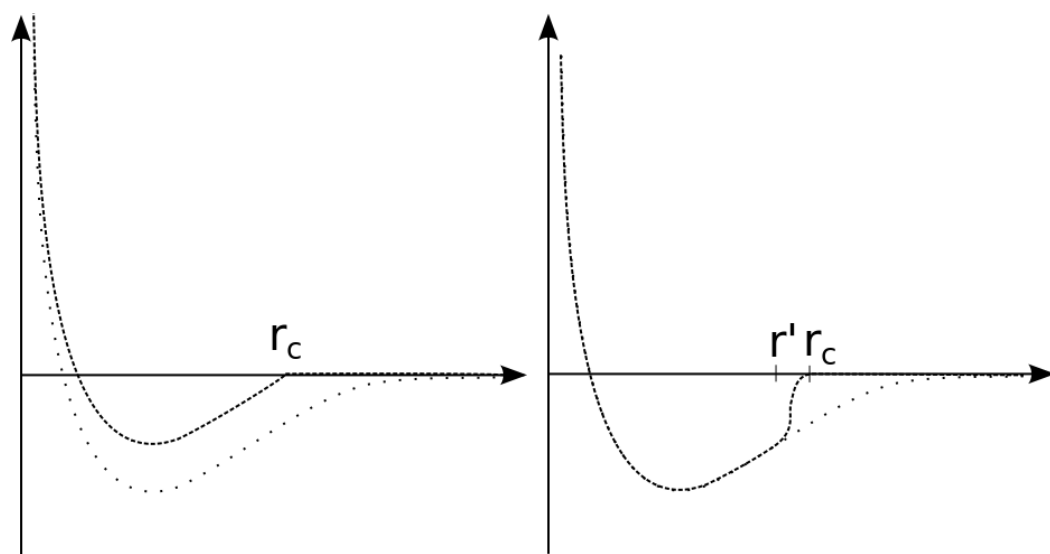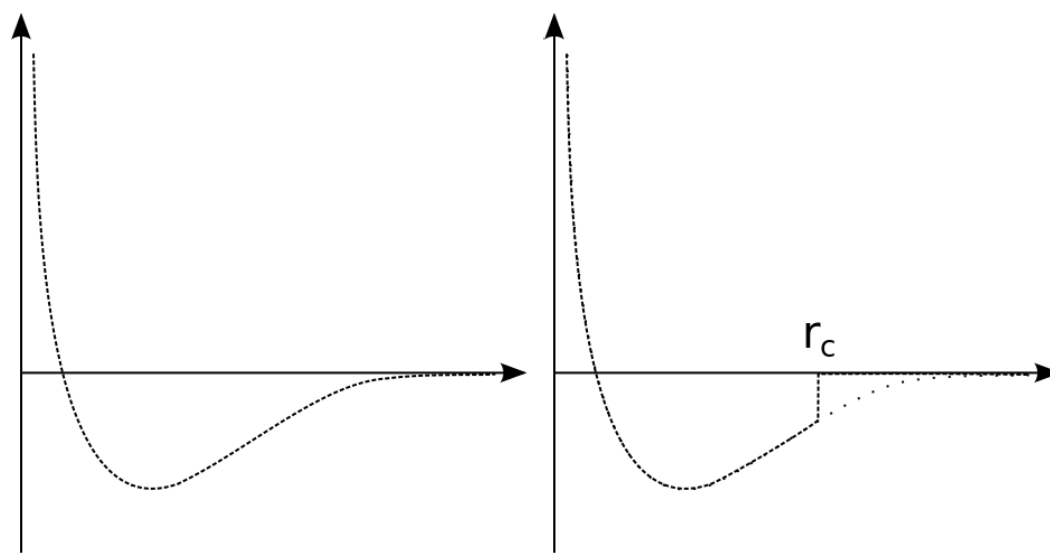
Figure 2.8: Cutoff methods

ergy function, we may restrict this summation by making an approximation. The largest contribution to the potential and forces comes from neighbours (real or periodic images) close to the particle of interest. This is called the *minimum image convention*, and is a natural consequence of the periodic boundary conditions.

Then in the *minimum image convention*, the calculation of the potential energy involves $\frac{1}{2}N(N-1)$ terms which may still be a very substantial calculation for a system of (for example) 1000 particles. A further approximation is based on the fact that the largest contribution to the potential and forces comes from neighbours close to the particle of interest, and therefore, is a standard practice to apply a *spherical cutoff*. This means setting the pair potential $V(r)$ to zero for $r \geq r_c$, where r_c is the cutoff distance. The dashed circle in figure 2.7 represents a cutoff region, and in this case particles B and $C4$ contribute to the force on A, since their centres lie inside such region. In a cubic simulation box of side L, the number of neighbours explicitly considered is reduced by a factor of approximately $4\pi r_c^3/3L^3$, and this may be a substantial saving. The introduction of a spherical cutoff should be a small perturbation, as the cutoff distance should be sufficiently large to ensure this. As an example, in the simulation of atoms interacting through Lennard-Jones potentials, the value of the pair potential at the boundary of a cutoff sphere of typical radius $r_c = 2.5\ \sigma$ is just 1.6 percent of the well depth.

Any cutoff introduces a truncation in the potential (Fig.2.8b). But it also introduces other problem: whenever a particle pair "crosses" the cutoff distance, the energy makes a little jump. A large amount of those little jumps will likely spoil the energy conservation in a MD calculation over the time. To avoid this problem the potential is usually shifted in order to make $V(r_c) = 0$ as seen in Fig.2.8c. But shifting only solves the energy discontinuity, not the force discontinuity. For this reason, to obtain a continuous energy and force it is common to alter the potential near r_c (Fig.2.8d) in order to make it "smooth" (that is second order derivable). There is no standard way to do this "smoothing".

Physical quantities are affected by the cutoff. The effects of truncation can be approximately estimated in bulk systems by considering an uniform continuum medium beyond the cutoff, but for geometries with free surfaces it is not possible to estimate easily the truncation effect.

2.3.3.2   Geometries with surfaces

The purpose of the periodic boundary conditions is to eliminate surface effects, but there are also situations where the interest is in the surfaces.

For surface simulations, is common to eliminate the periodic boundary

conditions in one direction (usually taken to be z) while retaining them in the orthogonal plane. In this way it is possible to simulate a slab with two free surfaces normal to z and indefinitely large in the xy plane.

There are circumstances where it is preferable to freeze some layers on one side of the slab at the perfect bulk-like crystal structure positions in order to simulate a one-surface material. Usually this is done when there is a massive perturbation of the surface, such as surface reconstructions (where there is a massive rearrangement of the atoms) or local melting. If a side of a slab is frozen, care must be taken to freeze a number of layers corresponding to a thickness of at least the cutoff radius (r_c) in order to avoid the possibility that one mobile atom could "see" the surface through the fixed atoms.

Finally, the wire geometry is obtained by using periodic boundary conditions in only one direction, thus having the wire axis along the PBC direction.

2.3.4 Molecular Dynamics

The molecular dynamics method is a computational tool for the simulation, modelling and study of the evolution of a set of particles from the interactions between them. In other words, from the knowledge of the characteristics of the particles and the forces generated by their interactions (usually represented by their potential energies), we can estimate the displacements of the particles and with that information we will be able to study the evolution of the system.

The molecular dynamics was introduced by Alder and Wainwright in the late 1950's [88, 89] to study the interactions of hard spheres. The first MD simulation of a realistic system was done by Rahman and Stillinger in their simulation of liquid water in 1974 [90] . Although having its origin in theoretical physics of fluids, the MD method gained popularity in materials science and since 1970 also in biochemistry and biophysics. In physics, MD is used to examine the dynamics of atomic-level phenomena that cannot be observed directly. It is also used to examine the physical properties of nanotechnological devices that have not or cannot yet be created.

The molecular dynamics is a powerful technique but it has limitations. The essential ingredient in a MD simulation is the calculation of the interactions between the particles.

Depending on the type of interactions we can classify three types of molecular dynamics:

D.F.T.: Density functional theory, an approximation to the many-body problem in quantum mechanics, based on first principles and which

gives a good description of the lower states of elemental semiconductors but not a good description of excited states[5]. On the other hand, this scheme is very demanding on computer resources and slow for big systems.

T.B.: Tight-Binding, a semi-empirical method adequate for greater number of particles and for covalent binding materials, but not adequate for metallic systems.

Empiric/semi-empiric: This scheme is the best option for very big systems and "long" periods of time, but it needs a careful choice of the interaction potential.

On the other hand, the macroscopic measurements and the molecular dynamics model are related by the statistical mechanics. So in order to link the model with the macroscopic knowledge is necessary to acquire enough data to make the proper statistics. Also, to place a proper system statistics is necessary to fulfill the ergodic theorem. Although proving that a system is ergodic is an unsolved problem in general (i.e. is not computable). That is, you can visit the whole phase space along a specific path of the system if this path is long enough. Not necessarily any path because it is possible for certain energies to have a potential barrier that prevents the trajectory from visiting certain areas of phase space of that state. This means that, in principle, integrating the trajectory in time will give us the volume of the phase space, but doing so is very difficult to calculate as well.

In Molecular Dynamics, the parameters that are naturally fixed are the volume, the total energy and the number of particles, i.e. "the *micro-canonical* ensemble" (NVE) (see Appendix in page 201). But in our model the temperature is one of the important parameters to maintain, so the *canonical* ensemble (NVT) is needed. So first, in order to simulate the temperature in our model we can add a random term to the velocities of the particles. Usually, in a MD simulation, the random velocities of the particles are initially set with the normalised Maxwell-Boltzmann distribution:

$$W(v_l) = \left(\frac{m_i}{2\pi\kappa_B T}\right)^{\frac{1}{2}} e^{-\frac{m_i v_l^2}{2\kappa_B T}} \tag{2.211}$$

with v_l the components of the velocity ($l = x, y, z$), m_i the mass of the particles, κ_B the Boltzmann constant, T the temperature, and the standard

---

[5]Despite recent improvements, there are still difficulties in using density functional theory to properly describe charge transfer excitations; transition states, global potential energy surfaces and some other strongly correlated systems; and in calculations of the band gap in semiconductors.

deviation $\sqrt{\frac{\kappa_B T}{m_i}}$. When doing this, the system may have a small total linear momentum, corresponding to a translational motion of the whole system due to the random choice of velocities and the finite number of particles. So, before starting the simulation, all the velocities are transformed by a factor to ensure the zero momentum condition $(\sum_i \vec{v_i}) = 0$. This operation is also performed from time to time during the simulation, because due to discretization and round-off errors the system may drift away from the zero total momentum condition.

It is possible to approximate the inter-atomic potential to an harmonic one, $\frac{1}{2}Kx^2$, near the minima. As the temperature is linked with the kinetic energy $\frac{1}{2}mx^2$ and our velocity distribution is initially a random Maxwell-Boltzmann distribution, then when the system acquires the condition of stability the total energy will be equally distributed between the potential and the kinetic energies.

The temperature is a measure of the average kinetic energy of the atoms. Thus if we initially set the kinetic energy distribution according to a temperature that doubles the target temperature, then after some time the energy will be equally distributed between kinetic and potential and we approximately will have our system at the wished temperature.

This method is only adequate for a range of temperatures in which the harmonic approximation is valid. Obviously this method is not adequate for temperatures greater than half of the fusion temperature. In order to solve these situations it is necessary to use other methods, like the thermostat. In this method the temperature is rescaled at each step in order to match the system temperature with the wished one. But in that situation the model does not correspond to a physical system, as we are modifying it artificially. That's why the thermostat techniques are usually set at the beginning of the calculation in order to fix the initial conditions, and then put the system in equilibrium in order to start the "real" simulation[6] [7] [8].

So the scheme is this: We begin the calculation by choosing a reasonable guess of the initial positions of the structure we want to calculate. Then the steepest descent method is used to bring the whole system to the minimum of the potential energy. Once the system is at the static equilibrium in the minimum of the potential, we set the temperature and begin the integration in time until we equilibrate the system again but now at the temperature of interest. Finally the system is integrated forward in time until we get enough

---

[6]If the system keeps the unstable condition after we turn of the thermostat,then we turn on and repeat the process.

[7]Typical thermostat $\frac{1}{2}\sum(v_x^2 + v_y^2 + v_z^2) = \frac{3}{2}N\kappa_B T$

[8]Berendsen temperature control factor $\lambda = \sqrt{1 + \frac{\Delta T}{100\Delta T}(\frac{T_0}{T} - 1)}$

data in order to make sure that enough of the space phase is sampled.

```
┌─────────────────────────┐
│   Set initial conditions │
│   r⃗ᵢ(t₀) and v⃗ᵢ(t₀)     │
└─────────────────────────┘
            │
            ▼
┌─────────────────────────┐
│     Get new forces       │
│       F⃗ᵢ(r⃗ᵢ)            │
└─────────────────────────┘
            │
            ▼
┌─────────────────────────────────┐
│   Solve the equations of motion  │
│  numerically over  a step time Δt│
│   r⃗ᵢ(tₙ) → r⃗ᵢ(tₙ + Δt)         │
│   v⃗ᵢ(tₙ) → v⃗ᵢ(tₙ + Δt)         │
└─────────────────────────────────┘
            │
            ▼
      ┌───────────┐
      │ t = t + Δt│
      └───────────┘
            │
            ▼
  ╱─────────────────────────────────╱
 ╱ Save new positions and velocities╱
╱─────────────────────────────────╱
            │
            ▼
        ◇ is t > t_max ? ◇
```
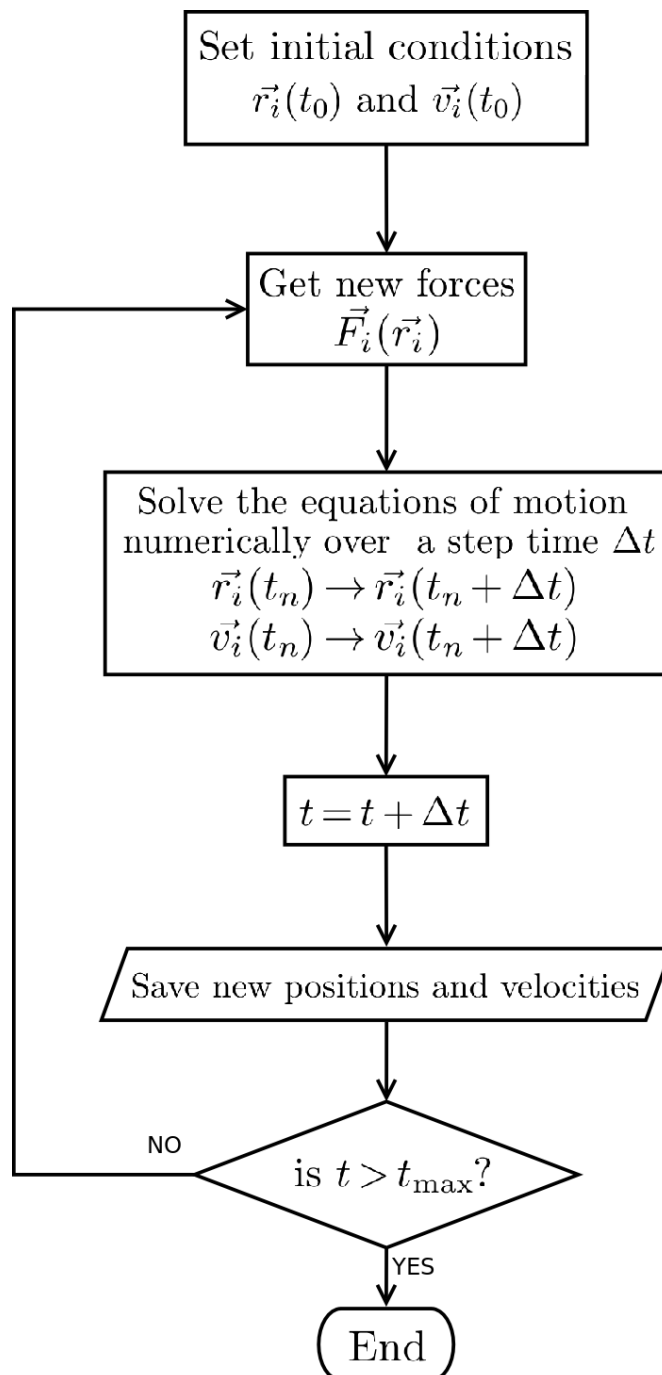
Figure 2.9: Basic Molecular Dynamics diagram.

2.3.4.1 The basic Molecular Dynamics algorithm

Molecular dynamics can be thought as the way Newton would have simulated the movement of planets in a solar system. . . if he have had a computer [91]. The method is simple, in principle:

1. **Initial conditions.** Let's assume that the positions $\vec{r_i}$ and velocities $\vec{v_i}$ of all the particles of a system at a time t are known.

2. **Force computation.** Also assume that the laws that govern the interaction between these particles are known, so it is possible to compute the force $\vec{F_i}$ exerted on every particle i.

3. **Integration.** Then the Newton's equations of motion for every one of the particles are solved in order to get their positions and velocities at a later time Δt:

$$
\begin{aligned}
\vec{r_i}(t + \Delta t) &= \vec{r_i}(t) + \vec{v_i}(t)\Delta t + \frac{1}{2}\frac{\vec{F_i}}{m_i}\Delta t^2 \\
\\
\vec{v_i}(t + \Delta t) &= \vec{v_i}(t) + \frac{\vec{F_i}}{m_i}\Delta t
\end{aligned}
\tag{2.212}
$$

4. **Loop back.** Return to step 1 with the newly computed positions and velocities.

2.3.4.2 Integration algorithms: Verlet

The engine of a molecular dynamics program is its time integration algorithm, required to integrate the equations of motion of the interacting particles and follow their trajectories.

Time integration algorithms are based on *finite difference methods*, where time is discretized on a finite grid, the *time step* Δt being the distance between consecutive points on the grid. Knowing the positions and some of their time derivatives at time t (the exact details depend on the type of algorithm), the integration scheme gives the same quantities at a later time $t + \Delta t$. By iterating the procedure, the time evolution of the system can be followed for long times.

Of course, these schemes are approximated, giving rise to some intrinsic errors. In particular, one can distinguish between

- *Truncation errors*, related to the accuracy of the finite difference method with respect to the true solution. Finite difference methods are usually

based on a Taylor expansion truncated at some term, hence the name. These errors do not depend on the implementation: they are intrinsic to the algorithm.

- *Round-off errors*, related to errors associated to a particular implementation of the algorithm. For instance, to the finite number of digits used in computer arithmetics.

Both errors can be reduced by decreasing Δt. For large Δt, truncation errors dominate, but they decrease quickly as Δt is decreased. For instance, the Verlet algorithm (to be discussed below) has a truncation error proportional to Δt^4 for each integration time step. Round-off errors decrease more slowly with decreasing Δt, and dominate in the small Δt limit. Using 64-bit precision in computer codes and hardware architectures helps to decrease round-off errors, making them negligible.

In Molecular Dynamics, the most commonly used time integration algorithm is, probably, the so-called Verlet algorithm [92, 93]. The basic idea is to write two third-order Taylor expansions for the positions $\vec{r}(t)$, one forward and one backward in time. Calling $\vec{v}$ the velocities, $\vec{a}$ the accelerations, and $\vec{b}$ the third derivatives of $\vec{r}$ with respect to t, one has

$$\vec{r}(t + \Delta t) = \vec{r}(t) + \vec{v}(t)\Delta t + (1/2)\vec{a}(t)\Delta t^2 + (1/6)\vec{b}(t)\Delta t^3 + O(\Delta t^4)$$
$$(2.213)$$
$$\vec{r}(t - \Delta t) = \vec{r}(t) - \vec{v}(t)\Delta t + (1/2)\vec{a}(t)\Delta t^2 - (1/6)\vec{b}(t)\Delta t^3 + O(\Delta t^4).$$

Adding the two expressions gives

$$\vec{r}(t + \Delta t) + \vec{r}(t - \Delta t) = 2\vec{r}(t) + \vec{a}(t)\Delta t^2 + O(\Delta t^4). \qquad (2.214)$$

And moving to the right the $t - \Delta t$ term gives

$$\vec{r}(t + \Delta t) = 2\vec{r}(t) - \vec{r}(t - \Delta t) + \vec{a}(t)\Delta t^2 + O(\Delta t^4). \qquad (2.215)$$

This is the basic form of the Verlet algorithm. Since we are integrating Newton's equations, $\vec{a}(t)$ is just the force divided by the mass, and the force is in turn a function of the positions $\vec{r}(t)$:

$$\vec{a}(t) = -(1/m)\nabla V(\vec{r}(t)). \qquad (2.216)$$

As one can inmediatly see, the truncation error of the algorithm when evolving the system by Δt is of the order of Δt^4, even if third derivatives do not appear explicitly. This algorithm is at the same time simple to implement, accurate and stable, explaining its large popularity among MD code developers.

A problem with this version of the Verlet algorithm is that velocities are not directly generated. While they are not needed for the time evolution, their knowledge is sometimes necessary. Actually, they are required to compute the kinetic energy K, whose evaluation is necessary to test the conservation of the total energy $E = K + V$. To overcome this difficulty, some variants of the Verlet algorithm have been developed. They give rise to exactly the same trajectory, and differ in what variables are stored in memory and at what times.

The best implementation of the same basic algorithm is the so-called *velocity Verlet* scheme, where positions, velocities and accelerations at time $t + \Delta t$ are obtained from the same quantities at time t in the following way:

$$
\begin{array}{rcl}
\vec{r}(t + \Delta t) & = & \vec{r}(t) + \vec{v}(t)\Delta t + (1/2)\vec{a}(t)\Delta t^2 \\
\vec{v}(t + \Delta t/2) & = & \vec{v}(t) + (1/2)\vec{a}(t)\Delta t \\
\vec{a}(t + \Delta t) & = & -(1/m)\nabla V(\vec{r}(t + \Delta t)) \\
\vec{v}(t + \Delta t) & = & \vec{v}(t + \Delta t/2) + (1/2)\vec{a}(t + \Delta t)\Delta t.
\end{array}
\tag{2.217}
$$

Note that we need $9N$ memory locations to save the $3N$ positions, velocities and accelerations, but we never need to have simultaneously stored the values at two different times for any of these quantities.

2.3.4.3 The Tersoff potential

In this work we will use the Tersoff potential for the calculation of the semiconductors molecular dynamics.

The Tersoff potential is a bond order potential in with we have a three-body potential depending on the bond length and angles. The Tersoff approach relies on the fact that the strength of the bonds depends on the environment defined as a series of factors that depends on the coordination of the atom.

Therefore this family of potentials have the general formulation:

$$
V_i = \frac{1}{2}\left(\sum_{i\neq j} A_{i,j}\Phi_R(r_{i,j}) + \sum_{i\neq j} B_{i,j}\Phi_A(r_{i,j})\right)
\tag{2.218}
$$

where Φ_R and Φ_A are the repulsive and attractive pair potential respectively, $r_{i,j}$ is the distance between the atoms i and j and A and B are the coordination factors.

In order to avoid energy conservation problems, we will smooth the potential and make it continuous and derivable inside the cutoff radius. Thus

we introduce a smoothing potential Φ_C so we can express the potential as:

$$V_i = \frac{1}{2} \sum_{i \neq j} \left(\Phi_C(r_{i,j}) [A_{i,j} \Phi_R(r_{i,j}) + B_{i,j} \Phi_A(r_{i,j})] \right) \tag{2.219}$$

The repulsive and atractive potentials are the Morse:

$$\Phi_R(r) = C_R e^{-\lambda_R r}$$

$$\Phi_A(r) = -C_A e^{-\lambda_A r} \tag{2.220}$$
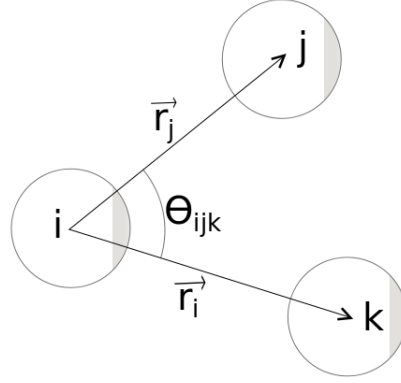
Figure 2.10: Three body scheme.

The smoothing-cutoff potential is:

$$\Phi_C(r) = \begin{cases} 1 & \text{if } r \leq R - D \\ \frac{1}{2}\left(1 - \sin\left(\frac{\pi(r-D)}{2D}\right)\right) & \text{if } R - D < r < R + D \\ 0 & \text{if } r \geq R + D \end{cases} \tag{2.221}$$

where R and D are the cutoff parameters that depend on the atoms involved.
And the coordination factors are:

$$A_{i,j} = \left(1 + \alpha^n \mu_{i,j}^n\right)^{\frac{-1}{2n}} \tag{2.222}$$

and

$$B_{i,j} = \left(1 + \beta^n \nu_{i,j}^n\right)^{\frac{-1}{2n}} \tag{2.223}$$

where

$$\mu_{i,j} = \sum_{k \neq i,j} \Phi_C(r_{i,k}) e^{\lambda_\mu^3 (r_{i,j} - r_{i,k})^3} \tag{2.224}$$

and

$$\nu_{i,j} = \sum_{k \neq i,j} \Phi_C(r_{i,k}) \gamma(\theta_{i,j,k}) e^{\lambda_\mu^3 (r_{i,j} - r_{i,k})^3} \tag{2.225}$$

with

$$\gamma(\theta_{i,j,k}) = 1 + \frac{c^2}{d^2} - \frac{c^2}{d^2 + (h - \cos(\theta_{i,j,k}))^2} \tag{2.226}$$

Where $\theta_{i,j,k}$ is the angle made by the links between the atoms $i - j$ and $i - k$, and the terms $C, \lambda, \alpha, \beta, c, d$ and h are parameters [85] that depend on the atoms and other characteristics like the kind of information we want from the system.

The term $\nu_{i,j}$ defines the effective coordination number of atom i, i.e. the number of nearest neighbours, taking into account the relative distance of two neighbours $r_{i,j} - r_{i,k}$ and the bond-angle θ. The function $\gamma(\theta_{i,j,k})$ has a minimum for $h = \cos(\theta_{i,j,k})$, the parameter d determines how sharp the dependence on angle is, and c expresses the strength of the angular effect.

	Si	Ge
C_R (eV)	1.8308×10^3	1.769×10^3
C_A (eV)	4.7118×10^2	4.1923×10^2
λ $(\mathring{A}^{-1})$	2.4799	2.4451
μ $(\mathring{A}^{-1})$	1.7322	1.7047
β	1.1000×10^{-6}	9.0166×10^{-7}
n	7.8734×10^{-1}	7.5627×10^{-1}
c	1.0039×10^5	1.0643×10^5
d	1.6217×10^1	1.5652×10^1
h	-5.9825×10^{-1}	-4.3884×10^{-1}
$(R - D)$ $(\mathring{A})$	2.7	2.8
$(R + D)$ $(\mathring{A})$	3.0	3.1

Table 2.2: Tersoff parameters for Si and Ge with $\alpha = 0$ [85]

2.3.5 Vibrational density of states

The Vibrational density of states (VDOS), also known as phonon density of states of a system, describes the number of states per interval of energy at each energy level that are available to the phonons. The VDOS is the integral on the Brillouin zone over all the phonon bands of the dispersion relations. The VDOS can be given as a function of energy or wave vector.

The dispersion relations of the system can be obtained from molecular dynamics by the autocorrelation function of the velocities, but due to the

fact that we will work with a great amount of data, we will calculate the VDOS directly by changing the order of the operations as the output of the MD method are sampled in time. In this way the data will be used from each time step instead of working with the data from each atom.

As we know, the thermodynamic properties of a solid are directly related to its phonon structure. The vibrational density of states describes the entire set of possible phonon states which determines the heat capacity of the system.

2.3.5.1   Velocity-Velocity correlation function

Once we get the evolution of the system by molecular dynamics it is possible to obtain the vibrational spectrum from the analysis of the velocities by the auto-correlation function[9]:

$$G(\tau) = <\vec{v_i}(t_0) \cdot \vec{v_i}(t_0 + \tau)>_{i,t_0} = \frac{1}{N} \sum_{i=1}^{N} \frac{1}{t_{max}} \sum_{t_0=1}^{t_{max}} \vec{v_i}(t_0) \cdot \vec{v_i}(t_0 + \tau) \quad (2.227)$$

This auto-correlation gives us the spectrum because when we auto-correlate the velocities, we are in fact looking for a time relation in the evolution of the velocities. That is, if we get a periodic movement, then at characteristic differences in the τ-time, we have the same velocities, and it is easy to see that these characteristic times are in fact multiples of the oscillation period. That is how the oscillation frequencies of the particles and the velocity auto-correlations are related. Therefore, the auto-correlation function has the information of the oscillation periods of the velocities.

Then, if we calculate the auto-correlation function and use a Fourier transform,

$$I(\nu) = \int_{-\infty}^{\infty} \exp(-2\pi\iota\nu\tau) \cdot G(\tau)d\tau \quad (2.228)$$

we will obtain the oscillation frequencies of the particles. The choice of a time step greater than the lowest semi-period of the system would produce a non-physical model (as explained in the Nyquist-Shannon theorem). Thus the knowledge of the frequencies of the system would be very useful for the selection of the adequate time step for the molecular dynamics model.

On the other hand due to the properties of Fourier transforms, we are able to simplify some of the calculus by making the auto-correlation inside

---

[9]The correlation of two continuous functions is defined by:
$\mathrm{Corr}(g,h) \equiv \int_{\infty}^{\infty} g(\tau + t)h(\tau)d\tau$

of the Fourier transformed data of the velocities. According to the correlation[10] theorem of Fourier transform we are able to calculate the convolution by multiplying their Fourier transformed data and then invert the Fourier transform. As the convolution and the correlation functions are related, it is possible to calculate directly the Fourier transform of the correlation by multiplying the Fourier transforms of the velocities (due to the fact that they are real).

2.3.6 Raman spectra

One of the most used methods for the determination of nanostructure's vibrational characteristics and properties is the Raman scattering. Raman scattering is the easiest method to perform and can be used to identify both the energy of optically active vibrational modes near the zone centre of the Brillouin zone, and the energy of electronic transitions.

The Raman spectra are obtained from the inelastic scattering of photons by matter. While most of the photons are scattered elastically (Rayleigh scattering) a small fraction is scattered by an excited state which changes the frequency of the scattered photon. This inelastic scattering was predicted by Adolf Smekal in 1923 [108].

The Raman effect was discovered by Sir Chandrasekhara Venkata Raman and Kariamanickam Srinivasa Krishnan [109, 110] in 1928 and virtually at the same time by Grigory S. Landsberg and Leonid I. Mandelstam [111].

In the Raman scattering there are energy exchanges between the photons and the particles. In perfect crystals, due to their periodic nature, only specific phonons are possible, and the Raman scattering only happens at certain allowed frequencies. On the other hand, in amorphous materials the spectral lines become broad due to the existence of more allowed phonons.

When the photon exchanges energy with the material there are two possible outcomes, the system absorbs the energy (Stokes scattering) or the system loses energy (anti-Stokes scattering). In both situations the energy differences are, in absolute value, the same as only the difference of the energy of the vibrational levels are relevant.

However, as the wave-vector of the photon is very much smaller than the Brillouin zone, all interactions between it and the phonons must occur near the Brillouin zone centre due to momentum conservation. Momentum conservation also enables one to calculate the polarisation of the phonon

---

[10]The Correlation Theorem is $\text{Corr}(g, h) \Leftrightarrow G(f)H(-f)$ with $g(t)$ and $h(t)$ the pair of functions to correlate and $G(f)$ and $H(f)$ the corresponding Fourier transforms. If the function is real, then $G(-f) = G^*(f)$ and the autocorrelation becomes $\text{Corr}(g, g) \Leftrightarrow |G(f)|^2$ the "Wiener-Khinchin Theorem"[94].

involved in the scattering, as depending on the orientation of the sample and the incident beam selection rules are created and thus particular modes are not allowed to interact. But, in nanostructures, this information is less prevalent as the samples tend to not have a uniform (or known) orientation, which makes observing photon polarisation (and hence phonons polarisation) impossible as the scattering cannot be linked with the orientation of the crystal structure.

The Raman spectra, the infrared spectra and fundamental vibrational-rotational spectra of dense systems (high pressure gases, liquids, and solids) are essentially classical. With that we mean that they can be computed and understood from a basically classical mechanics viewpoint plus some simple quantum corrections [112].

For a polarizable system, an incident photon can excite vibrational modes, thus changing the energy of the scattered photon by the amount of energy of the related vibrational states in the system.Therefore, the Raman scattering depends on the polarizability of the system.

Our theoretical calculation of the Raman spectra has several steps:

- First we use Molecular Dynamics to compute the atomic trajectories of the system.

- Then we calculate the time-dependent polarizability tensor from the variation of the positions of the particles.

- Then we use linear response theory to derive the Raman spectra from the polarizability time history. The linear response is only applicable in systems at equilibrium. Therefore we need to be sure that the system is not under outside perturbations, that is, undisturbed except for thermal fluctuations.

  - The Raman spectra (with dependence on time) are obtained from the autocorrelation function of the polarizability tensor [112, 113]

    * The polarizability tensor is obtained from the variation of the longitudinal bond polarizabilities.

  - The Raman spectra with dependence on frequency are obtained by Fourier transforming the autocorrelation function of the polarizability tensor.

- Then, if possible, the spectrum is averaged over the ensemble. To provide a sufficiently accurate ensemble average we must ensure that enough phase space is sampled.

2.3.6.1 Polarizability tensor

A molecule or atom placed in an electric field undergoes a deformation. Thus, the centroid of negative charges (electrons) is shifted slightly from that of positive charges (nuclei) from which an induced electronic moment $\vec{\mathcal{P}}$ appears. In the di- or polyatomic molecules and crystals, the atoms also move against each other giving an additional contribution called atomic polarizability.

Polarizabilities determine the dynamical response of a bound system to external fields, and provide insight into a molecule's internal structure.

For weak fields, the induced moment is proportional to the field following the relationship :

$$\vec{\mathcal{P}} = \bar{P}\vec{E} \tag{2.229}$$

where $\bar{P}$ is the tensor of polarizability and $\vec{E}$ the local field experienced by the molecule (known as local field).

The polarizability is the sum of two contributions. The electronic polarizability and the atomic polarizability. In molecules, the first one is by far the most important while the atomic polarizability plays a minor role although not negligible. On the other hand, in crystals the importance of the contributions is the opposite and the most important contribution is the atomic polarizability.

2.3.6.2 Bond-polarization method

In the Bond-polarization method the polarizability tensor is obtained from the summation of the polarizabilities of the bonds.

In this approach, the polarizability is modelled in terms of bond contributions:

$$\bar{P}(\vec{r}_{ij}) = \alpha(r_{ij})\bar{I} + \gamma(r_{ij})\left[\frac{\vec{r}_{ij}\vec{r}_{ij}}{|r_{ij}||r_{ij}|} - \frac{1}{3}\bar{I}\right] \tag{2.230}$$

Where $\bar{I}$ is the unit 2-tensor (a matrix), $\alpha(r_{ij})$ is the mean polarizability[11], $\gamma(r_{ij})$ describes the anisotropy of the polarizability[12] and $\vec{r}_{ij} = \vec{r}_{ij}(0) + \vec{r}_{ij}(t) = ((\vec{r}_j(0) - \vec{r}_i(0)) + (\vec{r}_j(t) - \vec{r}_i(t)))$ is a vector which defines the direction and the distance of a pair of nearest neighbour atoms at sites $\vec{r}_i$ and $\vec{r}_j$.

The bond polarizability model further assumes that the bond polarizabilities α_L and α_P and therefore α and γ only depend on the length of the

---

[11]$\alpha = \left(\frac{\alpha_L + \alpha_{PO} + \alpha_{PI}}{3}\right)$

[12]$\gamma = \alpha_L - \alpha_P$ where α_L and α_P correspond to the longitudinal and perpendicular bond polarizability, respectively.

bond. Thus the derivative of the bond polarizability with respect to the displacement of one of the atom reads:

$$\frac{\partial P_{\alpha\beta}}{\partial \vec{x_j}}\vec{x_j} = \qquad \frac{1}{3}(\alpha'_L(\vec{r_{ij}}) + 2\alpha'_P(\vec{r_{ij}}))(\vec{x_{\alpha ij}} \cdot \hat{\vec{r_{\beta ij}}})\bar{I} \qquad\qquad (2.231)$$

$$+(\alpha'_L(\vec{r_{ij}}) - \alpha'_P(\vec{r_{ij}}))(\vec{x_{\alpha ij}} \cdot \hat{\vec{r_{\beta ij}}})\left[\hat{\vec{r_{\alpha ij}}} \cdot \hat{\vec{r_{\beta ij}}} - \frac{1}{3}\bar{I}\right]$$

$$+\frac{(\alpha_L(\vec{r_{ij}}) - \alpha_P(\vec{r_{ij}}))}{\vec{r_{ij}}}\left[\vec{x_{\alpha ij}} \cdot \hat{\vec{r_{\beta ij}}} + \hat{\vec{r_{\alpha ij}}} \cdot \vec{x_{\beta ij}} - 2(\vec{x_{\alpha ij}} \cdot \hat{\vec{r_{\beta ij}}})(\hat{\vec{r_{\alpha ij}}} \cdot \hat{\vec{r_{\beta ij}}})\right]$$

where α'_L and α'_P are the derivatives of the bond polarizabilities with respect to bond length and $\hat{\vec{r}}$ indicates the unit vector. Therefore, when one type of bond occurs, the bond polarizability model is completely defined by three parameters:

$$\begin{aligned} \alpha' &= \frac{1}{3}(2\alpha'_P + \alpha'_L) \\ \gamma' &= (\alpha'_L - \alpha'_P) \\ \gamma &= (\alpha_L - \alpha_P) \end{aligned} \qquad\qquad (2.232)$$

The parameters of the bond polarizability model are usually obtained by fitting the experimental intensities. Following this procedure, the parameters of the bond polarizability model remain indeterminate by a scaling factor, because the experimental intensities are only known on a relative scale.

2.3.6.3   Deduction and calculation of the Raman spectra

Since the Raman transitions are associated [115] with the induced dipole moment $\vec{M}$, the scattered intensity $I(\omega)$ expected at the frequency ω of the Stokes spectra will be given by the fluctuation-dissipation theorem. The fluctuation-dissipation theorem is a powerful tool in statistical physics for predicting the behaviour of non-equilibrium thermodynamical systems. In this case instead of the irreversible dissipation of energy into heat from their reversible fluctuations at thermodynamic equilibrium we look into the energy transfer from and into an external electromagnetic source by the induced dipole moments. This theorem connects the linear response relaxation of a system from a prepared non-equilibrium state to its statistical fluctuation properties in equilibrium [116].

$$I(\omega) \sim \int_{-\infty}^{\infty} \langle M_S(t)M_S(0)\rangle_{av}\, e^{i\omega t}dt \qquad\qquad (2.233)$$

Let $\vec{u^I}$ be the unit vector parallel to the electric vector of the incident radiation $\vec{E^I}$ and $\vec{u^S}$ be the unit vector parallel to the electric vector of the

scattered radiation $\vec{E^S}$. $\hat{P}$ denotes the electric polarizability tensor. Then the induced dipole moment $\vec{M} = \bar{P} \cdot \vec{E^I} = \bar{P} \cdot \vec{u^I} E^I$ along $\vec{u^S}$ can be expressed as:

$$M_S = \vec{u^s} \cdot \vec{M} = \vec{u^s} \cdot (\bar{P} \cdot \vec{E^I}) = (\vec{u^s} \cdot \bar{P} \cdot \vec{u^I})E^I. \qquad (2.234)$$

Therefore:

$$I(\omega) \sim \int_{-\infty}^{\infty} \left\langle (\vec{u^s} \cdot \bar{P}(t) \cdot \vec{u^I})(\vec{u^s} \cdot \bar{P}(0) \cdot \vec{u^I}) \right\rangle_{av} e^{i\omega t} dt = \int_{-\infty}^{\infty} G(t)e^{i\omega t} dt \qquad (2.235)$$

Now we can calculate the average $G(t)$ in a discrete setting as:

$$G(\tau) = \left\langle \bar{P}(\tau)\bar{P}(0) \right\rangle_{av} = \frac{1}{t_{Max}} \sum_{t_0=1}^{t_{Max}} \bar{P}(t_0)\bar{P}(t_0 + \tau) \qquad (2.236)$$

Therefore the method we use for the calculation of the Raman spectra is:

$$\bar{G}(\lambda) = \frac{1}{\sqrt{2\pi}} \int_0^\infty \left[\frac{1}{t_{MAX}} \sum_{t_0=1}^{t_{MAX}} \bar{P}(t_0) \cdot \bar{P}(t_0 + \tau) \right] e^{-i\lambda\tau} d\tau \qquad (2.237)$$

by means of the series expansion:

$$P(t) = P_0 + \sum_j \frac{\partial P}{\partial \vec{x_j}} \vec{x_j} + \dots \qquad (2.238)$$

where the first term is not relevant, so we have in first order approximation:

$$G_{\alpha\beta}(\lambda) = \frac{1}{\sqrt{2\pi}} \int_0^\infty \left[\frac{1}{t_{MAX}} \sum_{t_0=1}^{t_{MAX}} \left[\sum_j \left(\frac{\partial P_{\alpha\beta}}{\partial \vec{x_j}} \vec{x_j}(t_0) \right) \cdot \sum_j \left(\frac{\partial P_{\alpha\beta}}{\partial \vec{x_j}} \vec{x_j}(t_0 + \tau) \right) \right] \right] e^{-i\lambda\tau} d\tau \qquad (2.239)$$

By the Bond-polarization method (eq.(2.230) and eq.(2.231)):

$$\sum_{j\gamma} \frac{\partial P_{\alpha\beta}}{\partial \vec{x_{j\gamma}}} \vec{x_{j\gamma}} = \sum_{i,j}^{links} \alpha'(\vec{r_{ij}})(\vec{x_{\alpha ij}} \cdot \hat{\vec{r}}_{\beta ij})\bar{I} + \gamma'(\vec{r_{ij}})(\vec{x_{\alpha ij}} \cdot \hat{\vec{r}}_{\beta ij}) \left[\hat{\vec{r}}_{\alpha ij} \cdot \hat{\vec{r}}_{\beta ij} - \frac{1}{3}\bar{I} \right]$$
$$+ \frac{\gamma(\vec{r_{ij}})}{\vec{r_{ij}}} \left[\vec{x_{\alpha ij}} \cdot \hat{\vec{r}}_{\beta ij} + \hat{\vec{r}}_{\alpha ij} \cdot \vec{x_{\beta ij}} - 2(\vec{x_{\alpha ij}} \cdot \hat{\vec{r}}_{\beta ij})(\hat{\vec{r}}_{\alpha ij} \cdot \hat{\vec{r}}_{\beta ij}) \right] \qquad (2.240)$$

$$\frac{\partial P_{\alpha\beta}}{\partial \vec{x_j}} \vec{x_j} = \alpha'(\vec{r_{ij}})(\vec{x_{\alpha ij}} \cdot \hat{\vec{r}}_{\beta ij})\bar{I} + \gamma'(\vec{r_{ij}})(\vec{x_{\alpha ij}} \cdot \hat{\vec{r}}_{\beta ij}) \left[\hat{\vec{r}}_{\alpha ij} \cdot \hat{\vec{r}}_{\beta ij} - \frac{1}{3}\bar{I} \right]$$
$$+ \frac{\gamma(\vec{r_{ij}})}{\vec{r_{ij}}} \left[\vec{x_{\alpha ij}} \cdot \hat{\vec{r}}_{\beta ij} + \hat{\vec{r}}_{\alpha ij} \cdot \vec{x_{\beta ij}} - 2(\vec{x_{\alpha ij}} \cdot \hat{\vec{r}}_{\beta ij})(\hat{\vec{r}}_{\alpha ij} \cdot \hat{\vec{r}}_{\beta ij}) \right] \qquad (2.241)$$

Where $\vec{r_{ij}} = \vec{r_j} - \vec{r_i}$ and $\vec{r_i}$ is the position of the "i" atom in equilibrium and is independent of time, $\vec{x_{ij}} = \vec{x_j} - \vec{x_i}$ and $\vec{x_i}$ is the displacement vector of the "i" atom from equilibrium. The parameters $\alpha' = \frac{1}{3}(2\alpha'_\parallel + \alpha'_\perp)$, $\gamma' = (\alpha'_\parallel - \alpha'_\perp)$ and $\gamma = (\alpha_\parallel - \alpha_\perp)$ are taken as[13] $\alpha' = 0, \gamma' = 1, \gamma = \frac{3r_{ij}}{8}$.

Finally we use the Alonso-Winer formula [117] $I \propto \frac{1}{\omega}(G_{xy}^2 + G_{xz}^2 + G_{yz}^2)$ in order to obtain the Raman spectra.

2.4   Models

In this section we will show the different classes of systems used in this work from the simplest to the more complex ones. We will also give the reasons to choose these systems.

There are many nanostructures of interest, from the fundamental point of view and for their possible applications. Among then we shall concentrate on superlattices of ZnO/MgO and III-nitrides, and nanowires and nanodots. These structures have been grown in recent years by different experimental groups. The number of materials forming these nanostructures is increasing, although the control and reproducible growth of many of them remain an open subject.

Because of this, we shall employ the continuum medium (elasticity theory) approach to obtain the qualitative properties of these systems with an economy of computing resources and a flexibility for different materials. In the case of more controlled systems, we shall use the discrete approach by means of the Molecular Dynamics.

2.4.1   Bulk

The bulk system is used as a model to test our VDOS and Raman methods. With the knowledge of the evolution of the "bulk" systems we will be able to discriminate the effects of the perfect crystalline structure of the material from other effects of the studied nanostructures, like the surface effect.

- Silicon, Germanium and Si_xGe_{1-x} alloys bulk systems will be analysed and the characteristic phonon frequencies of each system will be obtained. Also the number of particles needed for good statistics will be sought.

- The strain effects over the frequencies of the spectra will be analysed and therefore we will be able to identify strain effects on the systems.

---

[13]According to Aldes et al. [107] these are the values for Si "bulk".

In Molecular Dynamics the bulk system is simulated by the periodic boundary conditions as seen in Section 2.3.3 on page 70.

2.4.2 Surface

The surface systems are used to check the effects of surface reconstruction and the effect on the VDOS and Raman spectra. Due to the fact that surfaces have spatially inhomogeneous interactions as the particles in the surface "feel" in the direction perpendicular to the surface only the interactions in one way, we will see a different rearrangement of the particles from that seen in the "bulk".

With the data obtained from this system we will be able to compare with the "bulk" system and extract and discriminate the effects introduced to the vibrational spectra by the surfaces rearrangement.

2.4.3 Nanowire

Nanowires are systems of great interest due to the possible future use in nanoelectronics, photonics and acoustics due to their mechanical properties.

Many kinds of nanowires will be studied. Those with square and circular cross-sections are the nanowires usually studied. We also study the hexagonal cross-section nanowires as in [59]. Many of the semiconductor nanowires grown in different laboratories have the hexagonal prism shape. We show in Fig.2.11 the shape of GaN nanowires.

In the continuum method, square, circular and hexagonal cross-sections nanowires of different materials will be studied. The nanowires will be studied in the cases of solid structure and hollowed from the axis with different radius's holes. Also in the continuum method, core-shell nanowires of circular cross-section will be analysed with the equations obtained in page 34. In the discrete method, silicon nanowires will be studied with square, circular and hexagonal cross-sections and different radius/side.

2.4.4 Nanodot

The quantum dot studied in this work will be a "dome" kind. As shown in Fig.2.12, the dome is on a substrate and has multiple surface orientations. The substrate will be always silicon, and the dome composition will be varied between germanium and silicon-germanium alloys.

The effects of displacement defects will also be studied in the spectra.

The $Si-Ge$ alloys studied here are both homogeneous or non-homogeneous. The homogeneous dome will be built as a $Si_{0.65}Ge_{0.35}$ alloy. On the other
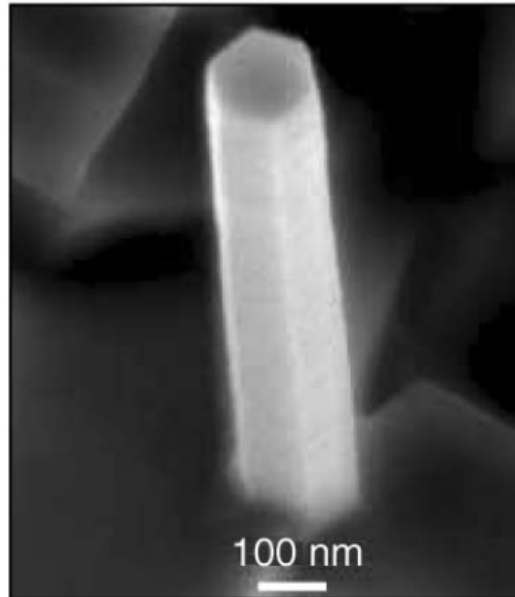
Figure 2.11: GaN nanowire. Source: P. Yang[59]
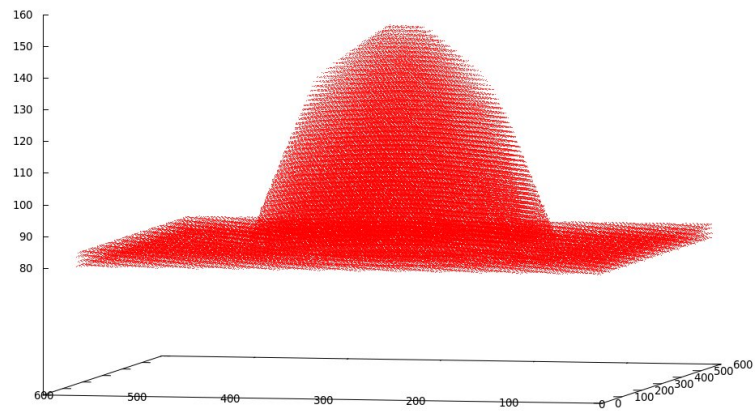
Figure 2.12: A view of the "Dome" quantum dot.

hand, the non-homogeneous dome will consist of two sections (as a simplification of the Rastelli experimental observations [118]). The lower section in contact with the substrate has one third ($\frac{1}{3}$) of the total height of the dome and a $Si_{0.83}Ge_{0.17}$ alloy composition. The upper section is a $Si_{0.66}Ge_{0.44}$ alloy having the remaining two thirds ($\frac{2}{3}$) height of the dome. Thus both kinds of domes are designed with approximately equal proportions of Si and Ge.

Chapter 3

Discussion

3.1 Acoustic waves in (0001) $III-N$ and MgO/ZnO superlattices. Analysis of superlattices with SGFM

Many problems of physical interest involve multi-layer systems. In many of these structures the constituent layers have thicknesses of a few nm. Among these systems the superlattices constitute a field of great interest due to their interesting physical properties and technological applications.

III-N semiconductors have been studied quite recently as a consequence of being good candidates for applications in optoelectronics [119, 120] and microelectronics [121]. These potential capabilities come from the wide range of direct bandgaps, 6.3 eV (AlN), 3.4 eV (GaN) and 0.7 eV (InN), that together with those of their ternary compounds cover the range from the infrared to the ultraviolet. In the wurtzite crystal structure, normally exhibited by these materials, there is a macroscopic polarization playing a capital role in the electrical and optical properties.

More recently the ZnO based materials are emerging as strong alternatives to the III-N. This is due to the fact that many properties of ZnO are similar to those of GaN. A very important fact, as compared to GaN, is the capability of growing ZnO single crystals [122] to be employed as substrates for the growth of thin film devices. This allows the production of high quality films by homoepitaxy and avoids the troubles with the dislocation formation due to epitaxial mismatch in GaN growth. Besides this, the ZnO bandgap (3.37 eV) [123] is quite close to that of GaN. It can also be varied in a systematic way by alloying with CdO [124] or MgO [125, 126]. On the other hand CdO and MgO do not appear naturally in the wurtzite structure. Nevertheless,

several experimental groups achieved the growth of ZnO/MgZnO multiple quantum wells [127, 128, 129, 130, 131]. It has also been found that a MgO layer can take wurtzite structure on a high-quality ZnO buffer layer when the thickness of the MgO layer is less than 10 nm [132].

Although there are no experimental values for the electronic and elastic properties of MgO in the wurtzite structure, several theoretical calculations [133, 134] have provided these values.

Superlattices (SL's) are important for applications in acoustics and other areas. There is a recent and very comprehensive review on the properties of acoustic waves in layered materials [135]. Superlattices can operate as phonon mirrors and filters [136, 137]. They can be employed also as acoustic cavities, where a layer with a different material or a different thickness is introduced in a finite superlattice [138, 139].

Not much is known about the acoustic properties of these systems. The acoustic waves of the III-N (001) zinc-blende superlattices were studied recently [26]. It was found that for the different propagation directions, due to the elastic anisotropy of the materials, wide acoustic band gaps were present, starting at reasonably low values of κd (κ being the absolute value of the parallel wavevector and d the superlattice period).

The basal plane of the wurtzite structure has transverse elastic isotropy allowing in this case a decoupling of the motion of the transverse acoustic wave travelling in this plane from the coupled displacements of the sagittal motion along the other two axes perpendicular to the transverse motion on the plane. Thus there will be different dispersion curves and gaps for the transverse motion in the basal plane interfaces and for the sagittal components. These gaps can exist for different ranges of frequency and parallel wavevector values, thus opening, in principle, different possibilities for applications of the acoustic waves in these superlattices.

As we are interested in the vibrational properties of these systems, we shall need a method able to deal with many different materials. Thus, we shall employ the surface Green Function Matching (SGFM) method [39, 40], which has proved to be a method specially well conceived for this task.

The systems considered here are superlattices formed by alternating layers of AlN/InN, AlN/GaN, GaN/InN and MgO/ZnO, respectively. A schematic view of the superlattices is given in Fig.2.4. There we show the layers of the constituent materials together with their elastic coefficients, mass densities and thicknesses. The crystal axes of all the materials forming the superlattices are aligned and the interfaces are (0001) basal planes of the wurtzite structure. Taking into account the transverse elastic isotropy of the hexagonal crystals we have to consider only the absolute value κ of the parallel wavevector $\vec{\kappa}$ in the basal plane.

In Table 3.4 we give the values of the mass densities and elastic constants of the wurtzite AlN, GaN and InN [140], together with those of wurtzite ZnO [141] and MgO [133, 134].

The velocities of the bulk acoustic waves propagating in the present geometry are:

$$v_{T1}^2 = \frac{C_{44}}{\rho} \quad , \quad v_{T2}^2 = \frac{C_{66}}{\rho} \quad , \quad v_L^2 = \frac{C_{11}}{\rho} \quad , \tag{3.1}$$

In the present case we have two different transverse wave velocities.

In Table 3.1 we give the velocities of the acoustic waves of the materials considered in Table 3.4. We can see that $v_{T1} > v_{T2}$ in all materials, except MgO, whose elastic data are obtained from theoretical calculations. It is seen that AlN has the highest velocity values for the different elastic waves of all the materials considered here.

Table 3.1: Velocities of the acoustic waves for AlN, GaN, InN, MgO$^{(a)}$ [133], MgO$^{(b)}$ [134] and ZnO, calculated with the data of Table 3.4.

Material	$v_{T1}(10^3$ m s$^{-1})$	$v_{T2}(10^3$ m s$^{-1})$	$v_L(10^3$ m s$^{-1})$
AlN	6.307	5.970	11.030
GaN	4.463	4.132	7.963
InN	2.816	2.655	5.722
MgO$^{(a)}$	4.294	5.416	7.875
MgO$^{(b)}$	3.547	4.060	7.372
ZnO	2.811	2.753	6.116

The Surface Green Function Matching (SGFM) explained in section 2.2.4 is used to study these layered systems.

3.1.1 (0001) superlattices

All the formal aspects needed for this study have been presented in section 2.2.4. We shall present now the results for the superlattices considered here.

The dispersion curves are presented as a function of the absolute value of the reduced parallel wavevector (κd) and the reduced frequency $\dfrac{\omega d}{v_t}$, being v_t the lowest velocity of the bulk transverse waves of the two materials forming the superlattice. We have considered the same maximum value for the frequency ω for all the different materials. Although these materials are piezoelectric, we shall not include here the effect of the piezoelectric coefficients. It can be expected that as in other cases [142] the changes thus introduced would not be very important.

For all the systems considered here we shall present results for three superlattices having the arbitrary values d_1=0.125d, d_2=0.875d, d_1=0.5d, d_2=0.5d and d_1=0.875d, d_2=0.125d, respectively. They have been chosen to cover three ranges where the layer thickness of material 1 is much smaller, equal or much bigger, respectively, than the layer thickness of material 2, to see if there are qualitative changes in the dispersion curves.

When comparing superlattices formed by different materials, the strict equivalence of both systems is not guaranteed by having the same values of the thicknesses of the constituent materials. In order to do this it would be necessary to normalise the size of the layers to the corresponding sound velocities [143].

We shall present now the dispersion curves of the sagittal and transverse acoustic waves as a function of κd.

Fig.3.1a presents the dispersion curves of the sagittal acoustic waves and Fig.3.1b gives the dispersion curves of the transverse acoustic waves for a (0001) AlN/InN superlattice with $d_1(AlN)$=0.125 d and $d_2(InN)$=0.875 d. For the transverse waves we can see a collection of not very wide gaps each one opening at higher κd and reduced frequency values. The first gap starts around κd=2, continuing to bigger κd values. The sagittal waves show less gaps of this kind, the first one starting around κd=6, while they also exhibit narrow pocket gaps.

Fig.3.1c and Fig.3.1d show the same information for a (0001) AlN/InN superlattice with $d_1(AlN)$=0.5 d and $d_2(InN)$=0.5 d. The gaps are much wider now than in the previous case, although the qualitative picture is the same.

Fig.3.1e and Fig.3.1f illustrate the case of the (0001) AlN/InN superlattice with $d_1(AlN) = 0.875$ d and $d_2(InN)$=0.125 d. We see that in this case the number of gaps present is smaller than in the two previous cases and the first one opens at higher reduced frequency values than in the former cases. In the case of the transverse waves the first gap is quite wide.

In the case of the transverse modes there are very small and narrow gaps starting at κd=0, not visible at the scale of the figure.

Fig.3.2 shows the dispersion curves of the acoustic waves for a (0001) AlN/GaN superlattice. In this case we have the two materials with higher transverse waves velocities. As we include the same range of real frequencies ω for all the materials, in the present case we shall have a smaller range of reduced frequencies than in the other cases considered here.

Fig.3.2a presents the dispersion curves of the sagittal acoustic waves and Fig.3.2b gives the dispersion curves of the transverse acoustic waves for the case $d_1(AlN)$=0.125 d and $d_2(GaN)$=0.875 d. We see here a similar picture to that shown in Fig.3.1a and Fig.3.1b, of several gaps for increasing values

of κd and reduced frequency.

Fig.3.2c and Fig.3.2d illustrate the case $d_1(AlN)$=0.5 d and $d_2(GaN)$=0.5 d. We obtain here less gaps, but the picture is similar to that shown in Fig.3.1c and Fig.3.1d.

Fig.3.2e and Fig.3.2f present the case $d_1(AlN)$=0.875 d and $d_2(GaN)$=0.125 d. The picture is quite similar to that seen in Fig.3.2c and Fig.3.2d, although the width of the gaps is smaller.

In the case of the transverse modes we see that many gaps start at κd=0 and they exist for almost all values of the parallel wavevector. They also appear for the sagittal waves, but are smaller.

Fig.3.3 presents the dispersion curves of the acoustic waves of a (0001) GaN/InN superlattice.

Fig.3.3a gives the dispersion curves of the sagittal acoustic waves and Fig.3.3b presents the dispersion curves of the transverse acoustic waves for the $d_1(GaN)$=0.125 d and $d_2(InN)$=0.875 d case. We obtain the same picture previously seen for other materials, although now there are less gaps and they are narrower.

Fig.3.3c and Fig.3.3d show the $d_1(AlN)$=0.5 d and $d_2(InN)$=0.5 d case. We obtain another time the picture of less gaps with bigger widths seen in the case of equal thicknesses.

Fig.3.3e and Fig.3.3f give the $d_1(GaN)$=0.875 d and $d_2(InN)$=0.125 d case. We see an analogous image to that previously obtained for these thicknesses. Now there are less gaps than in previous cases.

We see also in this case that the dispersion curves for the transverse waves have the gaps starting at κd=0. They are also present for the sagittal modes in Fig.3.3e but cover a small range of parallel wavevector values.

The three different superlattices show analogous behaviours for the three cases considered, $d_1 < d_2$, $d_1 = d_2$ and $d_1 > d_2$. They present different details but the overall behaviour of the dispersion curves corresponding to the three relative thicknesses considered here for the different constituent III-N materials is the same. A direct comparison with the results obtained for superlattices of the same materials in the zinc-blende structure [26] is not possible, due to the elastic anisotropy associated to the cubic systems. Propagation along the [100] and [110] directions allow for a decoupling in sagittal and transverse modes, not possible for arbitrary propagation directions. In those cases the dispersion curves exhibit similarities, but also differences with the behaviour presented here.

We shall consider now the MgO/ZnO superlattices. As quoted before there are no experimental values of the elastic constants of hexagonal MgO. Thus we shall consider the two sets of theoretical values given in Table 3.4 together with the experimental values of wurtzite ZnO [141] in order to see if

we obtain similar or different pictures for the dispersion curves of MgO/ZnO (0001) superlattices acoustic waves.

Fig.3.4 presents the dispersion curves of the acoustic waves of a MgO/ZnO (0001) superlattice, with the MgO elastic coefficients given in Gopal et al.[133].

Fig.3.4a gives the dispersion curves of the sagittal acoustic waves and Fig.3.4b presents the dispersion curves of the transverse acoustic waves for the $d_1(MgO)$=0.125 d and $d_2(ZnO)$=0.875 d case. We see now less gaps. The gaps are very narrow and the first one opens at a higher κd value than in the III-N superlattices.

Fig.3.4c and Fig.3.4d illustrate the $d_1(MgO)$=0.5 d and $d_2(ZnO)$=0.5 d case. The picture shown here is equivalent to that found in previous cases for equal thicknesses.

Fig.3.4e and Fig.3.4f present the $d_1(MgO)$=0.875 d and $d_2(ZnO)$=0.125 d case. The behaviour seen here is similar to that found in the III-N superlattices, the gaps being now quite narrow.

We see the gaps starting at κd=0 for the transverse modes.

In Fig.3.5 we show the dispersion curves of the acoustic waves of a MgO/ZnO (0001) superlattice with the MgO elastic coefficients given in Duan et al.[134]. The behaviour shown here is basically the same presented in Fig.3.4 but with narrower gaps in the present case.

Thus we see that all the superlattices studied here show the same qualitative features for each one of the three relative thicknesses considered in the work.

As we have presented the results for the sagittal and transverse waves in a separate way we illustrate now the dispersion curves for the acoustic waves including both polarisations. In Fig.3.6 we show the dispersion curves of the acoustic waves of a MgO/ZnO (0001) superlattice with the MgO elastic coefficients given in Duan et al.[134]. It is clear that there are band gaps for both polarisations. The picture presented in Fig.3.6 is valid for all the superlattices considered here, with differences in the ranges of existence of the band gaps for the different materials.

We shall discuss now briefly the dispersion curves as a function of the perpendicular wavevector (qd) for some fixed values of the parallel wavevector (κd). This approach is related to the complex band structure of acoustic phonons in superlattices [144, 145, 146]. This allows to see the evolution of the gaps with the relative thicknesses.

Fig.3.7 gives the lower dispersion curves of the sagittal and transverse acoustic waves of a MgO/ZnO (0001) superlattice, with the MgO elastic coefficients given in Gopal et al.[133] being $d_1(MgO) = 0.5$ d and $d_2(ZnO) = 0.5$ d, as a function of qd. We consider four different values for κd, 1, 3, 6, and 8, respectively. We see how the bands go to higher frequencies for

increasing κd values. In the case of the sagittal waves we see the interplay of the two branches. In Fig.3.7a we see some gaps at $qd \approx 1.1$, $qd \approx 1.6$ and $qd \approx 2.2$ respectively. Fig.3.7c and Fig.3.7e show the evolution of these gaps for increasing κd values. Fig.3.7g does not present this kind of gap in the frequency range shown there.

It is then quite clear that the dispersion curves of the sagittal modes show differences when compared to those of the transverse waves. The sagittal waves present in general wider gaps for intermediate and high κd values and narrow closed gaps having a variety of shapes in different ranges of values of κd and the reduced frequency. On the other hand the dispersion curves of the transverse waves present several narrow gaps starting at low values of κd and then starting at higher values of κd. They also show very narrow gaps opening at $\kappa d =0$.

It can be seen also that the behaviour shown here for the cases in which the material with higher velocity values has the bigger thickness is similar to that seen in Nougaoui et al.[26] for the [110] direction in the zinc-blende structure. In that case there are two different transverse waves propagating at different velocities like here.

The main feature of the studied superlattices is the presence of different gaps starting at nonzero κd values and going from low reduced frequency values to higher ones.

Due to the elastic isotropy of the basal plane of the hexagonal crystals it is possible to uncouple the motion of the transverse waves along the y axis from that of the sagittal modes coupling the motion along the x and z axes. We have seen that the transverse modes exhibit a series of narrow gaps starting at $\kappa d=0$ and some wider gaps starting at higher κd values. On the other hand the sagittal modes exhibit many wide and narrow gaps at different ranges of values of κd and reduced frequency. The overall image of the sagittal waves dispersion curves is quite different from that of the transverse waves. The features of the dispersion curves for each different thickness range studied here are essentially the same for all the superlattices considered in this work.

3.2 Fibonacci superlattices and other complex structures

The effects of the compositional or positional disorder on the properties of periodic structures has also been studied. One of the reasons for this interest is the localization or spatial confinement of the waves due to disorder. The

disorder can be low, intermediate or high. The highest degree of disorder is represented by the completely disordered system, where random perturbations are present [147]. The lowest degree of disorder is represented by the presence of a compositional or positional defect in the periodic structure. In this case highly localized modes may appear as very narrow bands within the gaps of the periodic structure. Because of this, these systems could be employed as frequency filters [137].

In the wide range of disordered systems the aperiodic ones are an intermediate case between the periodic and random systems. In these structures layers of, at least, two different materials can be arranged according to a given aperiodic sequence. The corresponding structures exhibit two different orders at different length scales. At the atomic level the crystalline order determined by the periodic disposition of atoms in each layer is present. On the other hand at longer scales the aperiodic order dictated by the growth of the different layers according to a given aperiodic sequence can be found. This allows to use the aperiodic order as a tool to modify different physical phenomena, with their own physical scales, by tuning the characteristic length scales. Many works have been done on the optical, electronic, vibrational and magnetic properties of aperiodic systems based on different generating sequences [148, 149, 150, 151, 152, 153].

The systems including aperiodic parts present interesting physical properties. This has been the case in the optical capabilities of aperiodic systems concerning second [154] and third harmonic generation [155], as well as localization of light in these systems [156, 157]. Hybrid-order devices formed by periodic and Fibonacci (aperiodic) blocks have been found to exhibit complementary optical responses [158]. Perfect optical transmission has been found in symmetric Fibonacci-class multilayers [159, 160]. Broad omnidirectional reflection bands have been predicted when combining Fibonacci sequences and periodic 1D photonic crystals [161]. Phonon confinement has been predicted in 1D periodic/Fibonacci structures [48, 49, 162], as well as in 1D Fibonacci systems with mirror symmetry [163, 164].

Although the full character of the aperiodic systems would be reached for very high generation orders of the different sequences, many characteristics can be obtained with lower generation orders. We shall use this approach in which we shall study different Fibonacci sequences forming the period of a superlattice.

The vibrational spectrum of aperiodic systems presents a highly fragmented character [165, 166]. By means of combinations of Fibonacci and periodic layer structures we can modify the structure of the primary and secondary gaps in the different frequency ranges. We have also an additional freedom, because we can start the Fibonacci sequence with a block A formed

by a slab of a given material followed by a block B formed by a slab of a different material , or viceversa, thus generating different layered systems.

As materials we shall consider wurtzite ZnO, MgO, GaN and AlN. All these materials are piezoelectric. In the case of materials belonging to the $6mm$ class with the C-axis parallel to the x_3 direction and the direction x_2 normal to the interface there is a decoupling between motion along the x_1 and x_2 directions and the motion along the x_3 direction, due to the symmetry [77]. We shall consider here only the transverse acoustic wave having the electric potential coupled to the elastic displacement u_3.

Although no experimental values for the electronic, elastic and piezo-electric data of MgO in the wurtzite structure are available, they can be obtained from theoretical calculations [134]. The data for ZnO are taken from [141, 167], whereas those of GaN and AlN are taken from [140, 168].

We shall study the transverse acoustic waves of Fibonacci superlattices of the above materials. We shall consider also the cases of more complex superlattices including Fibonacci and periodic parts.

We shall consider superlattices formed by the periodic repetition of material blocks according to the Fibonacci sequence. The A block is formed by layers of material 1, in our case: ZnO and GaN, respectively. The B block is formed by layers of material 2, in our case: MgO and AlN, respectively.

A finite Fibonacci generation is produced by recursive stacking with these A and B blocks, mapping the mathematical rule in the Fibonacci sequence

$$S_1 = \{A\} \ , \ \ S_2 = \{AB\} \ , \ \ S_3 = \{ABA\} \ , \ \ S_4 = \{ABAAB\} \ , \cdots , \ \ S_n = S_{n-1}S_{n-2} \ ,$$
$$(3.2)$$

or

$$\bar{S}_1 = \{B\} \ , \ \ \bar{S}_2 = \{BA\} \ , \ \ \bar{S}_3 = \{BAB\} \ , \ \ \bar{S}_4 = \{BABBA\} \ , \cdots , \ \ \bar{S}_n = \bar{S}_{n-1}\bar{S}_{n-2} \ ,$$
$$(3.3)$$

We shall consider also more complex superlattice systems formed by combining different Fibonacci sequences and hybrid systems including a given Fibonacci generation together with a finite periodic repetition of blocks AB (BA). All the superlattices considered here are obtained by stacking the material layers along the x_2 axis. A schematic view of the systems is presented in Fig.2.5. There we show the layers of the constituent materials together with the axes orientation and thicknesses. The crystal axes of all the materials forming the superlattices are aligned. Taking into account the transverse elastic isotropy of the hexagonal crystals we have to consider only the absolute value κ of the parallel wavevector $\vec{\kappa}$ in the interfaces.

We shall assume that the thicknesses of the different layers are $d_1(ZnO)$ = $d_1(GaN)$ = 1.7 nm, and $d_2(MgO)$ = $d_2(AlN)$ = 4.2 nm. We choose these values because they are equal to those of the first Fibonacci superlattices grown experimentally [169]. The superlattice period is $d = d_1 + d_2$. It is easy to see that in this case $d_1 = 0.29\, d$ and $d_2 = 0.71\, d$.

In Table 3.2 we give the mass densities, elastic, dielectric and piezoelectric coefficients , together with the velocities of the transverse acoustic waves for the materials considered here.

Table 3.2: Elastic, dielectric and piezoelectric constants and mass densities for ZnO [141, 167], MgO [134], GaN [140, 168] and AlN [140, 168] and the velocities of the transverse acoustic waves obtained from these data.

Material	C_{44} (GPa)	ϵ_{11} (10^{-11} F m^{-1})	e_{15} (C m^{-2})	ρ (10^3 kg m^{-3})	v_t (10^3 m s^{-1})
ZnO	42.5	7.38	.0.37	5.606	2.813
MgO	59.0	8.766	-0.428	3.6	4.119
GaN	105.0	8.58	-0.3	6.156	4.150
AlN	116.0	7.52	-0.48	3.255	6.048

We shall consider now the dispersion relation of the transverse acoustic waves of Fibonacci superlattices and other more complex superlattices whose periods are formed by Fibonacci generations and periodic parts. The period length of these systems will be quite different, due to its dependence on the number of A and B blocks.

We shall work with the reduced parallel wavevector κD and the reduced frequency $\dfrac{\omega D}{v_M}$, v_M being an average velocity as that of the classical binary superlattice [170], given by

$$v_M = \frac{v_1 v_2 D}{v_1 d_2 + v_2 d_1} \ , \tag{3.4}$$

which reflects the inner structure of the supercell modulation.

This can be generalized to the case of more complicated structures having N_1 layers of material 1 and N_2 layers of material 2, thus giving

$$v_M = \frac{v_1 v_2 D}{v_1 D_2 + v_2 D_1} \ , \tag{3.5}$$

being $D_1 = N_1 d_1$, $D_2 = N_2 d_2$ and $D = D_1 + D_2$.

We shall present in the following results for the second, third, fourth and fifth generation Fibonacci superlattice, in order to see the evolution of the

dispersion curves with increasing order generation. We must note that the second order Fibonacci generation, having AB as period, is nothing more than the classical superlattice. In the same way the third order Fibonacci generation, having as period AAB or BBA is also a normal superlattice having A or B layers with double thickness.

Fig.3.8a presents the dispersion curves of the transverse acoustic waves of a ZnO/MgO second generation Fibonacci superlattice. Fig.3.8b, 3.8c and 3.8d give the dispersion curves for superlattices having as periods a third, fourth and fifth Fibonacci generation, respectively.The first gap opens at κD=0 at $\omega D/v_M \sim 3$, but is very narrow and it is not seen at the scale of the figure. We can see in all the cases a wide second gap quite wide at non-zero κD values. There are higher gaps of similar characteristics. It can be seen that for the second and third generations the second gap is wide at higher κD values than the first one. On the other hand for periods formed by higher order generations the second gap is wide at lower κD values than the first one. The fifth generation exhibits all the features found in the dispersion curves of higher order generation periods. We have calculated also the dispersion curves neglecting the piezoelectric coupling. We have found no important changes in the dispersion curves. This is also true for all other systems studied in this work. Nevertheless, in the case of piezoelectric materials the inclusion of the piezoelectric coupling is mandatory to get the transverse surface waves [77, 171] and the transverse interface waves [172].

Fig.3.9a presents the dispersion curves of the transverse acoustic waves for a MgO/ZnO (BA) second generation Fibonacci superlattice (obviously coinciding with the periodic superlattice). Fig.3.9b, 3.9c and 3.9d give the dispersion curves for superlattices having as periods a third, fourth and fifth Fibonacci generation, respectively. We can see here changes due to the different ordering of the A and B blocks. Now we have BB pairs instead of AA ones. We see now that from the third generation onwards there is a closed and narrow gap just above the lower and wide gap. We observe also that a new feature appears from the fourth generation onwards. This is a closed and very narrow gap in the bands above the lower wide gap seen before. The higher gaps are narrower than those found in Fig.3.8 for the AB ordering. As before the fifth generation exhibits all the features found in higher order generation periods. We see here that the lower wide gap is not divided in parts by narrow bands as those appearing in Figure 3.8 for increasing order of periods.

Fig.3.10a presents the dispersion curves of the transverse acoustic waves for a GaN/AlN (AB) second generation superlattice. Fig.3.10b, 3.10c and 3.10d give the dispersion curves for superlattices having as periods a third, fourth and fifth Fibonacci generation respectively. In this case we see that we

have reasonably wide gaps opening at κD=0, for different frequency ranges. From the fourth generation onwards we see that the first gap starting at κD=0 becomes narrower and is only visible at non-zero κD values. The fifth generation exhibits all the features found in higher order generation periods.

Fig.3.11a presents the dispersion curves of the piezoelectric transverse acoustic waves for an AlN/GaN (BA) second generation superlattice. Fig.3.11b, 3.11c and 3.11d give the dispersion curves for superlattices having as periods a third, fourth and fifth Fibonacci generation respectively. In this case we see a similar situation to that found in Fig.3.9 for the MgO/ZnO (BA) system. From the fourth generation onwards there is a first closed gap opening at zero κD values above the first gap.

Due to the differences seen in the dispersion curves of the sequences ordered following the AB or BA stacking in the Fibonacci rule, it is reasonable to look for the changes introduced in the dispersion curves when combining Fibonacci sequences with both ordering schemes. This is presented in Fig.3.12 for the ZnO/MgO system. Fig.3.12a shows the dispersion curves of the piezoelectric transverse acoustic waves for the $ABBA$ system (second generations). This corresponds to a normal superlattice having double period. Fig.3.12b, 3.12c and 3.12d give the dispersion curves for superlattices with periods formed by joining both stackings of the fourth, fifth and sixth Fibonacci generations, respectively. The case corresponding to the third generation would be $ABABAB$ and corresponds to the binary superlattice stacking. In all the cases we see several lower gaps being wide at non-zero κD values and narrow higher gaps with closed form.

As it has been quoted before, the mixing of Fibonacci aperiodic blocks together with periodic blocks opens the possibility for new features in the dispersion relations of the acoustic waves in multilayer systems.

In Fig.3.13 we present the dispersion curves of a superlattice having as constituents a ZnO/MgO fourth Fibonacci generation and a single ZnO/MgO block, with different orderings. Fig.3.13a corresponds to to the $ABAAB/AB$ case. Fig.3.13b illustrates the $ABAAB/BA$ case. Fig.3.13c corresponds to the $BABBA/AB$ case and Fig.3.13d to the $BABBA/BA$ case. We can see that the region of the lower gaps is quite different in all the cases considered. We must compare with the dispersion curves of Fig.3.8c and Fig.3.9c corresponding to the fourth Fibonacci generation $ABAAB$ and $BABBA$ respectively, in order to see the changes introduced. Fig.3.13a shows only small differences when compared with Fig.3.8c. This can be easily understood because the additional AB block does not introduce any substantive change to the structure. On the other hand the BB block introduced in the superlattice corresponding to Fig.3.13b was not present in the original structure. The differences introduced in the dispersion curves for the lower frequencies are clear

and important, showing a wider first gap than in Fig.3.8c. Fig.3.13c when compared with Fig.3.9c shows important differences due to the presence of the AA pair not present in the fourth Fibonacci generation $BABBA$. We see now that the first gap is substituted by three narrower gaps. Fig.3.13d shows not important differences when compared to Fig.3.9c, because no new pairs are introduced in the structure.

The same is true for the GaN/AlN systems represented in Fig.3.14. Fig.3.14a and Fig.3.14d show almost no differences with Fig.3.10c and Fig.3.11c, respectively, for the reasons discussed above. In Fig.3.14b we can see a wide first gap starting at κD=0, than the one present in Fig.3.10c. It is clear there that the two lower gaps are quite different in both cases. This is due to the presence of the BB pair in the structure. In Fig.3.14c we see the influence of the AA pair in the narrow bands that appear now in the region of the first gap seen in Fig.3.11c.

In Fig.3.15 we present the case of a GaN/AlN superlattice whose period is formed by blocks $(ABAB)$ or $(BABA)$ sandwiched between two fourth order Fibonacci generations. In this way we have four material slabs in the periodic part and five material slabs in the aperiodic one. We can see now differences in the lower gaps region of Fig.3.15b and Fig.3.15c when compared with Fig.3.10c and Fig.3.11c respectively, for the reasons discussed above. In the same way there are not important differences in Fig.3.15a and Fig.3.15d when compared to Fig.3.10c and Fig.3.11c, respectively.

Fig.3.16 presents a complementary case in which the period is formed by the fourth Fibonacci generation sandwiched between two AB or BA blocks respectively. The results are analogous to those of Figure 3.15.

In the different superlattices studied here very narrow bands for fixed κD values, are present, thus indicating the existence of flat, or almost flat, bands. We shall illustrate this in Figure 3.17 for the case of the dispersion curves of Fig.3.12c at $\kappa D = 26.0$. Fig.3.17 gives the dispersion curves as a function of the superlattice reduced normal wavevector qD. We see some flat bands at different frequency ranges.

(a)   (b)

(c)   (d)

(e)   (f)
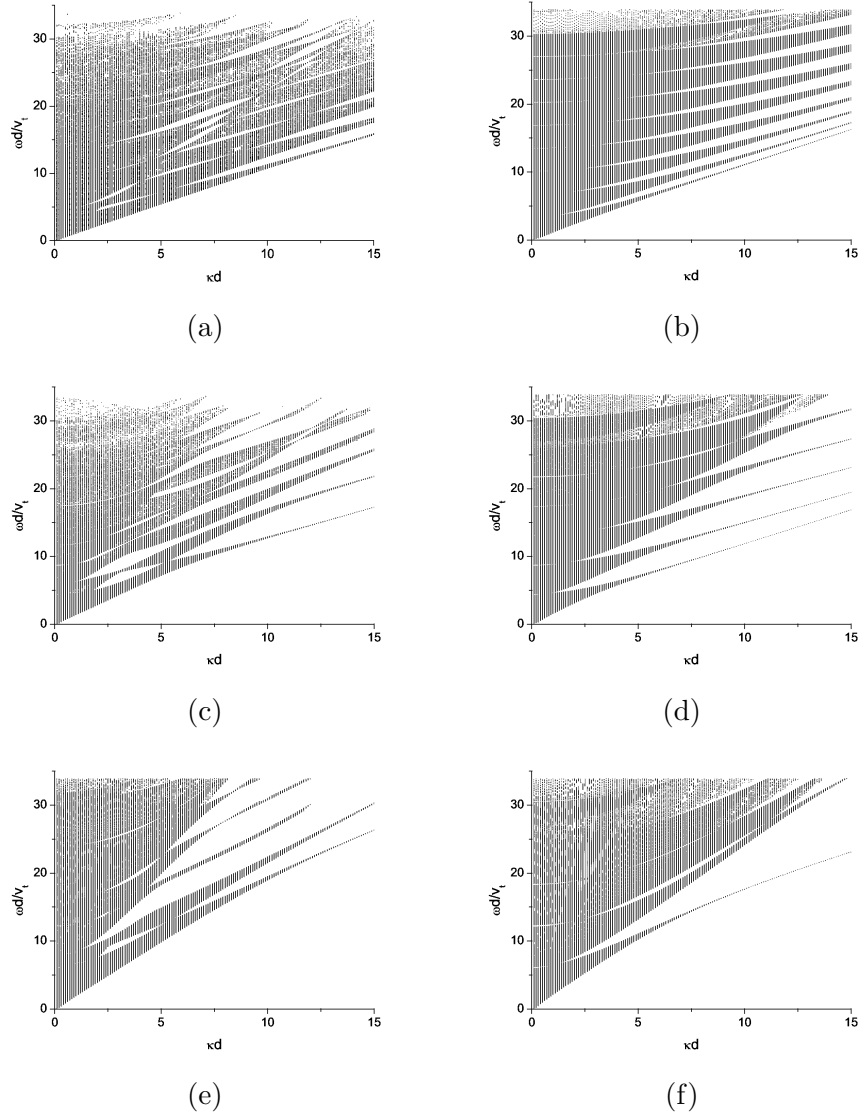
Figure 3.1:   Dispersion curves of the acoustic waves of a (0001) AlN/InN superlattice with: (a) sagittal, (b) transverse for d_1(AlN)=0.125d and d_2(InN)=0.875d;   (c) sagittal,   (d) transverse   for d_1(AlN)=0.5d and d_2(InN)=0.5d; (e) sagittal, (f) transverse for d_1(AlN)=0.875d and d_2(InN)=0.125d.

(a)   (b)

(c)   (d)

(e)   (f)
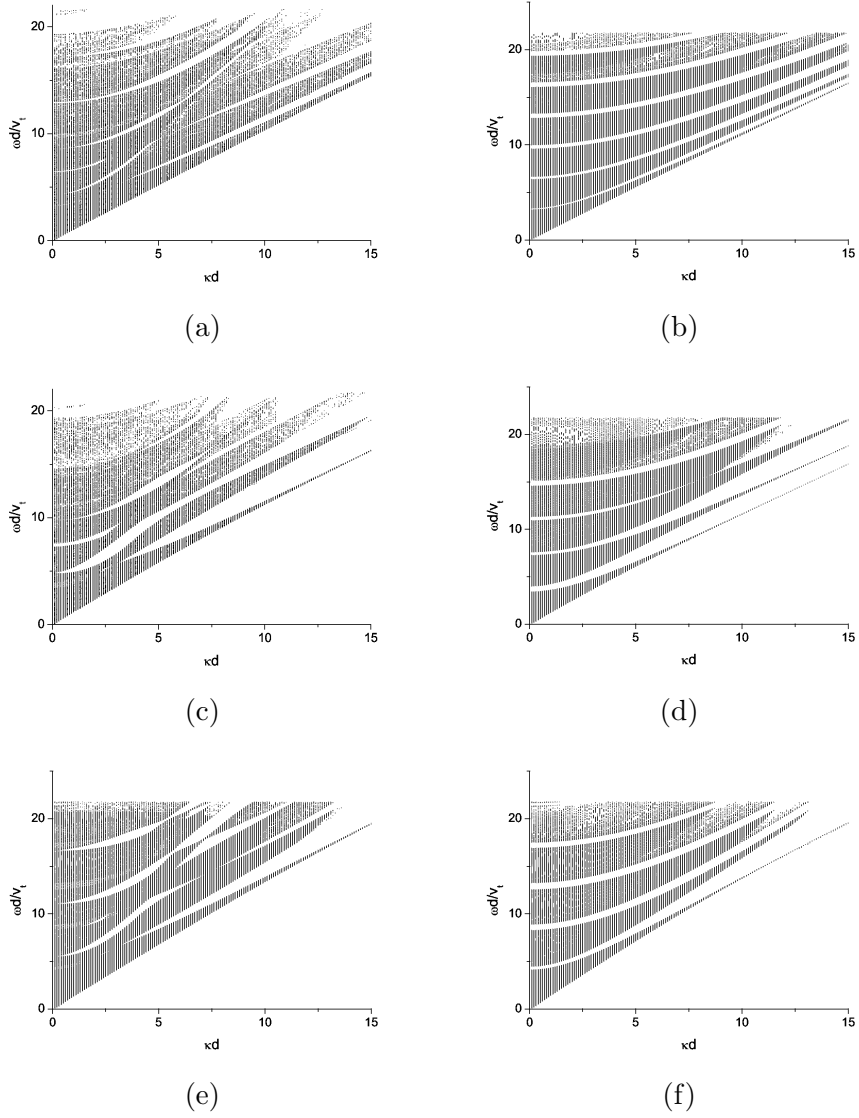
Figure 3.2: Dispersion curves of the acoustic waves of a (0001) AlN/GaN superlattice with: (a) sagittal, (b) transverse for d_1(AlN)=0.125d and d_2(GaN)=0.875d; (c) sagittal, (d) transverse for d_1(AlN)=0.5d and d_2(GaN)=0.5d; (e) sagittal, (f) transverse for d_1(AlN)=0.875d and d_2(GaN)=0.125d.
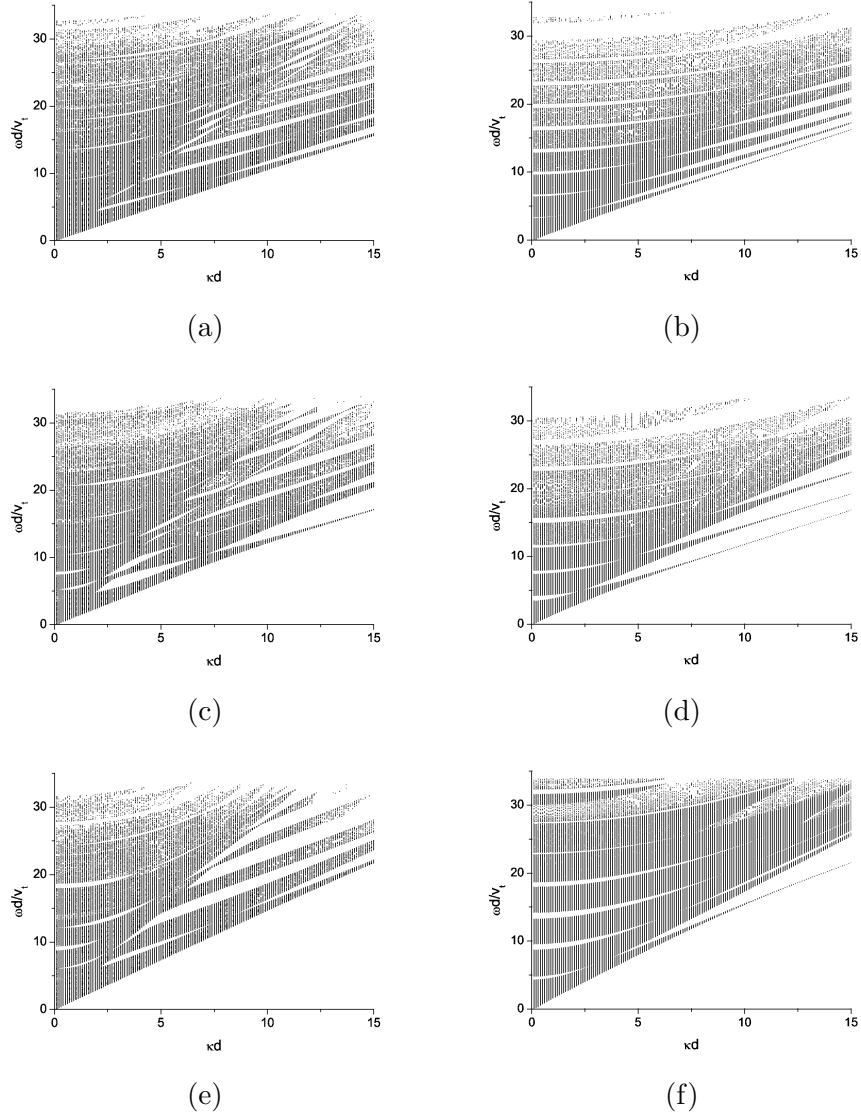
Figure 3.3: Dispersion curves of the acoustic waves of a (0001) GaN/InN superlattice with: (a) sagittal, (b) transverse for d_1(GaN)=0.125d and d_2(InN)=0.875d; (c) sagittal, (d) transverse for d_1(GaN)=0.5d and d_2(InN)=0.5d; (e) sagittal, (f) transverse for d_1(GaN)=0.875d and d_2(InN)=0.125d.
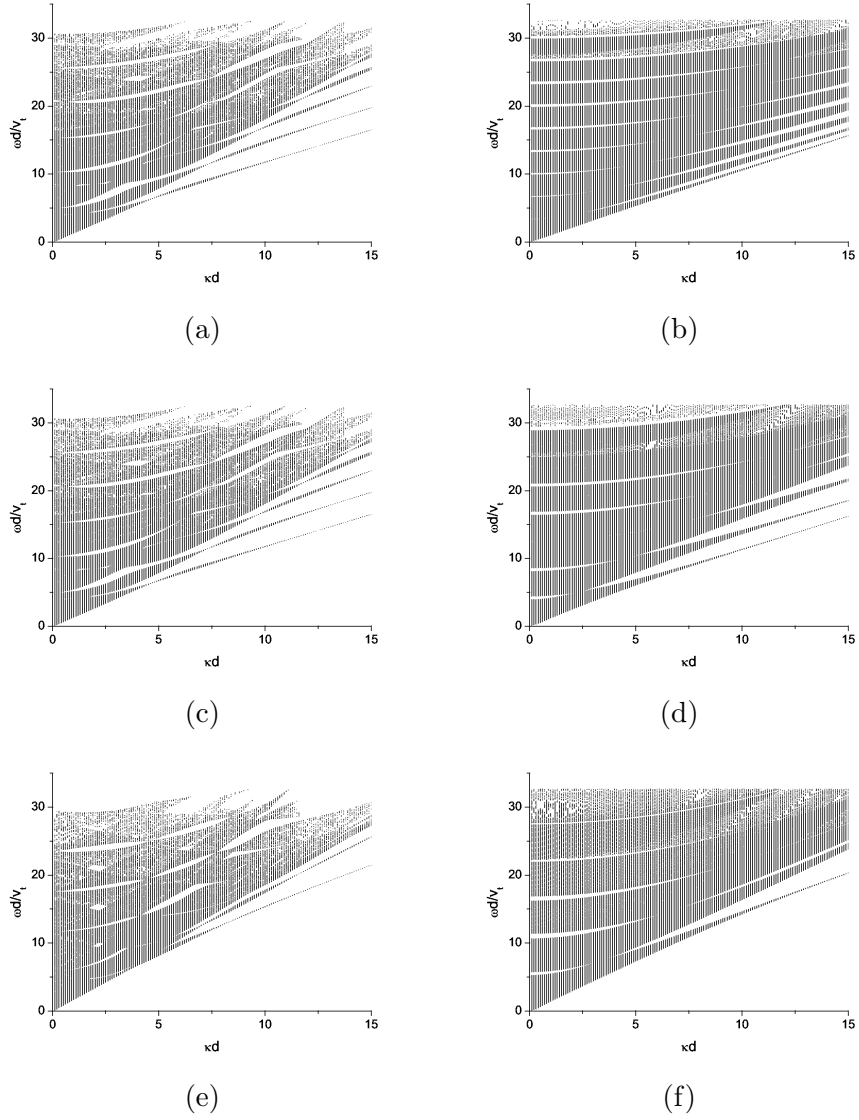
Figure 3.4: Dispersion curves of the acoustic waves of a (0001) MgO/ZnO superlattice with the MgO elastic coefficients given in Gopal et al. [133] and: (a) sagittal, (b) transverse for d_1(MgO)=0.125d and d_2(ZnO)=0.875d; (c) sagittal, (d) transverse for d_1(MgO)=0.5d and d_2(ZnO)=0.5d; (e) sagittal, (f) transverse for d_1(MgO)=0.875d and d_2(ZnO)=0.125d.
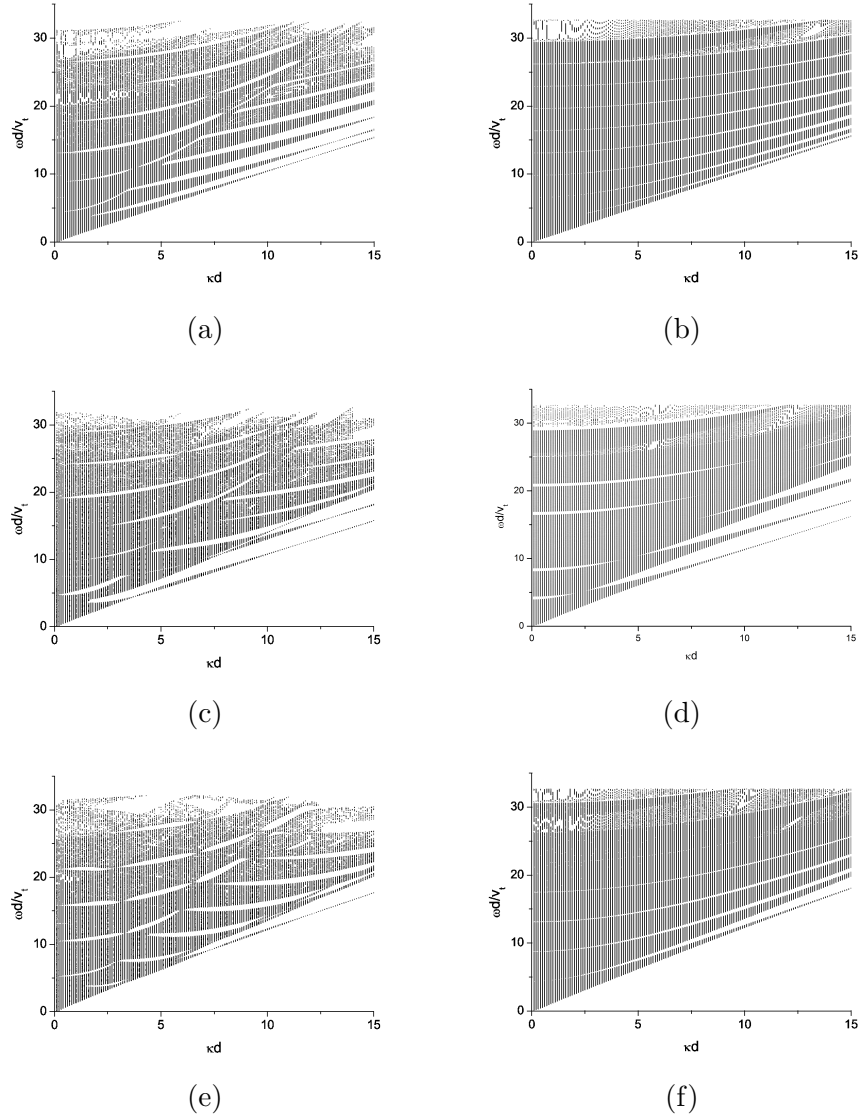
Figure 3.5: Dispersion curves of the acoustic waves of a (0001) MgO/ZnO superlattice with the MgO elastic coefficients given in Duan et al. [134] and: (a) sagittal, (b) transverse for d_1(MgO)=0.125d and d_2(ZnO)=0.875d; (c) sagittal, (d) transverse for d_1(MgO)=0.5d and d_2(ZnO)=0.5d; (e) sagittal, (f) transverse for d_1(MgO)=0.875d and d_2(ZnO)=0.125d.

(a)

(b)

(c)
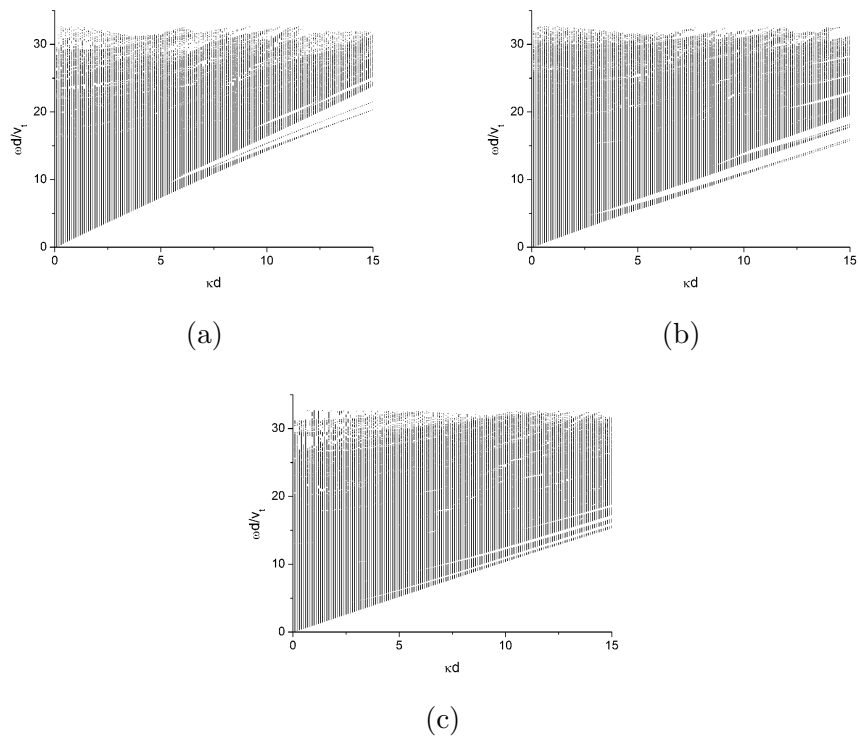
Figure 3.6: Dispersion curves of the acoustic waves of a (0001) MgO/ZnO superlattice with the MgO elastic coefficients given in Duan et al. [134] and: (a) d_1(MgO)=0.125d and d_2(ZnO)=0.875d; (b) d_1(MgO)=0.5d and d_2(ZnO)=0.5d; (c) d_1(MgO)=0.875d and d_2(ZnO)=0.125d.

(a)

(b)

(c)

(d)

(e)

(f)

(g)

(h)
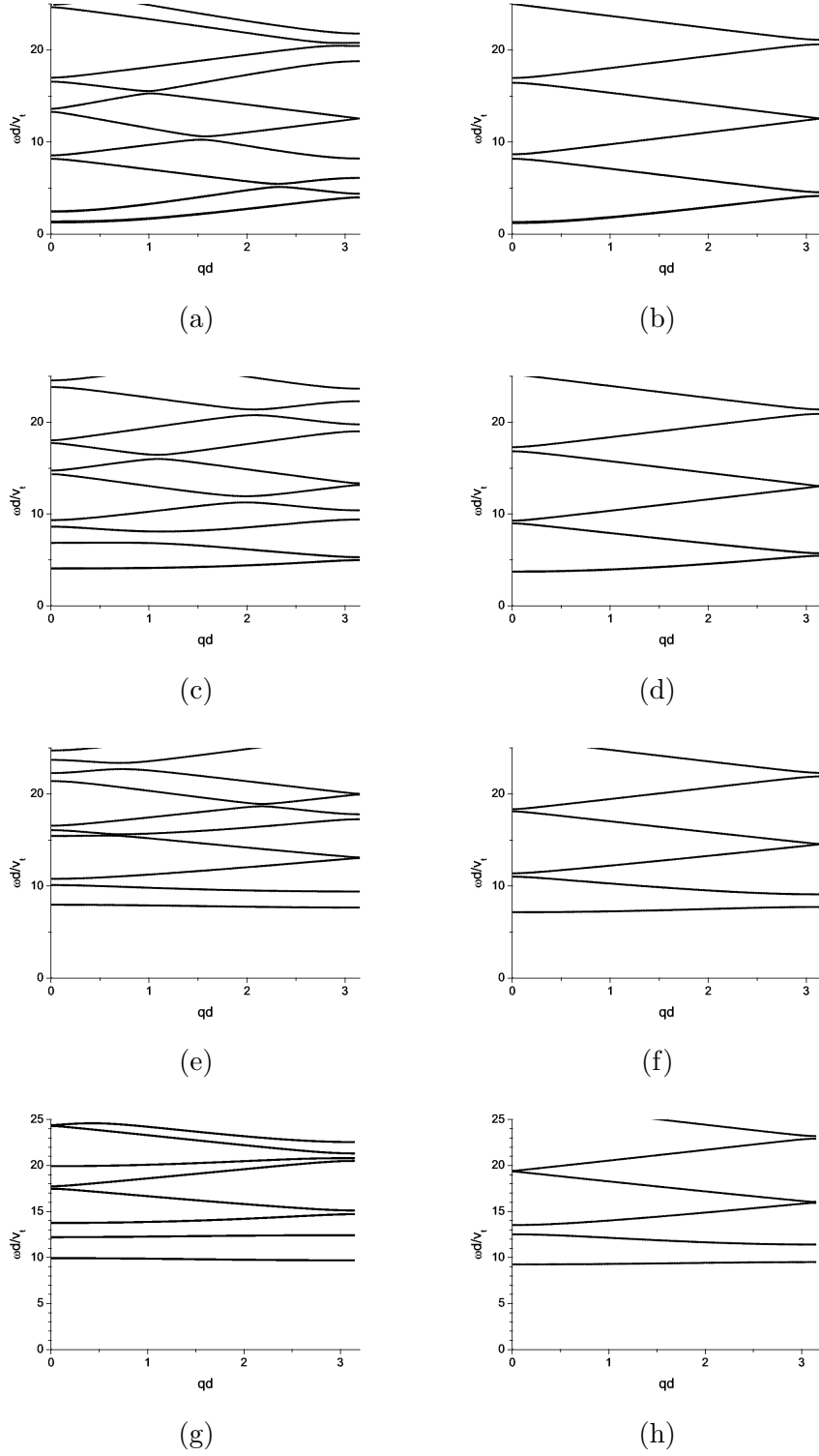
Figure 3.7: Normalized frequencies $\omega d/v_t$ versus qd of the acoustic waves of a (0001) MgO/ZnO superlattice with the MgO elastic coefficients given in Gopal et al. [133] having d_1(MgO)=d_2(ZnO)=0.5d: (a) sagittal, (b) transverse for κd=1; (c) sagittal, (d) transverse for κd=3; (e) sagittal, (f) transverse for κd=6; (g) sagittal, (h) transverse for κd=8.

(a)

(b)

(c)

(d)
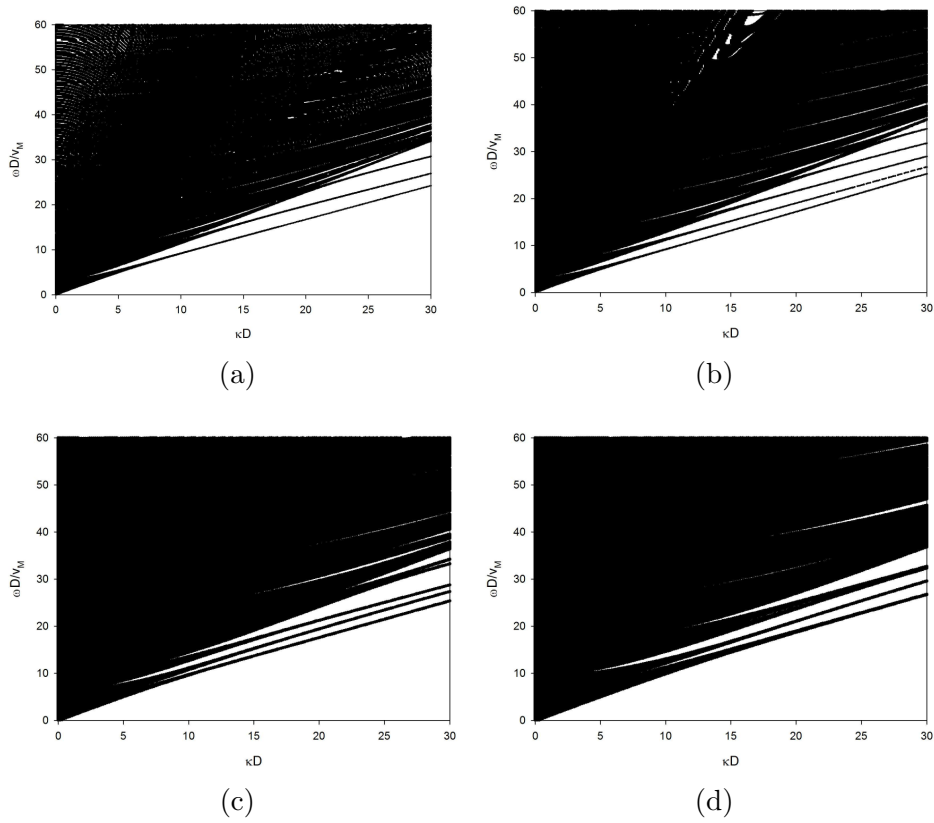
Figure 3.8: Dispersion curves of the transverse acoustic waves of a ZnO/MgO superlattice having as period: (a) a second Fibonacci generation; (b) a third Fibonacci generation; (c) a fourth Fibonacci generation; (d) a fifth Fibonacci generation.

(a)

(b)

(c)

(d)
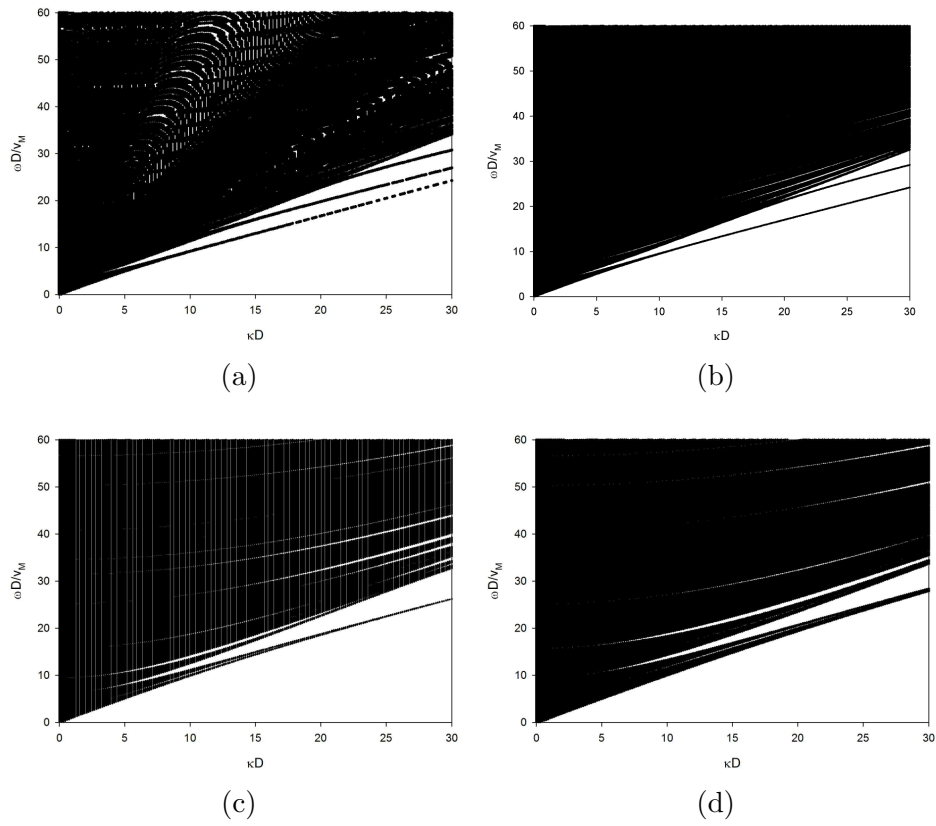
Figure 3.9: Same as Figure 3.8 for a MgO/ZnO (BA) superlattice.
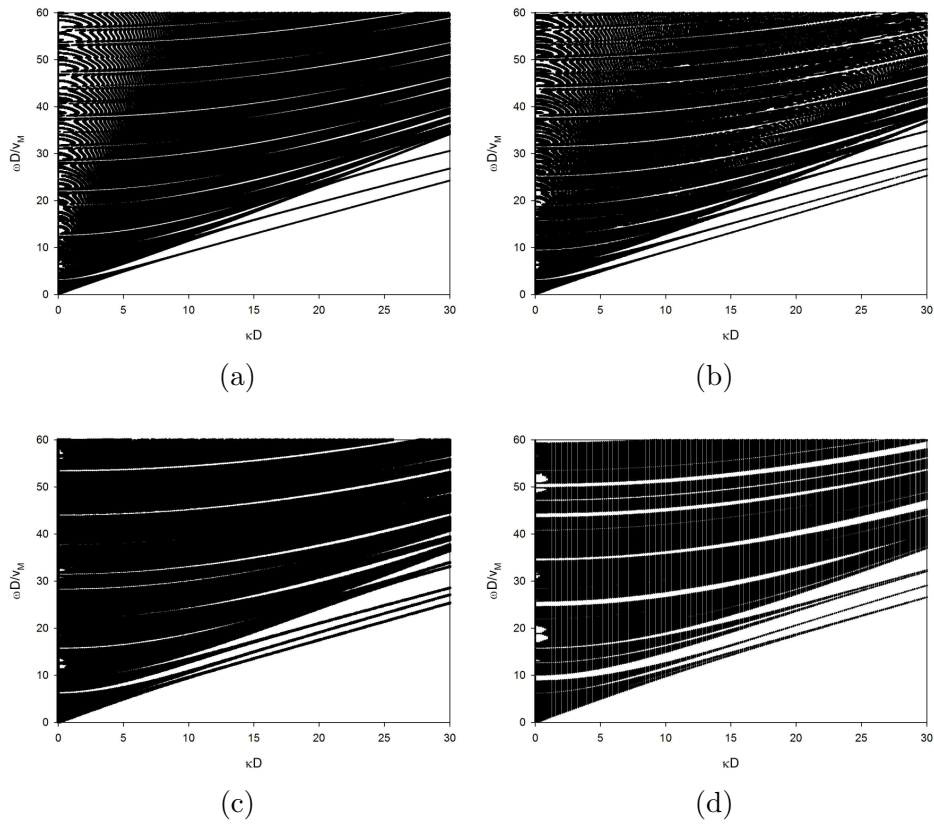
Figure 3.10: Same as Figure 3.8 for a GaN/AlN (AB) superlattice.

(a)

(b)

(c)

(d)
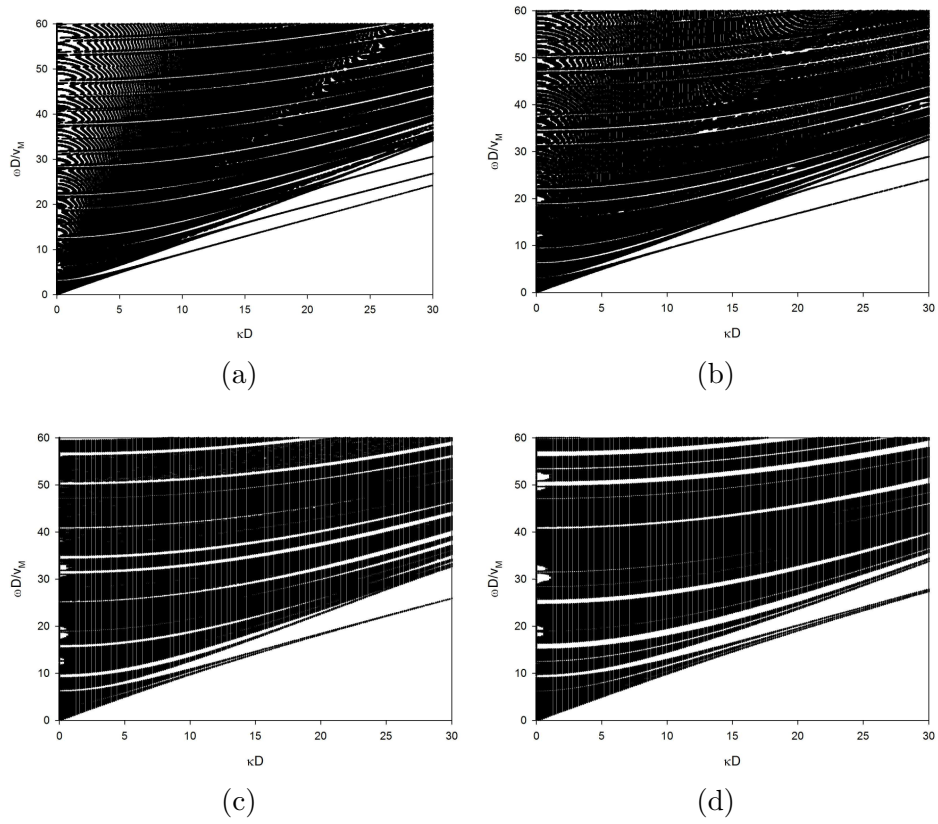
Figure 3.11: Same as Figure 3.8 for an AlN/GaN (BA) superlattice.
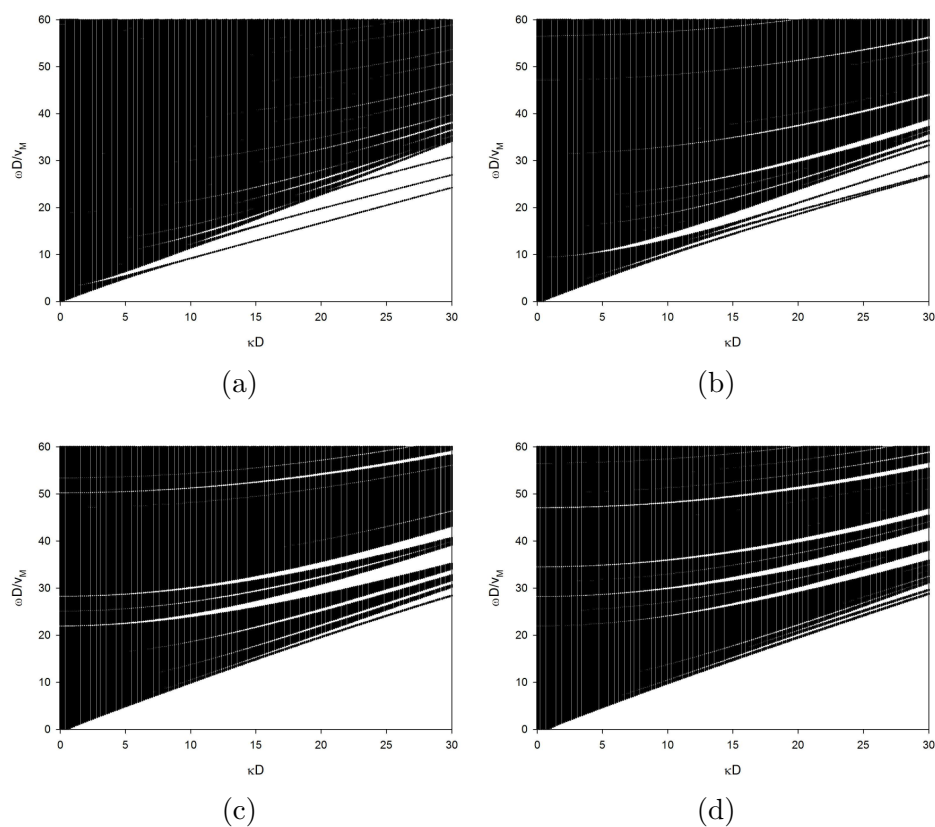
Figure 3.12: Dispersion curves of the transverse acoustic waves of ZnO/MgO superlattices having as periods $(AB...|BA...)$ blocks of: (a) a second Fibonacci generation; (b) a fourth Fibonacci generation; (c) a fifth Fibonacci generation; (d) a sixth Fibonacci generation.
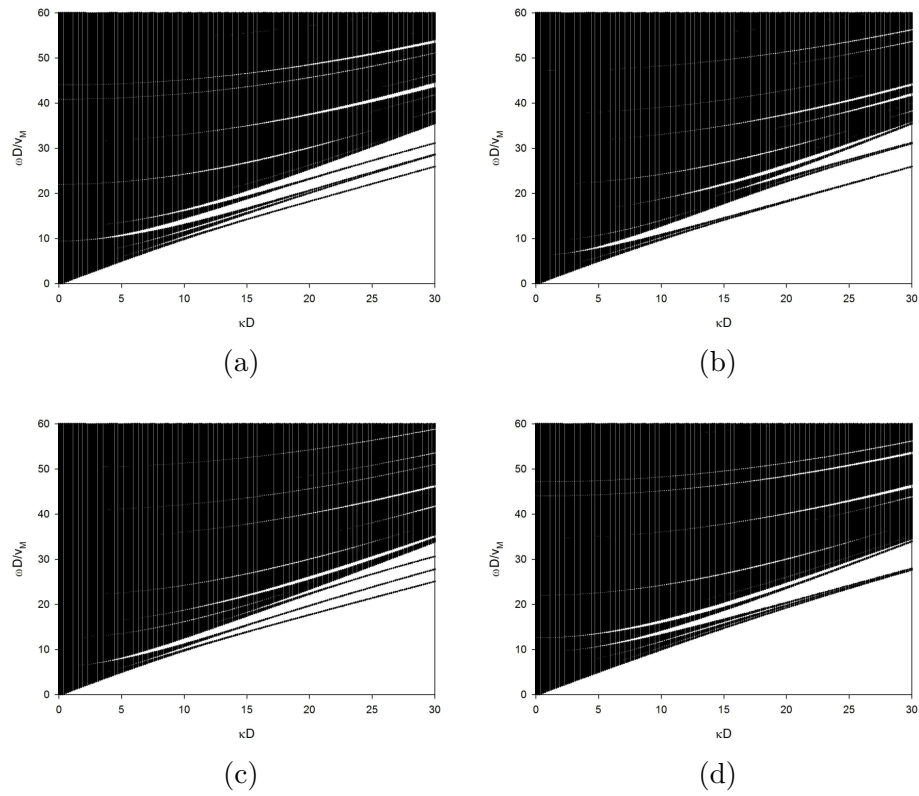
Figure 3.13: Dispersion curves of the transverse acoustic waves of ZnO/MgO superlattices having as periods the following stacking of layers: (a) $ABAAB|AB$; (b) $ABAAB|BA$; (c) $BABBA|AB$; (d) $BABBA|BA$.
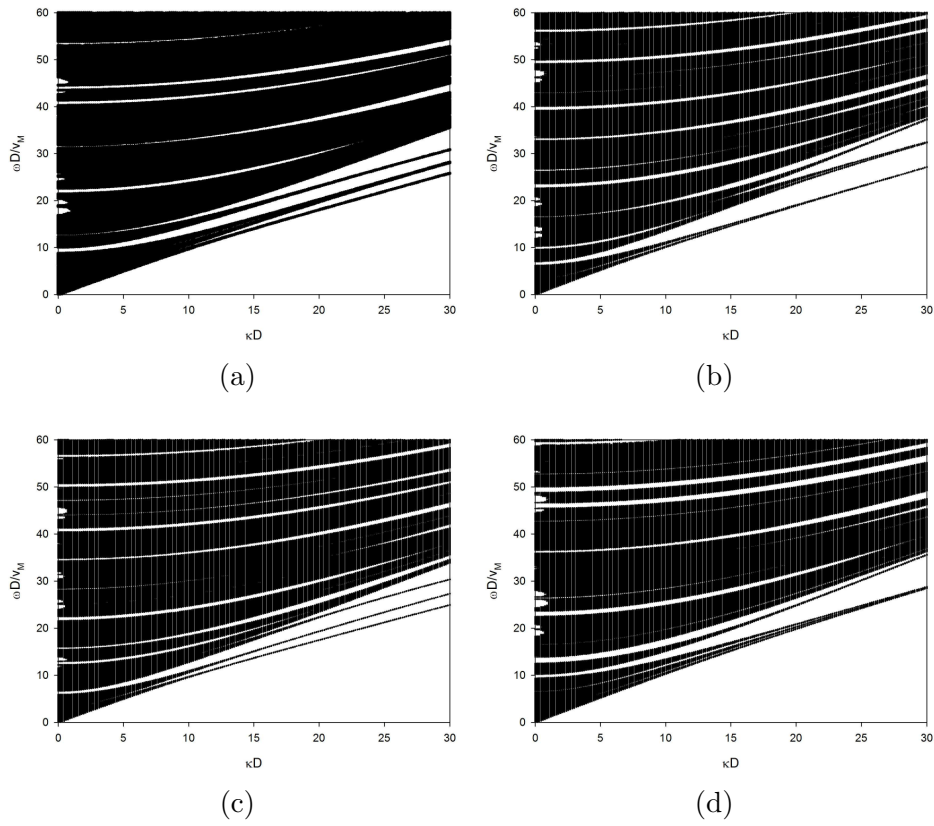
Figure 3.14: Same as Figure 3.13 for a GaN/AlN system.

(a)

(b)

(c)

(d)
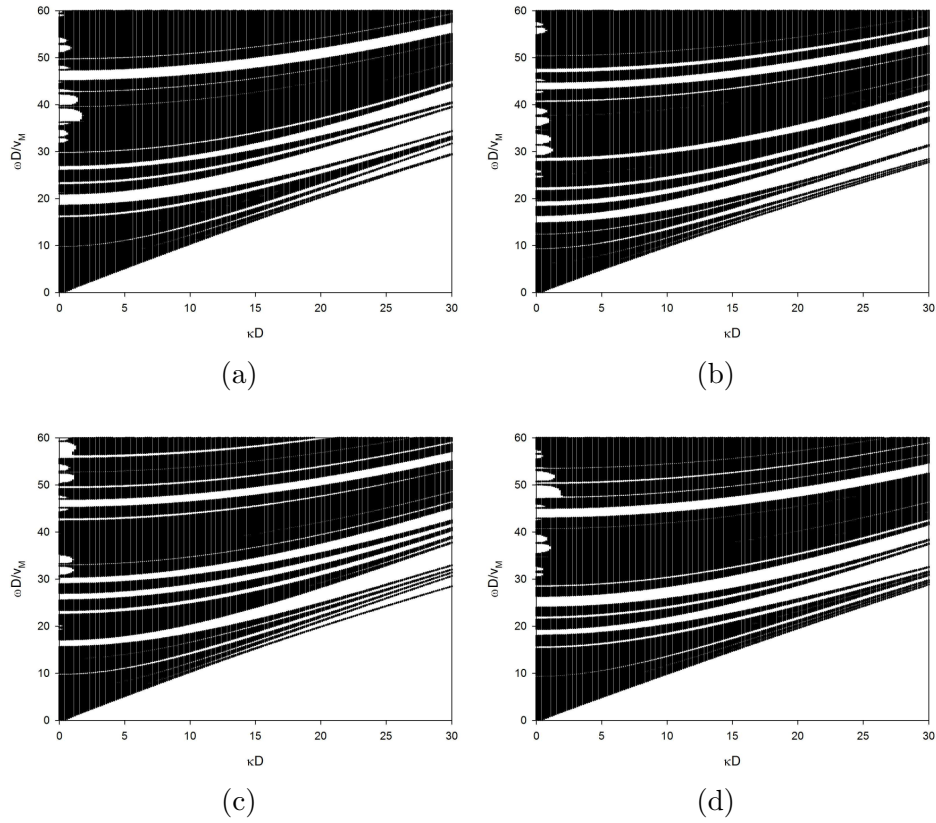
Figure 3.15:   Dispersion curves of the transverse acoustic waves of GaN/AlN superlattices having as periods the following stacking of layers: (a) $ABAAB|ABAB|ABAAB$; (b) $ABAAB|BABA|ABAAB$; (c) $BABBA|ABAB|BABBA$; (d) $BABBA|BABA|BABBA$.

(a)

(b)

(c)

(d)
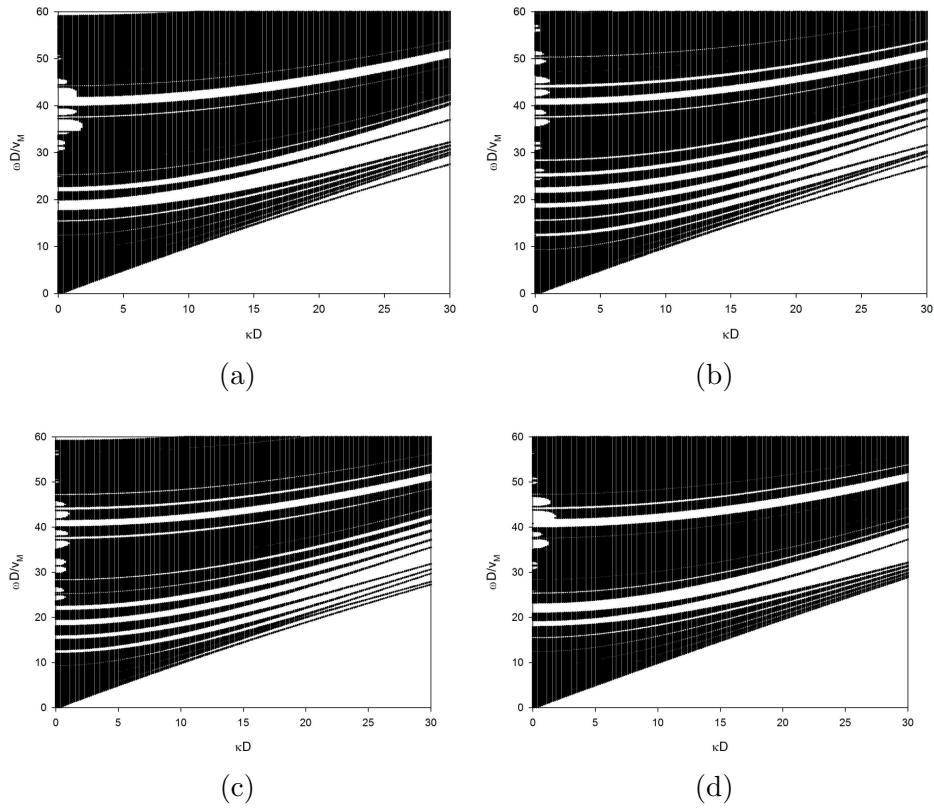
Figure 3.16: Dispersion curves of the transverse acoustic waves of GaN/AlN superlattices having as periods the following stacking of layers: (a) $ABAB|ABAAB|ABAB$; (b) $ABAB|BABBA|ABAB$; (c) $BABA|ABAAB|BABA$; (d) $BABA|BABBA|BABA$.
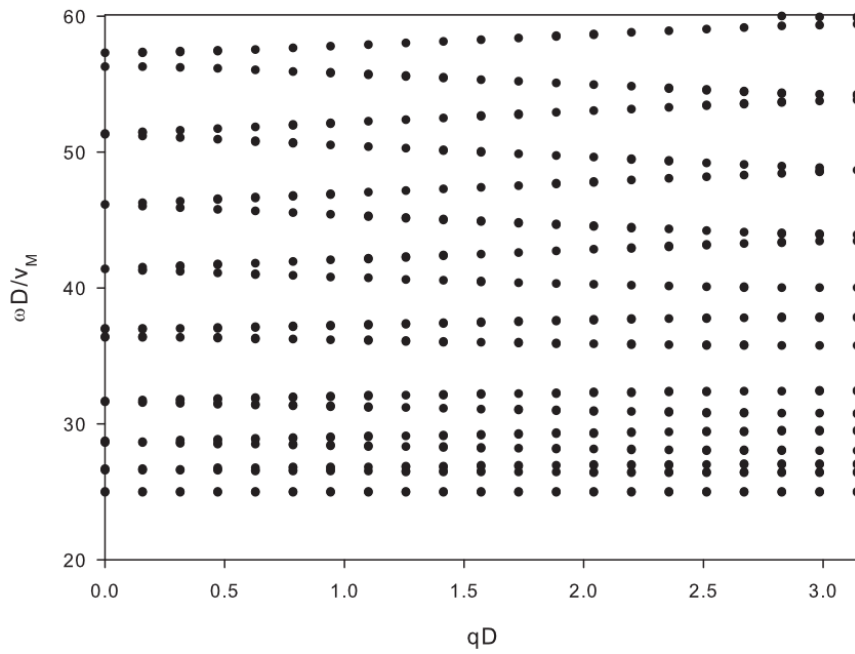
Figure 3.17: Dispersion curves of the transverse acoustic waves of ZnO/MgO superlattices having as periods $ABAABABA|BABBABAB$, for κD=26.0.
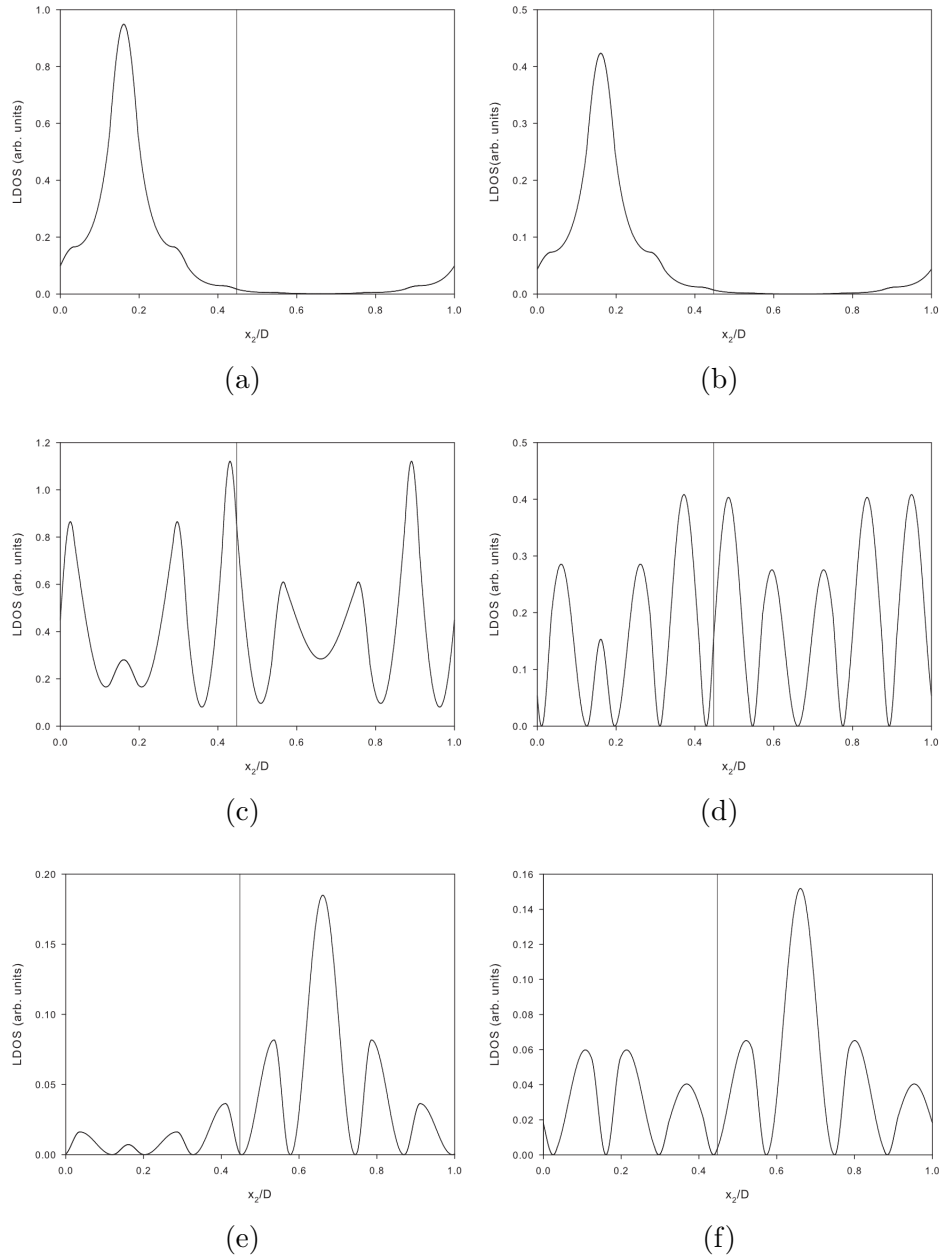
Figure 3.18: Local density of states along the superlattice period-length for several modes of those presented in Fig.3.17: (a) ($\frac{\omega D}{v_M}$=25.02, qD=0); (b) ($\frac{\omega D}{v_M}$=25.02, qD=π); (c) ($\frac{\omega D}{v_M}$=31.68, qD=0); (d) ($\frac{\omega D}{v_M}$=40.02, qD=π); (e) ($\frac{\omega D}{v_M}$=36.42, qD=0); (f) ($\frac{\omega D}{v_M}$=35.76, qD=π). The vertical line gives the position of the interface separating both fifth Fibonacci generations ($S_5|\bar{S}_5$) forming the superlattice period.

We shall look now at the spatial distribution of the spectral strength, represented by the local density of states (LDOS as a function of x_2/D), of some of the modes represented in Fig.3.17. This is obtained from the superlattice Green function $\mathbf{G}_S(\kappa, q, x_2, x_2', \omega^2))$ [43, 39]. Fig.3.18 gives this information for the following modes: (a) ($\frac{\omega D}{v_M}$=25.02, qD=0); (b) ($\frac{\omega D}{v_M}$=25.02, qD=π); (c) ($\frac{\omega D}{v_M}$=31.68, qD=0); (d) ($\frac{\omega D}{v_M}$=40.02, qD=π); (e) ($\frac{\omega D}{v_M}$=36.42, qD=0); (f) ($\frac{\omega D}{v_M}$=35.76, qD=π). We see that the lower frequency modes at the center and border of the Brillouin zone are confined to the domain of the $(AB\cdots)$ block in the superlattice period. We can see also that they are essentially localized in the AA zone corresponding to 0.125$\leq x_2/D \leq$0.197. There are intermediate frequency modes extended along the whole period. On the other hand we find also intermediate frequency modes predominantly confined to the domain of the $(BA\cdots)$ block in the superlattice period. In this case they are mainly localized in the BB zone corresponding to 0.57$\leq x_2/D \leq$0.75. Thus we see that in some of the systems analysed here there are flat or very narrow bands and that for some modes there exists the spatial confinement of the elastic displacement and the electric potential in the different parts of the total superlattice period.

We have found that by using the two kinds $(AB\cdots)$ and $(BA\cdots)$ of Fibonacci sequences we can modify the structure of the lower gap regions for the acoustic waves of the superlattice structures and materials considered here. Some modes are spatially confined in different parts of the superlattice period.

We have seen in this case that the possibility to use $(AB\cdots)$ and $(BA\cdots)$ Fibonacci sequences including AA and BB pairs allows for important modifications of the lower gaps region. It is possible to introduce narrow and flat bands that divide the original gaps in narrower ones. We have found modes at different frequency ranges having spatial confinement in one of the constituent parts of the superlattice period. This opens the possibility for their employ in frequency filters. The case of transverse acoustic waves propagating along symmetry directions of (100) and (110) interfaces of piezoelectric materials belonging to the cubic system is governed by equations similar to those of the hexagonal crystals studied here. Thus we can expect similar results to those presented here for analogous structures of cubic crystals.

3.3 Nanowire discussion

Nanowires are important for many applications. First, nanowires can be used as nanotechnology building blocks to reach higher device integration densities than conventional fabrication methods. Second, they have high interest for thermoelectric applications (energy transport by phonons deteriorate the performance) as the thermal conductivity shown in such materials can be drastically reduced compared with bulk. This large reduction in thermal conductivity was attributed to enhanced scattering of phonons on the surfaces of the nanochannels [173].

Vibrational properties are very important for the development of nanotechnological devices. For example, phonon scattering is an important feature for all sorts of electronic devices. It is then clear that the vibrational properties of nanowires are very important. In recent years nanowires of different materials have been grown in several laboratories by different techniques. They exhibit different forms; cylinders, square, rectangular and hexagonal prisms. Due to the dispersion of growth techniques, the quality of the samples varies greatly. Because of these problems and in order to obtain the maximum of general information for the different systems at a reasonable computational cost, we shall start our study by using of the elasticity theory. These results will be supplemented for Si/Ge systems with the Molecular Dynamics method.

Because the breathing modes provide a characteristic signature in spectroscopy for the nanowires, we shall devote part of the study to these modes in different materials.

3.4 Elastic waves in nanowires

In order to deal with nanowires of elastically anisotropic crystals and different cross-sections a theoretical method originally developed in resonant ultrasound spectroscopy to obtain the free vibrational modes of inhomogeneous objects [31, 32, 33, 34] can be used. Recent developments can be found in [35, 36, 37, 38]. The method studies the free vibrations of elastic anisotropic systems having arbitrary shape and mass density variation, thus being quite adequate for the present case. This is performed by expanding the elastic displacements in terms of a set of basis functions that are products of powers of the Cartesian coordinates, being then called the *xyz-algorithm*. The method has been applied to the study of acoustic modes in rectangular wires [23] and CNTs [37].

In order to illustrate how the different cross-sections affect the elastic
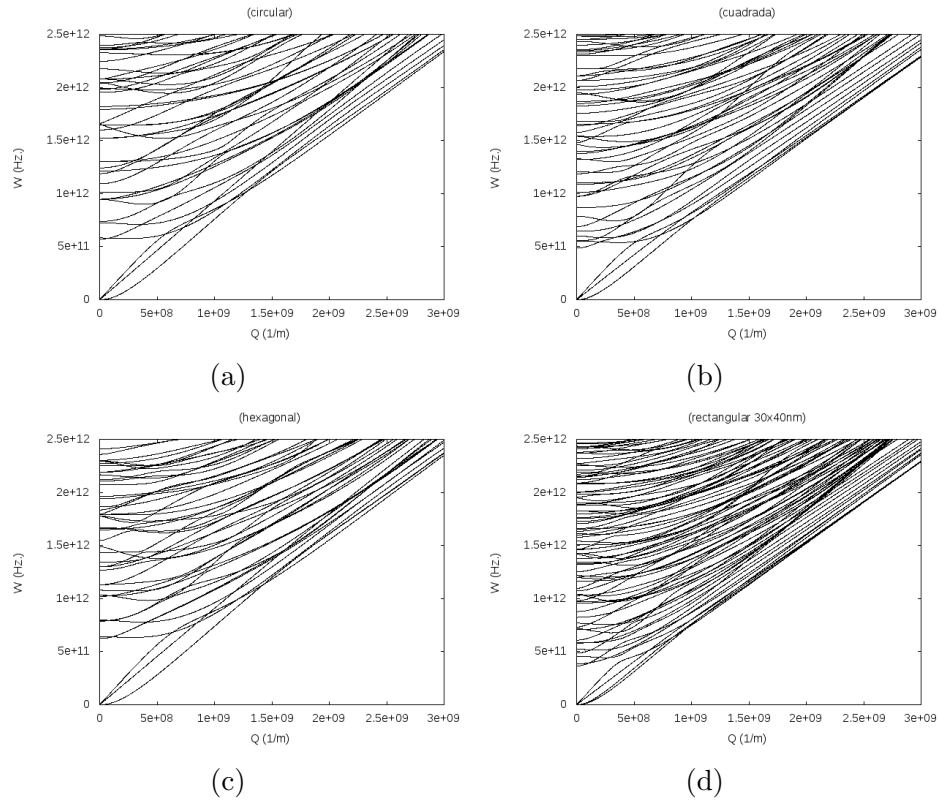
Figure 3.19: Dispersion relation curves for the elastic waves of a silicon nanowire having different cross-section: (a) circular with radius 30 nm; (b) square with side 30 nm; (c) hexagonal with side 30 nm; (d) rectangular with dimensions 30 nm X 40 nm.

waves dispersion relations on nanowires, we show in Fig.3.19 the dispersion relations for the elastic waves propagating in solid silicon nanowires, of different sections, as a function of the wavevector along the nanowire axis. We observe that Fig.3.19a wich presents the nanowire with circular cross-section is similar in the lower frequencies to the nanowire with hexagonal cross-section (Fig.3.19c). Also we observe that in the rectangular cross-section nanowire (Fig.3.19d), the lower mode degeneration observed in the other symmetric wires is now broken. The picture shown here is qualitatively the same in other materials.

3.4.1   Elastic waves in GaN nanowires

GaN has been widely studied because of its wide direct band and high carrier mobility thus having many possible applications. Besides this GaN nanowires

exhibit a low density of structural defects [174, 175] and they can be used in nanoelectronic devices [176]. Because of this and as no experimental data on the phonons of the III-nitride nanowires are available we shall concentrate on GaN nanowires in order to obtain the basic features for the III-nitride nanowires. We shall study also the influence of the cross-section shape on the vibrational modes by considering also circular cross-sections, a shape frequently found in other material nanowires. The influence of the thickness on the vibrational modes will be considered also. Wires with a zinc-blende structure, a possibility pointed in some theoretical studies [177, 178], will be considered and the differences with the wurtzite case will be analysed.

Table 3.3: Elastic constants and mass densities employed in our calculations for GaN wurtzite [179] and zinc-blende [180].

GaN	C_{11} (GPa)	C_{12} (GPa)	C_{13} (GPa)	C_{33} (GPa)	C_{44} (GPa)	C_{66} (GPa)	ρ (10^3 kg m^{-3})
wurtzite	390	145	106	398	105	123	6.15
zinc-blende	293	159			155		6.10

We shall discuss now the elastic waves propagating in infinite GaN nanowires of hexagonal cross-section. The grown GaN nanowires come from the wurtzite structure [60, 67, 68, 69]. On the other hand, theoretical studies allow also the existence of GaN nanotubes originating from the zinc-blende structure [177, 178], and we shall present some results for comparison. The elastic coefficients and mass densities for GaN wurtzite and zinc-blende are given in Table 3.3. The grown nanowires have sides ranging from $\simeq 1$ nm to several tens of nm. We shall consider two nanowires with side 1 nm and 10 nm, respectively, as representative of the thicknesses of the experimental samples and we assume them to be of infinite length. We have employed the "xyz" method explained in section 2.2.3. We have studied the convergence by considering different systems with different values of N. When comparing the results for $N = 11$, 12 and 13, respectively, we have seen that for $N = 12$ and 13 the differences are less than 10^{-10}, while the differences with the case $N = 11$ are bigger. Thus in all our calculations we have employed $N = 12$ as a good choice for accuracy and speed of calculation.

In order to number the different modes we shall use as reference the number of the modes at $Q = 0$ for increasing frequencies. In the following figures we shall present results for frequencies up to several THz, in some cases. In spite of the fact that some of these frequencies are strictly beyond the range of validity of the elasticity theory, they give a qualitative picture of the frequency spectra of these nanowires and thus they will be presented

here.
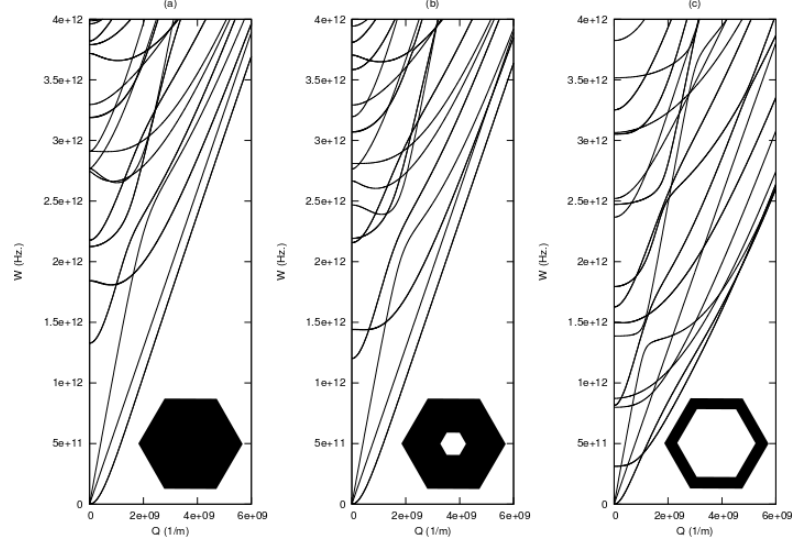
Figure 3.20: Dispersion relation for the elastic waves propagating in: (a) solid wurtzite nanowire of hexagonal cross-section and side 1 nm as a function of the wavevector along the nanowire axis; (b) hollow wurtzite nanowire of hexagonal cross-section, where the outer side is 1 nm and the inner side is 0.25 nm, as a function of the wavevector along the nanowire axis, and (c) hollow wurtzite nanowire of hexagonal cross-section, where the outer side is 1 nm and the inner side is 0.75 nm, as a function of the wavevector along the nanowire axis.

Fig.3.20a presents the dispersion relation for the elastic waves propagating in a solid wurtzite nanowire of side 1 nm as a function of the wavevector along the nanowire axis. We observe the three lower modes starting from zero frequency. We observe three lower modes starting from zero frequency instead of the four modes observed in other less symmetric wires [181, 182]. The lowest one is a doubly degenerate mode.This is the same situation observed in CNTs [55, 57] and square nanowires [23, 183]. It has a quadratic dependence on Q for low frequency values and corresponds to a bending of the wire [182], whereas for bigger Q values it takes a linear dependence. The other two modes have a linear variation with Q at low frequency values and correspond to a torsion mode and to the longitudinal acoustic mode [181, 182].

Fig.3.20b presents the dispersion relation for a hollow wurtzite nanowire where the inner side is 0.25 nm. We observe that all the modes with non-zero frequencies at Q=0 have now lower frequencies than in the solid wire. We see also that the third and fourth modes are now more separated. On the

other hand the fifth mode crosses the third one at high Q values.

This trend continues when we increase the size of the hollow part in the nanowire, as it can be seen in Fig.3.20c, where we present the dispersion relation for a hollow wurtzite nanowire with 0.75 nm as the inner side. Here the fourth mode crosses the three lower modes at low Q values. We see also that the third mode after the initial linear variation flattens at $Q=10^9\ m^{-1}$ and the latter increase does not reach the high frequency values seen in the previous figures.
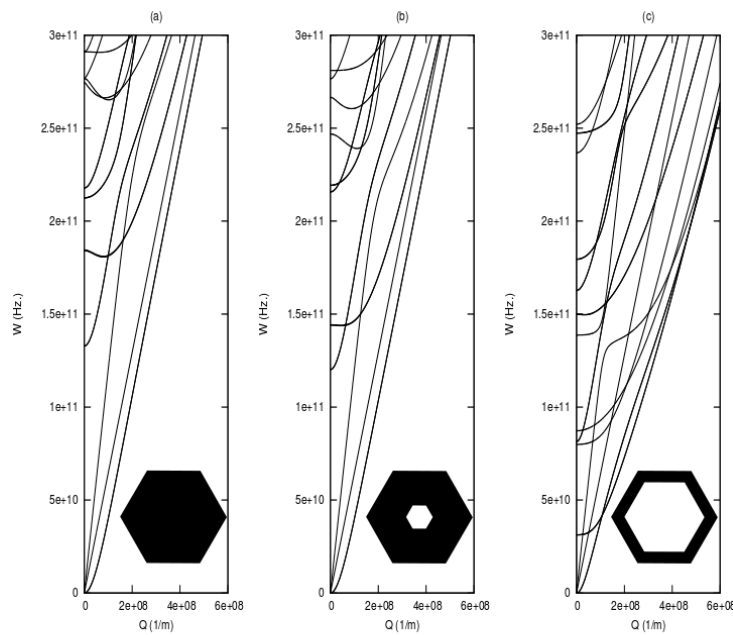
Figure 3.21: Dispersion relation for the elastic waves propagating in: (a) solid wurtzite nanowire of hexagonal cross-section and side 10 nm as a function of the wavevector along the nanowire axis; (b) hollow wurtzite nanowire of hexagonal cross-section, where the outer side is 10 nm and the inner side is 2.5 nm, as a function of the wavevector along the nanowire axis, and (c) hollow wurtzite nanowire of hexagonal cross-section, where the outer side is 10 nm and the inner side is 7.5 nm, as a function of the wavevector along the nanowire axis.

Now we shall consider a wider nanowire having 10 nm size. Fig.3.21a gives the dispersion relation for the solid wurtzite nanowire. We see now many more branches at lower frequencies than in the 1 nm side nanowire.

It is easy to see that the lower frequency modes have the same behavior previously seen in the 1 nm side nanowire.

In the case of hollow nanowires we obtain the same trends seen in the 1 nm side nanowire. This is evident in Fig.3.21b and 3.21c where we present the dispersion relation for the nanowires with 2.5 nm as inner side and 7.5 nm as inner side respectively.
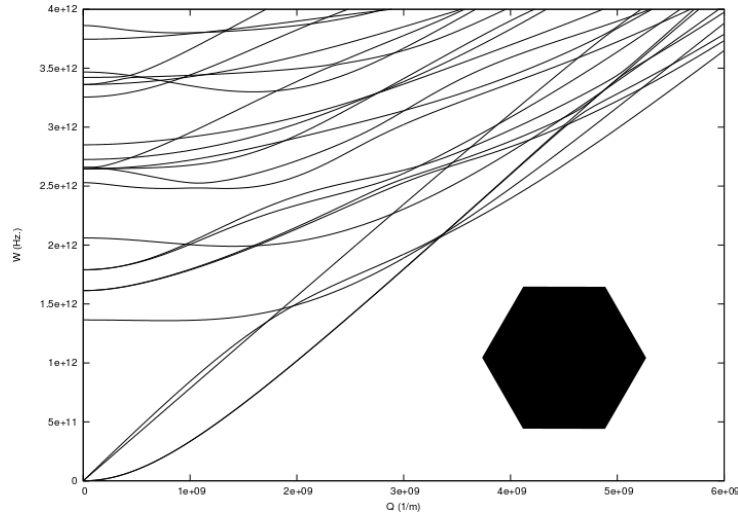
Figure 3.22: Dispersion relation for the elastic waves propagating in a solid zinc-blende nanowire of hexagonal cross-section and side 1 nm as a function of the wavevector along the nanowire axis.

We present in Fig.3.22 the dispersion relation for a solid zinc-blende nanowire of hexagonal cross-section and 1 nm side. Although the qualitative picture is the same than in the wurtzite case the dispersion relations are clearly different in both cases. The behavior of the three lower modes starting from zero frequency exhibit important differences. For the hollow wires the same trends discussed before are found.

We have also considered the wurtzite structure circular wire, that is the nanotube, in order to compare the results with those of the hexagonal cross-section. Fig.3.23 presents the dispersion relation for a solid wurtzite nanotube of radius 1 nm compared to the case of a solid wurtzite nanowire of side 1 nm. When comparing both dispersion relations we observe that the seven lower modes have very similar dispersion relations in both geometries in shape as in frequency value, but for higher modes the differences are evident both in shape and frequency values. This is also true for the case of the hollow nanotubes.

Besides the knowledge of the frequencies of the propagating modes it is
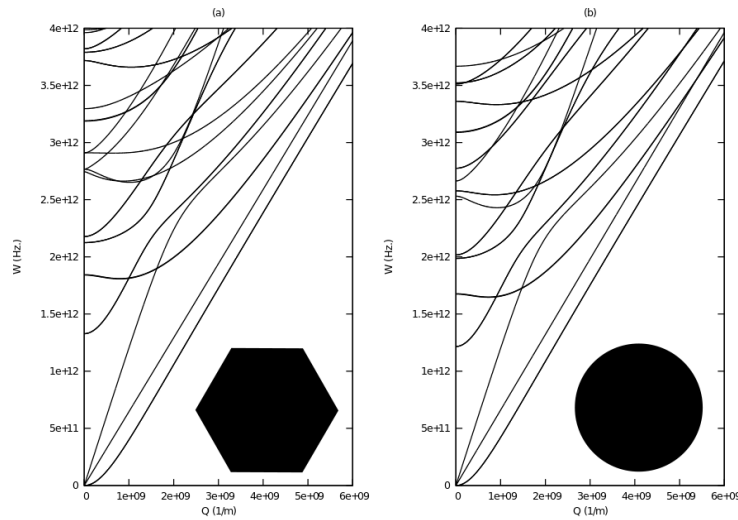
Figure 3.23: Dispersion relation for a solid wurtzite nanowire as a function of the wavevector along the nanowire axis: (a) hexagonal cross-section and side 1 nm; (b) circular cross-section and radius 1 nm.

also possible to obtain information on the displacement field of the modes. This can be obtained by means of the spatial distribution of the squared displacement vectors $|\mathbf{u}|^2$.

Fig.3.24a presents a projected view of $|\mathbf{u}|^2$ for the first mode of the solid wurtzite nanowire of side 1 nm at $Q=0$. We see here a constant value for all the points, thus corresponding to an uniform motion. This motion is perpendicular to the nanowire length. The second mode (not shown) is the broken degeneracy of the first mode. In the first mode the motion goes in the direction of two opposing vertices of the hexagon while in the second mode the oscillation goes perpendicular to a pair of opposite faces.

Fig.3.24b shows the third mode. In this mode the movement goes in the direction of the wire length. In these first modes the amplitude of the oscillations does not varies across the cross-section.

Fig.3.24c gives the same information for the fourth mode. We see how the displacements are mainly concentrated in the outer region of the wire, while decaying towards the wire inner part.

In Fig.3.24d we see the results for the fifth mode. In this case we see a similar behaviour, but now there is a narrow region near the hexagon x-axis where the displacement is zero. Similar behaviour has the sixth mode, Fig.3.24e, except that in this case the region of zero displacement is along the the y-axis.

Fig.3.24f gives the same information for the seventh mode. We see there

(a) Acoustic Mode 1   (b) Acoustic Mode 3   (c) Mode 4

(d) Mode 5   (e) Mode 6   (f) Mode 7

(g) Mode 8   (h) Mode 9   (i) Mode 10
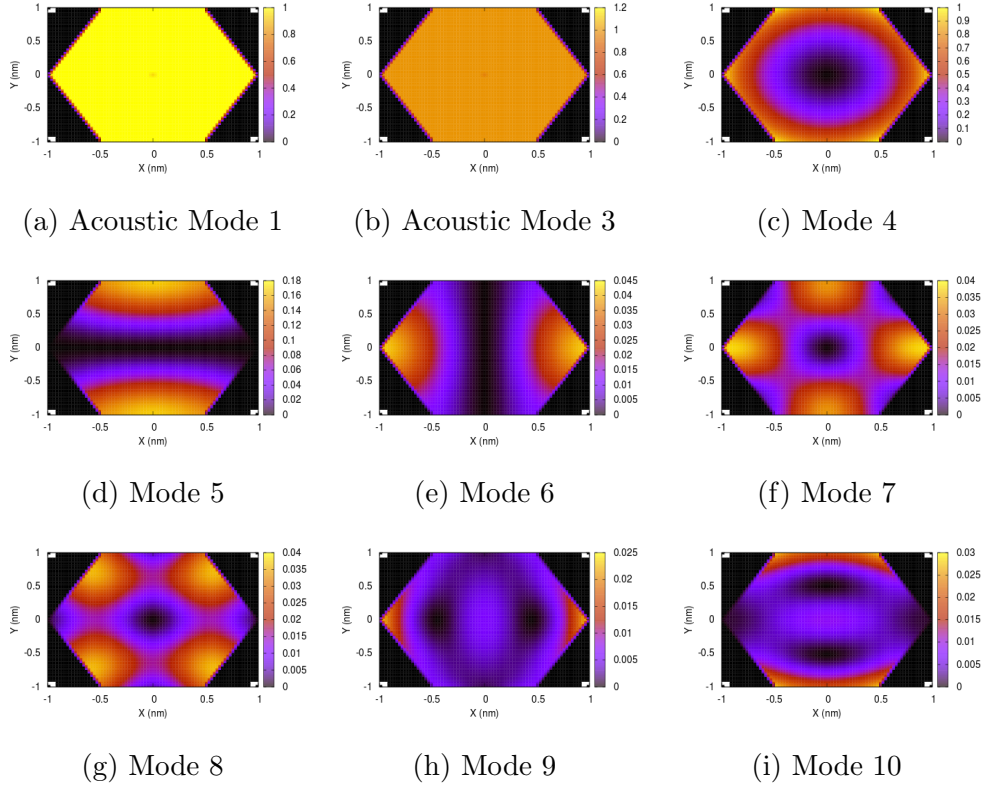
Figure 3.24: Projected view of $|u|^2$ for the first 10 modes of the solid wurtzite nanowire of side 1 nm at Q = 0.

that the bigger displacements are concentrated in a cruciform region around the inner centre of the hexagon. We have a similar situation in Fig.3.24g but with the cruciform region rotated 45°.

In fact the geometry of the cross-section breaks the degeneracy of the asymmetric modes as we see also in Figs.3.24h and 3.24i.

Fig.3.25 presents a projected view of $|\mathbf{u}|^2$ for several modes of the hollow wurtzite nanowire of side 1 nm and inner side 0.50 nm at Q=0.

Fig.3.25a gives the results for the first mode. We see that there is a constant value for all the nanowire regions, thus corresponding to a uniform motion.

Fig.3.25b shows the $|u|^2$ values of the third mode. This mode is also a uniform oscillation motion like Fig.3.25a but the oscillations are done in the direction of the wire length.

Fig.3.25c gives the results for the fourth mode. We see how the displacements are mainly concentrated in the outer region of the wire, while decaying

(a) Acoustic Mode 1   (b) Acoustic Mode 3   (c) Mode 4

(d) Mode 5   (e) Mode 6   (f) Mode 7

(g) Mode 8   (h) Mode 9   (i) Mode 10
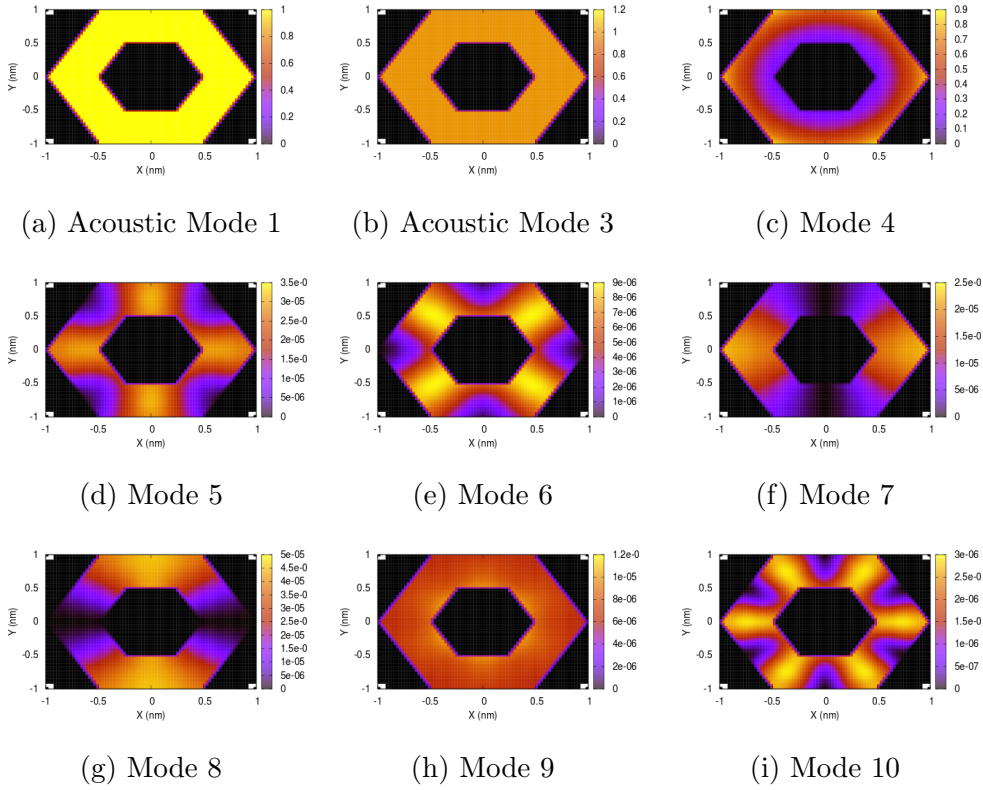
Figure 3.25: Projected view of $|u|^2$ for the first 10 modes of the hollow wurtzite nanowire of side 1 nm at Q = 0.

strongly towards a region near the wire hollow part.

In Fig.3.25d we see the results for the fifth mode. We see here the displacements having a cross shape with the highest values concentrated around the x- and y-axes. As in the previous nanowire, the hexagonal cross-section breaks the degeneracy of the modes represented in Figs.3.25d and 3.25e.

The results for the seventh mode are presented in Fig.3.25f. We appreciate that the displacements are zero in a region close to the y-axis of the hexagon. In Fig.3.25g the results for the broken degeneracy mode are given.

Fig.3.25h shows the 9th mode, which is a symmetric mode similar to Fig.3.25c but with the strongest displacements concentrated in the hollowed inner region of the wire.

Finally in Fig.3.25i the 10th mode shows the maximal displacements in planes connecting the inner and outer vertices of the hollowed hexagon cross-section.

In Fig.3.26 the projected view of the $|\mathbf{u}|^2$ for several modes of the solid

(a) Acoustic Mode 1   (b) Mode 3   (c) Acoustic Mode 4

(d) Mode 5   (e) Mode 6   (f) Mode 7

(g) Mode 8   (h) Mode 9   (i) Mode 10
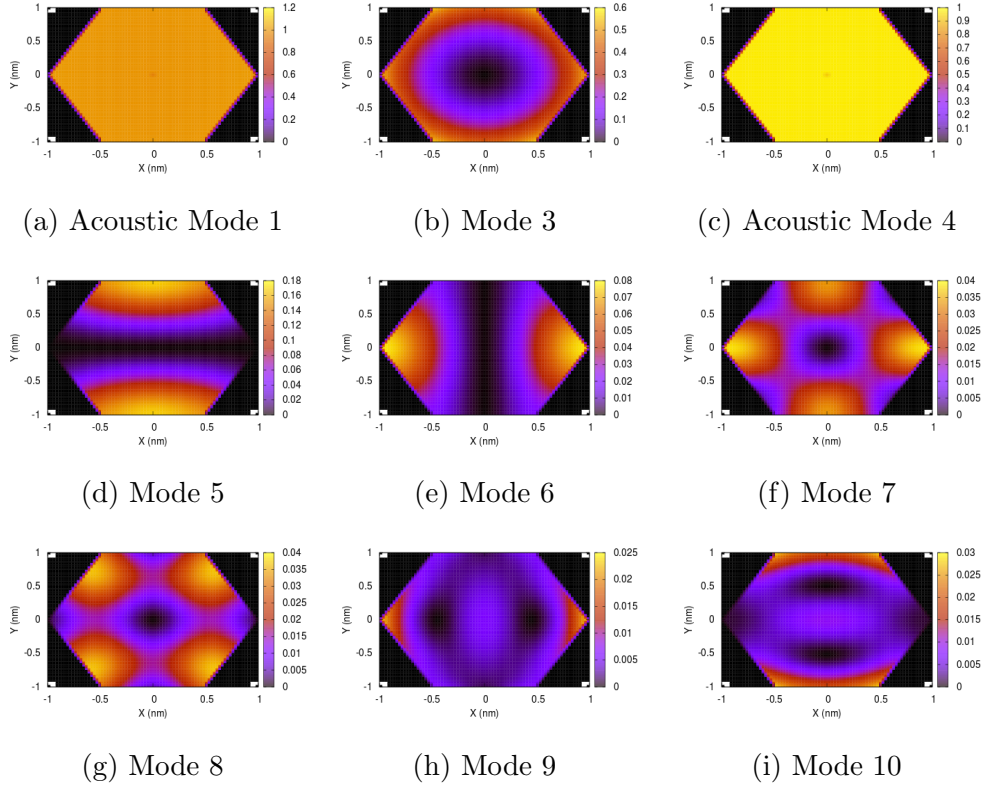
Figure 3.26: Projected view of $|u|^2$ for the first 10 modes of the solid wurtzite nanowire of side 1 nm at $Q = 1.4 \times 10^8 m^{-1}$.

wurtzite nanowire of side 1 nm at $Q = 1.4 \times 10^8 m^{-1}$ are shown. The results for the equivalent hollow nanowire is shown in Fig.3.27. The main differences with the Figs.3.24 and 3.25 are the order of the modes as the highest acoustic mode crosses the lower non acoustic mode as we can see in Fig.3.23.

Fig.3.28 presents a projected view of the $|\mathbf{u}|^2$ for several modes of the solid wurtzite nanowire of side 10 nm at $Q = 1.4 \times 10^8 m^{-1}$. Fig.3.28a gives the results for the first mode. We see that there is an almost constant value for all the nanowire regions, the highest values being near the outer region of the nanowire with a small decrease towards the inner part. Fig.3.28b gives the results for the third mode. We see how the displacements are mainly concentrated in the outer region of the wire, while decaying towards the wire inner part as in Fig.3.26b. Fig.3.28c shows that the highest acoustic mode crosses the lower non acoustic mode. In Fig.3.28d we see the results for the fifth mode. In this case we see a four lobe pattern for the displacements. Fig.3.28e is the broken degeneracy mode related to Fig.3.28d. The results

for the seventh mode are presented in Fig.3.28f. We see that in this case the lowest values are in a region near the x-axis having an ∞ shape. Finally modes eighth and ninth are shown in Figs.3.28g and 3.28h which are equivalent to those of the 1 nm side hexagonal nanowire modes Figs.3.26g and 3.26h respectively. Fig.3.28i shows the broken degeneracy of the mode by the hexagonal cross-section of the nanowire as in Fig.3.26i.

Analogous behaviours to those seen here can be found in lattice dynamic calculations for Si nanowires [181, 182].

Qualitatively analogous patterns are obtained for nanowires coming from the zinc-blende structure.

In conclusion, we have shown how to obtain the dispersion relations of the elastic waves in hexagonal cross-section nanowires coming from elastically anisotropic materials. We have studied solid and hollow nanowires and the differences in the frequency spectra have been discussed.

The case of nanowires coming from the zinc-blende structure, allowed in principle by theoretical studies, has been considered also. A comparison with nanotubes (circular cross-section) has been presented. We found that the lower modes have a very similar dispersion relation both in shape and frequency value, but higher frequency modes exhibit more important differences. The study of the squared displacement vectors $|\mathbf{u}|^2$ allow to see the spatial distribution of the different modes in the nanowires. There are several modes whose elastic displacement components concentrate around the borders of the nanowire and they decay towards the inner part of the nanowire. And in the hollow nanowire, there are modes with similar behaviour, where the elastic displacement components concentrate around the borders of the nanowire but they decay towards the outer part of the nanowire.

3.4.2 Elasticity model: Breathing modes

As it was told in Sections 2.2.2 and 2.2.3, radial acoustic breathing modes are a characteristic feature of nanotubes and nanowires spectra. In the case of cylinders, we were able to obtain the frequencies of these modes in a closed form, and an analytical expression for the lowest mode. The formula was a function of the mass density and the elastic constants of the material, and it was valid for general cylindrical anisotropy.

In the case of nanowires of non-circular cross-sections, no closed form expressions can be obtained, even for isotropic materials.

Many of the nanowires grown in the laboratories exhibit non-circular cross-sections, and the hexagonal cross-section is quite common.

We illustrate now the study of the behaviour of the lowest breathing mode frequency against the length of the hexagonal side. We employ the elasticity

(a) Acoustic Mode 1   (b) Mode 3   (c) Acoustic Mode 4

(d) Mode 5   (e) Mode 6   (f) Mode 7

(g) Mode 8   (h) Mode 9   (i) Mode 10
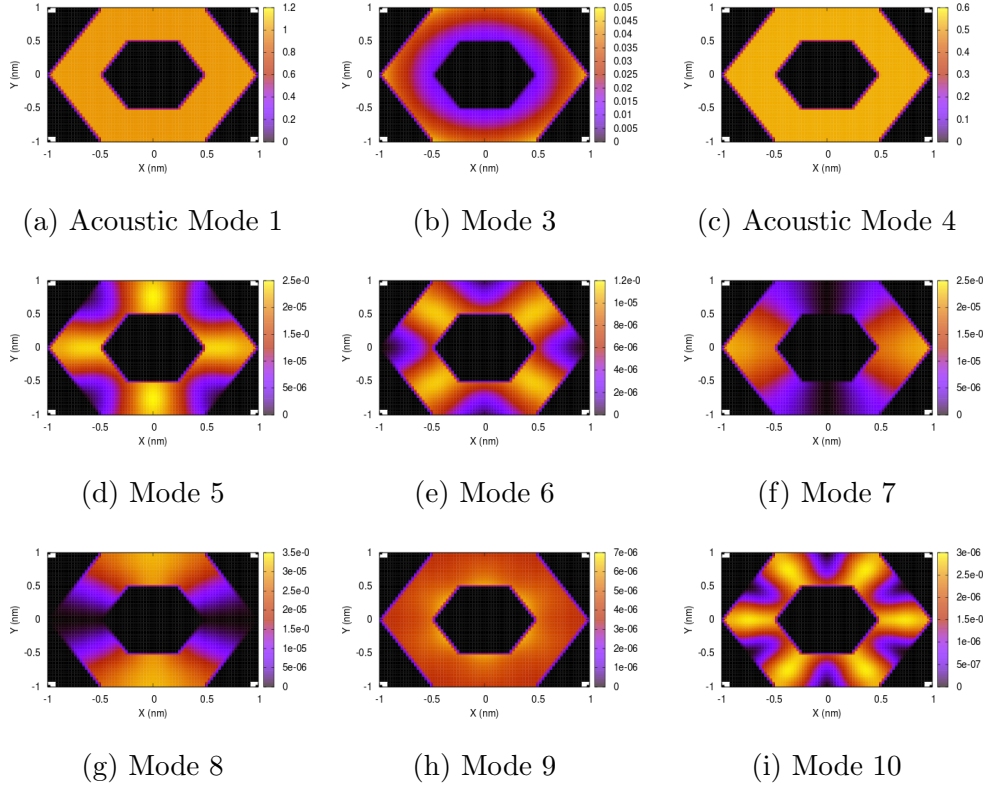
Figure 3.27: Projected view of $|u|^2$ for the first 10 modes of the hollow wurtzite nanowire of side 1 nm at Q $= 1.4 \times 10^8 m^{-1}$.

theory and the xyz-method explained before. This is shown in Fig.3.29c for $CdSe$ and in Fig.3.30c for ZnO. The elastic data and mass densities employed in our calculus are given in Table3.4. Fig.3.29a and Fig.3.30a present the elastic displacement of the breathing mode.

The behaviour of the frequency against the hexagon side-length is presented in Fig.3.29b and Fig.3.30b, whereas the behaviour of the frequency against the inverse of the side-length is shown in Fig.3.29c and Fig.3.30c. We see the $\frac{1}{a}$ behaviour in a clear way. As in the cylinder, the ratio with the side-length is maintained in the case of hexagonal prism nanowires. These results agree quite well with the experimental results for $CdSe$ [184] and ZnO [185] nanowires.

The results for the case of cylindrical cross-sections obviously follow the $\frac{1}{r}$ behaviour, with some small differences in the numerical values of the slope. Then is quite clear that the elasticity theory fairly accounts for the frequency values of the first breathing acoustic mode in nanowires.

(a) Acoustic Mode 1   (b) Mode 3   (c) Acoustic Mode 4

(d) Mode 5   (e) Mode 6   (f) Mode 7

(g) Mode 8   (h) Mode 9   (i) Mode 10
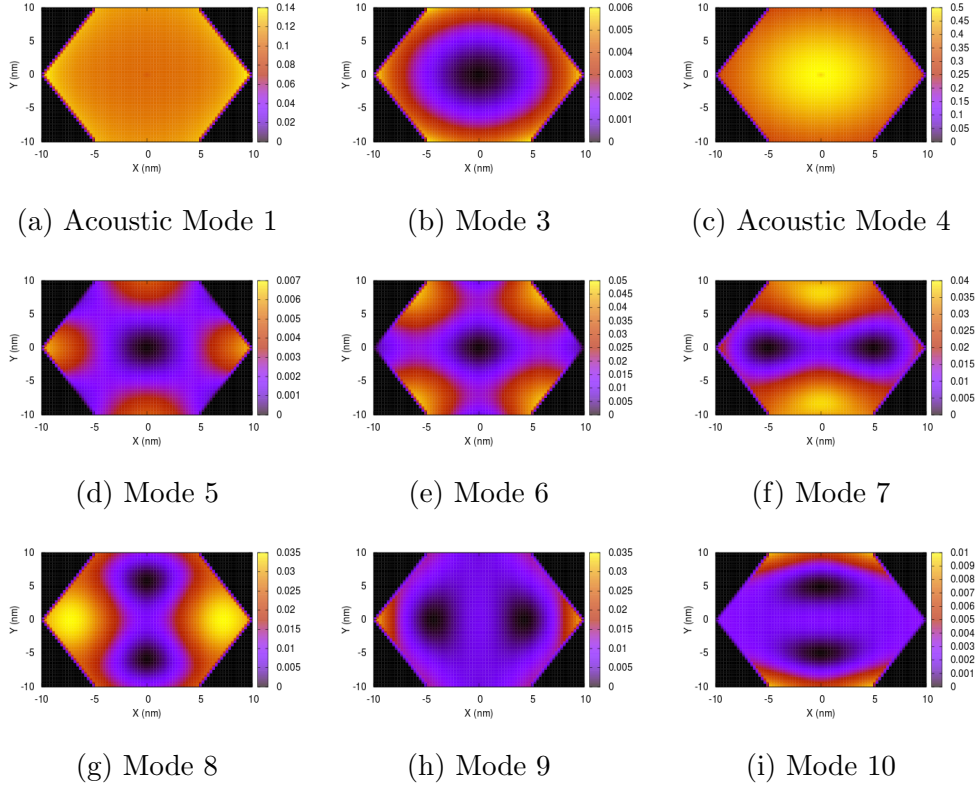
Figure 3.28: Projected view of $|u|^2$ for the first 10 modes of the solid wurtzite nanowire of side 10 nm at Q $= 1.4 \times 10^8 m^{-1}$.

The radial breathing modes (also known as pulsating modes) are calculated with the elasticity model looking for the pattern shown in Fig.3.29a (and Fig.3.30a. Then the evolution with the section size is analysed in Fig.3.29c and Fig.3.30c. The graphics are compared with the analytical equation obtained before (eq.2.50) where we see a total agreement with the $\frac{1}{a}$ relation of the frequency and the side of the hexagonal cross-section. Although the analytical formula (2.50) is specifically obtained for cylindrical nanowires, it is observed that, as in the cylinder, the ratio is maintained with the side-length in the case of hexagonal prism nanowires.

3.4.2.1   Acoustic breathing mode frequencies of Au, CdSe, InAs, GaAs, Ag and Bi nanowires

In recent years different groups have grown Au[66, 186, 187], CdSe[184], InAs[188], GaAs[189], Ag[190, 191] and Bi[70] nanowires. They have also obtained the frequency of the lowest acoustic breathing mode. We shall apply
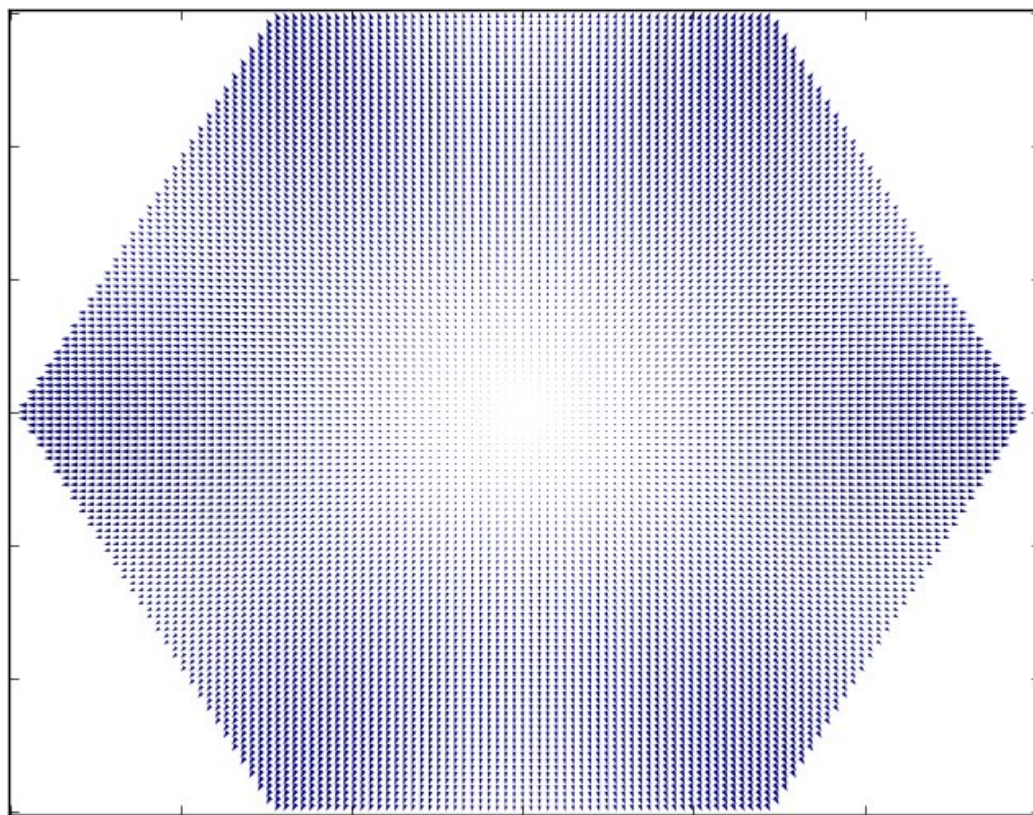
(a) Breathing mode of a CdSe nanowire.
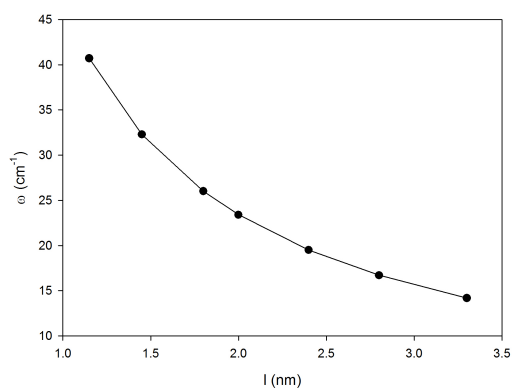
(b) Evolution of the Breathing mode frequency with the section size.
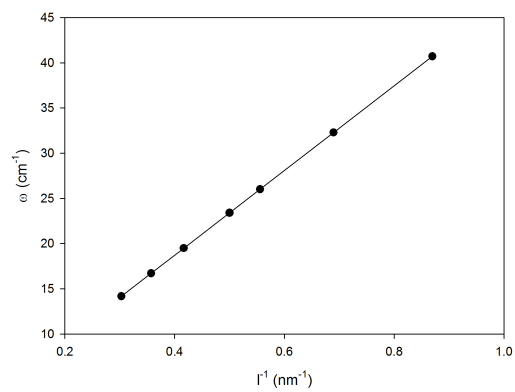
(c) Evolution of the Breathing mode frequency with the inverse of the section size.

Figure 3.29: Breathing mode of a CdSe nanowire of hexagonal cross-section.
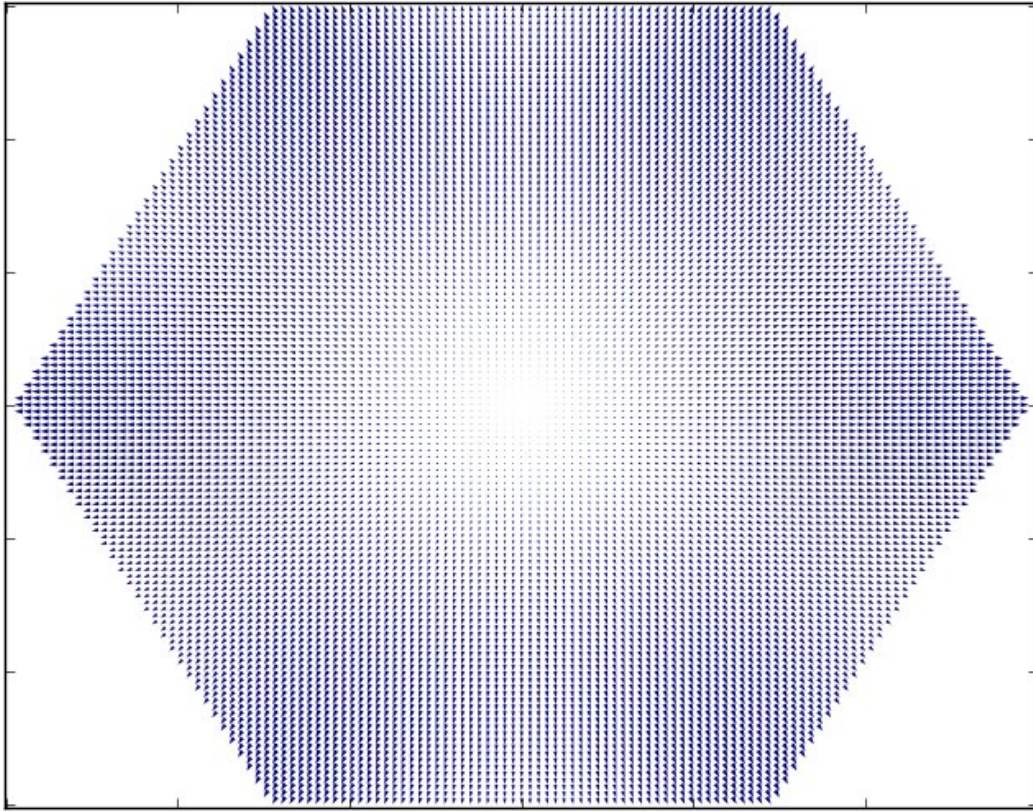
(a) Breathing mode of a ZnO nanowire.
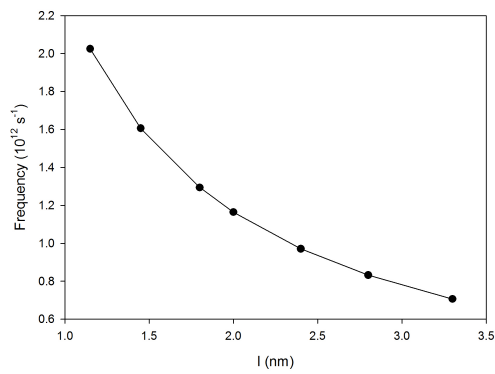
(b) Evolution of the Breathing mode frequency with the section size.
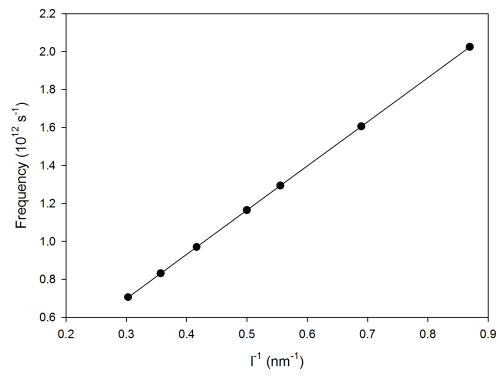
(c) Evolution of the Breathing mode frequency with the inverse of the section size.

Figure 3.30: Breathing mode of a ZnO nanowire of hexagonal cross-section.

now equation (2.64) in order to compare with the experimental results.

We present in Table 3.4 the elastic constants and mass densities of CdSe[192], InAs[193], InAs[194], Au[195], GaAs[196], Ag[197] and Bi[198]. The different materials in the nanowires belong to the hexagonal (CdSe, InAs), cubic (Au, GaAs, Ag) and trigonal (Bi) systems. Thus in all the studied cases $C_{11} = C_{22}$ (as seen in Section 2.2.2) and then $\mu=1$.

In the case of InAs the nanowires grown exhibit the wurtzite structure [188]. This form of InAs does not appear in the bulk and therefore no experimental values of the elastic coefficients are available. Thus, we have employed two different sets of elastic constants. The first one comes from *ab initio* calculations [193], whereas the second one [194] was obtained from the Martin approximation [199] allowing to obtain the elastic coefficients for an ideal wurtzite structure from those of the zinc-blende structure appearing in nature. The approximation is based on a rotation of the crystal structure and a correction due to the internal strain state. This approximation gives a reasonable accuracy for materials which can appear in the zinc blende and wurtzite structures.

We present in Table 3.5 a comparison with the experimental results. The experimental data come from different groups where different growth and detection techniques were employed. In some cases the samples grown do not comply strongly with the infinitely long cylinder approximation. Besides this, the samples grown are not cylindrical in shape in many occasions. Nevertheless we can see that the agreement with the experimental results is quite good for all the materials considered here. This good agreement can be justified at least in the case of metals, because theoretical studies indicate that the size effects on the elastic properties of nanostructures are very small for nanostructures having cross-section widths larger than 10 nm [200, 201, 202].

For hexagonal and other cross-sections the method put forward in Section 2.2.3 could be employed. Nanowires with low length/width ratios can be treated in the same way.

Nanowires are also grown along a z-axis in different directions. In that case the matrix elastic coefficients should be rotated to the new coordinate system and the new coefficients should be employed in the expressions presented before. In the case of the [110] direction, for example, it can be found that for cubic crystals we have $C'_{11} = (C_{11} + C_{12} + 2C_{44})/2$, $C'_{12} = C_{12}$ and $C'_{22} = C_{11}$ [203]. It is easy to see that in this case the μ index of Section 2.2.2 is not an integer.

3.4.2.2 Acoustic breathing mode frequencies of Au/Ag and ZnS/SiO$_2$ core-shell nanowires

Coherent acoustic phonons in Au/Ag core-shell nanowires have been studied recently [204]. Breathing modes were observed for core-shell samples having an Ag shell of $\sim$ 11 nm. These modes were not observed for samples having 4-7 nm Ag shells. This was due to the fact that the breathing mode period was small enough to be close to the electron-phonon relaxation time, $\sim$ 4 ps for the Au/Ag core-shell nanowires with 4 nm Ag nanoshell (h=2nm). In Table 3.6 we present our results obtained from eq.(2.80) for the different samples used by Wang et al. [204].

It can be seen that our theoretical prediction of 10.55 ps for the period of the thickest nanowire differs greatly of the experimental value $\sim$ 15 ps assigned to the breathing mode. The samples had an average length of 49 $\pm$ 8 nm and an average width of 30 $\pm$ 3 nm. In this case it is clear that the infinitely long cylinder hypothesis is not a very good one and a poorer agreement can be expected.

For the other nanowires the length/width ratio is bigger and the approximation would be more justified. We see how the acoustic breathing mode periods decrease towards the value of 4 ps indicated in Wang et al. [204] where no experimental values could be obtained.

Very long ZnS/SiO$_2$ core-shell nanowires have been produced quite recently [205]. The nanowires were characterized by using different experimental techniques. By means of transmission electron microscopy (TEM) and X-ray diffraction (XRD) analysis, it was found that the nanowires were formed by a single-crystalline ZnS core and an amorphous SiO$_2$ shell. It was found also that the ZnS core had the wurtzite structure and grew along the [0001] direction.

The length of the nanowires ranged from 1 mm to 1 cm, the diameter being approximately 30 nm. It was found that the different samples presented an average ZnS core radius of 13.84 nm and an average amorphous silica shell width of 1.59 nm. It is then clear that $L/R \gg 1$ in these core-shell nanowires, and the approximation of infinitely long cylinders employed in the former theoretical analysis is well justified.

We shall obtain the acoustic breathing mode frequencies of a ZnS/SiO$_2$ core-shell nanowire with core radius and shell width given above. We shall employ for the wurtzite ZnS core the elastic data of *Landolt − Börnstein* [206] and for the amorphous silica shell, being an isotropic material, the elastic data of Dieulesaint et al. [52], presented in Table 3.4.

In Table 3.7 we give the numerical values of the frequencies for the first five acoustic breathing modes, obtained from the solution of eq.(2.80). We give

also in Table 3.7 the variation of the frequency values of these modes when the width of the shell is decreased, arriving up to the modes of a ZnS nanowire having a radius of 15.43 nm. Figure 3.31 gives a visual representation of the variation of the frequencies of these modes against the radius of the ZnS core and figure 3.32 gives the normalized frequencies of the first five acoustic breathing modes of ZnS/SiO_2 core-shell nanowires, as a function of the ZnS core radius. The frequencies of each mode are normalized to the mode frequency value for the first ZnS core radius . The three first modes show a decreasing behaviour for increasing values of the radius. The fourth and fifth modes present some deviations at lower values of r, but they follow the behaviour seen before at higher values.

No experimental values for the frequencies of these modes are available, so the values presented here must be considered as theoretical first estimates.

The theoretical results present a very good agreement with the experimental results for the different nanowires. We must note that analogous estimates for the acoustic breathing modes of carbon, and other different materials, nanotubes obtained with the formulae of the elasticity theory (eq.(2.73)) compared quite well with experimental data and results of first principles calculations [30].

Table 3.4: Elastic constants for CdSe [192], InAs [193], InAs [194], Au [195], GaAs [196], Ag [197], Bi [198], ZnS [206], SiO$_2$ [52]; AlN, GaN and InN [140], elastic constants for MgO$^{(a)}$ [133], MgO$^{(b)}$ [134], ZnO[141] and mass densities employed in our calculations.

Material	C_{11} (10^{10} N m^{-2})	C_{12} (10^{10} N m^{-2})	C_{13} (10^{10} N m^{-2})	C_{33} (10^{10} N m^{-2})	C_{44} (10^{10} N m^{-2})	C_{14} (10^{10} N m^{-2})	ρ (10^{3} kg m^{-3})
CdSe	74.9	46.09	39.26	84.51	13.15	0.	5.604
InAs	110.3	42.8	32.1	120.9	27.3	0.	5.680
InAs	100.3	42.2	31.8	110.7	23.0	0.	5.680
Au	192.34	163.14	163.14	192.34	41.95	0.	19.320
GaAs	119.0	53.4	53.4	119.0	59.6	0.	5.317
Ag	192.5	163.0	163.0	192.5	42.4	0.	10.49
Bi	63.5	24.7	24.5	38.1	11.3	7.23	9.8
ZnS	122.0	58.0	43.0	138.	29.0	0.	4.089
SiO$_2$	78.5	16.1	16.1	78.5	31.2	0.	2.203
AlN	39.6	13.7	10.8	37.3	11.6		3.255
GaN	39.0	14.5	10.6	39.8	10.5		6.15
InN	22.3	11.5	9.2	22.4	4.8		6.81
MgO$^{(a)}$	22.2	9.0	5.8	10.9	10.5		3.58
MgO$^{(b)}$	19.46	10.45	9.99	11.96	5.9		3.58
ZnO	20.97	12.11	10.51	21.09	4.25		5.606

Table 3.5: Theoretical (t) and experimental (e) frequencies (ω, ν) and periods (T) of the lowest acoustic breathing mode of the different nanowires considered here.

Material	R (nm)	ω^t (cm^{-1})	ν^t (GHz)	T^t (ps)	ω^e (cm^{-1})	ν^e (GHz)	T^e (ps)
Au	13.0			11.1[195]			~11.0[66]
Au	14.5		81.01[195]			80.6[186]	
Au	52.0		22.6[195]			24.0[187]	
CdSe	2.0	21.6[192]			21.9[184]		
InAs	49.0			34.5[193]			38.3[188]
InAs	49.0			33.2[194]			38.3[188]
GaAs	157.5		9.7[196]			11.0[189]	
Ag	1.2			0.75[197]			0.88[190]
Ag	30.95			19.4[197]			19.1[191]
Bi	100.0		8.5[198]			9.5[70]	

Table 3.6: Frequencies, in units of 10^{11} s^{-1} and periods in ps of the lowest breathing acoustic mode of Au/Ag core-shell nanowires, for different values of the core radius and shell thickness (h_{shell}) corresponding to the widths in Wang et al.[204].

width	$r_{core}(nm)$	$h_{shell}(nm)$	$\omega(10^{11}s^{-1})$	T (ps)
30.0	9.5	5.5	5.95	10.55
23.0	8.0	3.5	7.52	8.35
19.0	7.0	2.5	8.91	7.05
17.0	6.5	2.0	9.81	6.41

3.5   Molecular dynamics: Bulk

In the next section we will study the characteristics of nanostructures of Si, Ge and Si-Ge alloys using Molecular Dynamics.

But first we need to identify the conditions necessary to address the nanostructures. Also, knowing the behavior of more simple cases will allow us to better understand more complex cases. For this, we will use first the well known bulk system.

In order to make a good approximation of the physical model of the vibrational characteristics of a molecular dynamics system, is necessary to

Table 3.7: Frequencies, in units of 10^{12} s^{-1}, of the first five breathing acoustic modes of ZnS/SiO$_2$ core-shell nanowires, for different values of the core radius and shell thickness.

r$_{core}(nm)$	h$_{shell}(nm)$	ω_1	ω_2	ω_3	ω_4	ω_5
13.840	1.590	0.802	2.005	3.156	4.269	5.344
14.230	1.200	0.792	1.987	3.139	4.274	5.389
14.630	0.800	0.782	1.966	3.112	4.249	5.381
15.000	0.430	0.773	1.945	3.081	4.211	5.338
15.130	0.300	0.769	1.937	3.069	4.195	5.320
15.330	0.100	0.764	1.925	3.051	4.171	5.289
15.400	0.030	0.763	1.921	3.044	4.162	5.278
15.425	0.005	0.762	1.920	3.042	4.159	5.274
15.430	0.000	0.7619	1.9196	3.0417	4.158	5.273

have an adequate statistics. Thereof if we want to fit the model correctly, we need a relatively big number of data points. The need of a good statistics is translated as a high number of particles and a great number of time steps.

In our case, we finally opted for study a system by taking 8500 steps of 1 femtosecond each. The first 500 steps are let for stabilisation of the system and thereof not taken into account in the auto-correlation calculus. For the correlation calculation we take the data points at 5 time steps intervals (in other words we take steps of 5 femtoseconds) up to a total of 1600 data points for the auto-correlation of velocities and the later Fourier transform.

3.5.1 Bulk: Statistics

For the "bulk" case we studied initially the influence of the correct statistics on the vibrational density of states. This is shown in Fig.3.33, for a series of systems in which the number of atoms in the base cell of calculation is progressively increased.

The objective of this analysis was to obtain the adequate number of atoms needed to have an enough accurate model, neither too small to be unrealistic nor too big to be numerically unaffordable.

As we see from Fig.3.33, the bigger the number of atoms the better the spectra. On the other hand the number of atoms is related to the calculation time. Therefore we need to choose a number of atoms big enough to make statistics and small enough to perform our calculation in a reasonable time.

In Table 3.8 we show the approximate time consumed by the calculation of different bulk systems.
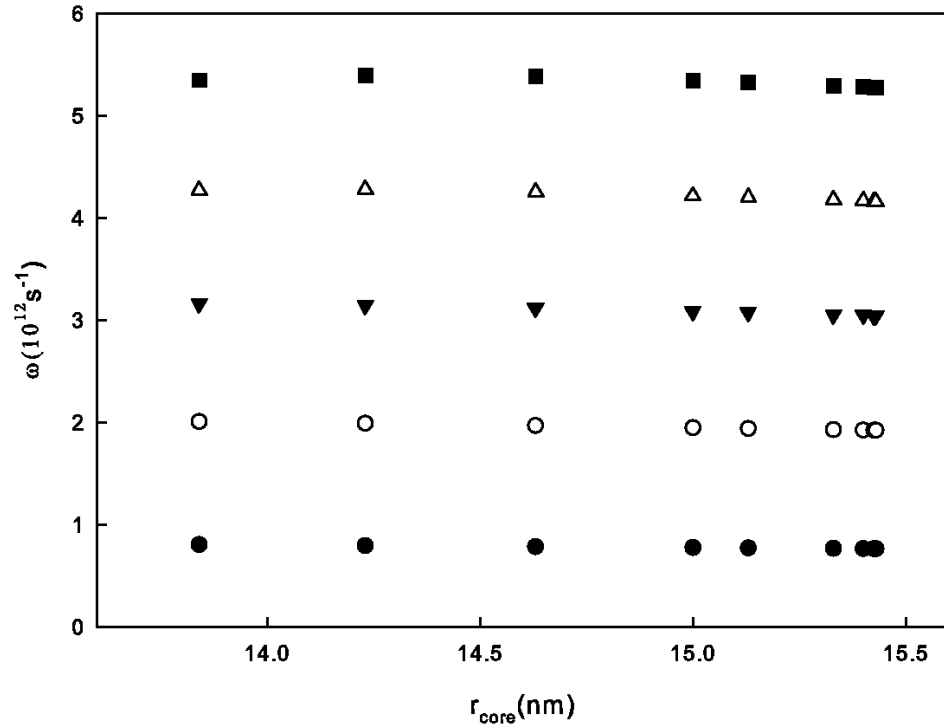
Figure 3.31:   Frequency values in units of $10^{12}s^{-1}$ for the first five acoustic breathing modes of a ZnS/SiO$_2$ core-shell nanowire as a function of the core radius.

Table 3.8: Approximate time spent in calculations.

Number of atoms	1000 steps	8500 steps	50000 steps
8000	45 s	6 min	35 min
27000	2.5 min	21 min	118 min
64000	6 min	48.5 min	282.5 min
125000	11 min	94.5 min	545 min
216000	19 min	162 min	954 min
343000	30.5 min	257.5 min	1509 min

We finally opted for systems having 216000 atoms in the calculation cell.
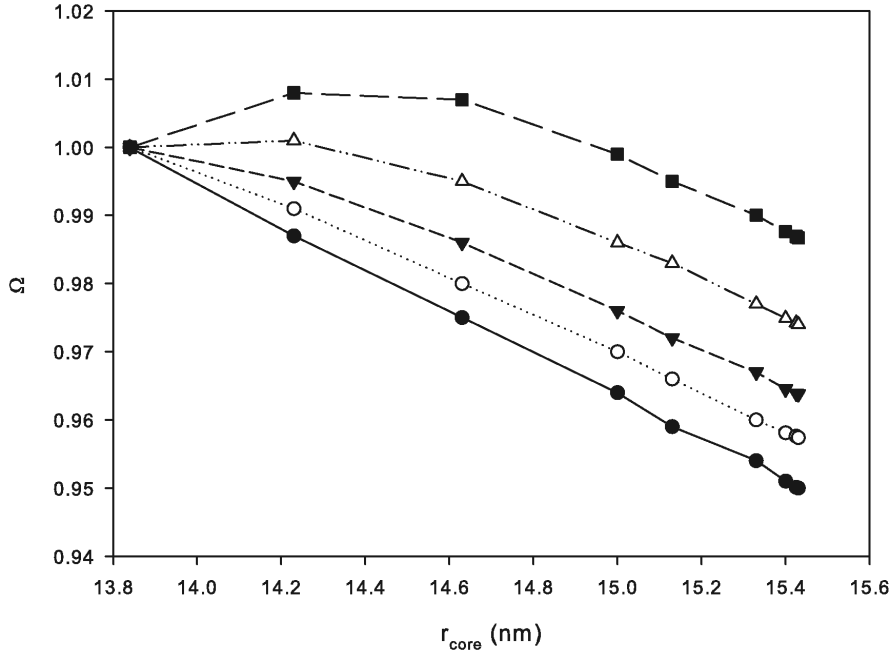
Figure 3.32: Normalized frequency values Ω (relative to the frequency value of each mode for the first ZnS core radius) of the first five acoustic breathing modes of a ZnS/SiO$_2$ core-shell nanowire (given in Table 3.7) as a function of the core radius. (1- •, 2- ∘, 3- ▼, 4- △, 5- ■).

3.5.2 Bulk: Strain

The strain and composition distribution in Si-Ge dots is closely related to their optical and electronic properties. Raman scattering of optical modes is expected to be very useful to characterise Si-Ge nanostructures [207].

In diamond structure crystals, the triple degenerate optical phonon modes at the centre of the Brillouin zone are infrared inactive, but Raman active.

The application of a static strain can lift the degeneracy of these modes by lowering the symmetry of the crystal.

The modifications introduced by the strain in the phonon spectra of diamond structure crystals were obtained in Ganesan et al. [208].

It was found that in the case of hydrostatic strain, in which the material is equally compressed or expanded in all the spatial directions, the degeneracy is not lifted. There is only a shift in the frequency of the degenerate mode. This shift is positive for compressive strains and negative for tensile strains (expansions).
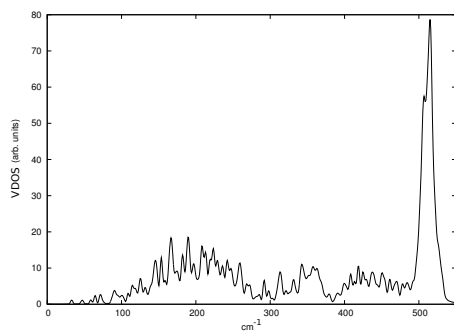
(a) Si "bulk" with 8000 atoms.
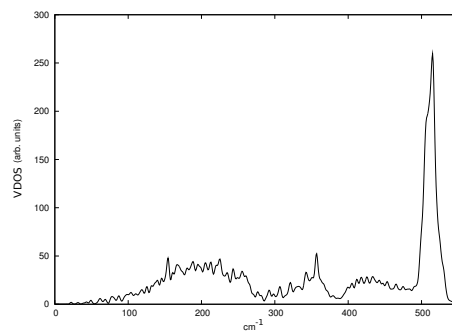
(b) Si "bulk" with 27000 atoms.
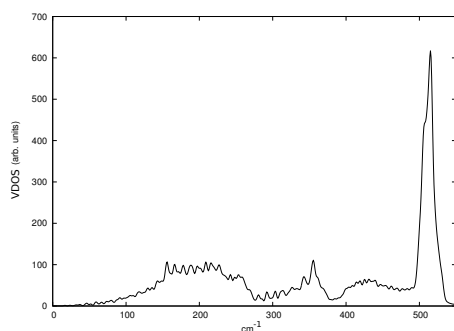
(c) Si "bulk" with 64000 atoms.
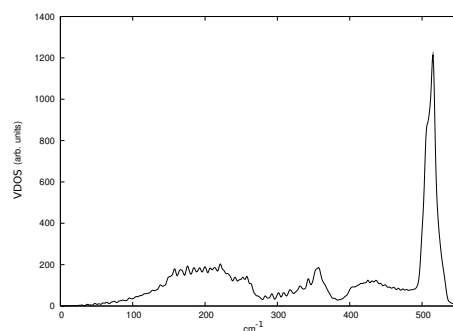
(d) Si "bulk" with 125000 atoms.
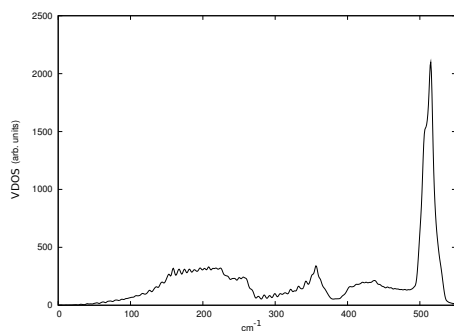
(e) Si "bulk" with 216000 atoms.
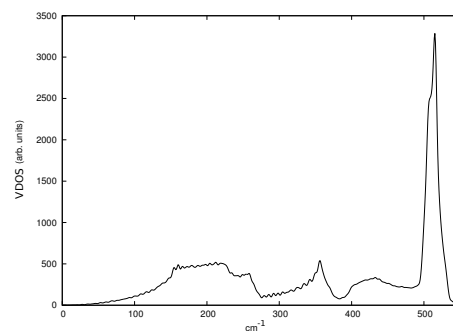
(f) Si "bulk" with 343000 atoms.

Figure 3.33: Evolution of the VDOS of bulk silicon and the number of atoms employed in the simulation.

In the case of uniaxial (plane) strain along the [001] and [111] directions, the degeneracy is partially lifted, obtaining a nondegenerate mode with eigenvectors parallel to the strain and a twofold degenerate mode with eigenvectors perpendicular to the strain.

For uniaxial strain along the [011] direction, the threefold degeneracy is completely lifted.

The induced shift of phonon frequencies is clearly seen in Fig.3.34. This effect on VDOS was observed in previous works [209]. In the case of hydrostatic strain a similar effect can be seen in the region of acoustic phonons.

From the Raman spectrum it is possible to calculate the composition [210] and the strain of a nanostructure from the positions and intensities of their Ge-Ge, Ge-Si and Si-Si peaks. But due to the fact that the method used in this work does not give the correct values of the intensities, it is not possible to use those methods based on fitting experimental data.

The displacements of the Raman spectra peaks are linear for small strains. In the plane strain case, their slope depends on the direction of the compression [211]. Also the uniaxial tensions generally result in the splitting of the peaks, for example along [011] it produces a triple splitting [212].

(a) Hydrostatic strain.   (b) Planar strain.
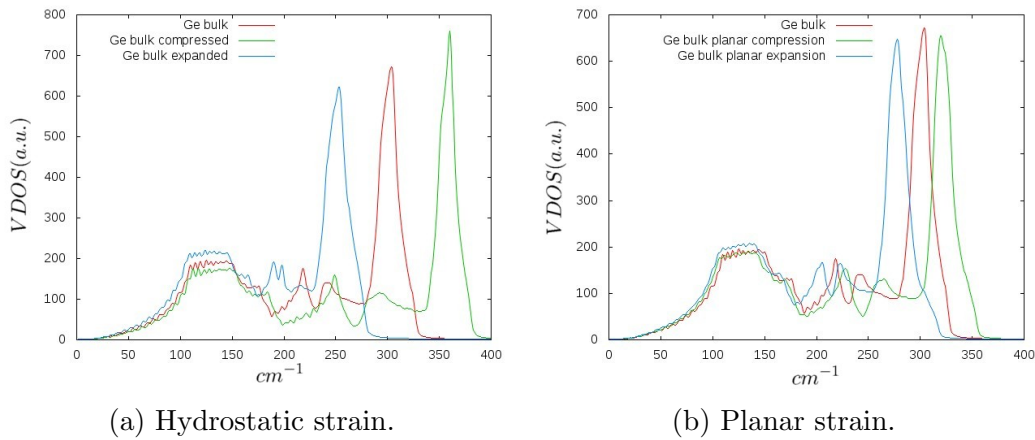
Figure 3.34: Strain effects on bulk germanium VDOS.

3.6 Molecular dynamics: Surface

The effects of the surfaces are shown in Fig.3.35a, and in Fig.3.35b we compare the VDOS of the surface against that of the "bulk". In these figures we see that the effect of the surfaces on the VDOS is to add peaks in the

(a) Si surface.

(b) Si bulk vs. surface (scaled to fit).
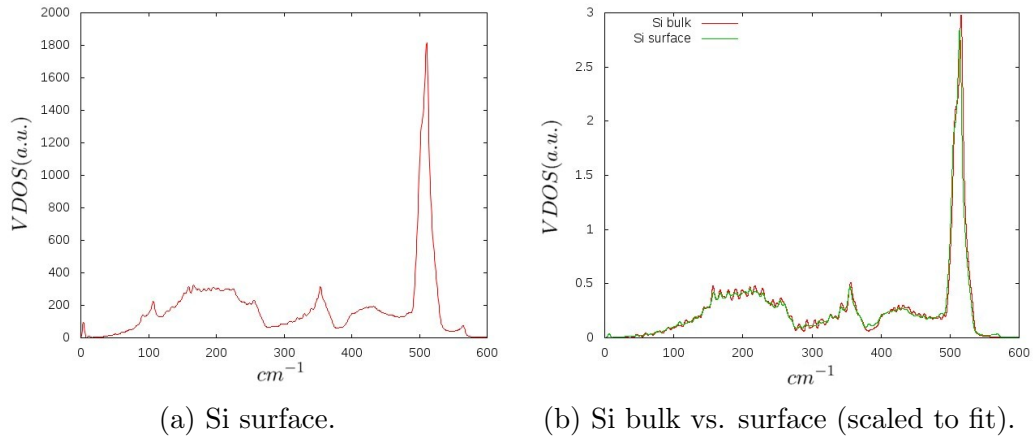
Figure 3.35: Surface effects on VDOS.

frequency region around 100 cm^{-1} in the Si. Also a new peak appears beyond the primary frequency of 500 cm^{-1}.

In Fig.3.35 there is a peak near zero frequency. This indicates the presence of atoms with an almost non-oscillatory motion probably due to a poorer convergence. Also, since the atoms of the surface have different binding properties due to the absence of neighbours, it is possible the presence of large amplitude displacements.

In Fig.3.36 we show the effects of the surface in the different spectra. Fig.3.36a is the already known vibrational density of states of silicon while Fig.3.36b shows the Raman spectra calculated for silicon bulk and its main peak $\sim 520cm^{-1}$. In Figs.3.36c and 3.36e the surface effects on the VDOS are shown as in 3.35b. In Figs. 3.36d and 3.36f we show the effect of the surfaces in the Raman spectra. In Fig.3.36f the effect on the silicon slab is clear with the adition of a new peak $\sim 575cm^{-1}$, but there is also the same peak in Fig.3.36d which is less visible due to the bulk surface ratio.

(a) VDOS of silicon bulk.

(b) Raman spectra of silicon bulk.

(c) VDOS of Si with a surface.

(d) Raman of Si with a surface.

(e) VDOS of a Si sheet (2 surfaces).

(f) Raman of a Si Sheet (2 surfaces).
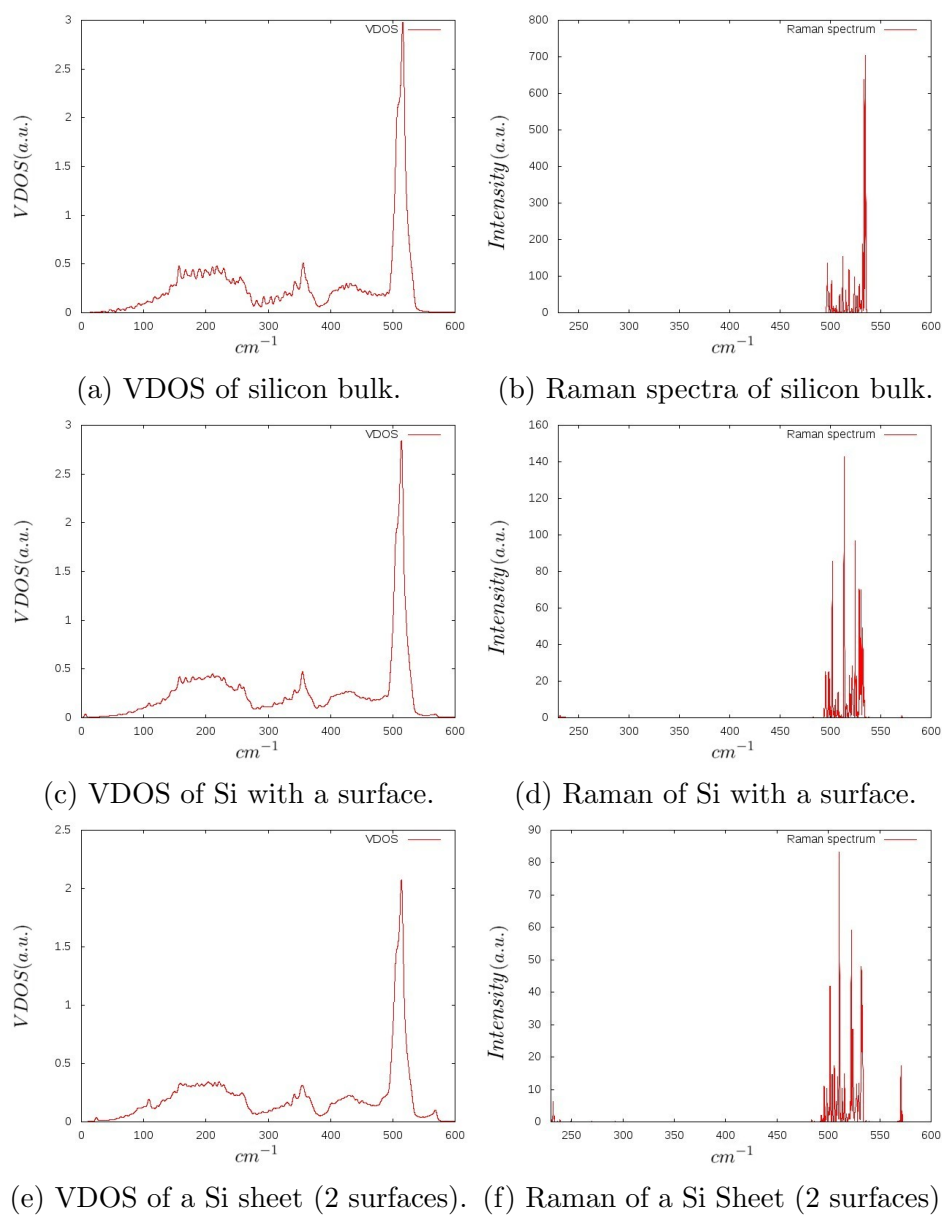
Figure 3.36: Comparatives of VDOS and Raman spectra of Si bulk and surfaces at T=150K.

In Fig.3.37 the effects of the double surface of a thick slab of a $Si_{0.65}Ge_{0.35}$ alloy are shown. Fig.3.37a shows similar characteristics to Figs.3.36. In Fig.3.37b we show the Raman spectrum of the SiGe alloy using the technique shown in subsection 2.3.6 on page 89 while in Fig.3.37c the Raman spectrum is convoluted with a Lorentz function in order to simulate experimental data. In this case, since experimental data are obtained from a sensor of finite dimensions, the collected data are mixed and blurred by the sensor.

We see in Figures 3.37b and 3.37c that the germanium-germanium interactions peak ($\sim 300 cm^{-1}$), the silicon-silicon interactions peak ($\sim 520 cm^{-1}$), and the silicon-germanium interactions ($\sim 400 cm^{-1}$) between those are shifted toward different frequencies, higher for the germanium and lower for the silicon, due to the stress associated with their different lattice constants ($\sim 5.43 \mathring{A}$ for silicon and $\sim 5.64 \mathring{A}$ for germanium).

3.7   Molecular dynamics: Quantum dot (Dome)

A quantum dot is a portion of matter whose three spatial dimensions are small enough to show discretization of the energy bands. This discretization of the quantum dots energy levels make them analogous to individual atoms and molecules. Besides this, it is possible to change (or control) the energy bands by changing their size dimensions.

Quantum dots are of great technological interest. They are particularly significant for optical applications due to their high extinction coefficient. In electronic applications they have been proven to operate like a single electron transistor and show the Coulomb blockade effect. Quantum dots have also been suggested as implementations of qubits for quantum information processing. In biology, quantum dots have been used in dyes due to their brightness and stability. Also they are a promising tool for cancer treatment. When functionalized to selectively bind to tumor cells, they can be used for detection or chemical delivering. Quantum dots may be able to increase the efficiency and reduce the cost of today's typical silicon photovoltaic cells as they can produce multiple excitons from one photon (multiple exciton generation).

Moreover, "dome" quantum dots are unique in having diverse and multiple surface crystallographic planes. Because of this, the vibrational properties of these systems are interesting from both theoretical and experimental point of view. Due to the characteristics of the vibrational density of states, the transport and thermal properties of quantum dots are quite different from the bulk ones.

In this section we are going to discuss the quantum dot under the Molec-
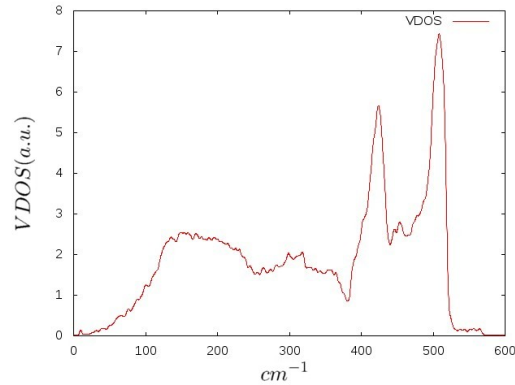
(a) VDOS of a $Si_{0.65}Ge_{0.35}$ alloy with a double surface.
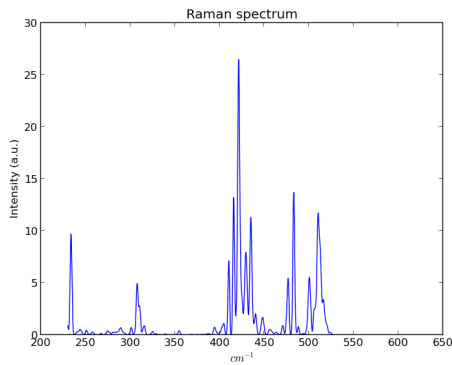
(b) Raman spectrum of a $Si_{0.65}Ge_{0.35}$ alloy with a double surface.
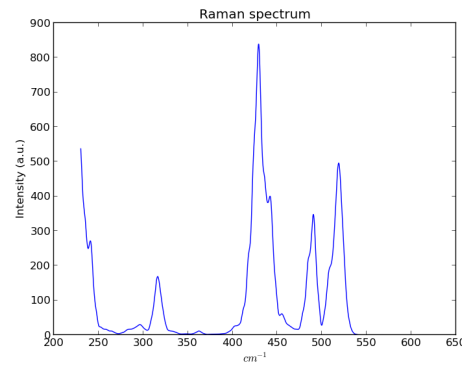
(c) Raman spectrum convoluted with a Lorentzian function of a $Si_{0.65}Ge_{0.35}$ alloy with a double surface.

Figure 3.37: Surface effects on VDOS and Raman spectra of $Si_{0.65}Ge_{0.35}$ alloy.

ular Dynamics method. The quantum dot chosen for the simulations is a "dome" as seen in Fig.2.12.

As defects are important in these systems, we study the differences in the VDOS and Raman spectra of perfect crystalline "domes" against those with a structural dislocation defect so that it is possible to find the differences between those systems. This will allow future analysis of possible defects from the spectra.
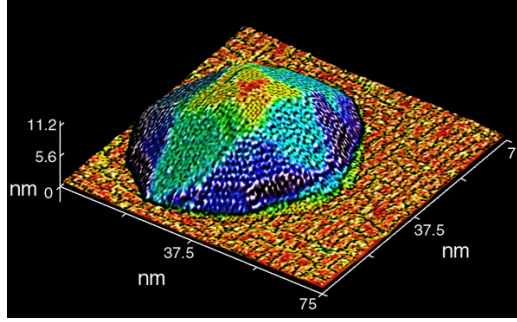
Figure 3.38: An atomic resolution scanning tunneling microscopy image of a Ge dome on a Si (001) surface. Source: Williams et al. [213]

3.7.1   Si and Ge domes

The first step in understanding the different spectra of Si-Ge dome alloys is the analysis of the pure Si and Ge "domes". In Fig.3.39b the vibrational density of states obtained coincide in shape with that previously calculated for the Ge surface in Fig.3.39a. As we see the VDOS does not provide much information about the "dome" structure. The Raman spectra in Fig.3.39c shows differences with the bulk ones (Fig.3.39d). In this case the Raman spectra were calculated three times with the same initial positions but with different random initial velocities (although generating the same temperature), in order to differentiate the spurious effects in the spectrum due to the fact that the molecular dynamics method usually only simulate a few femtoseconds of time, while experimentally the data acquisition takes longer times. Therefore recalculation of the system with different random initial velocities is a quick and poor man approach to longer calculations. In Fig.3.40a the Raman spectra obtained are convoluted with a Lorentzian and in Fig.3.40b the three Raman spectra are summed and convoluted with a Lorentz function to show how the experimental spectra will look like.

3.7.1.1   Displacement defects in the domes

There are two basic ways to reduce tensions between layers in heteroepitaxial growth. One way of release the elastic energy is the formation of coherent three-dimensional islands. The other way is by a plastic relaxation with displacement defects. An intriguing cyclic-growth regime is actually observed experimentally, involving a periodic flattening of the island shape each time a new dislocation nucleates in the island [214]. Thus such dislocations deeply influences the evolution of growing islands at larger volumes.

The displacement defect studied was a 60^0 misfit dislocation similar to

(a) VDOS of a Germanium surface.

(b) VDOS of a Germanium "Dome" quantum dot.

(c) Superposition of three Raman spectra of a Ge dome with different initial random velocities.

(d) Superposition of three Raman spectra of a Ge "Bulk" with different initial random velocities.
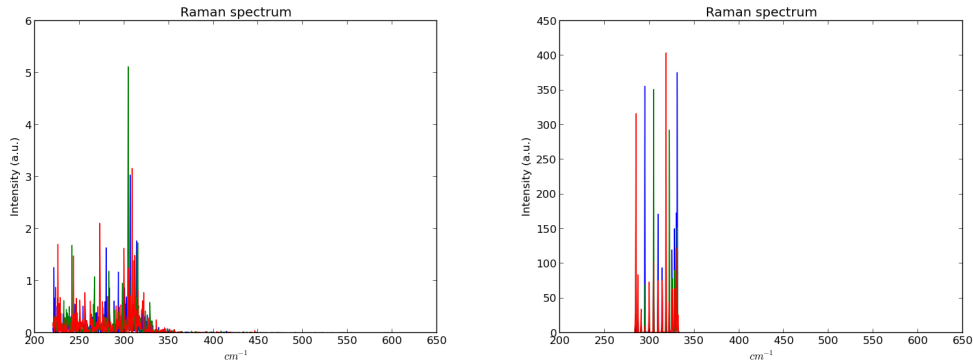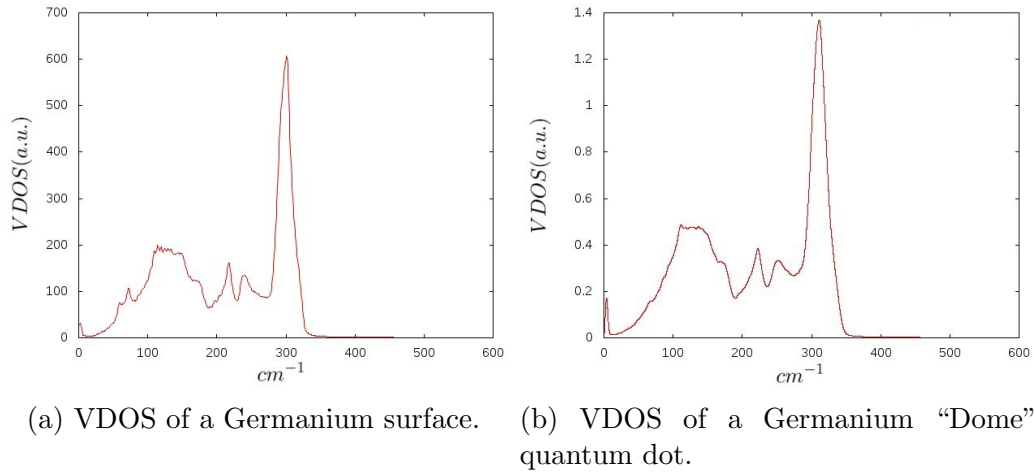
Figure 3.39: VDOS and Raman spectra of a Ge dome at T=150K.

the one shown in Fig.3.41. This defect is located in a point between the "dome" and the substrate.

In Fig.3.42 we compare the effects of the displacement defect on the Raman spectra. It is evident that the main effect of the dislocation is to shift and enlarge the main peak of the Raman spectrum. This is easy to understand because the defect changes the distances between some atoms and therefore there will be new strain effects. This shift and widening of the spectra main peak is visible in Fig.3.42 as there is only one dislocation defect in the interface between the dome and the substrate and therefore the number of atoms directly affected is small. The main Raman Germanium peak will be wider when more displacement defects are present.
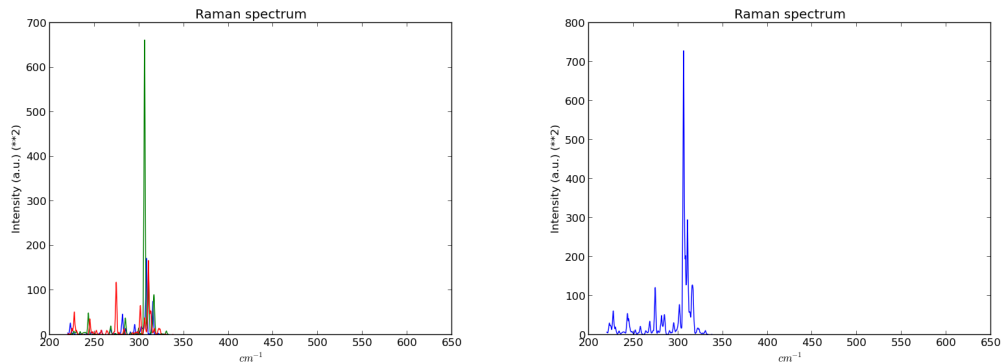
(a) Superposition of Raman spectra con-
voluted with a Lorentzian function of a
Germanium "Dome" quantum dot.

(b) Summation of the three Raman spec-
tra convoluted with a Lorentzian of a Ge
dome with different initial random veloc-
ities.

Figure 3.40: Raman spectra convoluted with a Lorentzian of a Ge dome at
T=150K.
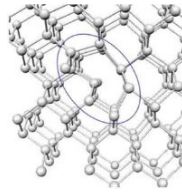
Figure 3.41: Detailed atomistic configuration of a 60^0 dislocation. (Source:
Gatti et al. [214])

3.7.2   Si-Ge alloy domes

3.7.2.1   Homogeneous versus non-homogeneous Si-Ge dome alloy

The VDOS and Raman spectra of an homogeneous $Si_{0.65}Ge_{0.35}$ "dome" are
shown in Fig.3.43. While the VDOS is similar to that of the surface $SiGe$
alloy (Fig.3.43a vs. Fig.3.37a), the Raman spectra are quite different and
more sensitive to the different crystallographic orientations of the surface.
As we see in Fig.3.38 the "dome" has different face orientations. These face
orientations may have different crystallographic surfaces as we can see in
Fig.3.44. These different surface orientations have different vibrations and
this translates into the spectra having slightly different peak positions.

In Fig.3.43b three Raman spectra are compared: the system always starts
with the same positions but the initial random velocities are different by
changing the seed factor in the random number algorithm. As previously
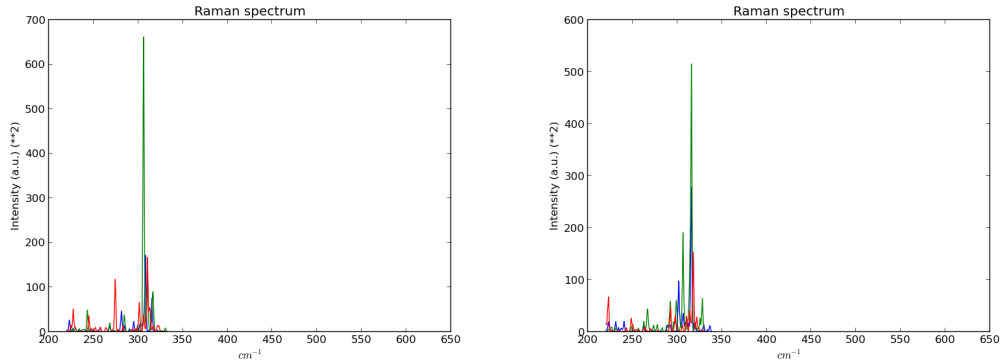
(a) Raman spectra convoluted with a Lorentzian of a perfect Germanium "Dome" quantum dot.

(b) Raman spectra convoluted with a Lorentzian of a Germanium "Dome" quantum dot with displacement defects.
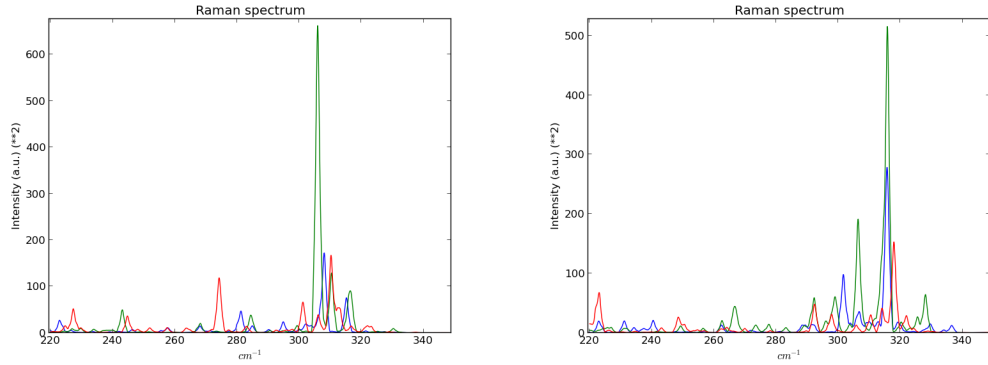
(c) Detail of the Raman spectra convoluted with a Lorentzian of a perfect Germanium "Dome" quantum dot.

(d) Detail of the Raman spectra convoluted with a Lorentzian of a Germanium "Dome" quantum dot with displacement defects.

Figure 3.42: Comparison of the Raman spectra convoluted with a Lorentzian of a Ge dome at T=150K with and without defects.

seen in the pure domes, we simulate the experiments by making a convolution of the calculated spectrum with a Lorentz function. This convolution also smooths the spectra. The differences of the "dome" system and the double surface in Fig.3.37 are obvious in the Raman spectra.

In Figs.3.45 the "dome" is $Si_{0.56}Ge_{0.44}$ in the $\frac{2}{3}$ upper part and $Si_{0.83}Ge_{0.17}$ in the $\frac{1}{3}$ lower part in contact with the Si substrate. This structure is a simplification of the data from Scanning-Probe-Microscopy-based nanotomography obtained by Rastelli et al. [118] for $SiGe$ quantum dots. While the VDOS in Fig.3.45a is almost identical to the homogeneous case (Fig.3.43a), the Ra-
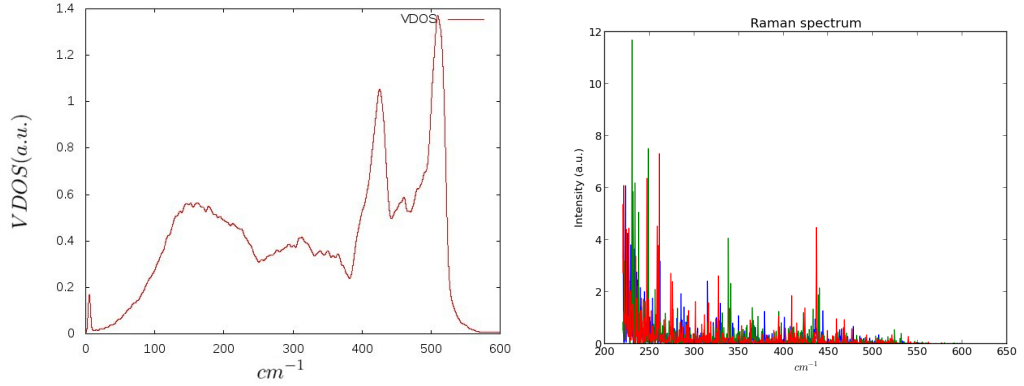
(a) VDOS of an homogeneous Si-Ge "Dome" quantum dot.

(b) Three Raman spectra with different initial random velocities.
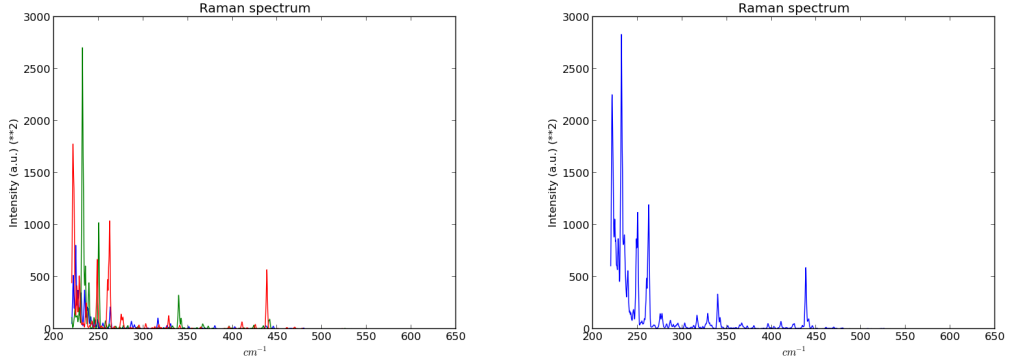
(c) Three Raman spectra convoluted with a Lorentzian.

(d) Summation of three Raman spectra convoluted with a Lorentzian.

Figure 3.43: VDOS and Raman spectra of a $Si_{0.65}Ge_{0.35}$ homogeneous alloy dome at T=150K.

man spectra are quite different, with Fig.3.45b showing Si peaks while in Fig.3.43b the Si-Ge peaks are more prominent. This is due to the fact that in the non-homogeneous dome there is a volume with similar concentrations of both kinds of atoms. This increases the probability to have a $Si - Ge$ interaction with respect to the homogeneous case in which the Si atoms almost double the Ge atoms. This makes, in this case, the Raman spectra a good tool to distinguish between homogeneous and non-homogeneous cases. This means that the Raman spectra help us to distinguish, in a broad way, the amount of different types of neighbours the atoms have by detecting the different inter-atomic bonds. This differentiation is observable in the Raman spectra but not in the VDOS. Raman spectroscopy is able to do this because it detects the vibrational modes near the centre of the Brillouin zone while
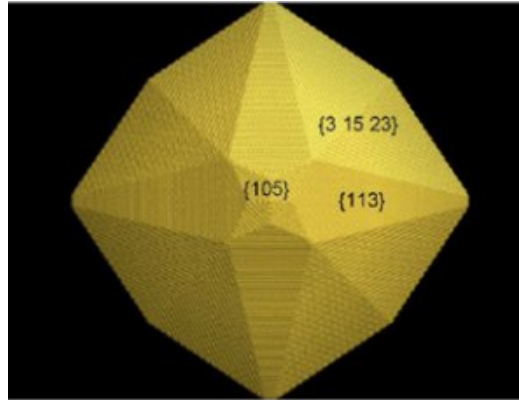
Figure 3.44: Perspective top view of the GeSi faceted dome-shaped structural model on a Si (001) surface. Source: Katcho et al. [215]

the VDOS is over all the Brillouin zone.

3.8 Molecular dynamics: Nanowires

We shall complete the study of the nanostructures with the case of Si nanowires of different cross-sections. These cross-sections are, in particular, square, circular and hexagonal with different sides or radii and grown along the main crystallographic directions.

In recent years the synthesis of radially and axially controlled nanowire systems has allowed the fabrication of novel devices based on nanowires. It has also allowed to produce single crystalline superlattice nanowires and complex core-shell nanostructures in IV and III-V semiconductor materials [216, 217, 218, 219, 220, 221, 222]. The growth of the Ge(Si)/Si(Ge) core-shell nanowires is of great interest due to their potential applications in advanced electronic and optoelectronic devices [223, 224]. Therefore we will also study the case of core-shell nanowires with a Ge core encapsulated/surrounded with Si.

In order to calculate the properties of the nanowires with the molecular dynamics method we used nanowires with 100 unit cells length as we found out that they offered similar spectra as bigger (1000 unit cells) length nanowires, but requiring less computational time.

As in the "dome" case, the VDOS and Raman spectra are obtained for different nanowires. We study nanowires with different cross-sections, as grown by diferent experimental groups.

The nanowires studied by molecular dynamics are composed of silicon atoms grown in wires of square, circular and hexagonal cross section. These
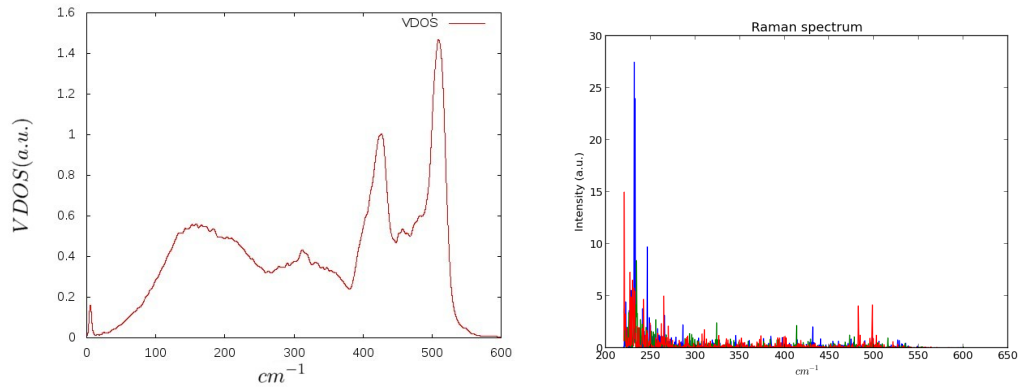
(a) VDOS of an non-homogeneous *SiGe* "Dome" quantum dot.

(b) Three Raman spectra with different initial random velocities.
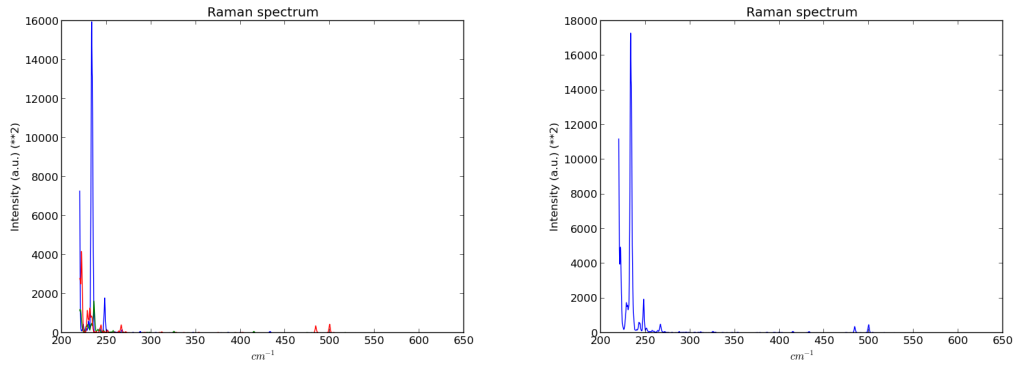
(c) Three Raman spectra convoluted with a Lorentzian.

(d) Summation of three Raman spectra convoluted with a Lorentzian.

Figure 3.45: VDOS and Raman spectra of a *SiGe* non-homogeneous alloy dome at T=150K.

Figure 3.46: Crystallographic orientations.

nanowires were grown along the [001], [011] and [111] crystallographic directions. Also we take into account the different possible orientations of the surface sides in the cases of square and hexagonal cross sections.
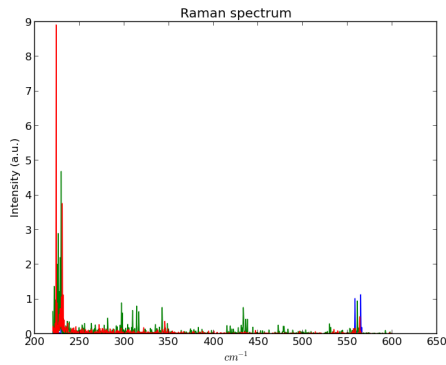
(a) Raman spectra with 3 unit cells cross-section side.
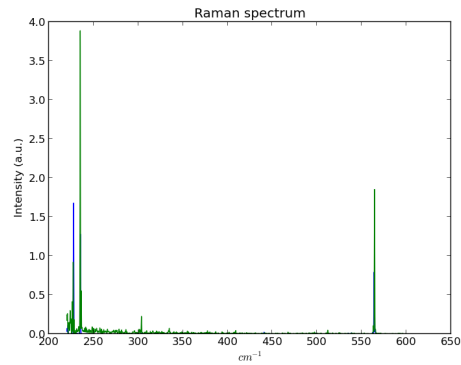
(b) Raman spectra with 3 unit cells cross-section and (011) sides.
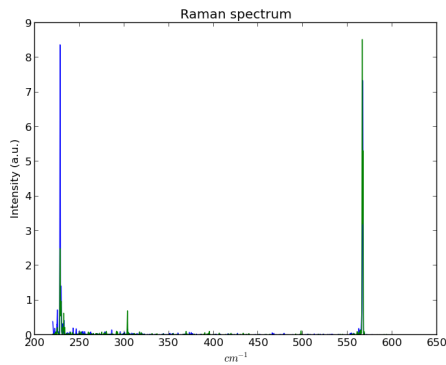
(c) Raman spectra with 5 unit cells cross-section side.
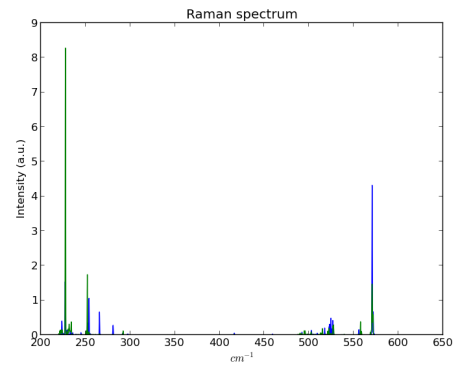
(d) Raman spectra with 5 unit cells cross-section and (011) sides.
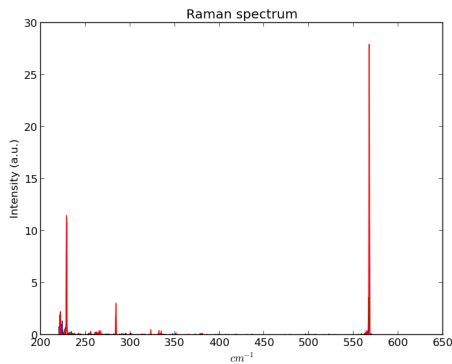
(e) Raman spectra with 7 unit cells cross-section side.
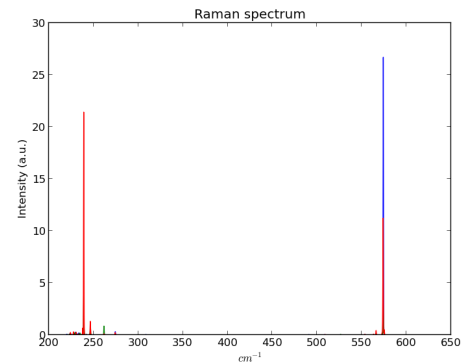
(f) Raman spectra with 7 unit cells cross-section and (011) sides.

Figure 3.47: Raman spectra of a square cross-section Si nanowire of 100 unit cells length [001] at T=150K.

In Fig.3.47 the spectra of a silicon square cross-section nanowire grown along the [001] crystallographic direction are shown. In Figs. 3.47a, 3.47c and 3.47e all the nanowire faces are (001). The main peak of the Raman spectra of the square section nanowire moves and converge as the side increases; this effects are shown in Fig.3.48 and in Table 3.9.

(a) Zoom on the Raman spectra with 3 unit cells cross-section side.

(b) Zoom on the Raman spectra with 5 unit cells cross-section side.

(c) Zoom on the Raman spectra with 7 unit cells cross-section side.
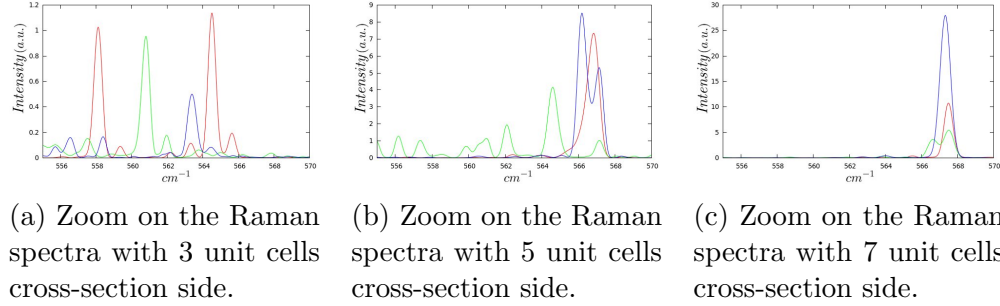
Figure 3.48: Zoom over the main peak of the Raman spectra of a square cross-section Si nanowire of 100 unit cells length [001] at T=150K.

Table 3.9: Position of the main peak(s) of the square cross-section nanowire Raman spectra.

3 unit cells	5 unit cells	7 unit cells
$558.12 \ cm^{-1}$ $564.51 \ cm^{-1}$	$566.83 \ cm^{-1}$	$567.50 \ cm^{-1}$
$560.80 \ cm^{-1}$	$564.61 \ cm^{-1}$	$567.52 \ cm^{-1}$
$563.39 \ cm^{-1}$	$567.13 \ cm^{-1}$	$567.34 \ cm^{-1}$
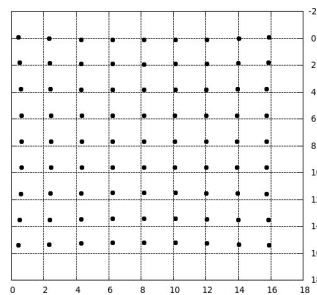
Figure 3.49: Top view of a square cross-section Si nanowire of 100 unit cells length and three unit cell side grown in the [001] direction with (011) sides.

In Figs. 3.47b, 3.47d and 3.47f the spectra correspond to nanowires having two (001) crystallographic surfaces and the other two being (011) crystallographic surfaces. As we can see there is a shift of the main Si peak

that implies compression forces on the (011) faces according to what we saw in Fig.3.34. This strain may come from surface deformation of the (011) faces. This deformation can be seen in Fig.3.49 where the sides of the square cross-section are slightly curved.
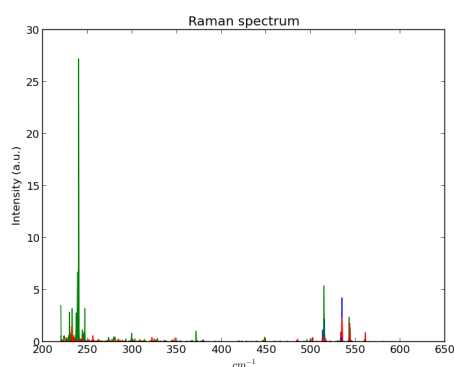
(a) Three Raman spectra of a Si nanowire with square cross-section of 3 unit cells side.
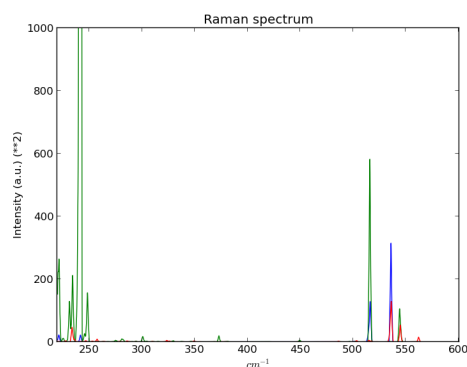
(b) Three Raman spectra convoluted with a Lorentzian of a Si nanowire with square cross-section of 3 unit cells side.
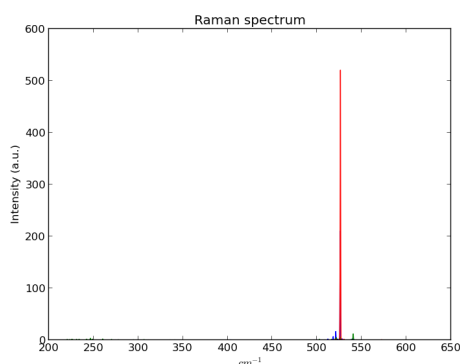
(c) Three Raman spectra of a Si nanowire with square cross-section of 5 unit cells side.
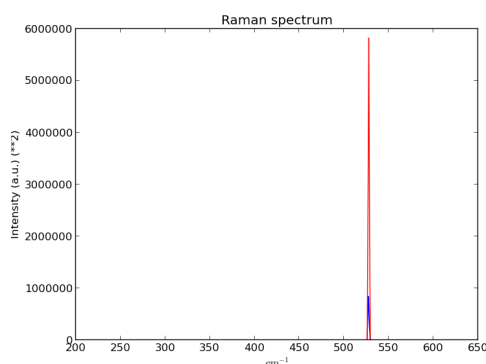
(d) Three Raman spectra convoluted with a Lorentzian of a Si nanowire with square cross-section of 5 unit cells side.

Figure 3.50: Raman spectra of a square cross-section Si nanowire of 100 unit cells length [011] at T=150K.

In Fig.3.50 the square cross-section nanowires are grown in the [011] direction. Fig.3.50a shows three Raman spectra of the Si nanowire of three unit cells side. Here the main peak of the Si spectra is not as clear as in Fig.3.50c but we can see that the peaks are in a position similar to those of the relaxed "bulk" (~ 520 cm^{-1}). In Fig.3.50b we convolute the Raman

spectra of the three unit cells square cross-section side with a Lorentzian function in order to simulate the experimental data. In Fig.3.50d the same operation is done to simulate the experimental data of a five unit cells side square cross-section nanowire.

We note here that the five unit cells side Raman spectrum is more "clear" and more similar to the bulk spectra than the three unit cells one. This can be easily explained by considering that as the wire radius grows, its surfaces effect behaviour is expected to decrease and thus the bulk behaviour becomes more visible.

In Fig.3.51 the square cross-section nanowires are grown in the [111] direction. In Figs.3.51a and 3.51c three Raman spectra of three unit cells and five unit cells each are shown. In those spectra the main peak of the Si Raman is as expected, but the same peak has less intensity in Fig.3.51e. In Figs. 3.51b, 3.51d and 3.51f the Raman spectra are convoluted with a Lorentzian function.

Finally in Fig.3.52 the square cross-section nanowires are also grown in the [111] direction but with suitable dimension for a better comparison with the section area of the circular and hexagonal nanowires, since the area of the hexagon is larger than the area of a square having the same size on its side, but smaller than the area of a square whose side has twice the side of the hexagon. Fig.3.52a shows three Raman spectra of six unit cells side [111] cross-section square nanowire, while in Figs.3.52c and 3.52e the 10 and 14 unit cells are shown. The Raman spectra convoluted with Lorentzian of those nanowires are shown in Figs. 3.52b, 3.52d and 3.52f. Here we observe that in Fig.3.52d one of the calculations gives a huge $\sim 400\ cm^{-1}$ signal while the other two give signals comparable to the $\sim 550\ cm^{-1}$ one, although slightly bigger. The $\sim 400\ cm^{-1}$ signal is also present but clearly smaller in Fig.3.52f. When comparing the Raman spectra of Fig.3.52d and Fig.3.51f we find a very small signal for the Si main peak ($\sim 550\ cm^{-1}$) whereas there is a bigger signal for the $\sim 400\ cm^{-1}$ peak. It is interesting that the same effect happens for those nanowires of "similar" dimensions.
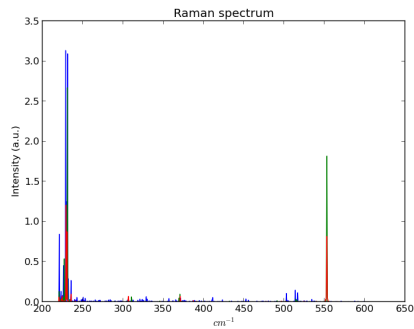
(a) Raman spectra of a 3 unit cells cross-section side nanowire.
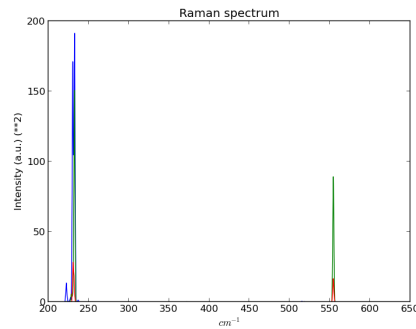
(b) Three Raman spectra convoluted with a Lorentzian of a 3 unit cells side nanowire.
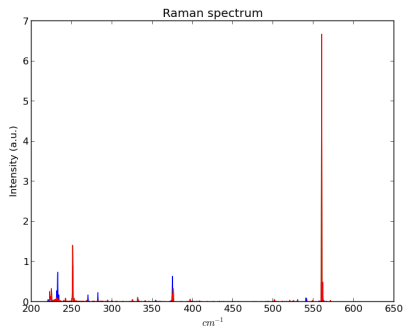
(c) Raman spectra of a 5 unit cells cross-section side nanowire.
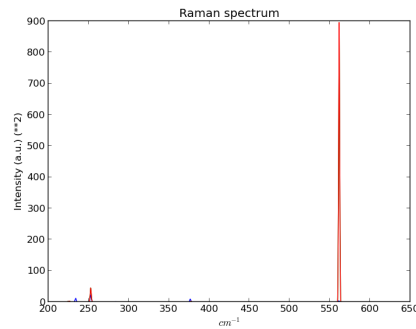
(d) Three Raman spectra convoluted with a Lorentzian of a 5 unit cells side nanowire.
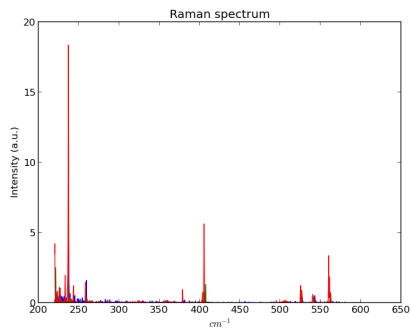
(e) Raman spectra of a 7 unit cells cross-section side nanowire.
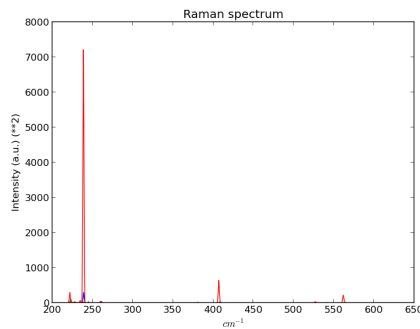
(f) Three Raman spectra convoluted with a Lorentzian of a 7 unit cells side nanowire.

Figure 3.51: Raman spectra of a square cross-section Si nanowire of 100 unit cells length [111] at T=150K.
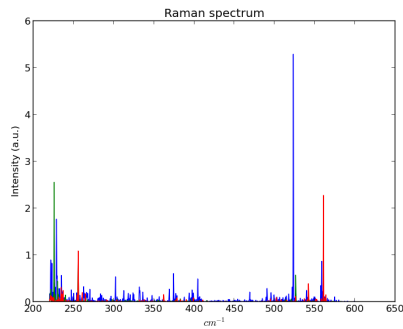
(a) Raman spectra of a 6 unit cells cross-section side nanowire.
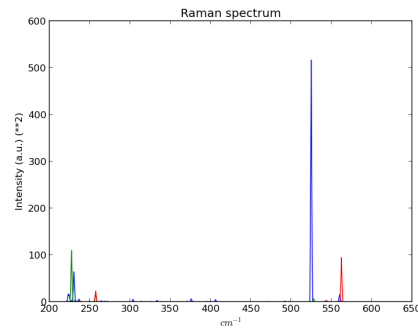
(b) Three Raman spectra convoluted with a Lorentzian of a 6 unit cells side nanowire.
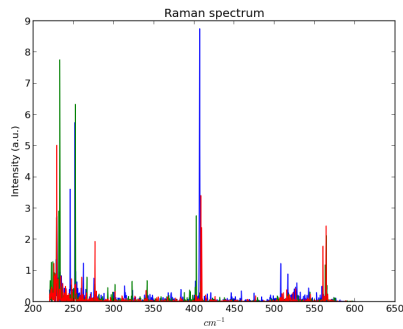
(c) Raman spectra of a 10 unit cells cross-section side nanowire.
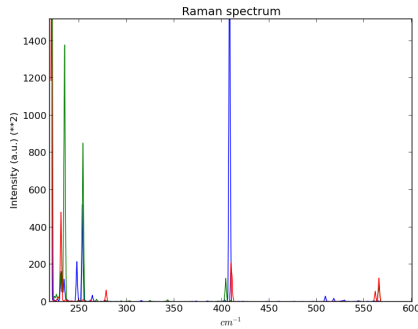
(d) Three Raman spectra convoluted with a Lorentzian of a 10 unit cells side nanowire.
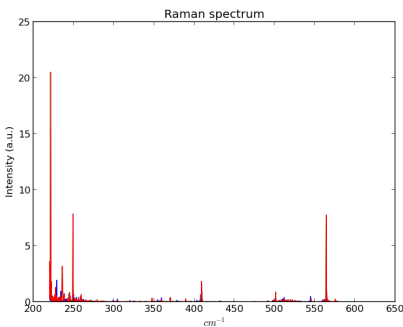
(e) Raman spectra of a 14 unit cells cross-section side nanowire.
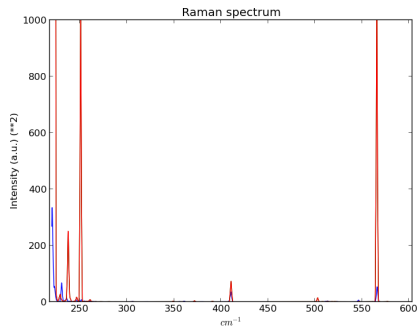
(f) Three Raman spectra convoluted with a Lorentzian of a 14 unit cells side nanowire.

Figure 3.52: Raman spectra of a square cross-section Si nanowire of 100 unit cells length [111] and cross-sections sizes comparable to the hexagonal and circular cases, at T=150K.
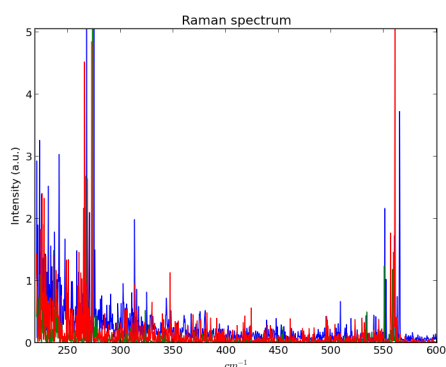
(a) Three Raman spectra of a circular cross-section 3 unit cells radius nanowire.
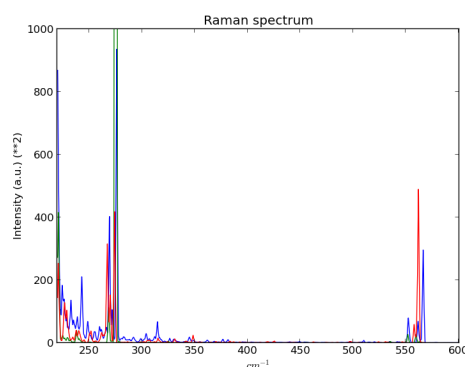
(b) Three Raman spectra convoluted with a Lorentzian of circular cross-section 3 unit cells radius nanowire.
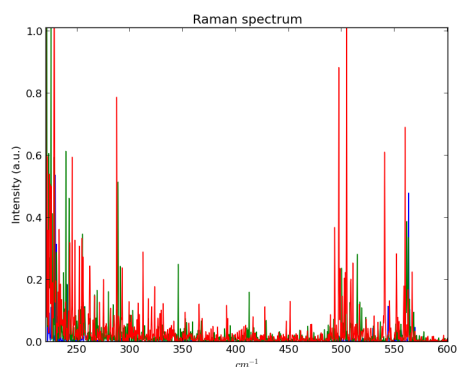
(c) Three Raman spectra of a circular cross-section 5 unit cells radius nanowire.
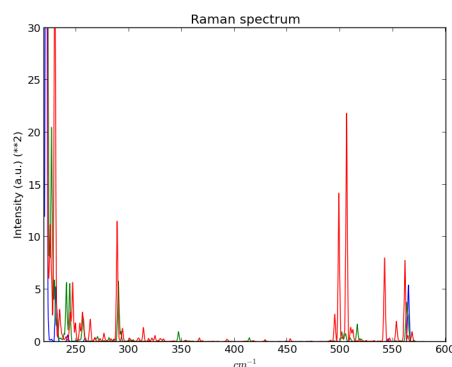
(d) Three Raman spectra convoluted with a Lorentzian of circular cross-section 5 unit cells radius nanowire.

Figure 3.53: Raman spectra of a circular cross-section Si nanowire of 100 unit cells length [001] at T=150K.

In Fig.3.53 the Raman spectra of a cylindrical Si nanowire grown in the [001] direction are shown. In Fig.3.53a and 3.53c the Raman spectra of three and five unit cells radius cylindrical nanowire show more "noise[1]" than in the square cross-section cases as now the surface cannot be associated to a single crystallographic direction, so here we have a situation more similar to the "dome" system. In Figs. 3.53b and 3.53d the convolution of the spectra with a Lorentzian shows us several main peaks for the cylindrical case. This

---

[1]The origin of this "noise" are the different strains that provoke displacements and splitting (due to the breaking of the degeneracy) of the Raman peaks, as discussed in Section 3.5.2

means that there are different strains in the material depending mostly on the surface orientation. Also in some cases there are important secondary peaks as shown for the five unit cells radius in figure (3.53d).

In Fig.3.54 the spectra of a cylindrical Si nanowire grown along the [011] direction are shown. Here, as we see in Figs.3.54a and 3.54c the spectra are not "noisy" as compared to the [001] cases. This could mean that the [011] growth direction is more stable than the [001] for cylindrical nanowires.
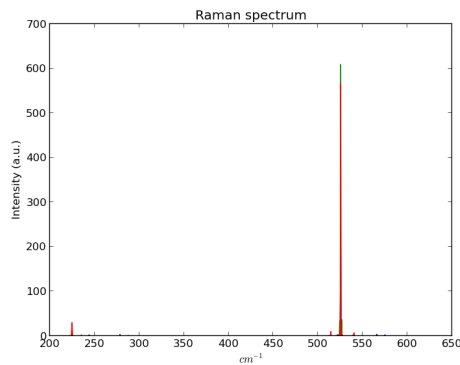
(a) Three Raman spectra of a Si cylindrical nanowire with 3 unit cells radius.
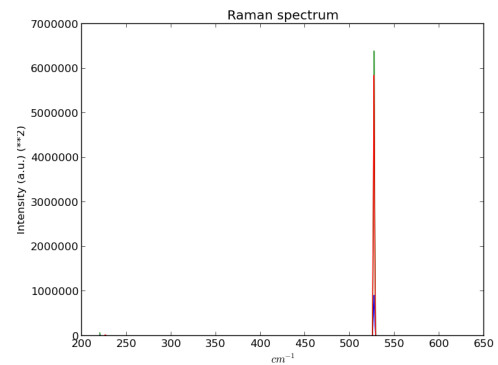
(b) Raman spectra convoluted with a Lorentzian of a 3 unit cells radius cylindrical nanowire.
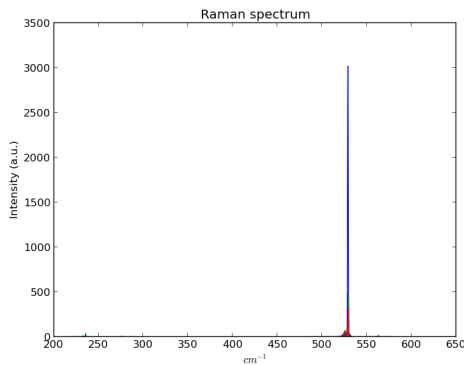
(c) Three Raman spectra of a Si nanowire with circular cross-section of 5 unit cells radius.
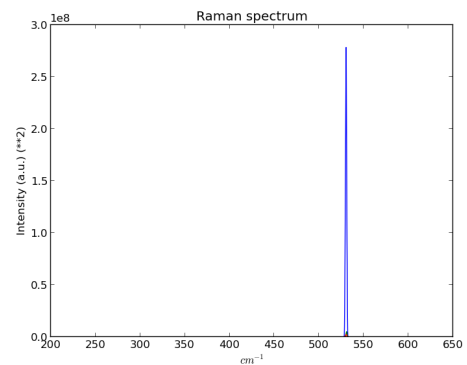
(d) Raman spectra convoluted with a Lorentzian of a 5 unit cells radius cylindrical nanowire.

Figure 3.54: Raman spectra of a circular cross-section Si nanowire of 100 unit cells length [011] at T=150K.

In Fig.3.55 the spectra of a cylindrical Si nanowire grown in the [111] direction are shown. Fig.3.55a shows more "noise" than the [011] cases but

less than the [001] cases. The dramatic signal reduction for the Si main peak seen in the case of the square nanowire with 10 unit cells side grown along [111] is also present for the circular nanowire grown along [111] with five unit cells radius.
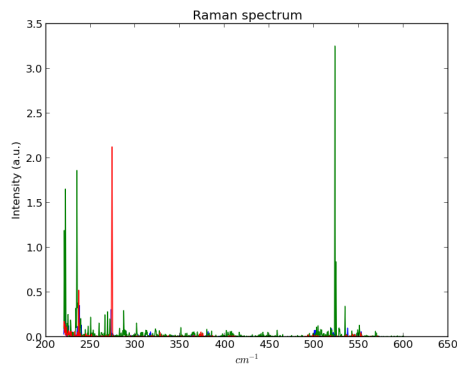
(a) Three Raman spectra of a Si cylindrical nanowire with 3 unit cells radius.
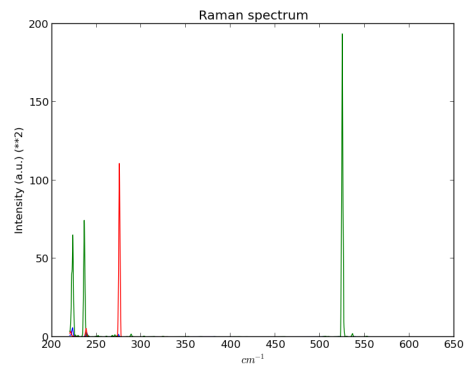
(b) Raman spectra convoluted with a Lorentzian of a 3 unit cells radius cylindrical nanowire.
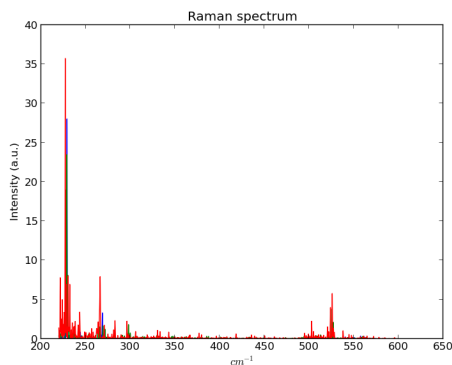
(c) Three Raman spectra of a Si cylindrical nanowire with 5 unit cells radius.
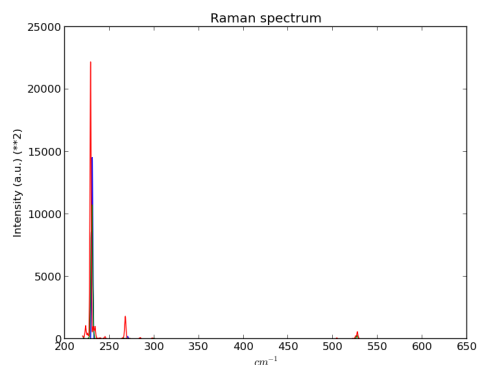
(d) Raman spectra convoluted with a Lorentzian of a 5 unit cells radius cylindrical nanowire.

Figure 3.55: Raman spectra of a circular cross-section Si nanowire of 100 unit cells length [111] at T=150K.

(a) Si nanowire grown in   (b) Si nanowire grown in   (c) Si nanowire grown in
the [001] direction.   the [011] direction.   the [111] direction.
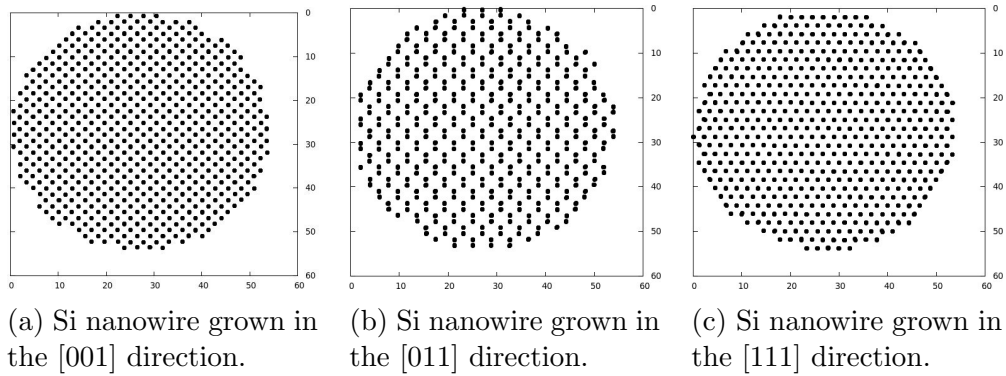
Figure 3.56: Top view of circular cross-sections Si nanowires of 100 unit cells
length and five unit cell radius grown in diferent directions.

In Fig.3.56 we show the top-view of the circular cross-section Si nanowires
studied here. We can see in these top-views the projection of the crystalline
structure on a plane perpendicular to the length of the nanowire.
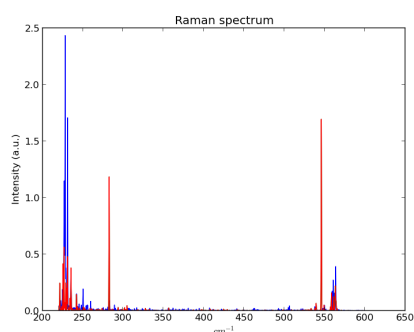
(a) Three Raman spectra of an hexagonal cross-section nanowire of 3 unit cells side.
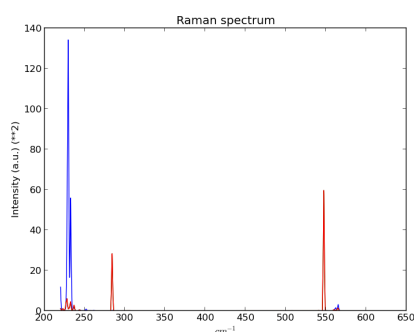
(b) Raman spectra convoluted with a Lorentzian of a 3 unit cells side hexagonal cross-section nanowire.
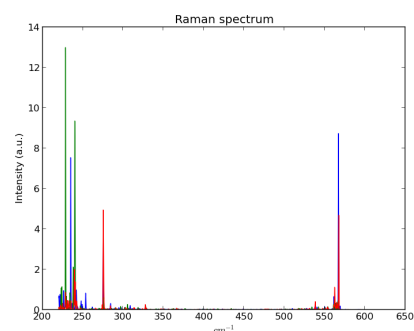
(c) Three Raman spectra of an hexagonal cross-section nanowire of 5 unit cells side.
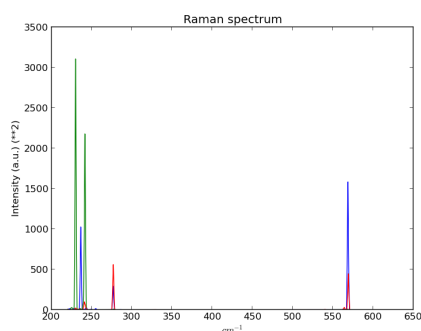
(d) Raman spectra convoluted with a Lorentzian of a 5 unit cells side hexagonal cross-section nanowire.
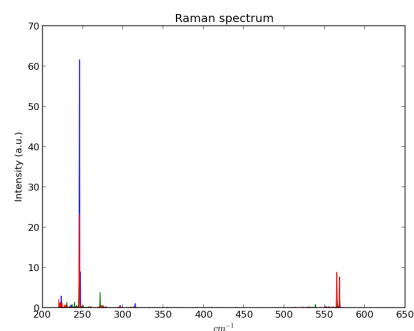
(e) Three Raman spectra of an hexagonal cross-section nanowire of 7 unit cells side.

(f) Raman spectra convoluted with a Lorentzian of a 7 unit cells side hexagonal cross-section nanowire.

Figure 3.57: Raman spectra of a hexagonal cross-section Si nanowire of 100 unit cells length [001] at T=150K.

In Fig.3.57 the spectra of a hexagonal cross-section nanowire grown along the [001] direction are shown.

(a) Si nanowire with two (001) faces.

(b) Si nanowire with two (011) faces.
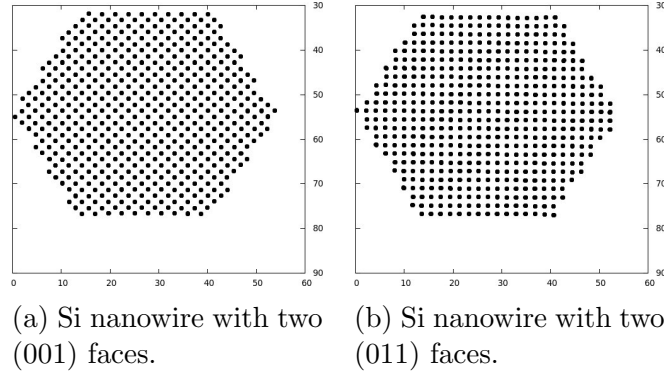
Figure 3.58: Top view of hexagonal cross-sections Si nanowires of 100 unit cells length and five unit cell radius grown in the [001] direction.

The hexagonal nanowires of Fig.3.57 are constructed with two (001) faces[2]. In Fig.3.59 we put those two faces with the [011] crystallographic directions[3]. The top view of this kind of nanowires are shown in Fig.3.58. We put these faces in this crystallographic orientation by rotating the crystal along the growth axis before "cutting" the faces of the nanowire. The 45^0 rotation on the long axis that we applied changes two of the sides from the crystallographic orientation [001] to [011]. In this way we can look for differences in the spectra as the faces of an hexagon are at 60^0 while a (011) face is at 45^0 from a (001). The Raman spectra of the "(011) faces" nanowires show an important decrease in the intensity of the $\sim 500\ cm^{-1}$ peaks. This effect is independent of the cross-section size, thus we cannot assume that the origin of this effect is the finite dimensionality but that it is related to the faces orientation.

---

[2]The other faces are $(0, \frac{2521}{2911}, \frac{1}{2}) \simeq (0, 5, 3)$.
[3]The other faces are $(0, \frac{2911}{7953}, \frac{7953}{5822}) \simeq (0, 3, 10)$.
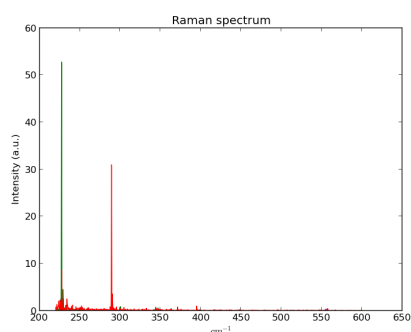
(a) Three Raman spectra of an hexagonal cross-section nanowire of 3 unit cells side.
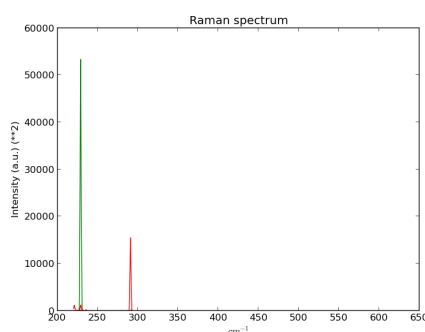
(b) Raman spectra convoluted with a Lorentzian of a 3 unit cells side hexagonal cross-section nanowire.
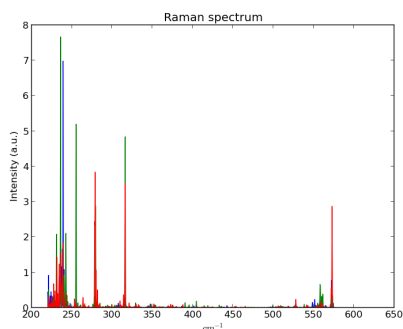
(c) Three Raman spectra of an hexagonal cross-section nanowire of 5 unit cells side.
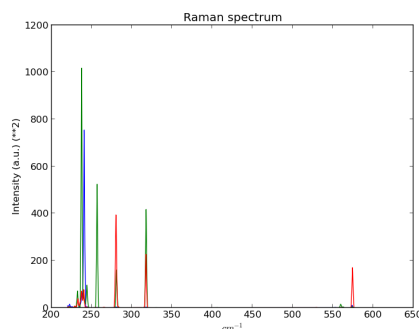
(d) Raman spectra convoluted with a Lorentzian of a 5 unit cells side hexagonal cross-section nanowire.
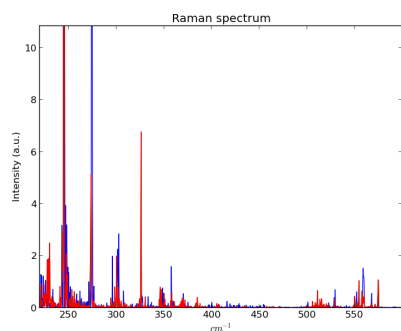
(e) Three Raman spectra of an hexagonal cross-section nanowire of 7 unit cells side.

(f) Raman spectra convoluted with a Lorentzian of a 7 unit cells side hexagonal cross-section nanowire.

Figure 3.59: Raman spectra of a hexagonal cross-section Si nanowire of 100 unit cells length [001] at T=150K and made with two (011) faces.

(a) Si nanowire with two (001) faces.

(b) Si nanowire with two (011) faces.
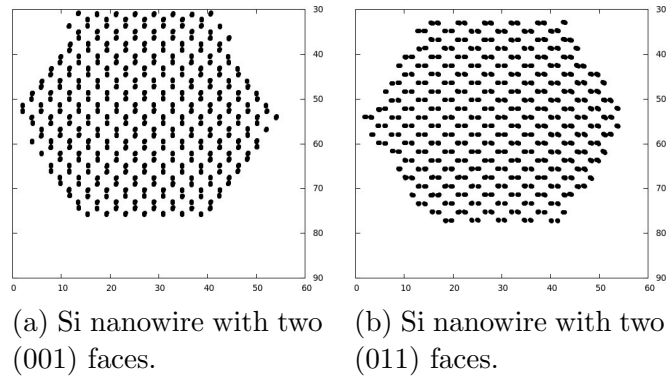
Figure 3.60: Top view of hexagonal cross-sections Si nanowires of 100 unit cells length and five unit cell radius grown in the [011] direction.

In Fig.3.61 the spectra of a hexagonal cross-section nanowire grown in the [011] direction are shown. The top view of this kind of nanowire is shown in Fig.3.60a. These Raman spectra are quite similar to the bulk, with the exception of the 200-250 cm^{-1} peaks that exhibit most of the nanowires.

As in the previous situation, we calculate in Fig.3.61 the [011] case with two (001) faces, and now we study the case with two (011) faces. This configuration has a top view configuration shown in Fig.3.60b. In Figs.3.62 the Raman spectra are similar to the previous case (Fig.3.61). The 90^0 rotation on the long axis that we applied changes two of the sides from the crystallographic orientation [001] to [011] as we can see in Fig.3.46.

In Fig.3.64 the spectra of the hexagonal nanowire grown in the [111] direction are shown. As we can see in Fig.3.63 where the top view of this kind of nanowire is shown, this configuration fits with the regular hexagon for several units cells of the diamond structure as the sides of the hexagon and the crystallographic faces orientation are very similar.
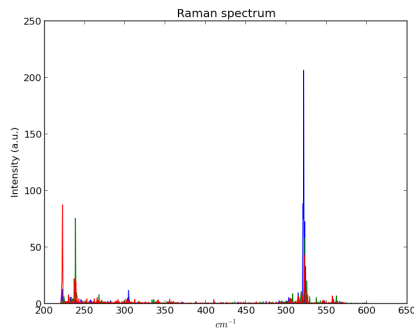
(a) Three Raman spectra of an hexagonal cross-section nanowire of 3 unit cells side.
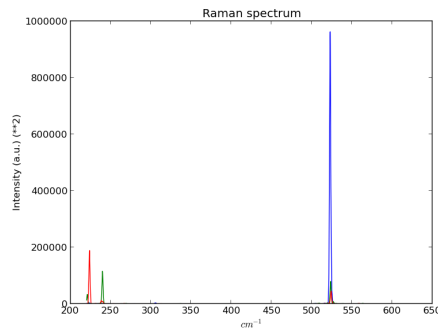
(b) Raman spectra convoluted with a Lorentzian of a 3 unit cells side hexagonal cross-section nanowire.
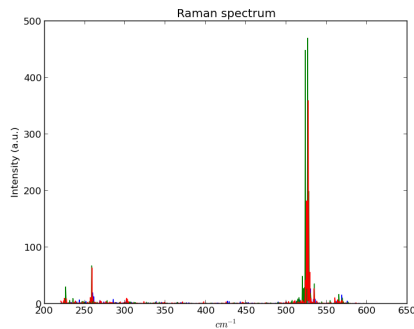
(c) Three Raman spectra of an hexagonal cross-section nanowire of 5 unit cells side.
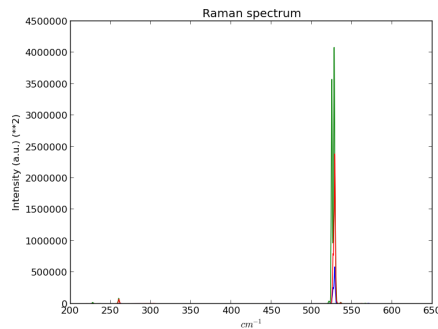
(d) Raman spectra convoluted with a Lorentzian of a 5 unit cells side hexagonal cross-section nanowire.
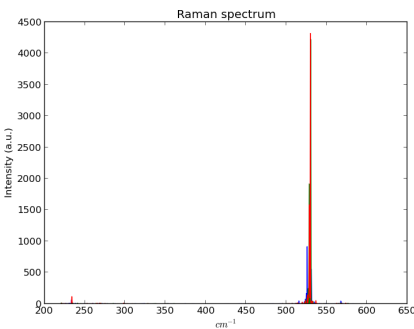
(e) Three Raman spectra of an hexagonal cross-section nanowire of 7 unit cells side.

(f) Raman spectra convoluted with a Lorentzian of a 7 unit cells side hexagonal cross-section nanowire.

Figure 3.61: Raman spectra of a hexagonal cross-section Si nanowire of 100 unit cells length [011] at T=150K.

(a) Three Raman spectra of an hexagonal cross-section nanowire of 3 unit cells side.
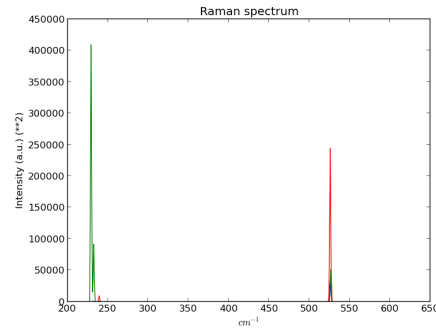
(b) Raman spectra convoluted with a Lorentzian of a 3 unit cells side hexagonal cross-section nanowire.
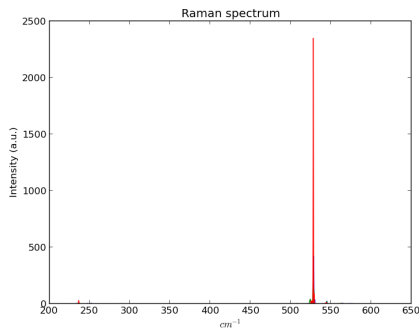
(c) Three Raman spectra of an hexagonal cross-section nanowire of 5 unit cells side.
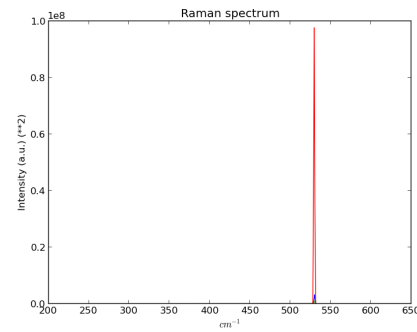
(d) Raman spectra convoluted with a Lorentzian of a 5 unit cells side hexagonal cross-section nanowire.
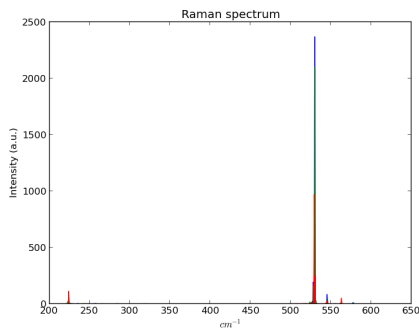
(e) Three Raman spectra of an hexagonal cross-section nanowire of 7 unit cells side.

(f) Raman spectra convoluted with a Lorentzian of a 7 unit cells side hexagonal cross-section nanowire.

Figure 3.62: Raman spectra of a hexagonal cross-section Si nanowire of 100 unit cells length [011] at T=150K and rotated 45^0 on the long axis.
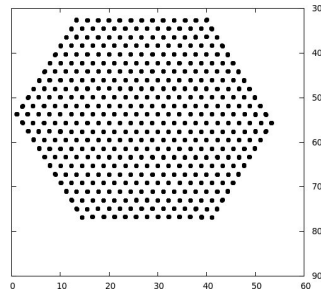
Figure 3.63: Top view of hexagonal cross-sections Si nanowires of 100 unit cells length and five unit cell radius grown in the [111] direction.

In these Raman spectra there is a visible $\sim 400 \ cm^{-1}$ (LO) peak as in the cases of square cross-sections nanowires grown in the same crystallographic direction. This peak is related to the (longitudinal) optical phonons in other points of the Brillouin zone. In general the spectra of the hexagonal nanowire are qualitatively similar to those of the cylindrical nanowire. On the other hand, the attenuation effect on the $\sim 550 \ cm^{-1}$ peak of the nanowires with diameters of 10 unit cells seen in the cases of the square and circular cross-sections is not evident in the five unit cell hexagonal cross-section side nanowires. As we see in Fig.3.63 the hexagonal cross-section nanowires grown in the [111] direction have quite regular (011) faces. Thus probably the attenuation of the $\sim 550 \ cm^{-1}$ peak may be linked to the non-(011) faces.
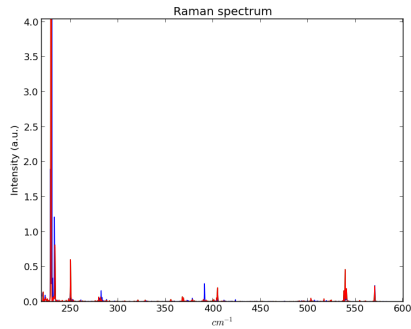
(a) Three Raman spectra of an hexagonal cross-section nanowire of 3 unit cells side.
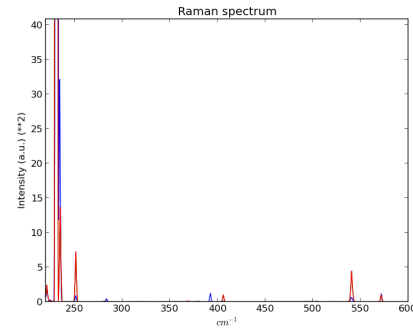
(b) Raman spectra convoluted with a Lorentzian of a 3 unit cells side hexagonal cross-section nanowire.
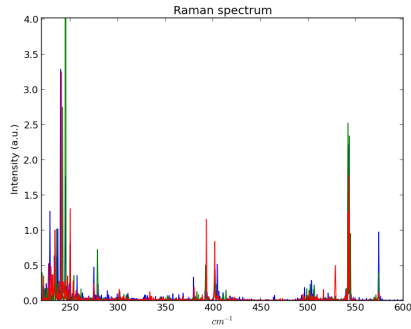
(c) Three Raman spectra of an hexagonal cross-section nanowire of 5 unit cells side.
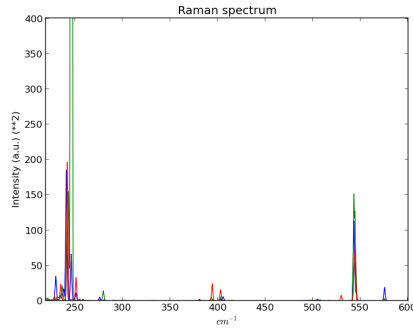
(d) Raman spectra convoluted with a Lorentzian of a 5 unit cells side hexagonal cross-section nanowire.
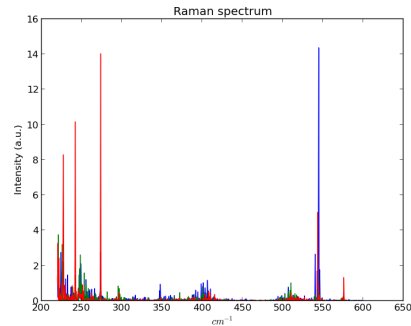
(e) Three Raman spectra of an hexagonal cross-section nanowire of 7 unit cells side.

(f) Raman spectra convoluted with a Lorentzian of a 7 unit cells side hexagonal cross-section nanowire.

Figure 3.64: Raman spectra of a hexagonal cross-section Si nanowire of 100 unit cells length [111] at T=150K.
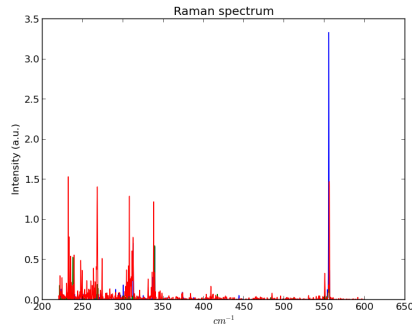
(a) Raman spectra of a [001] core-shell.
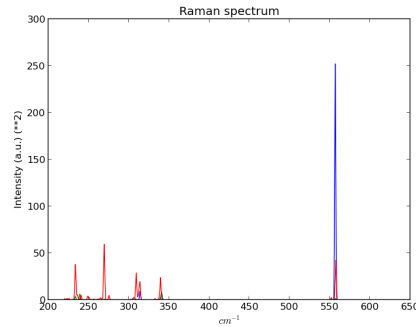
(b) Three Raman spectra convoluted with a Lorentzian of a [001] core-shell nanowire.
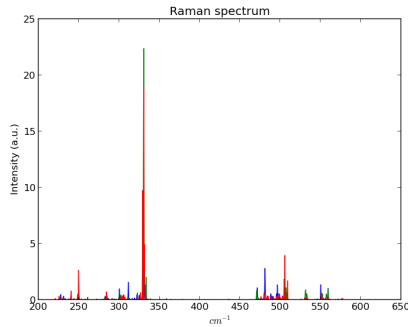
(c) Raman spectra of a [011] core-shell nanowire.
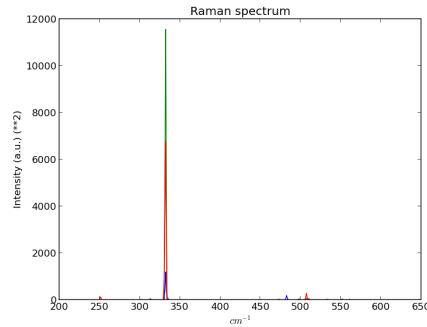
(d) Three Raman spectra convoluted with a Lorentzian of a [011] core-shell nanowire.
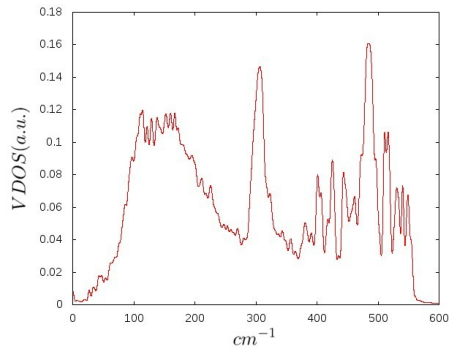
(e) VDOS of a [001] core-shell nanowire.
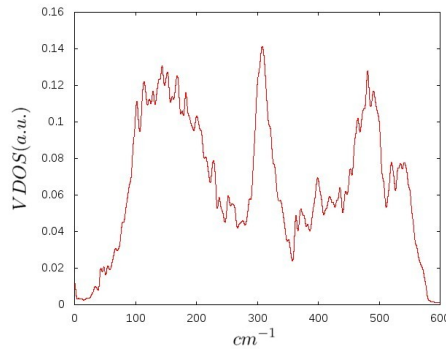
(f) VDOS of a [011] core-shell nanowire.

Figure 3.65: Raman spectra and VDOS of a cylindrical cross-section core-shell nanowire of 100 unit cells length at T=150K.

Finally, core-shell cylindrical nanowires with a Ge core of three unit cells

radius and a Si shell of four unit cells radius (one unit cell thickness) are shown in Fig.3.65. In Fig.3.65a the core-shell nanowire is grown in the [001] direction while in Fig.3.65c the wire is grown in the [011] direction.

As we see in Figs. 3.65e and 3.65f it is difficult to distinguish the crystallographic orientation of the nanowires by means of the VDOS but it is easy with the Raman spectra (Fig.3.65b for the [001] case and Fig.3.65d for the [011] case). Figs.3.65a and 3.65b show a strong influence of the Si shell on the Raman spectra while in Figs. 3.65c and 3.65d the main signal comes from the Ge core. This strong dependence of the Raman spectra on the crystallographic orientation can be explained through the Raman spectra of the cylindrical Si nanowires. Previously, in the Si nanowire of circular cross-section, the main peak ($\sim 500\ cm^{-1}$) was stronger in the nanowire grown in the [011] crystallographic direction than in the [001] case. Thus we have here that in Fig.3.65d the Ge peak is masking the rest of the signal.

The VDOS (Figs.3.65e and 3.65f) of the core-shell systems compared to the VDOS of the Ge surface and "dome" (Figs. 3.39a and 3.39b) and the VDOS of the Si bulk and surface (Fig. 3.35) show that the acoustic intensity maxima is at the same level as the Ge-Ge and Si-Si peaks. Due to the fact that in the Si-Ge homogeneous "dome", the Ge is always mixed with Si, then it is not possible to see the Ge-Ge peak. On the other hand, in the core-shell nanowire the Ge-Si interactions are restricted to the neighbourhood of the core-shell interface region. This translates in the presence of a visible Ge-Ge peak in the VDOS. The Si shell is also under strain, and this shows mainly in the region close to the Si peak at high frequency.

We have obtained a way to identify a variety of nanowires by means of the Raman spectra. The VDOS of different nanowires showed the same structure regardless of the cross-section shape, therefore it was not useful for the identification or characterisation of the nanowires. On the other hand, the Raman spectra are sensitive to the cross-section shape. They are sensitive also to the different crystallographic surfaces present in the nanowire. We have found a drastic reduction of the $\sim 550 cm^{-1}$ peak in some cases (square and circular nanowires with 10 unit cells side). More work is needed to explain why this effect is not observed in the hexagonal equivalent nanowire.

Chapter 4

Concluding remarks and expectatives

In this work we have studied the vibrational properties of nanostructures by means of theoretical simulation techniques. The vibrational properties of these systems play an important role in many phenomena, but they have been less studied than their electronic and optical counterparts.

The nanostructures studied here such as nanowires, domes (quantum dots) and superlattices are of current interest and they are being grown in different laboratories in increasing number and for different materials. These systems are of great interest because of their potential technological applications in various fields. Due to the different experimental techniques employed to produce these nanostructures, there is a wide dispersion in the quality of the samples. The simulation techniques employed in our studies are well adapted to obtain characteristics of the vibrational properties of these systems with a reasonable computing cost.

We have considered two different approaches to study the vibrational properties: the continuum approach based on the linear elasticity theory, and the discrete medium approach based on molecular dynamics methods. In our studies we have worked on various systems with different sizes to see the dimensional behaviour of these effects. In the case of quantum dots we have studied different systems with and without structural dislocation defects to ascertain their effects on the vibrational properties. The use of techniques based in the continuum model and the discrete one allows for complementary approaches to the study of these phenomena.

Within the continuum model, based on the linear theory of elasticity, we obtained a general expression for the frequencies of the acoustic radial modes of nanowires, nanotubes and the secular determinants for the "core-shell" systems and circular cross-section "composites", having a general cylindrical

anisotropy, as they are a characteristic signature in the spectra. The results obtained for this kind of *Si*, *ZnO*, *GaN*, *Au*, *Ag* and *CdSe* nanosystems gave excellent agreement when compared to the experimental results [226].

In the case of nanostructures based on elastically anisotropic materials and having non-circular cross-section no closed form solution is possible. In this case a flexible technique based on the methods employed for the study of resonant ultrasonic scattering [34] (method *"XYZ"*) can be employed. We have expanded this technique in order to study hexagonal cross-sections prisms [227]. This shape is presented by many nanowires of different materials grown experimentaly. In this way we have obtained the dispersion curves and the displacement vectors for many nanowires of materials belonging to the hexagonal and cubic systems.

Multilayer systems constitute another area of interest. III–nitrides and *MgO/ZnO* superlattices are very interesting systems because of their potential applications in different areas of micro and nano-electronics. To study their vibrational properties we have employed the "Surface Green Function Matching" (SGFM) method [40]. This method is specially well adapted to study multilayer systems of materials with elastic anisotropy. We studied the properties of periodic and aperiodic superlattices of these materials for different relative thicknesses of the constituent materials. Because these materials belong to the hexagonal crystal, there is a decoupling of the transverse and sagittal vibrations, when grown along the C-axis. The existence of two transverse thresholds in this case, opens interesting possibilities not present in isotropic materials with only a transverse wave threshold or more anisotropic materials where all the polarisations mix [228]. Structures including aperiodic blocks show localised modes with selective spatial localisation. Therefore they could be used as frequency filters [229].

The discrete media model based on the Molecular Dynamics technique generally provides more accurate results and a higher range of validity than those based on the continuum model, albeit with a higher computational cost. The method used in this thesis is the Molecular Dynamics based on empirical potentials, and specifically the Tersoff potential for silicon and germanium, using Verlet algorithm for time integration. From the molecular dynamics simulation it was obtained the vibrational density of states by the velocity autocorrelation, and the Raman spectrum, which was calculated by the linear response theory from the bond-polarisation approximation.

Expectatives

In the case of continuum models, finite-element methods could be employed to study some of the nanostructures considered, in particular core-shell and functionally graded systems, formed by general anisotropic materials. These methods can also be used in different civil engineering problems.

The Molecular Dynamics could be used to study thermal properties of nanostructures. It would allow also the study of the effects of stress and strain on the nanostructures.

In order to extend the study to other materials, the design of new potentials would be needed.

Chapter 5

Resumen y conclusiones

En este trabajo se han estudiado las propiedades vibracionales de nanoestructuras mediante técnicas teóricas de simulación. Las propiedades vibracionales de estos sistemas juegan un papel importante en muchos fenómenos, pero han sido menos estudiadas que sus homólogas electrónicas y ópticas.

Las nanoestructuras estudiadas aquí, como los nanohilos, los domos (puntos cuánticos) y superredes son de interés actual y están siendo crecidas en diferentes laboratorios en número creciente y en diferentes materiales. Estos sistemas son de gran interés por sus posibles aplicaciones tecnológicas en diversos ámbitos. Debido a las diferentes técnicas experimentales empleados para producir estas nanoestructuras, hay una amplia gama en la calidad de las muestras. Las técnicas de simulación empleadas en nuestros estudios están bien adaptadas para obtener las características de las propiedades vibracionales de estos sistemas a un coste computacional razonable.

Hemos empleado dos enfoques diferentes para estudiar las propiedades vibracionales de los nanosistemas: el enfoque continuo en base a la teoría lineal de la elasticidad, y el enfoque de medio discreto basado en métodos de dinámica molecular. En nuestros estudios hemos trabajado en diferentes sistemas y con diferentes tamaños para ver el comportamiento dimensional de estos efectos. En el caso de puntos cuánticos hemos estudiado diferentes sistemas con o sin defectos estructurales de dislocación para determinar sus efectos sobre las propiedades vibracionales. El uso de técnicas basadas en el modelo del medio continuo y del medio discreto permite enfoques complementarios para el estudio de estos fenómenos.

En el modelo de medio continuo, basado en la teoría lineal de la elasticidad, se ha obtenido una expresión general para las frecuencias de los modos acústicos radiales de nanohilos, nanotubos y los determinantes seculares para los sistemas "núcleo-envoltura" ("core-shell") y compuestos de sección circular que tengan anisotropía general cilíndrica dado que son una

señal característica en el espectro. Los resultados obtenidos para este tipo de nanosistemas de Si, ZnO, GaN, Au, Ag y $CdSe$ presentaron un excelente acuerdo con los resultados experimentales [226].

En el caso de nanoestructuras basadas en materiales con anisotropía elástica y sección transversal no circular no es posible hallar una solución en forma cerrada. En este caso se puede utilizar una técnica basada en los métodos empleados para el estudio de la dispersión ultrasónica resonante [34] (método *"XYZ"*). Hemos extendido esta técnica al estudio de nanohilos con sección transversal hexagonal [227]. Esta forma se presenta en muchos nanohilos de diferentes materiales obtenidos experimentalmente. De esta manera hemos obtenido las curvas de dispersión y los vectores de desplazamiento para muchos nanohilos que pertenecen a los sistemas hexagonal y cúbico.

Los sistemas multicapa constituyen otro área de interés. Las superredes basadas en III–nitruros y MgO/ZnO son sistemas muy interesantes debido a su potencial aplicacion en diferentes áreas de micro y nano-electrónica. Para estudiar sus propiedades vibracionales hemos empleado el método "Surface Green Function Matching" (SGFM) [40]. Este método está especialmente bien adaptado para estudiar los sistemas de múltiples capas de materiales con anisotropía elástica. Se estudiaron las propiedades de las superredes periódicas y aperiódicas de estos materiales para diferentes espesores relativos de los materiales constituyentes. Debido a que estos materiales pertenecen a la estructura cristalina hexagonal, existe un desacoplo de las vibraciones transversales y sagitales, cuando estas superredes se crecen a lo largo del eje-C. En estos casos, la existencia de dos umbrales transversales abre interesantes posibilidades no presentes en materiales isótropos con sólo un umbral de onda transversal o materiales anisótropos de menor simetría donde todas las polarizaciones se mezclan [228]. Las estructuras que incluyen bloques aperiódicos poseen modos localizados con localización espacial en diferentes partes de la estructura. Por lo tanto pueden ser candidatos para filtros de frecuencia [229].

El modelo de medio discreto basado en la técnica de dinámica molecular proporciona resultados en general más precisos y con un mayor rango de validez que los métodos basados en el modelo de medio continuo, aunque con un mayor costo computacional. El método usado en esta tesis es el de dinámica molecular basado en potenciales empíricos y en concreto el potencial para silicio y germanio de Tersoff, usando el algoritmo de Verlet para la integración en el tiempo. A partir de la simulación de dinámica molecular se obtuvo tanto la densidad de estados vibracionales a partir de la autocorrelación de las velocidades, como el espectro Raman, el cual fue calculado mediante la teoría de respuesta lineal a partir de la aproximación de polar-

ización de enlace.

Desarrollos futuros

En el caso de los modelos continuos, se podria emplear el método de elementos finitos para estudiar algunas de las nanoestructuras consideradas en este trabajo, especialmente los sistemas "núcleo-estructura" y los funcionales gradados, formados por materiales anisótropos. Estos métodos también pueden ser aplicados a diversos problemas de ingeniería.

Las propiedades térmicas de nanoestructuras podrían estudiarse con los métodos de dinámica molecular. Sería también posible realizar estudios sobre efectos de tensión y deformación en las propiedades de nanoestructuras.

Para poder extender el estudio a otros materiales sería necesaria la obtención de nuevos potenciales.

Appendix A: Nanostructures

A nanostructure is defined as any system with at least one dimension measured on the scale of nanometres. This definition is quite wide and cover structures with confined dimensions ranging from hundreds of nanometres to structures with only one atom thickness. Here we will show the most common structures studied which are considered the most appealing for future developments or the most fundamental.

General basic nanostructures

Nanowires

Nanowires are systems having two dimensions of nanometer size while the third one is some order of magnitude bigger or unrestricted. Nanowires can be stand-alone, suspended or placed on a substrate. These structures can be as thin as a single chain of atoms [230]. Usually these chains are attached to an atomic force microscope on one extreme and to a substrate on the other one.

In general, as electrons in a nanowire are constricted in two directions, the conductance shows quantum confinement and the energy levels are different from the traditional continuum of energy levels or bands found in bulk materials. This quantum confinement manifest in some nanowires under the form of discrete values in the electrical conductance. In fact, the energy of the electrons going through a thin nanowire can assume only discrete values [230], which are multiples of the Von Klitzing constant $\sigma = \frac{\nu e^2}{h}$, with e the electron charge, ν the filling factor and h the Planck constant. There is also scattering from the wire constrict boundaries, whose effect will be very significant whenever the wire width is below the free electron mean free path of the bulk material. Finally, nanowire conductivity may be strongly influenced by edge reconstruction effects.

Typically grown Si nanowires have diameters ranging from 10 nm to hundreds of nanometres and they show the same internal structure as the bulk. Thinner nanowires that have been grown or placed on a substrate show a dif-

ferent structure usually determined by the interaction between the nanowire
and the substrate. As the nanowire becomes thinner, the surface reconstruc-
tion effects become more important and change the nanowire properties.

Nanodots

Nanodots are structures constricted to the nanoscale in all the tree dimen-
sions. These structures are usually experimentally grown not as stand-alone
systems but also suspended in a medium (or embedded) or on a surface in
order to have their properties measured. Thus these systems are not true
zero-dimensional from the physical point of view because they are influenced
by their interaction with either the embedding material or the substrate.

Carbon based nanostructures
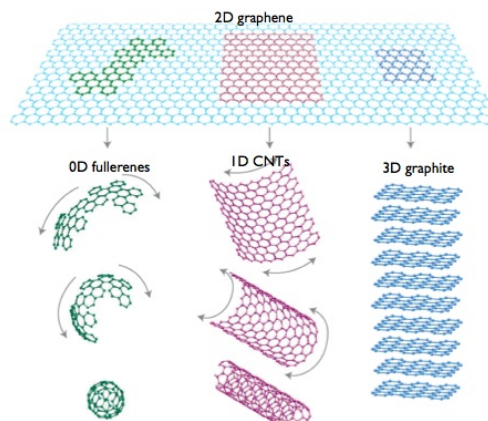
Figure 5.1: Carbon based nanostructures (Source: Geim and Novoselov
[231]).

Nanotubes

Carbon nanotubes are the sp^2 allotropes of carbon which show a cylindrical
structure. These structures have been obtained with very high ratios of
length versus diameter.

There exist single walled and multiple walled carbon nanotubes. The
second kind consists of several tubes within each other as a Matrioska (the
Russian doll), or a single continuous sheet rolled up several times.

Singled-walled carbon nanotubes are made from a single sheet of graphite
(also known as graphene) rolled up into a tube. The combination of the radius
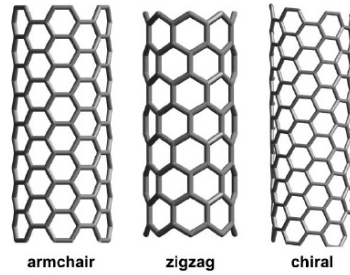
Figure 5.2: Carbon nanotubes.

and the angle of the rolled graphene sheet dictates the properties of the nanotube. There are two kinds of nanotubes: chiral and achiral. The achiral nanotube is symmorphic and has a mirror image that is identical to the original structure. On the other hand the mirror image of the chiral nanotube is not identical, but it shows spiral symmetry. The way the graphene sheet is wrapped is represented by a pair of indices (n,m), where n and m are integers and indicate the number of unit vectors needed in order to construct the carbon tube. With the two primitive lattice vectors of graphene:

$$\vec{a_1} = \left(\frac{\sqrt{3}a}{2}, \frac{a}{2}, 0 \right)$$

$$\vec{a_2} = \left(\frac{\sqrt{3}a}{2}, -\frac{a}{2}, 0 \right)$$

(5.1)

where $a = \sqrt{3}\, a_{c-c}$, being $a_{c-c} = 0.142\ nm$ the nearest neighbour bond length. Therefore the chirality vector is defined as:

$$C_h = n \cdot \vec{a_1} + m \cdot \vec{a_2} \rightarrow (n, m)$$

(5.2)

This chiral vector is perpendicular to the nanotube axis and represents the two points which would join when the sheet of graphene is rolled up to form the nanotube.

There are two types of achiral carbon nanotubes: the *armchair* whose indices are (m,m) and the *zig-zag* with (n,0) indices. The other possible combinations of indices correspond to chiral carbon nanotubes.

The diameter of the carbon nanotube can be obtained from their indices as:

$$D = \frac{a}{\pi}\sqrt{n^2 + m^2 + nm}$$

(5.3)
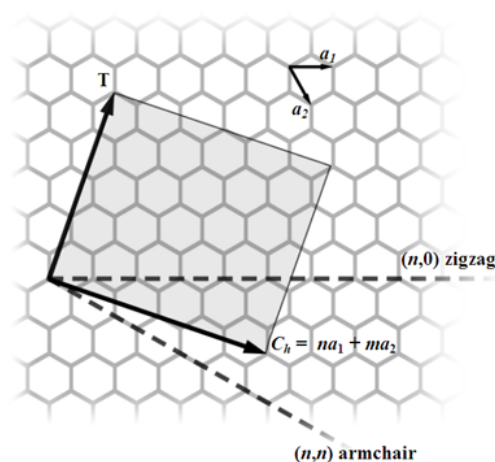
Figure 5.3: Carbon nanotubes indices and nomenclature.

Since their discovery, the carbon nanotubes have earned reputation due to the novel properties they show. Those properties make them potentially very useful in many technological aspects.

Fullerenes

The Buckminsterfullerene is a molecule of C_{60} and is the first and smallest of the Fullerene family.
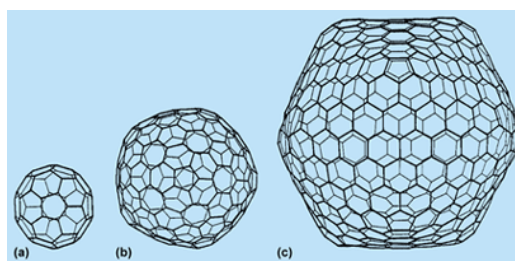
Figure 5.4: Fullerenes.

Fullerenes are hollow carbon nanoballs one atom thick. Those atoms are arranged into series of connecting hexagons and pentagons. For the C_{60} the patterns of pentagons and hexagons are arranged so the pentagons do not touch each other and the hexagons are surrounded by three pentagons and three hexagons.

The most interesting properties of fullerenes are their thermal resistivity and the superconductivity.

Graphene

The graphene is the sp^2 allotrope of carbon which is known as a true 2D structure. It is also the base structure for fullerenes (0D), carbon nanotubes (1D) and graphite (3D).
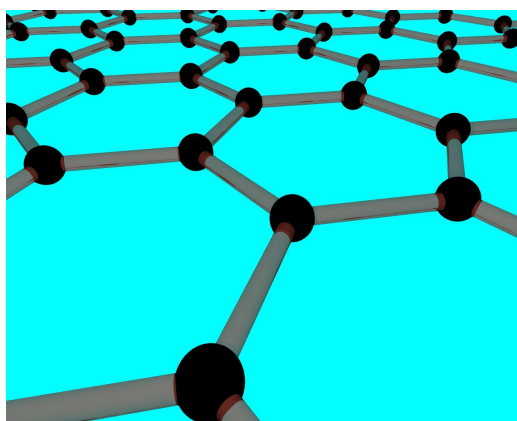
Figure 5.5: Graphene.

The graphene structure is an hexagonal lattice of carbon atoms with ripples (when suspended) that may be intrinsic to graphene as a result of the instability of two-dimensional crystals.

The electronic properties of graphene are different of most materials due to the 2D structure. Graphene in its pure form is a gapless semi-metal with electronic dispersion relations that shows, at energies near the Fermi level, a linear relation in the two kind of corners[1] of the two-dimensional hexagonal Brillouin zone. This linear dispersion is responsible of the behaviour of the electrons in graphene. These electrons and holes near the Fermi level have a zero effective mass with gives them a relativistic particle behaviour, but with the Fermi velocity in graphene taking the role of the speed of light, described by the Dirac equation for spin-half particles. The electrons in graphene are not relativistic particles but the equations that govern their motion are very similar to those of massless relativistic particles and then the electrons and holes are called Dirac fermions, and the six corners of the Brillouin zone are called the Dirac points. Graphene exhibits unique electronic properties such as high electron mobility and anomalous Quantum Hall effect, among others.

Ab initio calculations show that a graphene sheet is thermodynamically unstable with respect to other fullerene structures if its size is less than about 20 nm and becomes the most stable one (as in graphite) only for sizes larger

---

[1]These two points are called the Dirac points.

than 24,000 carbon atoms. The flat graphene sheet is also known to be unstable with respect to scrolling i.e. rolling up to form nanotubes which have a lower-energy state.

Appendix B: Nanowires

Nanowires are usually defined as structures with two sides constrained to the nanoscale and one side with much greater dimension or with a relatively "infinite" size. The nanowires grown or experimentally obtained nowadays show an aspect ratio ranging from 10 to 100 between the length and the side/diameter. With those sizes, the nanowires exhibit both surface and quantum mechanical size effects. Therefore they are also known as *quantum wires*.

Semiconductor nanowires have unique properties that make them excellent candidates for the next generation of nano-electronic devices. As those wires show a limited cross-section, they have quantum confinement effects that increase their electronic band gap.

There are two approaches to the fabrication of nanostructures: top-down and bottom-up. The top-down approach begins with a large piece of material with is cut or milled down to make the nanosystems with very well known techniques such as lithography, etching or electrophoresis. In the bottom-up approach the nanostructure is built from the constituent elements in a similar way as does the nature in living organisms.

Top-down fabrication

This approach seeks to fabricate nanostructures from larger structures.

Ion-beam, scanning-prove or electron -beam are quite flexible techniques for this purpose.

Also the technologies that came from conventional solid-state silicon methods in microelectronics are now able to fabricate elements having dimensions smaller than 100 nm, thus falling under the definition of nanotechnology.

Focused ion beams: This technique is similar to a scanning electron microscope but using focused ions instead of electrons and can directly remove material, or even deposit material when suitable precursor gases are applied at the same time. For example, this technique is routinely

used to create sub-100 nm sections of material for analysis in Transmission Electron Microscopy. This method uses the sputtering effect of the focused ions to etch or machine surfaces.

Laser Ablation: This is a simple method where the sample material is heated by a high power laser in order to evaporate the material at the focusing point of the laser beam. The evaporated material is then gathered and mixed into an inert gas which is pumped out the system. The disadvantage of this technique is that the internal structure of the nanowire consists of a serie of grains, which could reduce the mean-free-path of phonons and electrons due to boundary scattering.

Suspended nanowires: A suspended nanowire is a wire produced in a high-vacuum chamber held at the longitudinal extremities. Suspended nanowires can be produced by:

- The chemical etching of a larger wire.

- The bombardment of a larger wire, typically with highly energetic ions.

- Indenting the tip of a STM in the surface of a metal near its melting point, and then retracting it.

Bottom-up fabrication

This approach seeks to fabricate nanostructures from smaller components, molecules or even individual atoms. This is done by many chemical-mechanical methods, from classic chemistry to atomic force microscopes manipulation.

DNA: Biology demonstrate the molecular fabrication possibilities of DNA. For example, ribosomes, found in every cell, read the genetic information and use it to direct the assembly of sequences of amino acids. This amino acids together with DNA form the working parts of a wide range of molecular machines, including the ribosomes themselves.

Scanning probe lithography: The tips of the atomic force microscope (AFM) can be used as a nanoscale "write head" to deposit a chemical upon a surface in a desired pattern in a process called dip pen nanolithography. Also individual atoms may be manipulated using the tip of a scanning tunneling microscope (STM).

Vapor-liquid-solid: This is a common technique for nanowire fabrication. This technique uses an evaporated source material or a gas which are

exposed to a catalyst. In order to fabricate nanowires the best catalysts are liquid metal nanoclusters like for example gold. The catalyst nanoclusters are deposited on a substrate or directly self-assembled from a thin film by dewetting. The evaporated or gas source enters the nanoclusters wich then begin to saturate until they reach the supersaturation state and then the source solidifies on the substrate which works as a nucleation seed and grows from the nanocluster. With this technique, physical characteristics of the grown nanowires may be tuned in a controllable way, depending on the size and physical properties of the liquid nanoclusters. Also the nanowire length can be adjusted by timing the exposure to the gas source and compound nanowires with super-lattices of different materials can be grown by switching the gas sources..

Solution-phase synthesis: Solution-phase synthesis consists in the chemical grow of free nanowires in a solution. It can produce nanowires of many types of materials. Solution-phase synthesis has the advantage that it can produce very large quantities of nanowires, compared to methods that produce nanowires on a surface. In one technique, the polyol synthesis, ethylene glycol is both solvent and reducing agent. This technique is particularly versatile at producing nanowires of lead, platinum, and silver.

Template synthetic method: The template synthesis method uses another nanostructured material as a mold to cast the nanowires.

In template-assisted synthesis of nanostructures, the chemical stability and mechanical properties of the template, as well as the diameter, uniformity and density of the pores are important characteristics to consider.Templates frequently used for nanowire synthesis include anodic alumina, nanochannel glass, ion track-etched polymers and mica.

Porous anodic alumina templates are produced by anodization of pure *Al* films in selected acids. Under carefully chosen anodization conditions, the resulting oxide film possesses a regular hexagonal array of parallel and nearly cylindrical channels. The self-organization of the pore structure in an anodic alumina template involves two coupled processes: pore formation with uniform diameters and pore ordering. The pores form with uniform diameters because of a delicate balance between electric field-enhanced diffusion which determines the growth rate of the alumina, and dissolution of the alumina into the acidic electrolyte. The pores are believed to self-order because of mechanical stress at the aluminum–alumina interface due to expansion

during the anodization. This stress produces a repulsive force between the pores, causing them to arrange in a hexagonal lattice. Depending on the anodization conditions, the pore diameter can be systematically varied from $\leq$ 10 nm up to 200 nm with a pore density in the range of $10^9 \rightarrow 10^{11} \frac{pores}{cm^2}$ [232]. It has been shown by many groups that the pore size distribution and the pore ordering of the anodic alumina templates can be significantly improved by a two-step anodization technique, where the aluminum oxide layer is dissolved after the first anodization in an acidic solution followed by a second anodization under the same conditions. Another type of porous template commonly used for nanowire synthesis is the template type fabricated by chemically etching particle tracks originating from ion bombardment, such as track-etched polycarbonate membranes, and also mica films.

Appendix C: Statistical ensembles used in Molecular Dynamics

Micro-canonical ensemble (NVE)

The scheme of *Molecular Dynamics* implies the calculation of the new positions at each time step. This means that without modifications, the system does not change the number of particles and the total energy (within the computer accuracy). Adding the standard periodic boundary conditions (Chapter 2.3.3), then the system volume of each cell is constant. So it naturally comes that the typical MD system is under the micro-canonical ensemble. However, it is often more interesting to simulate other ensembles as the canonical ensemble (constant temperature) or the isotermal-isobaric ensemble (constant pressure). In order to sample these ensembles, some modifications to the standard scheme must be introduced.
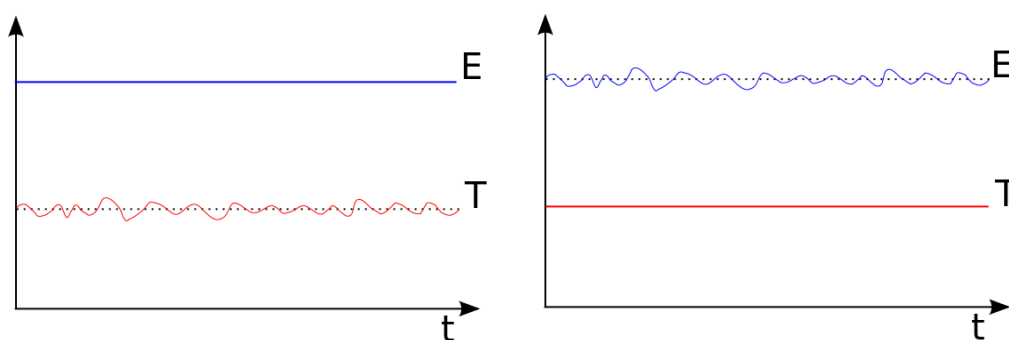
(a) Micro-canonical. (b) Canonical.

Figure 5.6: Microcanonical vs. Canonical, "Big" system.

Canonical ensemble (NVT)

The canonical ensemble is defined as a system where the number of particles N, the volume V and the temperature T are constants.

The canonical ensemble is important for the study of the behaviour of systems at different temperatures.

The temperature of a system is related to the average kinetic energy of the particles. For example, in an ideal gas $PV = Nk_BT$ where k_B is the Boltzmann constant, and T the absolute temperature, the total kinetic energy can be calculated, by the definition of pressure:

$$P = \frac{F}{L^2} = \frac{Nm < v^2 >}{3V} \tag{5.4}$$

where F is the force, $V = L^3$ is the volume, m is the mass of the particles and $< v >$ is the mean velocity of the particles. So:

$$Nk_BT = PV = \frac{Nm < v^2 >}{3} \tag{5.5}$$

and $< v^2 >= \frac{\sum(v_x^2+v_y^2+v_z^2)}{N}$, thus:

$$\frac{1}{2}m \sum(v_x^2 + v_y^2 + v_z^2) = \frac{3}{2}Nk_BT \tag{5.6}$$

Therefore a simple way to control the temperature is by scaling the velocities, i.e. at each time step the velocities are scaled according to $v' = \chi v$. One of such scaling methods for controlling the temperature is the Berendsen thermostat [233] where the velocity rescaling parameter is given by:

$$\chi = \sqrt{1 + \frac{\Delta t}{\tau}\left(\frac{T_0}{T} - 1\right)}, \tag{5.7}$$

where Δt is the time step, T is the current temperature, T_0 is the desired temperature and τ is a time constant that determines the "speed" of the adjustment.

Another method, similar to velocity rescaling is to constrain the velocities by a Gaussian constraint method [234]. Alternatively, the temperature can be held constant by a heat bath. In this method, originally due to Andersen [235], the velocity of a randomly selected particle is replaced by one chosen from the Maxwell-Boltzmann distribution. This is equivalent to a collision with a particle in an imaginary heat bath.

A final possibility is the extended system method. Similarly to the Andersen thermostat, the system is assumed to be in contact with a heat bath.

However, in this case the interaction between the simulated system and the heat bath is modelled by an interchange of energy between them. In the original formulation of this method due to Nosé [236], this was handled by an extended Hamiltonian, with an extra degree of freedom s, which acts as a time scaling parameter. Hoover then reformulated this without the extra degree of freedom [237]. The equations of motion for this thermostat are:

$$\begin{aligned}
\dot{\vec{r}} &= \frac{\vec{p}}{m} \\
\dot{\vec{p}} &= \vec{F} - \zeta\vec{p} \\
\dot{\zeta} &= \frac{N_f k_B T_0}{Q}\left(\frac{T}{T_0} - 1\right),
\end{aligned}$$

(5.8)

where ζ is a friction coefficient, N_f is the number of degrees of freedom, and Q is the thermal inertia coefficient, which describes the rate of energy exchange between the system and the heat bath, $\vec{F}$ is the force, $\vec{r}$ are the positions, $\vec{p}$ are the momenta, and T and T_0 are the current and the desired temperatures respectively.

Isothermal-isobaric ensemble (NPT)

Many experiments are performed at constant temperature and pressure, so the isothermal-isobaric (NPT) ensemble is commonly used for MD simulations. Many of the methods used for controlling the temperature of a simulation can be adapted to control the pressure, with the pressure being modified by changing the size of the simulation cell. The change in the simulation cell can be isotropic where the cell shape remains unchanged or anisotropic where the cell shape changes. One simple method due to Berendsen et al. [233] involves coupling the system to a pressure bath. At each step the volume of the box is scaled by a factor of a parameter η and so the centre of mass coordinates are scaled by a factor of $\eta^{\frac{1}{3}}$, i.e. $\vec{r}' = \eta^{\frac{1}{3}}\vec{r}$. The system is then made to obey the equation

$$\dot{P} = \frac{P_0 - P}{\tau_P}$$

(5.9)

where P is the current pressure, P_0 is the desired pressure, and τ_P is a time constant that determines the "speed" of the adjustment equivalent to τ in the Berendsen thermostat.

Barostats in the spirit of the Nosé-Hoover thermostat have also been proposed. One such barostat that generates proper NPT ensemble averages has been proposed by Melchionna et al [238]. Here the equations of motion

are given by:

$$
\begin{aligned}
\dot{\vec{r}} &= \frac{\vec{p}}{m} + \eta(\vec{r} - \vec{r}_{cm}) \\
\dot{\vec{p}} &= \vec{F} - (\eta + \zeta)\vec{p} \\
\dot{\zeta} &= \frac{1}{\tau_T^2}\left(\frac{T}{T_0} - 1\right) \\
\dot{\eta} &= \frac{1}{Nk_BT_0\tau_P^2}V(P - P_0) \\
\dot{V} &= 3\eta V,
\end{aligned}
\tag{5.10}
$$

where $\vec{r}$ are the positions, $\vec{p}$ are the momenta (do not mistake with the pressures P and P_0) , $\vec{r}_{cm}$ are the system centre of mass coordinates, N is the number of particles, and τ_T and τ_P are the thermostat and barostat time constants. These constants are typically set to $\tau_T \sim$ 1ps and $\tau_P \sim$ 0.1ps [238, 239]. In this set of equations of motion, η is the volume scaling factor and ζ is the friction coefficient, which regulates the system's temperature.

Bibliography

[1] R. Feynman, *Miniaturization pp. 282-296.* Gilbert. H. D. (Reinhold, New York), 1961.

[2] K. E. Drexler, "Productive nanosystems: the physics of molecular fabrication," *Physics Education*, vol. 40, pp. 339–346, 2005.

[3] S. Pelaez-Machado, *Structural and mechanical properties of metallic nanowires in the border between crystallinity and weird configurations.* PhD thesis, Universidad Autónoma de Madrid, 2012.

[4] M. P. Allen and D. J. Tildesley, *Computer Simulation of Liquids.* Oxford Science Publications, 1987.

[5] G. H. Zeng, J. E. Bowers, J. M. O. Zide, A. C. Gossard, W. Kim, S. Singer, A. Majumdar, R. Singh, Z. Bian, Y. Zhang, and A. Shakouri, "ErAs:InGaAs/InGaAlAs superlattice thin-film power generator array," *Applied Physics Letters*, vol. 88, p. 113502, 2006.

[6] T. Gorishnyy, C. K. Ullal, M. Maldovan, G. Fytas, and E. L. Thomas, "Hypersonic Phononic Crystals," *Phys. Rev. Lett.*, vol. 94, p. 115501, 2005.

[7] J. Zimmermann, P. Pavone, and G. Cuniberti, "Vibrational modes and low-temperature thermal properties of graphene and carbon nanotubes: Minimal force-constant model," *Physical Review B*, vol. 78, p. 045410, 2008.

[8] P. Debye, "The theory of specific warmth," *Ann. Phys.*, vol. 39, p. 789, 1912.

[9] L. D. Landau and E. M. Lifshitz, *Theory of Elasticity.* Butterworth-Hienemann, Washington, DC, 1988.

[10] R. Saito, G. Dresselhaus, and M. S. Dresselhaus, *Physical Properties of Carbon Nanotubes.* Imperial College Press, London, 1998.

[11] R. Saito, M. Fujita, G. Dresselhaus, and M. S. Dresselhaus, "Electronic structure of graphene tubules based on C_{60}," *Physical Review B*, vol. 46, p. 1804, 1992.

[12] S. Reich, J. Maultzsch, and C. Thomsen, "Tight-binding description of graphene," *Physical Review B*, vol. 66, p. 035412, 2002.

[13] S. Reich, C. Thomsen, and P. Ordejon, "Electronic band structure of isolated and bundled carbon nanotubes," *Physical Review B*, vol. 65, p. 155411, 2002.

[14] B. K. Agrawal, S. Agrawal, and R. Srivastava, "Ab initio study of small diameter (6,6) armchair carbon nanoropes: orientational dependent properties," *J. Phys.: Cond. Matt.*, vol. 15, p. 6931, 2003.

[15] M. F. Lin and K. W. K. Shung, "Plasmons and optical properties of carbon nanotubes," *Physical Review B*, vol. 50, p. 474, 1994.

[16] H. Bruus and K. Flensberg, *Many-body quantum theory in condensed matter physics - an introduction.* Oxford University Press, 2004.

[17] R. Rurali and N. Lorente, "Metallic and semimetallic silicon $< 100 >$ nanowires," *Phys. Rev. Lett.*, vol. 94, p. 026805, 2005.

[18] R. Rurali and N. Lorente, "On the properties of surface reconstructed silicon nanowires," *Nanotechnology*, vol. 16, p. S250, 2005.

[19] J. Hu, M. Ouyang, P. Yang, and C. M. Lieber, "Controlled growth and electrical properties of heterojunctions of carbon nanotubes and silicon nanowires," *Nature*, vol. 399, p. 48, 1999.

[20] P. Mishra and K. P. Jain, "Raman, photoluminiscence and optical absortion studies on nanocrystaline silicon," *Mat. Sci. and Eng. B*, vol. 95, p. 202, 2002.

[21] N. G. Shang, U. Vetter, I. Gerhards, H. Hofsäss, C. Ronning, and M. Seibt, "Luminiscence centres in silica nanowires," *Nanotechnology*, vol. 17, p. 3215, 2006.

[22] J. Fernandez-Rossier and J. J. Palacios, "Magnetism in Graphene Nanoislands," *Phys. Rev. Lett.*, vol. 99, p. 177204, 2007.

[23] N. Nishiguchi, Y. Ando, and M. N. Wybourne, "Acoustic phonon modes of rectangular quantum wires," *J. Phys.:Condens. Mater*, vol. 9, pp. 5751–5764, 1997.

[24] J. Shiomi and S. Maruyama, "Non-Fourier heat conduction in a single-walled carbon nanotube: Classical molecular dynamics simulations," *Physical Review B*, vol. 73, p. 205420, 2006.

[25] B. L. N. Kennett, *Introduction to Continuum Mechanics.*

[26] A. Nougaoui, N. Ouchani, V. R. Velasco, D. Bria, E. H. El Boudouti, and J. Ben Ali, "Acoustic waves in (001) InN–AlN and InN–GaN superlattices," *Surface Science*, vol. 605, p. 1324, 2011.

[27] H. Aynaou, A. Nougaoui, E. H. El Boudouti, D. Bria, V. R. Velasco, and B. Djafari-Rouhani, "Comparative study of the sagittal elastic waves in metallic and semiconductor multilayer systems between periodic and Fibonacci superlattices," *Surface Science*, vol. 584, pp. 199–213, 2005.

[28] D. C. Gazis, "Three-dimensional investigation of the propagation of waves in hollow circular cylinders: I. Analytical foundation," *Journal of the Acoustical Society of America*, vol. 31, no. 5, pp. 568–573, 1959.

[29] I. Mirsky, "Vibrations of orthotropic, thick, cylindrical shells," *Journal of the Acoustical Society of America*, vol. 36, no. 1, pp. 41–51, 1964.

[30] V. R. Velasco and M. C. Muñoz, "Vibrations in cylindrical shells with transverse elastic isotropy: Application to III–V nitride nanotubes," *Surface Science*, vol. 603, pp. 2950–2957, 2009.

[31] H. H. Demarest Jr., "Cube-Resonance Method to Determine the Elastic Constanst of Solids," *Journal of the Acoustical Society of America*, vol. 49, pp. 768–775, 1971.

[32] W. M. Visscher, A. Migliori, T. M. Bell, and R. A. Reinert, "On the normal modes of free vibration of inhomogeneous and anisotropic elastic objects," *Journal of the Acoustical Society of America*, vol. 90, pp. 2154–2162, 1991.

[33] J. Maynard, "Resonant Ultrasound Spectroscopy," *Phys. Today*, vol. 49, pp. 26–31, 1996.

[34] A. Migliori and J. Sarrao, *Resonant Ultrasound Spectroscopy.* Wiley-Interscience, New York, 1997.

[35] H. Ogi, P. Heyliger, H. Ledbetter, and S. Kim, "Mode-selective resonance ultrasound spectroscopy of a layered parallelepiped," *Journal of the Acoustical Society of America*, vol. 108, no. 6, pp. 2829–2834, 2000.

[36] H. Ogi, Y. Kawasaki, M. Hirao, and H. Ledbetter, "Acoustic spectroscopy of lithium niobate: Elastic and piezoelectric coefficients," *Journal of Applied Physics*, vol. 92, pp. 2451–2456, 2002.

[37] G. Li, G. A. Lamberton Jr., and J. R. Gladden, "Acoustic modes of finite length homogeneous and layered cylindrical shells: Single and multiwall carbon nanotubes," *Journal of Applied Physics*, vol. 104, p. 033524, 2008.

[38] M. Hirao, H. Ogi, and K. Sato, "Interface Delamination of Layered Media: Acoustic Spectroscopy and Modal Analysis," *IEEE Transactions on Ultrasonics, Ferroelectrics and Frequency control*, vol. 51, pp. 439–443, 2004.

[39] R. Pérez-Alvarez, F. García-Moliner, and V. R. Velasco, "Simultaneous surface Green function matching for N interfaces," *Journal of Physics: Condensed Matter*, no. 7, pp. 2037–2049, 1995.

[40] F. Garcia-Moliner and V. R. Velasco, *Theory of Single and Multiple Interfaces*. World Scientific, 1992.

[41] L. Fernández-Alvarez and V. R. Velasco, "Elastic waves in polytype superlattices," *Journal of Physics: Condensed Matter*, vol. 8, pp. 6531–6541, 1996.

[42] L. Fernández, V. R. Velasco, and F. Garcia-Moliner, "Transverse acoustic waves in piezoelectric superlattices," *Europhysics Letters*, vol. 3, no. 6, pp. 723–728, 1987.

[43] F. Garcia-Moliner and V. R. Velasco, "Surface Green function matching," *Surface Science*, vol. 299/300, pp. 332–345, 1994.

[44] J. E. Zárate, L. Fernández-Alvarez, and V. R. Velasco, "Transverse elastic waves in Fibonacci superlattices," *Superlattices and Microstructures*, vol. 25, pp. 519–526, 1999.

[45] D. Bergeron, N. Shtinkov, R. A. Masut, and P. Desjardins, "Green function matching method for one- and zero-dimensional heterostructures," *Physical Review B*, vol. 72, p. 245308, 2005.

[46] F. Garcia-Moliner, "Why Green functions for matching?," *Microelectronics Journal*, vol. 36, pp. 876–881, 2005.

[47] J. E. Zarate and V. R. Velasco, "Elastic waves in graded-composition systems," *Superlattices and Microstructures*, vol. 28, no. 3, pp. 217–230, 2000.

[48] A. Montalbán, V. R. Velasco, J. Tutor, and F. J. Fernández-Velicia, "Phonon confinement in one-dimensional hybrid periodic/quasiregular structures," *Physical Review B*, vol. 70, p. 132301 (4 pp), 2004.

[49] A. Montalbán, V. R. Velasco, J. Tutor, and F. J. Fernández-Velicia, "Phonons in hybrid Fibonacci/periodic multilayers," *Surface Science*, vol. 603, pp. 937–943, 2009.

[50] L. Fernández-Alvarez and V. R. Velasco, "Sagittal elastic waves in Fibonacci superlattices," *Physical Review B*, vol. 57, no. 22, pp. 14141–14147, 1998.

[51] A. Montalbán, V. R. Velasco, J. Tutor, and F. J. Fernández-Velicia, "Selective spatial localization of the atom displacements in one-dimensional hybrid quasi-regular (Thue-Morse and Rudin-Shapiro)/periodic structures," *Surface Science*, vol. 601, pp. 2538–2547, 2007.

[52] E. Dieulesaint and D. Royer, *Elastic Waves in Solids*. John Wiley & Sons Ltd., 1980, p.151.

[53] M. A. Stroscio and M. Dutta, *Phonons in Nanostructures*. Cambridge University Press, Cambridge, 2001.

[54] H. Suzuura and T. Ando, "Phonons and electron-phonon scattering in carbon nanotubes," *Physical Review B*, vol. 65, p. 235412, 2002.

[55] G. D. Mahan, "Oscillations of a thin hollow cylinder: Carbon nanotubes," *Physical Review B*, vol. 65, p. 235402, 2002.

[56] S. V. Goupalov, "Continuum model for long-wavelength phonons in two-dimensional graphite and carbon nanotubes," *Physical Review B*, vol. 71, p. 085420, 2005.

[57] L. Chico, R. Pérez-Alvarez, and C. Cabrillo, "Low-frequency phonons in carbon nanotubes: A continuum approach," *Physical Review B*, vol. 73, p. 075425, 2006.

[58] M. Mitra and S. Gopalakrishnan, "Vibrational characteristics of single-walled carbon-nanotube: Time and frequency domain analysis," *Journal of Applied Physics*, vol. 101, p. 114320, 2007.

[59] P. Yang, "The Chemistry and Physics of Semiconductor Nanowires," *MRS Bulletin*, vol. 30, pp. 85–91, 2005.

[60] M. C. Lu, Y. L. Chueh, L. J. Chen, L. J. Chou, H. L. Hsiao, and A.-B. Yang, "Synthesis and Formation Mechanism of Gallium Nitride Nanotubular Structure," *Electrochem. Solid State Lett.*, vol. 8, p. G153, 2005.

[61] M. Abramowitz and I. A. Stegun, *Handbook of Mathematical Functions*. Dover, New York, 1970.

[62] I. Mirsky, "Wave propagation in transversely isotropic circular cylinders. Part I," *Journal of the Acoustical Society of America*, vol. 37, pp. 1016–1022, 1965.

[63] I. Mirsky, "Wave propagation in transversely isotropic circular cylinders. Part II. Numerical results," *Journal of the Acoustical Society of America*, vol. 37, pp. 1022–1026, 1965.

[64] E. K. Sittig and G. A. Coquin, "Visualization of plane-strain vibration modes of a long cylinder capable of producing sound radiation," *Journal of the Acoustical Society of America*, vol. 48, no. 5p2, pp. 1150–1159, 1970.

[65] V. Rovenski and O. Rand, *Analytical Methods in Anisotropic Elasticity with Symbolic Computational Tools*. Birkhäuser, 2005.

[66] M. Hu, X. Wang, G. V. Hartland, P. Mulvaney, J. Perez-Juste, and J. E. Sader, "Vibrational Response of Nanorods to Ultrafast Laser Induced Heating: Theoretical and Experimental Analysis," *J. Am. Chem. Soc.*, vol. 125, pp. 14925–14933, 2003.

[67] J. Hu, Y. Bando, D. Golberg, and Q. Liu, "Gallium Nitride Nanotubes by the Conversion of Gallium Oxide Nanotubes," *Angewandte Chemie International Edition*, vol. 42, p. 3493, 2003.

[68] J. Goldberger, R. R. He, Y. Zhang, S. Lee, H. Yan, H. J. Choi, and P. Yang, "Single-crystal gallium nitride nanotubes," *Nature*, vol. 422, pp. 599–602, 2003.

[69] B. Liu, Y. Bando, C. Tang, G. Shen, D. Golberg, and F. Xu, "Wurtzite-type faceted single-crystalline GaN nanotubes," *Appl. Phys. Lett.*, vol. 88, p. 093120, 2006.

[70] A. A. Kolomenskii, S. N. Jerebtsov, H. Liu, H. Zhang, Z. Ye, Z. Luo, W. Wu, and H. A. Schuessler, "Observation of coherent acoustic and optical phonons in bismuth nanowires by a femtosecond pump-probe technique," *Journal of Applied Physics*, vol. 104, p. 103110, 2008.

[71] E. O. Schäfer-Nolte, T. Stoica, T. Gotschke, F. Limbach, E. Sutter, P. Sutter, and R. Calarco, "Highly polarized Raman scattering anisotropy in single GaN nanowires," *Applied Physics Letters*, vol. 96, p. 091907, 2010.

[72] K. W. Adu, H. R. Gutiérrez, U. J. Kim, G. U. Sumanasekera, and P. C. Eklund, "Confined Phonons in Si Nanowires," *Nano Letters*, vol. 5, pp. 409–414, 2005.

[73] R. Agrawal, B. Peng, and H. D. Espinosa, "Experimental-Computational Investigation of ZnO nanowires Strength and Fracture," *Nano Letters*, vol. 9, pp. 4177–4183, 2009.

[74] R. Agrawal, B. Peng, E. E. Gdoutos, and H. D. Espinosa, "Elasticity Size Effects in ZnO Nanowires: A Combined Experimental-Computaional Approach," *Nano Letters*, vol. 8, pp. 3668–3674, 2008.

[75] C. M. Haapamaki, *Growth of InAs/InP Nanowires by Molecular Beam Epitaxy.* PhD thesis, McMaster University, 2012.

[76] A. J. Kulkarni and M. Zhou, "Tunable thermal response of ZnO nanowires," *Nanotechnology*, vol. 18, p. 435706, 2007.

[77] J. L. Bleustein, "A new surface wave in piezoelectric materials," *Applied Physics Letters*, vol. 13, no. 12, pp. 412–413, 1968.

[78] V. R. Velasco, "Study of interface and surface elastic waves in piezoelectric materials by using the Surface Green Function Matching (SGFM) Method," *Surface Science*, vol. 128, pp. 117–127, 1983.

[79] M. Born and J. R. Oppenheimer, "Zur Quantentheorie der Molekeln [On the Quantum Theory of Molecules]," *Annalen der Physik*, vol. 389, pp. 457–484, 1927. in German.

[80] C. P. Robert and G. Casella, *Monte carlo statistical methods.* Springer, 2004.

[81] J. P. Hansen and I. R. McDonald, *Theory of simple liquids.* Academic Press, 2006.

[82] J. E. Lennard-Jones, "On the Determination of Molecular Fields," *Proc. R. Soc. Lond. A*, vol. 106, pp. 463–477, 1924.

[83] F. Ercolessi, *A molecular dynamics primer*. Spring College in Computational Physics, ICTP, Trieste, June 1997.

[84] F. H. Stillinger and T. A. Weber, "Computer Simulation of Local Order in Condensed Phases of Silicon," *Physical Review B*, vol. 31, p. 5262, 1985.

[85] J. Tersoff, "Modeling solid-state chemistry: Interatomic potentials for multicomponent systems," *Phys. Rev. Lett.*, vol. 39, pp. 5566–5568, 1989.

[86] M. Born and T. von Karman, "Über Schwingungen in Raumgittern," *Physik Z*, vol. 13, pp. 297–309, 1912.

[87] M. L. Klein and J. J. Weis, "The dynamical structure factor $S(\mathbf{S},\omega)$ of solid $\beta - N_2$," *J. Chem. Phys*, vol. 67, pp. 217–224, 1977.

[88] B. J. Alder and T. E. Wainwright, "Phase Transition for a Hard Sphere System," *The Journal of Chemical Physics*, vol. 27, p. 1208, 1957.

[89] B. J. Alder and T. E. Wainwright, "Studies in Molecular Dynamics. I. General Method," *The Journal of Chemical Physic*, vol. 31, p. 459, 1959.

[90] A. Rahman and F. Stillinger, "Propagation of sound in water. A molecular-dynamics study," *Physical Review A*, vol. 10, pp. 368–378, 1974.

[91] D. C. Rapaport, *The art of molecular dynamics simulation*. Cambridge University Press, 1997.

[92] L. Verlet, "Computer "Experiments" on Classical Fluids. I. Thermodynamical Properties of Lennard-Jones Molecules.," *Physical Review*, vol. 159(1), pp. 98–103, July 1967.

[93] L. Verlet, "Computer "Experiments" on Classical Fluids. II. Equilibrium Correlation Functions.," *Physical Review*, vol. 165(1), pp. 201–214, January 1968.

[94] W. H. Press, S. A. Teukolsky, W. T. Vetterling, and B. P. Flannery, *Numerical recipes in fortran*. Cambridge university Press, 1992.

[95] B. J. Berne and R. Pecora, *Dynamic Light Scattering*. Wiley, New York, 1976.

[96] A. Putrino and M. Parrinello, "Anharmonic Raman Spectra in High-Pressure Ice from Ab Initio Simulations," *Physical Review Letters*, vol. 88, p. 176401, 2002.

[97] J. A. Board and R. J. Elliott, "Shell model molecular dynamics calculations of the Raman spectra of molten NaI," *Journal of Physics: Condensed Matter*, vol. 1, pp. 2427–2440, 1989.

[98] S. Guha, J. Menendez, J. B. Page, and G. B. Adams, "Empirical bond polarizability model for fullerenes," *Physical Review B*, vol. 53, p. 13106, 1996.

[99] R. Saito, T. Takeya, and T. Kimura, "Raman intensity of single-wall carbon nanotubes," *Physical Review B*, vol. 57, p. 4145, 1998.

[100] M. V. Wolkenstein *C. R. Acad. Sci. URSS*, vol. 30, p. 791, 1941.

[101] M. Volkenstein *Dokl. Akad. Nauk. SSSR*, vol. 32, p. 185, 1941.

[102] P. Umari, A. Psaquarello, and A. Dal Corso, "Raman scattering intensities in α -quartz: A first-principles investigation," *Physical Review B*, vol. 63, p. 094305, 2001.

[103] G. W. Chantry, *The Raman Effect*, vol. 1. Dekker, New York, 1971.

[104] M. A. Eliashevich and M. V. Wolkenstein *J. Phys. URSS*, vol. 9, p. 101, 1944.

[105] S. Baroni, S. de Gironcoli, and P. Giannozzi, "Phonon Dispersion in $Ga_xAl_{1-x}As$ Alloys," *Physical Review Letters*, vol. 65, p. 84, 1990.

[106] R. Alben, D. Weaire, J. E. Smith Jr, and M. H. Brodsky, "Vibrational properties of amorphous Si and Ge," *Physical Review B*, vol. 11, p. 2271, 1975.

[107] B. Aldes, S. Fernbach, and M. Rotenberg, *Methods in computational physics*, vol. 15. 1976.

[108] A. Smekal, "Zur Quantentheorie der Dispersion," *Naturwissenschaften*, vol. 11, no. 43, pp. 873–875, 1923.

[109] C. V. Raman and K. S. Krishnan, "A New Type of Secondary Radiation.," *Nature*, vol. 121, no. 3048, p. 501, 1928.

[110] R. Singh, "C. V. Raman and the Discovery of the Raman Effect," *Physics in Perspective*, vol. 4, pp. 399–420, 2002.

[111] G. Landsberg and L. Mandelstam, "Eine neue Erscheinung bei der Lichtzerstreuung in Krystallen," *Naturwissenschaften*, vol. 16, no. 28, p. 557, 1928.

[112] P. H. Berens, S. R. White, and K. R. Wilson, "Molecular dynamics and spectra. II. Diatomic Raman," *J. Chem. Phys.*, vol. 75, p. 515, 1981.

[113] P. H. Berens and K. R. Wilson, "Molecular dynamics and spectra. I. Diatomic rotation and vibration," *J. Chem. Phys.*, vol. 74, p. 4872, 1981.

[114] F. Pezzoli, *Raman Spectroscopy of Si_{1-x} Ge_x micro and nanostructures.* PhD thesis, Universita degli Studi di Milano-Bicocca, 2007.

[115] S. Bratos, "Raman Study of Liquids. I. Theory of the Raman Spectra of Diatomic Molecules in Inert Solutions," *Phys. Rev. A*, vol. 4, no. 3, p. 1078, 1971.

[116] D. Chandler, *Introduction to Modern Statistical Mechanics.* Oxford University Press, 1987.

[117] M. I. Alonso and K. Winer, "Raman spectra of c-Si_{1-x} Ge_x alloys," *Physical Review B*, vol. 39, p. 10056, 1989.

[118] A. Rastelli, M. Stoffel, A. MAlachias, T. Merdzhanova, G. Katsaros, K. Kern, T. H. Metzger, and O. G. Schmidt, "Three-Dimensional Composition Profiles of Single Quantum Dots Determined by Scanning-Prove-Microscopy-Based Nanotomography," *Nano Letters*, vol. 8, no. 5, pp. 1404–1409, 2008.

[119] S. Nakamura and G. Fasol, *The Blue Laser Diode.* Berlin, Springer, 1987.

[120] S. Nakamura and S. F. Chichibu, *Introduction to Nitride Semiconductor Blue Laser and Light-Emitting Diodes.* London, Taylor and Francis (p.317), 2000.

[121] U. K. Mishra, Y. Wu, B. Keller, S. Keller, and S. Denbaars, "GaN microwave electronics," *IEEE Trans. Microwave Theory Technol.*, vol. 46, p. 756, 1998.

[122] D. Norton, Y. Heo, M. Ivill, K. Ip, S. Pearton, M. Chisholm, and T. Steiner, "ZnO: growth, doping & processing," *Materials Today*, vol. 7, no. 6, pp. 34–40, 2004.

[123] Ü. Özgür, Y. I. Alivov, C. Liu, A. Teke, M. A. Reshchikov, S. Doğan, V. Avrutin, S.-J. Cho, and H. Morkoç, "A comprehensive review of ZnO materials and devices," *Journal of Applied Physics*, vol. 98, p. 041301 (103 pp), 2005.

[124] T. Makino, Y. Segawa, M. Kawasaki, A. Ohtomo, R. Shiroki, K. Tamura, T. Yasuda, and H. Koinuma, "Band gap engineering based on $Mg_xZn_{1-x}O$ and $Cd_yZn_{1-y}O$ ternary alloy films," *Applied Physics Letters*, vol. 78, p. 1237 (3 pages), 2001.

[125] A. Ohtomo, M. Kawasaki, T. Koida, K. Masubuchi, H. Koinuma, Y. Sakurai, Y. Yoshida, T. Yasuda, and Y. Segawa, "$Mg_xZn_{1-x}O$ as a II–VI widegap semiconductor alloy," *Applied Physics Letters*, vol. 72, pp. 2466–2468, 1998.

[126] A. Ohtomo, M. Kawasaki, I. Ohkubo, H. Koinuma, T. Yasuda, and Y. Segawa, "Structure and optical properties of $ZnO/Mg_{0.2}Zn_{0.8}O$ superlattices," *Applied Physics Letters*, vol. 75, p. 980, 1999.

[127] T. Makino, C. H. Chia, N. T. Tuan, H. D. Sun, Y. Segawa, M. Kawasaki, A. Ohtomo, K. Tamura, and H. Koinuma, "Room-temperature luminescence of excitons in ZnO/(Mg, Zn)O multiple quantum wells on lattice-matched substrates," *Applied Physics Letters*, vol. 77, no. 7, pp. 975–977, 2000.

[128] T. Makino, K. Tamura, C. H. Chia, Y. Segawa, M. Kawasaki, A. Ohtomo, and H. Koinuma, "Radiative recombination of electron–hole pairs spatially separated due to quantum-confined Stark and Franz–Keldish effects in $ZnO/Mg_{0.27}Zn_{0.73}O$ quantum wells," *Applied Physics Letters*, vol. 81, no. 13, pp. 2355–2357, 2002.

[129] T. Gruber, C. Kirchner, R. Kling, F. Reuss, and A. Waag, "ZnMgO epilayers and ZnO−−ZnMgO quantum wells for optoelectronic applications in the blue and UV spectral region," *Applied Physics Letters*, vol. 84, no. 26, pp. 5359–5361, 2004.

[130] B. P. Zhang, N. T. Binh, K. Wakatsuki, C. Y. Liu, Y. Segawa, and N. Usami, "Growth of ZnO/MgZnO quantum wells on sapphire substrates and observation of the two-dimensional confinement effect," *Applied Physics Letters*, vol. 86, p. 032105 (3pp), 2005.

[131] S. Fujita, H. Tanaka, and S. Fujita, "MBE growth of wide band gap wurtzite MgZnO quasi-alloys with MgO/ZnO superlattices for deep ultraviolet optical functions," *Journal of Crystal Growth*, vol. 278, pp. 264–267, 2005.

[132] S. Fujita, T. Takagi, H. Tanaka, and S. Fujita, "Molecular beam epitaxy of $Mg_xZn_{1-x}O$ layers without wurzite-rocksalt phase mixing from $x = 0$ to 1 as an effect of ZnO buffer layer," *physica status solidi (b)*, vol. 241, no. 3, pp. 599–602, 2004.

[133] P. Gopal and N. A. Spalding, "Polarization, Piezoelectric Constants, and Elastic Constants of ZnO, MgO, and CdO," *Journal of Electronic Materials*, vol. 35, pp. 538–542, 2006.

[134] Y. Duan, L. Qin, G. Tang, and L. Shi, "First-principles study of ground- and metastable-state properties of XO (X = Be, Mg, Ca, Sr, Ba, Zn and Cd)," *Eur. Phys. J. B*, vol. 66, pp. 201–209, 2008.

[135] E. H. El Boudouti, B. Djafari-Rouhani, A. Akjouj, and L. Dobrzynski, "Acoustic waves in solid and fluid layered materials," *Surface Science Reports*, vol. 64, pp. 471–594, 2009.

[136] D. Bria, B. Djafari-Rouhani, A. Bousfia, E. H. El Boudouti, and A. Nougaoui, "Absolute acoustic band gap in coupled multilayer structures," *Europhysics Letters*, vol. 55, p. 841, 2001.

[137] M. Trigo, A. Bruchhausen, A. Fainstein, B. Jusserand, and V. Thierry-Mieg, "Confinement of Acoustical Vibrations in a Semiconductor Planar Phonon Cavity," *Physical Review Letters*, vol. 89, p. 227402 (4 pages), 2002.

[138] N. D. Lanzillotti-Kimura, A. Fainstein, A. Lemaître, and B. Jusserand, "Nanowave devices for terahertz acoustic phonons," *Applied Physics Letters*, vol. 88, p. 083113 (3 pages), 2006.

[139] P. Lacharmoise, A. Fainstein, B. Jusserand, and V. Thierry-Mieg, "Optical cavity enhancement of light–sound interaction in acoustic phonon cavities," *Applied Physics Letters*, vol. 84, p. 3274 (3 pages), 2004.

[140] I. Vurgaftman and J. R. Meyer, "Band parameters for nitrogen-containing semiconductors," *Journal of Applied Physics*, vol. 94, no. 6, pp. 3675–3696, 2003.

[141] T. B. Bateman, "Elastic Moduli of Single-Crystal Zinc Oxide," *Journal of Applied Physics*, vol. 33, no. 11, pp. 3309–3312, 1962.

[142] L. Fernández and V. R. Velasco, "Transverse elastic waves propagating along symmetry directions of piezoelectric superlattices," *Surface Science*, vol. 185, 1987.

[143] B. Jusserand, D. Paquet, F. Mollot, F. Alexandre, and G. L. Roux, "Influence of the supercell structure on the folded acoustical Raman line intensities in superlattices," *Physical Review B*, vol. 35, pp. 2808–2817, 1987.

[144] A. Nougaoui and B. Djafari-Rouhani, "Elastic waves in periodically layered infinite and semi-infinite anisotropic media," *Surface Science*, vol. 185, pp. 125–153, 1987.

[145] A. Nougaoui and B. Djafari-Rouhani, "Dynamics of infinite and semi-infinite piezoelectric superlattices: Shear horizontal waves and effective medium approximation," *Surface Science*, vol. 185, pp. 154–174, 1987.

[146] A. Nougaoui and B. Djafari-Rouhani, "Complex band structure of acoustic waves in superlattices," *Surface Science*, vol. 199, pp. 623–637, 1988.

[147] D. Berdekas and S. Ves, "Lattice dynamics and Raman scattering by phonons of GaAs/AlAs(001) superlattices," *Journal of Physics: Condensed Matter*, vol. 21, p. 275405 (14pp), 2009.

[148] E. Maciá and F. Dominguez-Adame, *Electrons, Phonons and Excitons in Low Dimensional aperiodic Systems*. Editorial Complutense, Madrid, 2000.

[149] E. L. Albuquerque and M. Cottam, "Theory of elementary excitations in quasiperiodic structures," *Physics Reports*, vol. 376, pp. 225–337, 2003.

[150] W. Steurer and D. Sutter-Widmer, "Photonic and phononic quasicrystals," *J. Phys. D: Appl. Phys.*, vol. 40, p. R229, 2007.

[151] E. Maciá Barber, *Aperiodic Structures in Condensed Matter. Fundamentals and Applications*. CRC Press, Boca Raton, 2009.

[152] J. Milton Pereira Jr and R. N. Costa Filho, "Dipole-exchange spin waves in Fibonacci magnetic multilayers," *Physics Letters A*, vol. 344, pp. 71–76, 2005.

[153] S. V. Grishin, E. N. Beginin, Y. P. Sharaevskii, and S. A. Nikitov, "Dissipative soliton generation in an active ring resonator based on magnonic quasicrystal with Fibonacci type structure," *Applied Physics Letters*, vol. 103, p. 022408 (4 pp.), 2013.

[154] S. N. Zhu, Y. Y. Zhu, Y. Q. Qin, H. F. Wang, C. Z. Ge, and N. B. Ming, "Experimental Realization of Second Harmonic Generation in Fibonacci Optical Superlattice of LiTaO$_3$," *Physical Review Letters*, vol. 78, pp. 2752–2755, 1997.

[155] Y. B. Chen, C. Zhang, Y. Y. Zhu, S. N. Zhu, H. T. Wang, and N. B. Ming, "Optical harmonic generation in a quasi-phase-matched three-component Fibonacci superlattice LiTaO$_3$," *Applied Physics Letters*, vol. 78, no. 5, p. 577, 2001.

[156] W. Gellermann, M. Kohmoto, B. Sutherland, and P. C. Taylor, "Localization of light waves in Fibonacci dielectric multilayers," *Physical Review Letters*, vol. 72, pp. 633–636, 1994.

[157] T. Hattori, N. Tsurumachi, S. Kawato, and H. Nakatsuka, "Photonic dispersion relation in a one-dimensional quasicrystal," *Physical Review B*, vol. 50, no. 6, pp. 4220–4223, 1994.

[158] E. Maciá, "Exploiting quasiperiodic order in the design of optical devices," *Physical Review B*, vol. 63, p. 205421 (8 pp), 2001.

[159] X. Huang, Y. Wang, and C. Gong, "Numerical investigation of light-wave localization in optical Fibonacci superlattices with symmetric internal structure," *Journal of Physics: Condensed Matter*, vol. 11, no. 39, pp. 7645–7651, 1999.

[160] X. Q. Huang, S. S. Jiang, R. W. Peng, and A. Hu, "Perfect transmission and self-similar optical transmission spectra in symmetric Fibonacci-class multilayers," *Physical Review B*, vol. 63, p. 245104 (9 pp), 2001.

[161] J. W. Dong, P. Han, and H. Z. Wang, "Broad Omnidirectional Reflection Band Forming by the Combination of Fibonacci Quasi-periodic and Periodic One-dimensional Photonic Crystals," *Chin.Phys.Lett.*, vol. 20, no. 11, pp. 1963–1965, 2003.

[162] H. Aynaou, E. H. El Boudouti, B. Djafari-Rouhani, A. Akjouj, and V. R. Velasco, "Propagation and localization of acoustic waves in Fibonacci phononic circuits," *Journal of Physics: Condensed Matter*, vol. 17, no. 27, pp. 4245–4262, 2005.

[163] A. Montalbán, V. R. Velasco, J. Tutor, and F. J. Fernández-Velicia, "Vibrational properties of quasiregular systems with mirror symmetry," *Surface Science*, vol. 594, pp. 174–191, 2005.

[164] A. C. Hladky-Hennion, J. O. Vasseur, S. Degraeve1, C. Granger1, and M. de Billy, "Acoustic wave localization in one-dimensional Fibonacci phononic structures with mirror symmetry," *Journal of Applied Physics*, vol. 113, p. 154901 (7pp), 2013.

[165] M. Kohmoto, L. P. Kadanoff, and C. Tang, "Localization Problem in One Dimension: Mapping and Escape," *Physical Review Letters*, vol. 50, pp. 1870–1872, Jun 1983.

[166] E. Maciá and F. Domínguez-Adame, "Physical Nature of Critical Wave Functions in Fibonacci Systems," *Physical Review Letters*, vol. 76, pp. 2957–2960, Apr 1996.

[167] I. B. Kobiakov, "Elastic, piezoelectric and dielectric properties of ZnO and CdS single crystals in a wide range of temperatures," *Solid State Communications*, vol. 35, pp. 305–310, 1980.

[168] M. S. Shur, A. D. Bykhovski, P. Gaska, and M. A. Khan, *GaN based Pyroelectronics and Piezoelectronics, in Handbook of Thin Film Devices, Volume 1: Heterostructures for High Performance Devices, Ed. , .* Colin E. C. Wood, pp 299-339, Academic Press, San Diego, 2000.

[169] R. Merlin, K. Bajema, R. Clarke, F. Juang, and P. Bhattacharya, "Quasiperiodic GaAs-AlAs Heterostructures," *Physical Review Letters*, vol. 17, pp. 1768–1770, 1985.

[170] B. Jusserand and M. Cardona, *Light Scattering in Solids V.* Springer, Berlin, 1989.

[171] Y. V. Gulyaev, "Electroacustic surface waves in solids," *JETP Lett.*, vol. 9, pp. 37–38, 1969.

[172] C. Maerfeld and P. Tournois, "Pure Shear Elastic Surface Wave Guided by the Interface of Two Semi-Infinite Media," *Appl. Phys. Lett.*, vol. 19, pp. 117–118, 1971.

[173] H. Karamitaheri, N. Neophytou, M. K. Taheri, R. Faez, and H. Kosina, "Calculation of Confined Phonon Spectrum in Narrow Silicon Nanowires Using the Valence Force Method," *Journal of Electronic Materials*, vol. 42, no. 7, pp. 2091–2097, 2013.

[174] R. Calarco, R. J. Meijers, R. K. Debnath, T. Stoica, E. Sutter, and H. Lüth, "Nucleation and growth of GaN nanowires on Si(111) performed by molecular beam epitaxy," *Nano Letters*, vol. 7, no. 8, pp. 2248–2251, 2007.

[175] R. Meijers, T. Richter, R. Calarco, T. Stoica, H.-P. Bochem, M. Marso, and H. Lüth, "GaN-nanowhiskers: MBE-growth conditions and optical properties," *Journal of Crystal Growth*, vol. 289, pp. 381–386, March 2006.

[176] C. Lieber and Z. Wang, "Functional Nanowires," *MRS Bull.*, vol. 32, pp. 99–104, 2007.

[177] S. M. Lee, Y. H. Lee, Y. G. Hwang, J. Elsner, D. Porezag, and T. Frauenheim, "Stability and electronic structure of GaN nanotubes from density-functional calculations," *Physical Review B*, vol. 60, p. 7788, 1999.

[178] J. W. Kang and H. J. Hwang, "Atomistic study of III-nitride nanotubes," *Comput. Mater. Sci.*, vol. 31, p. 237, 2004.

[179] A. Polian, M. Grimsditch, and I. Grzegory, "Elastic constants of gallium nitride," *Journal of Applied Physics*, vol. 79, p. 3343, 1996.

[180] A. F. Wright, "Elastic properties of zinc-blende and wurtzite AlN, GaN, and InN," *Journal of Applied Physics*, vol. 82, p. 2833, 1997.

[181] T. Thonhauser and G. D. Mahan, "Phonon modes in Si[111] nanowires," *Physical Review B*, vol. 69, p. 075213, 2004.

[182] H. Peelaers, B. Partoens, and F. M. Peeters, "Phonon Band Structure of Si Nanowires: A Stability Analysis," *Nano Letters*, vol. 9, pp. 107–111, 2009.

[183] S. Mizuno and N. Nishiguchi, "Acoustic phonon modes and dispersion relations of nanowire superlattices," *Journal of Physics: Condensed Matter*, vol. 21, p. 195303, 2009.

[184] H. Lange, M. Mohr, M. Artemyev, U. Woggon, and C. Thomsen, "Direct Observation of the Radial Breathing Mode in CdSe Nanorods," *Nano Letters*, vol. 8, no. 12, pp. 4614–4617, 2008.

[185] P. M. Chassaing, F. Demangeot, and N. Combe, "Raman scattering by acoustic phonons in wurzite ZnO prismatic nanoparticles," *Physical Review B*, vol. 79, p. 155314, 2009.

[186] P. Zijlstra, A. L. Tchebotareva, J. W. M. Chon, M. Gu, and M. Orrit, "Acoustic Oscillations and Elastic Moduli of Single Gold Nanorods," *Nano Letters*, vol. 8, no. 10, pp. 3493–3497, 2008.

[187] T. A. Major, A. Crut, B. Gao, S. S. Lo, N. D. Fatti, F. Vallée, and G. V. Hartland, "Damping of the acoustic vibrations of a suspended gold nanowire in air and water environments," *Phys. Chem. Chem. Phys.*, vol. 15, pp. 4169–4176, 2013.

[188] S. O. Mariager, D. Khakhulin, H. T. Lemke, K. S. Kjær, L. Guerin, L. Nuccio, C. B. Sørensen, M. M. Nielsen, and R. Feidenhans'l, "Direct Observation of Acoustic Oscillations in InAs Nanowires," *Nano Lett.*, vol. 10, pp. 2461–2465, 2010.

[189] H. Sakuma, M. Tomoda, O. Matsuda, T. Fukui, K. Tomioka, I. A. Veres, and O. B. Wright, "Acoustic Modes of GaAs Nanopillars Studied with Ultrashort Optical Pulses," *Proceedings of Symposium on Ultrasonic Electronics*, vol. 31, pp. 153–154, 2010.

[190] J. Burgin, P. Langot, A. Arbouet, J. Margueritat, J. Gonzalo, C. N. Afonso, F. Vallée, A. Mlayah, M. D. Rossell, and G. V. Tendeloo, "Acoustic Vibration Modes and Electron–Lattice Coupling in Self-Assembled Silver Nanocolumns," *Nano Letters*, vol. 8, no. 5, pp. 1296–1302, 2008.

[191] H. Staleva, S. E. Skrabalak, C. R. Carey, T. Kosel, Y. Xia, and G. V. Hartland, "Coupling to light, and transport and dissipation of energy in silver nanowires," *Physical Chemistry Chemical Physics*, vol. 11, pp. 5889–5896, 2009.

[192] C. F. Cline, H. L. Dunegan, and G. W. Henderson, "Elastic constants of hexagonal BeO, ZnS, and CdSe," *Journal of Applied Physics*, vol. 38, p. 1944, 1967.

[193] S. Q. Wang and H. Q. Ye, "First-principles study on elastic properties and phase stability of III–V compounds," *Phys. Stat. sol. (b)*, vol. 240, pp. 45–54, 2003.

[194] M. W. Larsson, J. B. Wagner, M. Wallin, P. Håkansson, L. E. Fröberg, L. Samuelson, and L. R. Wallenberg, "Strain mapping in free-standing heterostructured wurtzite InAs/InP nanowires," *Nanotechnology*, vol. 18, p. 015504 (8pp), 2007.

[195] J. R. Neighbours and G. A. Alers, "Elastic Constants of Silver and Gold," *Physical Review*, vol. 111, no. 3, pp. 707–712, 1958.

[196] C. W. Garland and K. C. Park, "LowTemperature Elastic Constants of Gallium Arsenide," *Journal of Applied Physics*, vol. 33, p. 759, 1962.

[197] Y. A. Chang and L. Himmel, "Temperature Dependence of the Elastic Constants of Cu, Ag, and Au above Room Temperature," *Journal of Applied Physics*, vol. 37, p. 3567, 1966.

[198] Y. Eckstein, A. W. Lawson, and D. H. Reneker, "Elastic Constants of Bismuth," *Journal of Applied Physics*, vol. 31, p. 1534, 1960.

[199] R. M. Martin, "Relation between Elastic Tensors of Wurtzite and Zinc-Blende Structure Materials," *Physical Review B*, vol. 6, no. 12, pp. 4546–4553, 1972.

[200] S. Cuenot, C. Frétigny, S. Demoustier-Champagne, and B. Nysten, "Surface tension effect on the mechanical properties of nanomaterials measured by atomic force microscopy," *Physical Review B*, vol. 69, p. 165410, 2004.

[201] L. G. Zhou and H. Huang, "Are surfaces elastically softer or stiffer?," *Applied Physics Letters*, vol. 84, p. 1940, 2004.

[202] G. Yun and H. S. Park, "Surface stress effects on the bending properties of fcc metal nanowires," *Physical Review B*, vol. 79, p. 195421, 2009.

[203] V. R. Velasco and F. Garcia-Moliner, "Theory of surface waves in anisotropic cubic crystals," *J. Phys. C : Solid St. Phys.*, vol. 13, pp. 2237–2256, 1980.

[204] L. Wang, A. Kiya, Y. Okuno, Y. Niidome, and N. Tamai, "Ultrafast spectroscopy and coherent acoustic phonons of Au–Ag core–shell nanorods," *J. Chem. Phys.*, vol. 134, p. 054501 (6 pp), 2011.

[205] D. Moore, J. R. Morber, R. L. Snyder, and Z. L. Wang, "Growth of Ultralong ZnS/SiO_2 Core-Shell Nanowires by Volume and Surface Diffusion VLS Process," *J. Phys. Chem. C*, vol. 112, pp. 2895–2903, 2008.

[206] O. *Landolt − Börnstein* in: Madelung, *New Series, Group III: Solid State Physics. Low Frequency Properties of Dielectric Crystals: Elastic Constants.* Springer, Berlin, 1993.

[207] P. H. Tan, K. Brunner, D. Bougeard, and G. Abstreiter, "Raman characterization of strain and composition in small-sized self-assembled Si/Ge dots," *Physical Review B*, no. 68, p. 125302 (6pp.), 2003.

[208] S. Ganesan, A. A. Maradudin, and J. Oitmaa, "A Lattice Theory of Morphic Effects in Crystals of the Diamond Structure," *Annals of Physics*, vol. 56, pp. 556–594, 1970.

[209] Y. Xu and G. Li, "Strain effect analysis on phonon thermal conductivity of two-dimensional nanocomposites," *Journal of Applied Physics*, vol. 106, p. 114302 (13pp.), 2009.

[210] A. Picco, E. Bonera, F. Pezzoli, E. Grilli, O. G. Schmidt, F. Isa, S. Cecchi, and M. Guzzi, "Composition profiling of inhomogeneous SiGe nanostructures by Raman spectroscopy," *Nanoscale Research Letters*, vol. 7, p. 633 (6pp.), 2012.

[211] E. Anastassakis, A. Pinczuk, and E. Burstein, "Effect of static uniaxial stress on the Raman spectrum of silicon," *Solid State Communications*, vol. 8, pp. 133–138, 1970.

[212] F. Cerdeira, C. J. Buchenauer, F. H. Pollak, and M. Cardona, "Stress-Induced Shifts of First-Order Raman Frequencies of Diamond- and Zinc-Blende-Type Semiconductors," *Physical Review B*, vol. 5, p. 580, 1972.

[213] R. S. Williams, G. Medeiros-Ribeiro, T. I. Kamins, and D. A. A. Ohlberg, "Chemical Thermodynamics of the Size and Shape of Strained Ge Nanocrystals Grown on Si (001)," *Accts. Chem. Res.*, vol. 32, pp. 425–433, 1999.

[214] R. Gatti, A. Marzegalli, V. A. Zinovyev, F. Montalenti, and L. Miglio, "Modeling the plastic relaxation onset in realistic SiGe islands on Si(001)," *Physical Review B*, vol. 78, p. 184104 (12pp.), 2008.

[215] N. Katcho, M.-I. Richard, M. Proietti, H. Renevier, C. Leclere, V. Favre-Nicolin, J. Zhang, and G. Bauer, "Diffraction Anomalous Fine Structure study and atomistic simulation of Ge/Si nanoislands," *Nuclear Instruments and Methods in Physics Research B*, no. 284, pp. 58–63, 2012.

[216] N. Sköld, L. S. Karlsson, M. W. Larsson, M.-E. Pistol, W. Seifert, J. Trägårdh, and L. Samuelson, "Growth and Optical Properties

of Strained GaAs−Ga$_x$In$_{1-x}$P Core−Shell Nanowires," *Nano Letters*, vol. 5, no. 10, pp. 1943–1947, 2005.

[217] K. Tateno, H. Gotoh, and Y. Watanabe, "GaAs/AlGaAs nanowires capped with AlGaAs layers on GaAs(311)B substrates," *Applied Physics Letters*, vol. 85, no. 10, pp. 1808–1810, 2004.

[218] H.-M. Lin, Y.-L. Chen, J. Yang, Y.-C. Liu, K.-M. Yin, J.-J. Kai, F.-R. Chen, L.-C. Chen, Y.-F. Chen, and C.-C. Chen, "Synthesis and Characterization of Core−Shell GaP@GaN and GaN@GaP Nanowires," *Nano Letters*, vol. 3, no. 4, pp. 537–541, 2003.

[219] L. J. Lauhon, M. S. Gudiksen, D. Wang, and C. M. Lieber, "Epitaxial core–shell and core–multishell nanowire heterostructures," *Nature*, vol. 420, pp. 57–61, 2002.

[220] W. Lu, J. Xiang, B. P. Timko, Y. Wu, and C. M. Lieber, "One-dimensional hole gas in germanium-silicon nanowire heterostructures," *Proceedings of the National Academy of Sciences*, vol. 102, pp. 10046–10051, 2005.

[221] A. K. Singh, V. Kumar, R. Note, and Y. Kawazoe, "Pristine semiconducting [110] silicon nanowires," *Nano Letters*, vol. 5, no. 11, pp. 2302–2305, 2005.

[222] J. T. Arantes and A. Fazzio, "Theoretical investigations of Ge nanowires grown along the [110] and [111] directions," *Nanotechnology*, vol. 18, p. 295706 (6pp), 2007.

[223] H.-C. Luan, D. R. Lim, K. K. Lee, K. M. Chen, J. G. Sandland, K. Wada, and L. C. Kimerling, "High-quality Ge epilayers on Si with low threading-dislocation densities," *Applied Physics Letters*, vol. 75, no. 19, pp. 2909–2911, 1999.

[224] X. Peng, F. Tang, and P. Logan, "Band structure of Si/Ge core-shell nanowires along the [110] direction modulated by external uniaxial strain," *Journal of Physics: Condensed Matter*, vol. 23, p. 115502 (8pp), 2011.

[225] D. Martínez-Gutiérrez and V. R. Velasco, "General expressions for the dispersion relation of acoustic radial (breathing) modes in cylinders and cylindrical shells of general anisotropic crystals (http://arxiv.org/pdf/1207.0379)," July 2012.

[226] D. Martínez-Gutiérrez and V. R. Velasco, "Acoustic breathing mode frequencies in cylinders, cylindrical shells and composite cylinders of general anisotropic crystals. Application to nanowires," *Physica E: Low-dimensional Systems and Nanostructures*, vol. 54, pp. 86–92, 2013.

[227] D. Martínez-Gutiérrez and V. R. Velasco, "Acoustic waves of GaN nitride nanowires," *Surface Science*, vol. 605, pp. 24–31, Jan. 2011.

[228] D. Martínez-Gutiérrez and V. R. Velasco, "Acoustic waves in (0001) III-N and MgO/ZnO superlattices," *Surface Science*, vol. 609, pp. 119–128, 2013.

[229] D. Martínez-Gutiérrez and V. R. Velasco, "Transverse acoustic waves in piezoelectric ZnO/MgO and GaN/AlN Fibonacci-periodic superlattices," *Surface Science*, vol. 624, pp. 58–69, 2014.

[230] H. Ohnishi, Y. Kondo, and K. Takayanagi, "Quantized conductance through individual rows of suspended gold atoms," *Nature*, vol. 395, p. 1998, 780.

[231] A. K. Geim and K. S. Novoselov, "The rise of graphene," *Nature Materials*, vol. 6, no. 183, 2007.

[232] M. S. Dresselhaus, Y.-M. Lin, O. Rabin, M. R. Black, J. Kong, and G. Dresselhaus, *Springer Handbook of Nanotechnology: 4 Nanowires*. Springer Berlin Heidelberg, 2010.

[233] H. J. C. Berendsen, J. P. M. Postma, W. F. Van Gunsteren, A. Di-Nola, and J. R. Haak, "Molecular dynamics with coupling to an external bath," *The Journal of Chemical Physics*, vol. 81, p. 3684, 1984.

[234] D. Evans, "The isothermal/isobaric molecular dynamics ensemble," *Physics Letters A*, vol. 98, pp. 433–436, 1983.

[235] H. C. Andersen, "Molecular dynamics simulations at constant pressure and/or temperature," *The Journal of Chemical Physics*, vol. 72, p. 2384, 1980.

[236] S. Nosé, "A molecular dynamics method for simulations in the canonical ensemble," *Molecular Physics*, vol. 52, pp. 255–268, 1984.

[237] W. Hoover, "Canonical dynamics: Equilibrium phase-space distributions," *Physical Review A*, vol. 31, pp. 1695–1697, 1985.

[238] S. Melchionna, G. Ciccotti, and B. Lee Holian, "Hoover NPT dynamics for systems varying in shape and size," *Molecular Physics*, vol. 78, pp. 533–544, 1993.

[239] H. A. Stern, "Simple algorithm for isothermal-isobaric molecular dynamics.," *Journal of computational chemistry*, vol. 25, pp. 749–761, 2004.